



Green Machining of Aerospace Grade 7075 Aluminium Alloy with Improved Tungsten Carbide and Niobium Carbide Based Cutting Tool Inserts

Madala Litshani Brian

745325

School of Mechanical, Industrial and Aeronautical Engineering

University of Witwatersrand

Johannesburg, South Africa

Supervisor: Prof. R. M. Genga

Co-supervisor: Prof. C. Polese

A dissertation submitted to the Faculty of Engineering and the Built Environment, University of the Witwatersrand, Johannesburg, South Africa in fulfillment of the requirements for the degree of Masters of Science in Mechanical Engineering


2022

DECLARATION

I Madala Litshani Brian (student number: 745325) am a student registered for the degree MSc Mechanical Engineering (full time) in the academic year 2022.

I hereby declare the following:

- I am aware of plagiarism (the use of someone's work without their permission and/or without acknowledging the original source) is wrong.
- I confirm the work submitted for assessment for the above degree is my own unaided work except where I have explicitly indicated otherwise.
- I have followed the required conventions in referencing the thoughts and ideas of others.
- I understand that the University of the Witwatersrand may take disciplinary action against me if there is a disbelief that this is not my own unaided work or that I have failed to acknowledge the source of the ideas or words in my writing.

Signature of candidate:.....

Date: 28/04/2022.....

ABSTRACT

The performances of cutting inserts produced from samples of varied compositions were investigated, Tungsten Carbide (WC) and Niobium Carbide (NbC) based inserts were compared under different test conditions. The NbC offer advantages as an alternative to WC due to the high risk of supply associated with WC. This research study compared and analyzed the effects of spark plasma sintering (SPS), liquid phase sintering (LPS), and additions of TiC and Mo₂C on machining performance of WC-Co and NbC-Ni inserts. The SPS resulted in similar Vickers Hardness (HV₃₀) and Fracture Toughness (K_{IC}) to the LPS produced WC-Co samples and the SPS slightly increased HV₃₀ for the NbC-Co samples. The additions of TiC and Mo₂C further improved HV₃₀ and K_{IC} for both WC-Co and NbC-Ni samples. The SPS and Mo₂C addition resulted in NbC-Ni sample having similar HV₃₀ to WC-Co samples. Inserts produced from the sintered samples were used for face milling of aluminium alloy 7075 at 200-800 m/min cutting speeds and 2-0.5 mm depths of cut. The feed rate was also altered to maintain a constant rate of material removal for each cutting insert. Each cutting insert machined under dry, flood, and MQL conditions for 20 minutes cutting time. Flank wear, temperatures, cutting forces, and machined surface roughness were recorded for each minute of cutting. The WC-Co inserts had lower Flank Wear Rates (FWR), machining forces (F_{R, ave}), and temperatures (T_a) than the NbC-Ni inserts during roughing, semi-finishing, and finishing under dry, flood, and MQL conditions. The SPS produced inserts had lower FWR than LPS produced inserts under dry and MQL conditions during roughing, semi-finishing, and finishing. The LPS produced inserts had lower FWR than SPS produced inserts under flood conditions during roughing, semi-finishing, and finishing. The application of MQL reduced FWR, F_{R, ave}, and T_a compared to dry during roughing, semi-finishing, and finishing. The application of flood lubrication increased FWR, F_{R, ave}, and reduced T_a compared to dry during roughing, semi-finishing, and finishing. The MQL application resulted in lower FWR, F_{R, ave}, and T_a than flood during roughing, semi-finishing, and finishing. During finishing, the SPS produced inserts achieved better surface integrity than LPS inserts under dry, flood, and MQL conditions. The application of MQL and flood lubricants increased machined surface roughness (R_a). Although the MQL produced the highest R_a, the R_a was within 0-0.9 μm.

DEDICATION

I dedicate this work to the almighty God who made the completion of this research work possible. I would also like to dedicate this work to my mother, Mrs Rhabela Violet Madala who has been my strength and support throughout the course of my research study.

ACKNOWLEDGEMENTS

I thank God for His grace, favour, and for making the completion of my research study possible.

Appreciation to family and friends for their support and motivation during hard work and perseverance towards completion of the research project.

I would like to appreciate my mother, Mrs R. V. Madala for all the support, encouragement, and motivation.

I express my deepest appreciation to my supervisors, Prof. Rodney M. Genga and Prof. Claudia Polese for their guidance, motivation, engagements, and contributions to the course of my research study. It was an honour to work and share knowledge with them.

TABLE OF CONTENTS

DECLARATION	i
ABSTRACT.....	ii
DEDICATION	iii
ACKNOWLEDGEMENTS	iv
LIST OF FIGURES	xi
LIST OF TABLES	xviii
GLOSSARY	xix
NOMENCLATURE	xxi
Chapter 1: Introduction	1
1.1 Purpose of study.....	1
1.2 Background of Study	1
1.2.1 Cemented Carbides Background.....	1
1.2.2 Tool Failure.....	2
1.2.3 Lubrication.....	2
1.3 Research Motivation	3
1.4 Dissertation Outline	4
Chapter 2: Literature Review	6
2.1 History of Aluminium and Classification of 7075 Aluminium Alloy	6
2.1.1 Effects of Alloying Elements.....	7
2.1.2 Machinability of AA7075	8
2.1.2.1 Cutting Forces	9
2.1.2.2 Tool Life	10
2.1.2.3 Surface Roughness.....	10
2.2 Carbide-Based Cutting Inserts	10
2.2.1 Tungsten Carbide	14
2.2.2 Niobium Carbide.....	16
2.3 Milling and Mixing Carbide Powders.....	16
2.4 Sintering Techniques	17
2.4.1 Spark Plasma Sintering	19

2.4.2 Liquid Phase Sintering	22
2.4.3 SPS versus LPS	26
2.5 Mechanical Properties	26
2.5.1 Hardness	26
2.5.2 Fracture Toughness	27
2.6 Carbide Additives	27
2.7 Wear Mechanisms	27
2.7.1 Abrasive Wear	27
2.7.2 Adhesive Wear	28
2.7.3 Diffusive Wear	28
2.7.4 Chemical Wear	28
2.7.5 Wear due to Plastic Deformation	28
2.8 Tool Wear	28
2.8.1 Crater Wear	29
2.8.2 Flank Wear	29
2.8.3 Chipping	30
2.8.4 Notch	30
2.9 CNC Milling Machine	30
2.10 Machining Parameters	31
2.10.1 Cutting Speed	31
2.10.2 Feed Rate	33
2.10.3 Depth of Cut	34
2.11 Lubrication	35
2.11.1 Flood	35
2.11.2 MQL	35
Chapter 3: Objectives	37
Chapter 4: Apparatus	38
4.1 Workpiece Preparation	38
4.2 Cemented Carbides (Cutting inserts)	39

4.3 Insert Holder (Tool)	42
4.4 GX1000 CNC Machine.....	42
4.5 Kistler Dynamometer.....	43
4.6 Flir Thermal Imaging Camera.....	44
4.7 Emissivity Test.....	45
4.8 Flank Wear Measurements.....	46
4.9 Surface Roughness.....	47
4.10 Lubricant Analysis	47
Chapter 5: Experimental Procedures.....	49
5.1 Face Milling Test Conditions.....	49
5.2 Force Measurement.....	52
5.2.1 Kistler Dynamometer Calibration.....	52
5.2.2 Precautions.....	53
5.3 CNC Face Milling.....	53
5.3.1 Workpiece Machining.....	53
5.3.2 Precautions.....	54
5.4 Lubrication.....	54
5.4.1 Dry Conditions.....	54
5.4.2 Flood Lubricating Condition.....	54
5.4.3 MQL Lubricating Conditions.....	55
5.4.4 Precautions.....	55
5.5 Temperature Measurement.....	56
5.5.1 Flir Thermal Imaging Camera Calibration (Emissivity test).....	56
5.5.2 Measurement.....	56
5.5.3 Precautions.....	57
5.6 Surface Roughness.....	57
5.6.1 Roughness Measurements.....	57
5.6.2 Precautions.....	58
5.7 Insert Wear Measurement.....	58

5.7.1 Flank Wear Measurement	58
5.7.2 Precautions	59
5.8 Flood and MQL analysis.....	59
5.8.1 Sample Preparation	60
5.8.1.1 Precudure	60
5.8.1.2 Precautions.....	60
5.8.2 Lubricant analysis	60
5.8.2.1 Procedure	60
5.8.2.2 Precautions.....	60
Chapter 6: Data Processing.....	61
6.1 Cutting Forces	61
6.2 Cutting Temperatures.....	62
6.3 Flank Wear Rates.....	63
6.4 Surface Roughness.....	63
Chapter 7: Results	65
7.1 Mechanical Properties.....	65
7.1.1 Hardness (HV ₃₀).....	66
7.1.1.1 Hardness of WC-Cr ₃ C ₂ -Co sample	66
7.1.1.2 Hardness of WC-Mo ₂ C-TiC-Co sample	66
7.1.1.3 Hardness of NbC-TiC-Ni sample.....	66
7.1.1.4 Hardness of NbC- Mo ₂ C-TiC-Ni sample	66
7.1.2 Fracture Toughness (K _{1C})	67
7.1.2.1 Fracture Toughness of WC-Cr ₃ C ₂ -Co sample	67
7.1.2.2 Fracture Toughness of WC-Mo ₂ C-TiC-Co sample.....	67
7.1.2.3 Fracture Toughness of NbC-TiC-Ni sample	67
7.1.2.4 Fracture Toughness of NbC- Mo ₂ C-TiC-Ni sample	67
7.2 Flank Wear Rates.....	68
7.3 Roughing.....	69
7.3.1 Dry	69
7.3.2 Flood	73
7.3.3 MQL.....	78
7.3.4 Dry versus Flood.....	83

7.3.5 Dry versus MQL	84
7.3.6 Flood versus MQL	85
7.3.7 Overall Analysis of Roughing.....	86
7.4 Semi-Finishing.....	87
7.4.1 Dry	87
7.4.2 Flood	91
7.4.3 MQL.....	96
7.4.4 Dry versus Flood.....	101
7.4.5 Dry versus MQL	101
7.4.6 Flood versus MQL	103
7.4.7 Overall Analysis of Semi-Finishing.....	103
7.5 Finishing	104
7.5.1 Dry	105
7.5.2 Flood	111
7.5.3 MQL.....	117
7.5.4 Dry versus Flood.....	123
7.5.5 Dry versus MQL	125
7.5.6 Flood versus MQL	126
7.5.7 Overall Analysis of finishing	128
7.6 Lubricant Analysis.....	129
7.6.1 Flood Lubricants	129
7.6.2 Minimum Quantity Lubricant.....	130
Chapter 8: Discussion	131
8.1 Mechanical Properties of WC and NbC based inserts	131
8.1.1 Hardness.....	131
8.1.2 Fracture Toughness.....	132
8.2 Flank Wear Rate	132
8.3 Roughing.....	132
8.3.1 Tool Wear	133

8.3.2 Average Resultant Force.....	133
8.3.3 Average Temperature.....	134
8.4 Semi-Finishing.....	135
8.4.1 Tool Wear	135
8.4.2 Average Resultant Force.....	135
8.4.3 Average Temperature.....	136
8.5 Finishing	137
8.5.1 Tool Wear	137
8.5.2 Average Resultant Force.....	138
8.5.3 Average Temperature.....	139
8.5.4 Average Surface Roughness	139
Chapter 9: Conclusion and recommendations	140
9.1 Conclusion	140
9.2 Recommendations.....	141
References.....	142

LIST OF FIGURES

Figure 2.1. Graph of average thrust forces (F_z) at different cutting speeds during drilling of Al alloys 6061-T6, 7075-T6, A356-T0, and A319-T0 (Kouam et al., 2010)..... 9

Figure 2.2. Graph of average thrust forces (F_z) at different feed rates and cutting speeds during drilling for AA7075 (Songmene et al., 2011)..... 10

Figure 2.3. Number of times a country is the leading global producer of group of elements of economic value (Survey, 2015)..... 12

Figure 2.4. Percentage share of consumption of elements of tungsten (W) worldwide (Garside, 2019) 12

Figure 2.5. Illustrated tungsten percentage use in each industry internationally in 2017 (Reutte, 2017) 13

Figure 2.6. Hardness ranks of minerals and technical compounds (Woydt & Mohrbacher, 2014)..... 17

Figure 2.7. Neck formation and resulted grain growth (German et al., 2006)..... 19

Figure 2.8. Neck growth between spherical particles as a function of sintering dwell time and temperature (German et al., 2006) 21

Figure 2.9. Spark Plasma Sintering chamber (TotalMateria, 2012)..... 21

Figure 2.10. Spark Plasma Sintering equipment setup (Mamedov, 2002)..... 22

Figure 2.11. Spark plasma sintered samples (TotalMateria, 2012)..... 22

Figure 2.12. The microstructure of changes that occur during the LPS process (German et al., 2009) 23

Figure 2.13. a) Contact angles indicating good and poor wetting, and b) compact swelling and binder phase coming out of the sample due to poor wettability during the LPS process (German et al., 2009) 24

Figure 2.14. Densification at 1600 °C for alumina-glass with different liquid vol.% (German et al., 2009; Kwon & Messing, 1990)..... 25

Figure 2.15. LPS of alumina-glass with 10% liquid volume at 1600 °C with different particle sizes (Mataix, 2016)..... 25

Figure 2.16. Flank and rake faces where flank and crater wear occur (Viktor, 2011)..... 29

Figure 2.17. Measures of crater and flank wear (Dadic, 2013)..... 30

Figure 2.18. Cutting force decrease as the cutting speed increase (Mohammad et al., 2017) 32

Figure 2.19. Graph of cutting speed against cutting edge temperature at different depths of cut (Mohammad et al., 2017)..... 32

Figure 2.20. The change of the resultant cutting force (FR) as a function of feed rate at different cutting speeds (Altas & Caliskan, 2016)..... 33

Figure 2.21. Schematic diagram of milling process. Note, a_p is the axial depth of cut and a_e is the radial depth of cut (Muhammad et al., 2017)..... 34

Figure 2.22. Axial depth of cut versus machining time and surface roughness for mild steel (Baskar, 2010).....	34
Figure 2.23. Donhad polluted coolant waste bin (Ginting et al., 2015).....	35
Figure 4.1. Third angle orthogonal projection of the AA7075 plate with dimensions 1000 x 990 x 20mm	38
Figure 4.2. Third angle orthogonal projection of the workpiece with dimensions 200 x 160 x 20mm	38
Figure 4.3. Startrite 30RWH, model 600 band-saw machine	39
Figure 4.4. a) Cutting insert used during machining and b) insert holder used to hold inserts during wear measurements.....	41
Figure 4.5. Inserts drawing with dimensions.	41
Figure 4.6. Cutting tool.....	42
Figure 4.7. a) The Bridgeport GX1000 CNC machine and b) the Fanuc series oi-MC control panel..	42
Figure 4.8. a) Dry, b) Flood and c) MQL lubricating conditions during machining trials	43
Figure 4.9. Kistler 5697A DAQ System and Multi-Channel Charge Amplifier.....	44
Figure 4.10. Thermal Imaging Camera.....	44
Figure 4.11. Elite Thermal Systems Furnace.....	45
Figure 4.12. Thermometer, Silicone Gel, K-Type fluke thermocouples, and Heat resistant tape	45
Figure 4.13. Nikon SMZ1500 Optical Microscope	46
Figure 4.14. Computer desktop connected to the Nikon SMZ1500 optical microscope	46
Figure 4.15. SRT-6210 roughness tester.....	47
Figure 4.16 a) Leco GCxGC-TOF Low resolution mass spectrophotometer and b) Sample holder	48
Figure 6.1. Calibration curve showing average resultant force versus time for the first 40 seconds of the calibration run	62
Figure 7.1. Graph of sample hardness (HV_{30}) against fracture toughness (K_{IC}).....	66
Figure 7.2. Maximum flank wear of a) G1-L, b) G1-S, c) R1-L, d) M1-L and e) W1-S inserts after dry roughing at cutting speed of 200 m/min and 2 mm depth of cut	70
Figure 7.3. Graph of maximum flank wear (VB_{Max}) against cutting time during dry roughing	70
Figure 7.4. Graph of flank wear rate (FWR) against insert hardness (HV_{30}) during dry roughing	71
Figure 7.5. Graph of flank wear rate (FWR) against Fracture toughness (K_{IC}) for dry roughing.....	71
Figure 7.6. Graph of average resultant force ($F_{R, ave}$) against flank wear rate (FWR) during dry roughing	72
Figure 7.7. Graph of average Temperature (T_a) against flank wear rate (FWR) during dry roughing .	72
Figure 7.8. Graph of average resultant force ($F_{R, ave}$) against insert hardness for dry roughing.....	73
Figure 7.9. Graph of average resultant force ($F_{R, ave}$) against Fracture toughness (K_{IC}) during dry roughing	73
Figure 7.10. Maximum flank wear of a) R1-L, b) M1-S, c) W1-L and d) W1-S inserts after flood roughing at cutting speed of 200 m/min and 2 mm depth of cut	75

Figure 7.11. Graph of maximum flank wear (VB_{Max}) against cutting time during flood roughing	75
Figure 7.12. Graph of flank wear rate (FWR) against insert hardness (HV_{30}) during flood roughing .	76
Figure 7.13. Graph of flank wear rate (FWR) against insert fracture toughness (K_{IC}) during flood roughing	76
Figure 7.14. Graph of average resultant force ($F_{R, ave}$) against flank wear rate (FWR) during flood roughing	77
Figure 7.15. Graph of average resultant force ($F_{R, ave}$) against insert hardness (HV_{30}) during flood roughing	77
Figure 7.16. Graph of average resultant force ($F_{R, ave}$) against fracture toughness (K_{IC}) during flood roughing	78
Figure 7.17. Maximum flank wear of a) G1-L, b) G1-S, c) R1-L, d) M1-L, and e) W1-S inserts after MQL roughing at cutting speed of 200 m/min and 2 mm depth of cut.....	79
Figure 7.18. Graph of maximum flank wear ($V_{B max}$) against cutting time (min) during MQL roughing	80
Figure 7.19. Graph of flank wear rate (FWR) against insert hardness (HV_{30}) during MQL roughing .	80
Figure 7.20. Graph of flank wear rate (FWR) against fracture toughness (K_{IC}) during MQL roughing	81
Figure 7.21. Graph of average resultant force ($F_{R, ave}$) against flank wear rate (FWR) during MQL roughing	81
Figure 7.22. Graph of average temperature (T_a) against flank wear rate (FWR) during MQL roughing	82
Figure 7.23. Graph of average resultant force ($F_{R, ave}$) against insert hardness (HV_{30}) during MQL roughing	82
Figure 7.24. Graph of average resultant force ($F_{R, ave}$) against fracture toughness (K_{IC}) during MQL roughing	83
Figure 7.25. Graph of average resultant force ($F_{R, ave}$) against flank wear rate (FWR) during dry and flood roughing.....	84
Figure 7.26. Graph of average resultant force ($F_{R, ave}$) against flank wear rate (FWR) during dry and MQL roughing	84
Figure 7.27. Graph of average temperature (T_a) against flank wear rate (FWR) during dry and MQL roughing	85
Figure 7.28. Graph of average resultant force ($F_{R, ave}$) against flank wear rate (FWR) during flood and MQL roughing	85
Figure 7.29. Maximum flank wear of a) G1-L, b) G1-S, c) R1-L, d) M1-L, and e) W1-S inserts after dry semi-finishing at cutting speed of 400 m/min and 1 mm depth of cut	88
Figure 7.30. Graph of flank wear (VB_{Max}) against cutting time (min) during dry semi-finishing	88

Figure 7.31. Graph of flank wear rate (FWR) against insert hardness (HV_{30}) during dry semi-finishing	89
Figure 7.32. Graph of flank wear rate (FWR) against fracture toughness (K_{IC}) during dry semi-finishing	89
Figure 7.33. Graph of average resultant force ($F_{R, ave}$) against flank wear rate (FWR) during dry semi-finishing	90
Figure 7.34. Graph of average temperature (T_a) against flank wear rate (FWR) during dry semi-finishing	90
Figure 7.35. Graph of average resultant force ($F_{R, ave}$) against insert hardness (HV_{30}) during dry semi-finishing	91
Figure 7.36. Graph of average resultant force ($F_{R, ave}$) against fracture toughness (K_{IC}) during dry semi-finishing	91
Figure 7.37. Maximum flank wear of a) R1-L, b) M1-L, c) W1-L and d) W1-S inserts after flood semi-finishing at cutting speed of 400 m/min and 1 mm depth of cut.....	92
Figure 7.38. Graph of maximum flank wear (VB_{Max}) against cutting time (min) during flood semi-finishing	93
Figure 7.39. Graph of flank wear rate (FWR) against insert hardness (HV_{30}) during flood semi-finishing	93
Figure 7.40. Graph of flank wear rate (FWR) against fracture toughness (K_{IC}) during flood semi-finishing	94
Figure 7.41. Graph of average resultant force ($F_{R, ave}$) against flank wear rate (FWR) during flood semi-finishing	94
Figure 7.42. Graph of average resultant force ($F_{R, ave}$) against insert hardness (HV_{30}) during flood semi-finishing	95
Figure 7.43. Graph of average resultant force ($F_{R, ave}$) against fracture toughness (K_{IC}) during flood semi-finishing	95
Figure 7.44. Maximum flank wear of a) G1-L, b) G1-S, c) R1-L, d) M1-L, W1-L, and f) W1-S inserts after MQL semi-finishing at cutting speed of 400 m/min and 1 mm depth of cut.....	97
Figure 7.45. Graph of Flank wear (VB_{Max}) against cutting time (min) during MQL semi-finishing....	97
Figure 7.46. Graph of flank wear rate (FWR) against insert hardness (HV_{30}) during MQL semi-finishing	98
Figure 7.47. Graph of flank wear rate (FWR) against fracture toughness (K_{IC}) during MQL semi-finishing	98
Figure 7.48. Plot of average resultant force ($F_{R, ave}$) against flank wear rate (FWR) during MQL semi-finishing	99
Figure 7.49. Graph of average Temperature (T_a) against flank wear rate (FWR) during MQL semi-finishing	99

Figure 7.50. Graph of average resultant force ($F_{R, ave}$) against insert hardness (HV_{30}) during MQL semi-finishing	100
Figure 7.51. Graph of average resultant force ($F_{R, ave}$) against fracture toughness (K_{IC}) during MQL semi-finishing.	100
Figure 7.52. Graph of average resultant force ($F_{R, ave}$) against flank wear rate (FWR) during dry and flood semi-finishing	101
Figure 7.53 Graph of average resultant force ($F_{R, ave}$) against flank wear rate (FWR) during dry and MQL semi-finishing.....	102
Figure 7.54. Graph of average temperature (T_a) against flank wear rate (FWR) during dry and MQL semi-finishing	102
Figure 7.55. Graph of average resultant force ($F_{R, ave}$) against flank wear rate (FWR) during flood and MQL semi-finishing.....	103
Figure 7.56. Maximum flank wear of a) G1-L, b) G1-S, c) R1-L, d) M1-L, and e) W1-S inserts after dry finishing at cutting speed of 800 m/min and 0.5 mm depth of cut	106
Figure 7.57. Graph of maximum flank wear (VB_{Max}) against cutting time (min) during dry finishing	106
Figure 7.58. Graph of flank wear rate (FWR) against insert hardness (HV_{30}) during dry finishing... ..	107
Figure 7.59. Graph of flank wear rate (FWR) against insert fracture toughness (K_{IC}) during Dry finishing	107
Figure 7.60. Graph of average resultant force ($F_{R, ave}$) against flank wear rate (FWR) during dry finishing	108
Figure 7.61. Graph of average Temperature (T_a) against flank wear rate (FWR) during dry finishing	108
Figure 7.62. Graph of average surface roughness (R_a) against flank wear rate (FWR) during dry finishing	109
Figure 7.63. Graph of average surface roughness (R_a) against average resultant force ($F_{R, ave}$) during dry finishing	109
Figure 7.64. Graph of average surface roughness (R_a) against average temperature (T_a) during dry finishing	110
Figure 7.65. Graph of average resultant force ($F_{R, ave}$) against insert hardness (HV_{30}) during dry finishing	110
Figure 7.66. Graph of average resultant force ($F_{R, ave}$) against fracture toughness (K_{IC}) during dry finishing	111
Figure 7.67. Maximum flank wear of a) G1-L, b) G1-S, c) R1-L, d) M1-L, e) W1-L, and f) W1-S inserts after flood finishing at cutting speed of 800 m/min and 0.5 mm depth of cut.....	112
Figure 7.68. Graph of maximum flank wear (VB_{Max}) against time (min) during flood finishing.....	113
Figure 7.69. Graph of flank wear rate (FWR) against insert hardness (HV_{30}) during flood finishing 113	

Figure 7.70. Grap of flank wear rate (FWR) against fracture toughness (K_{IC}) during flood finishing	114
Figure 7.71. Graph of average resultant force ($F_{R, ave}$) against flank wear rate (FWR) during flood finishing	114
Figure 7.72. Graph of average surface roughness (R_a) against flank wear rate (FWR) during flood finishing	115
Figure 7.73. Graph of average surface roughness (R_a) against average resultant force ($F_{R, ave}$) during flood finishing	115
Figure 7.74. Graph of average resultant force ($F_{R, ave}$) against insert hardness (HV_{30}) during flood finishing	116
Figure 7.75. Graph of average resultant force ($F_{R, ave}$) against fracture toughness (K_{IC}) during flood finishing	116
Figure 7.76. Maximum flank wear of a) G1-L, b) G1-S, c) R1-L, d) M1-L, e) W1-L, and f) W1-S inserts after MQL finishing at cutting speed of 800 m/min and 0.5 mm depth of cut	118
Figure 7.77. Graph of maximum flank wear (VB_{Max}) against cutting time during MQL finishing	118
Figure 7.78. Graph of flank wear rate (FWR) against insert hardness (HV_{30}) during MQL finishing	119
Figure 7.79. Graph of flank wear rate (FWR) against fracture toughness (K_{IC}) during MQL finishing	119
Figure 7.80. Graph of average resultant force ($F_{R, ave}$) against flank wear rate (FWR) during MQL finishing	120
Figure 7.81. Graph of average temperature (T_a) against flank wear rate (FWR) during MQL finishing	120
Figure 7.82. Graph of average surface roughness (R_a) against flank wear rate (FWR) during MQL finishing	121
Figure 7.83. Graph of average surface roughness (R_a) against average resultant force ($F_{R, ave}$) for MQL finishing	121
Figure 7.84. Graph of average surface roughness (R_a) against average temperature (T_a) during MQL finishing	122
Figure 7.85. Graph of average resultant force ($F_{R, ave}$) against insert hardness (HV_{30}) during MQL finishing	122
Figure 7.86. Graph of average resultant force ($F_{R, ave}$) against fracture toughness (K_{IC}) during MQL finishing	123
Figure 7.87. Graph of average resultant force ($F_{R, ave}$) against flank wear rate (FWR) during dry and flood finishing	124
Figure 7.88. Graph of average surface roughness (R_a) against flank wear rate (FWR) during dry and flood finishing	124
Figure 7.89. Graph of average resultant force ($F_{R, ave}$) against flank wear rate (FWR) during dry and MQL finishing	125

Figure 7.90. Graph of average temperature (T_a) against flank wear rate (FWR) during dry and MQL finishing	126
Figure 7.91. Graph of average surface roughness (R_a) against flank wear rate (FWR) during dry and MQL finishing	126
Figure 7.92. Graph of average resultant force ($F_{R, ave}$) against flank wear rate (FWR) during flood and MQL finishing	127
Figure 7.93. Graph of average surface roughness (R_a) against flank wear rate (FWR) during flood and MQL finishing	127

LIST OF TABLES

Table 2.1 Listed AA7075 alloying elements and their corresponding chemical compositions	7
Table 2.2. Current Risk of supply of chemical or element groups which are of economic value (Survey, 2015)	11
Table 2.3. Principal Physical properties of Niobium Carbide compared to Tungsten Carbide	13
Table 2.4. Summary of health and safety classifications (Niobelcon, 2007).....	15
Table 2.5. SPS vs LPS	26
Table 4.1. Cutting inserts and the edges used for each machining criterion.....	40
Table 5.1: Milling test conditions, apply dry, flood, and MQL lubricating conditions for rouging, semi-finishing, and finishing. Test no. are machining test counts.....	50
Table 5.2: Inserts abbreviations and their compositions.....	51
Table 5.3: Calculated constant rate of material removal in volume.....	51
Table 7.1. Compositions and mechanical properties of cutting samples	65
Table 7.2. Flank wear rates (FWR) of each insert after face milling.....	68
Table 7.3: Comparison of VB_{Max} , FWR, $F_{R, ave}$, and T_a during dry roughing.....	69
Table 7.4. Comparison of VB_{Max} , FWR, and $F_{R, ave}$ during flood roughing	74
Table 7.5: Comparison of VB_{Max} , FWR, $F_{R, ave}$, and T_a during MQL roughing	79
Table 7.6: Comparison of VB_{Max} , FWR, $F_{R, ave}$, and T_a during dry semi-finishing.....	87
Table 7.7: Comparison of VB_{Max} and FWR, $F_{R, ave}$ during flood semi-finishing.	92
Table 7.8. Comparison of VB_{Max} , FWR, $F_{R, ave}$, and T_a during MQL semi-finishing.	96
Table 7.9. Comparison of VB_{Max} , $F_{R, ave}$, T_a , and R_a during dry finishing.....	105
Table 7.10. Comparison of VB_{Max} , $F_{R, ave}$, and R_a during flood finishing.....	112
Table 7.11. Comparison of VB_{Max} , FWR, $F_{R, ave}$, T_a , and R_a during flood finishing	117

GLOSSARY

Al	Aluminium
WC	Tungsten Carbide
W	Tungsten
Co	Cobalt
NbC	Niobium Carbide
Ni	Nickel
Binder	A material added to the mixture of carbide powders that is partially or fully melted to cement solid powder particles together increasing the ductility and strength of the final sintered composite material
Vickers Hardness	Indentation test performed to measure material's hardness using a diamond pyramid
Fracture Toughness	Material's resistance to crack propagation
n	Total number of
z	Number of teeth
wt. %	Weight Percentage
vol. %	Volume Percentage
μF	Micro Farad
kV	Kilo Volts
kA	Kilo Ampere

NOMENCLATURE

SYMBOL	DESCRIPTION	UNIT
R_a	Surface Roughness	μm
$R_{a, \text{ave}}$	Average Surface Roughness	μm
R_t	Maximum height of the roughness profile	μm
R_q	Root mean square roughness	μm
R_z	Average maximum height of the roughness profile	μm
σR_a	Standard deviation for surface roughness	μm
$R_{a, \text{error}}$	Standard error in surface roughness	μm
HV_{30}	Vickers Hardness	GPa
K_{IC}	Fracture Toughness	$\text{MPa}\cdot\text{m}^{1/2}$
t	Tool Life	min
F_R	Resultant Force	N
F_X	Force in the x-axis direction	N
F_Y	Force in the y-axis direction	N
F_Z	Force in the z-axis direction	N
$F_{R, \text{ave}}$	Average Resultant Force	N
T_{Max}	Maximum temperature	$^{\circ}\text{C}$
T_a	Average Temperature	$^{\circ}\text{C}$
T_{ERROR}	Error in temperature	$^{\circ}\text{C}$
FWR	Flank wear rate	μm
N	Spindle speed	RPM
v_c	Cutting speed	m/min
v_f	Feed rate	m/min
VB_{max}	Maximum flank wear	μm
f_z	Feed per tooth	mm

SYMBOL	DESCRIPTION	UNIT
a_e or a_r or R_d	Radial depth of cut	mm
a_p	Axial depth of cut	mm
$n_{critical}$	Critical Ball Spindle Speed	RPM
D	Mill ball diameter	mm
d	Cutting width	mm

Chapter 1: Introduction

1.1 Purpose of study

Cemented carbides have a remarkable history in machining and industrial productions with application in the aerospace, transport, and automotive industries. The interest in cemented carbides is in their combination of mechanical properties. Cemented carbides are made of hard and brittle material (carbide) and a more ductile material (binder metal) which are mixed, pressed together, and sintered into a composite cutting material (Prakash & Vinod, 2014). Mechanical properties of cemented carbides such as hardness (HV_{30}), transverse rupture toughness (TRS), and fracture toughness (K_{IC}) are improved in different ways including heat treatments and addition of different additives at different weight percentages (wt.%). The common carbide additives include Mo_2C , TiC, VC, and Cr_3C_2 (Upadhyaya et al., 1998) which have been reported to alter physical properties of carbide powders such as crystal structure, morphology, particle sizes as well as the catalytic behavior in carbide production (Souto et al., 2018).

The most common and preferred compositions of cemented carbides are Tungsten Carbide (WC) and Cobalt (Co). However, the main concerns with the application of WC and Co are firstly the lack of supply of Tungsten (W) and Co which are considered minerals of economic value (Upadhyaya et al., 1998). The second main concern is the potential harsh behaviour that WC and Co may have on the environment and workers (Norgren et al., 2015). The third challenge is the cost implications and health hazards associated with flood lubrication (Boubekri & Shaikh, 2014). These concerns will be discussed in this reading in attempt to compare and report alternative lubricating conditions, carbides, and binding metals with good comparable mechanical properties. Green machining of 7075 aluminium alloy is the main objective of this research study with the use of improved WC and Niobium Carbide (NbC) based inserts. Green machining refers to the use of vegetable oils for lubrication during machining and compare with flood and dry machining (Boubekri & Shaikh, 2014). This study investigates the possibility of NbC in place of WC, Nickel (Ni) in place of Co, and Minimum Quantity Lubrication (MQL) in place of flood lubrication.

1.2 Background of Study

1.2.1 Cemented Carbides Background

Cemented carbides are useful in different industries that practice machining of the aerospace aluminium alloy 7075-T6. The interest in cemented carbides is for their combination of toughness (their ability to deform plastically, absorbing energy without failure) and hardness (their ability to withstand certain loads without plastically deforming) (Upadhyaya et al., 1998). Cemented carbides are manufactured by

a powder metallurgy process where a carbide powder and a binding metal are mixed, pressed, and sintered into a dense composite material.

The most common composites of cemented carbides are WC and Co. Tungsten carbide is the hard component while cobalt is the tough component. Cutting inserts manufactured from WC-Co composite are reported to have a good combination of hardness (HV_{30}) and fracture toughness (K_{IC}) (Sun et al., 2019). However, in many cases, a good solubility has been realised between Co and Al at high machining temperatures (Yan et al., 2008) initiating chemical wear hence reducing the shelf life of the cutting inserts (Upadhyaya et al., 1998). Cobalt has also been reported to be carcinogenic with the potential to cause lung cancer (Norgren et al., 2015). Advantages of NbC over WC include better chemical stability with Nickel (Ni) binder metal (Huang et al., 2015), NbC is less dense (weight, $1/2\rho_{(WC)}$), and NbC has less environmental and health risks while Tungsten Oxides (eg. WO_3) are suspected to be carcinogenic (Huang, S et al., 2016).

1.2.2 Tool Failure

Inserts fail when subjected to unfavourable machining conditions. Tool failures can be categorised into three modes which include fracture failure (due to high thrust forces), temperature failure (high temperature rises) and gradual wear (crater wear and flank wear) (Snowball & Millner, 1968). Gradual and temperature failures are resultants of tool-workpiece friction at high cutting speeds (Popa et al., 2012). Gradual wear is the most tolerable since it allows longer use of inserts whereas fracture failure and temperature failure (also referred to as premature failures) require immediate insert replacement (Nelson & Millner, 1972). Machining parameters determine the shelf life of inserts and the success of machining processes. These parameters include cutting speeds, feed rates, rake angles, and the depth of cutting; the responses observed thereafter are temperature rises (result of friction at high cutting speeds), cutting forces (function of feed rates), and roughness of machined surfaces.

This research study focuses on three parameters, cutting speed, feed rate, and depth of cutting. The condition of a cutting can be monitored throughout the machining process directly by the use of optical microscopic scales Secondary Electronic Microscope (SEM), or indirectly by monitoring physical responses such as temperatures (using Thermal Imaging Camera), cutting forces (using Kistler Force Plate), and surface roughness (using surface roughness tester) (Straffelini, 2015). Direct methods are only applicable in laboratory and indirect methods are used in industry (Snowball & Millner, 1968).

1.2.3 Lubrication

The first lubricant development known as heavy steam lubrication was reported to improve the cutting speed by a factor of 2 or 3 enabling machining at lower cutting forces (Boubekri & Shaikh, 2014). Flood cooling is the traditional technique applied for lubricating, cooling, and clearing chips during machining

practices. Generally, mechanical and chemical advantages of lubricants include lowered cutting temperatures, enhanced dimensional stability (ability to withstand high temp) (Zadshakoyan & Pourmostaghimi, 2015), prevents chip welding on the insert which further improves dimensional stability (Jantunem, 2002), clearing away chips to improve tool efficiency (MaClure et al., 2007), reduced friction (Carter, 2013), surface finish (Dewes et al., 1999), and makes automated material handling practical (Lawal et al., 2013).

Flood coolants have been reported to be expensive to purchase and maintain; they have also been reported to pose environmental and health threats (Boubekri & Shaikh, 2014). Flood lubricant maintenance includes drying wet chips before the coolant can be disposed of or recycled for reuse. Green ways of disposal are rather costly. It is imperative to investigate better alternatives and ways to minimise the use of lubricants. The Minimum Quantity Lubrication (MQL) also known as micro-lubrication applies a coolant at low flow rates (50-500ml/hr) reducing the amount of use significantly (Boubekri & Shaikh, 2014) and still achieves adequate cooling and lubrication. The MQL oil to be investigated in the course of this study was manufactured from natural vegetable oils and pose minimal environmental threats hence facilitating green machining.

The MQL technique ensures coolant evaporation on application (leaving a cooling effect on the tool-workpiece interface) producing dry chips and the cost of maintenance is saved (Wang & Clarens, 2013). Coolants can be applied internally through the cutting tool or with a separate nozzle and the former is reported to achieve better lower temperatures (Da Silva et al., 2013). Other benefits of MQL include: reduced cutting forces for milling and drilling (Naves et al., 2013), 15% operation costs cut off (Leo Dev Wins & Varadarajan, 2012), minimised wear (Ghani et al., 2013), better operation at high cutting speeds, enhanced cutting performance, and lowered temperatures (Siniawski & Bowman, 2009).

1.3 Research Motivation

The great interest in aluminium alloys is in their characteristic properties; good mechanical strength, low density (good strength-weight ratio), fairly good machinability, and high corrosion resistance. Aluminium is of great use in the aerospace industry providing great performances and lower operating costs. However, Al alloys faced a decline in use in the aerospace industry threatened by a potential substitute known as graphite composites according to Harradine et al. (Harradine & Quinlivan, 1989). Graphite Epoxy Composites were introduced and standardised for the primary structure of aeroplanes, which are less dense and giving 20% better fuel efficiency (Harradine & Quinlivan, 1989).

Aluminium products/alloys proved to be less costly to produce as compared to composites and the use of composites for a complete aeroplane structure would be costly. The ideal way to cut costs of production and maintenance of composites was to couple them with aluminium alloys (including

AA7075). However, combining AA7075 with graphite composites was later realised to magnify corrosion caused by a galvanic cell created between the two hence a significant increase in operating and maintenance costs (Warren, 2004). Composites are not compatible with AA7075 which calls for improvements or elimination of composites and return to the use of AA7075. Inert organic fibres with high modulus were reported to be some of the few possible future alternatives for composites however they were still in research development (Warren, 2004).

The limited availability and lack of supply (import) of tungsten (W) and Cobalt (Co) in South Africa and the rest of the world is a drive for this research to investigate alternative metal elements with similar mechanical properties. China is ranked the most producing of W and Co, leading global producer of more than 60% of manufacturing firms worldwide (Survey, 2015).

This study investigates green machining of AA7075 with improved WC & NC based inserts with the aim to replace WC with NbC and Co with Ni in attempt to avoid the lack of supply associated with W and Co elements and to eliminate the potential environmental and health problems associated with Co and tungsten oxides (WO_3). This research study also looks into the possible ways to cut down cost of machining production by improving the tool life with the focus on machining conditions and MQL lubrication. Another objective of this research study is to reduce the costs by minimizing the use of lubricants and introducing the MQL application technique. The MQL technique also ensures elimination of health problems associated with flood cooling lubricants. The improved inserts with longer shelf life will support and improve the high volumes of AA7075 material production for new airplanes and for maintenance. Lubrication with MQL will also help improve the tool life and improve the rates of production of AA7075 materials significantly.

1.4 Dissertation Outline

This study attempts to optimise the machining parameters for face milling of AA7075 and performance analysis and comparison between WC-Co and NbC-Ni cutting inserts. The cutting inserts were produced by Liquid Phase Sintering (LPS) and Spark Plasma Sintering (SPS) and carbide additives were added to WC-Co and NbC-Ni aiming to improve mechanical properties. The effects of mechanical properties on tool wear, cutting forces, and temperatures were investigated and correlations were drawn from results. In this study, face milling was conducted under dry, flood, and MQL conditions. The MQL and flood lubricants were applied during roughing, semi-finishing, and finishing in an attempt to reduce cutting forces, temperatures, surface roughness (R_a), clearing chips, and prolong tool life of cutting inserts. The measurements taken were analysed and the effects of MQL and flood were compared to dry. The effects of tool wear, cutting forces, temperatures on surface integrity were also investigated. The cutting speeds, feed rate, and depths of cut were altered to maintain a constant rate of material removal during roughing, semi-finishing, and finishing.

Chapter 2 is a literature review on the AA7075 workpiece material, machinability, sintering techniques, mechanical properties, wear mechanisms, face milling parameters, MQL, and flood lubrication.

Chapter 3 outlines the objectives of this research study.

Chapter 4 lists the apparatus and equipment's used for this research.

Chapter 5 describes the experimental procedures followed in obtaining measurements.

Chapter 6 has the data analysis calculations made in analysing measurements.

Chapter 7 reports the results obtained during face milling processes.

Chapter 8 discusses the trends and correlations observed in the results.

Chapter 9 concludes with the overall observed correlations and recommendations for future work.

Chapter 2: Literature Review

2.1 History of Aluminium and Classification of 7075 Aluminium Alloy

Aluminium (Al) alloys have a great mark in the history of aircraft manufacture which goes a long way in the aerospace industry from the early 20th century during World War I (1915) (Turner & St. Nowarra, 1971), World War II (1942), and the Space Explorations (1957) (Grosz & Geralt, 1971). Wood was a useful material for aircraft primary structures until Al alloys were developed and standardised for aerospace in 1945 (Yoshio, 2015). The density of wood is 1/3 times that of Al however with relatively poor mechanical properties, i.e. low tensile (2.1MPa) and yield strength (3.5MPa) (Henry & McGraw, 1991). The low weight-strength ratio robs aircraft of rigidity at elevated heights and vacuum pressures. Aluminium alloys were better alternatives, light-weight metal with very interesting thermal, and mechanical properties making aircrafts fuel (kerosene) efficient hence less CO₂ emissions (Aerospace, 2016). Aerospace companies such as Boeing still challenge the principal use of Al products (Warren, 2004) and their ability to compete in the market with alternatives of high tensile strength, yield strengths, and longer fatigue life (Jilani, 2014).

Research encourages performance improvements and cost effectiveness of Al alloys with interest in the low costs of production. Pure aluminium is known for its extremely low mechanical strengths (tensile of 0.0896MPa) compared to other metals such as Titanium (Ti), steel alloys etc. (Metal-Supermarkets, 2015) and Al alloys were developed to match the required characteristics. Different Al alloy grades include 2524-T3, 6013-T6, 2324-T39, 7055-T7751, 7075-T6, and other cast alloys (Nesterenko et al., 2019). Aluminium alloys are the main useful materials for fuselage, wings, and support structures of aircraft. Aluminium alloy 7075 was developed and standardised mainly for aerospace with fair machinability and good mechanical strengths (tensile 572.26MPa) (Nesterenko et al., 2019). This alloy was developed solely for improved mechanical properties by Cryogenic Treatment (CT) that allows phase transformation within alloys (Mohan et al., 2016).

The choice of materials for manufacture comes with greater responsibility to consider characteristic properties of alloying elements, environmental effects, toxicity, resistance to corrosion etc. Aluminium alloy 7075 comprises of Zinc (5.6 - 6.1%), Magnesium (2.1 – 2.5%), and Copper (1.2 – 1.6%) (Imran & Khan, 2019) which are the main alloying elements, other elements are mentioned in Table 2.1 (Mohammed & Anwar Khan, 2019). Zinc is much less toxic and gives AA7075 high resistance to corrosive conditions (Aerospace, 2016). Production of AA7075 products is costlier considering the difficulties of machining that are encountered. It is reported machining difficulties are counteracted by the use of smaller tool rake angles (Da Silva et al., 2013). However, there are other families of alloys

such as wrought alloys with excellent machinability. They make use of larger tool rake angles and observed low thrust forces at lower cutting speeds and lower feed speeds.

Table 2.1 Listed AA7075 alloying elements and their corresponding chemical compositions

Composition	Wt%
Zn	5.1-6.1
Si	0.40
Fe	0.50
Ti	0.20
Cu	1.2-2.0
Mn	0.30
Mg	2.1-2.9
Cr	0.18-0.28
Other	0.65
Balance	Al

2.1.1 Effects of Alloying Elements

Zinc

Machining difficulties encountered with Al include fractures which can be due to high machining forces and high temperature rises; however, Zn is added to improve the machinability. Other elements with similar effects are Tin (Sn) and Lead (Pb). Zinc also improves corrosion resistance in AA7075 alloy.

Silicon

Silicon has outstanding property improvement observed when added to AA7075 with no significant increase in weight. Firstly, the addition of Si in a uniformly distributed manner with smooth round-shaped particles increases the ductility of Al alloys (Totten & MacKenzie, 2003). Increased corrosion resistance is also one of the benefits of Si addition however the effect is minimal (Singh & Singh, 2017).

Iron

The addition of iron to AA7075 has both positive and negative effects on the strength and corrosion of Al alloys. The addition of iron increases the mechanical strength of AA7075 (Singh & Singh, 2017). However, iron reduces ductility and iron effect negatively on resistance to corrosion. The needle-like phases formed during solidification of the alloy are reported to increase stress and AA7075 cracks initiate at these points (Singh & Singh, 2017).

Manganese

Manganese improves mechanical properties at high temperatures and reduces shrinkage on solidification during work hardening in the same manner as silicon. The needle-like phases of iron that are regarded as stress risers are transformed into spherical form by Mn preventing cracks (Singh & Singh, 2017).

Copper

Copper has the most significant effect on high temperature strengths of Al alloys with no negative effects on mechanical strengths. Increased mechanical strength is observed without a decrease in ductility, this happens when copper is evenly distributed in solid phase. However, a decrease in corrosion resistance is reported due to the oxide film spread over the surface and the Al-Cu alloy is electronically negative such that only Al-Cu alloy can corrode in contact with another Al-Cu alloy (Singh & Singh, 2017).

Magnesium

Magnesium main role is for precipitation and as lighter than Al as it is with comparable mechanical strengths, its addition produces high strength with good ductility. When added at enough proportions, heat treatment is made easier and faster. Magnesium is also reported to increase the modulus elasticity and corrosion resistance (Singh & Singh, 2017). Only high amounts of Mg addition (up to 12%) allows for proper castability, low percentage additions (2-4%) gives poor castability.

2.1.2 Machinability of AA7075

Aluminium alloys are a class of metals with the highest machinability in comparison to other metals amongst a category of lightweight metals (Songmene et al., 2011). Alloying elements such as mentioned in section 2.1.1 increases the mechanical properties and machinability of AA7075. Mechanical properties such as hardness and fracture toughness are further altered by heat treatment (Tash et al., 2006). Machinability of the workpiece material is dependent on machining parameters which include machining forces, chip formation mode, surface finish, and tool life (Songmene et al., 2011). Machining

parameters such as cutting forces, tool life, and surface finish are affected by cutting insert compositions, production processes and mechanical properties.

Kouam et al. conducted a study of Al alloys behaviour during drilling and AA7075 was reported to be more sensitive to alteration of cutting speeds than other Al alloys (Kouam et al., 2010). It is also reported that drilling can also be performed more effectively by a milling machine with similar behaviors towards machining parameters. Although response variables such as cutting forces, temperatures and surface roughness differ in values, they however showed a similar behavior in drilling and milling (Ali et al., 2013)

2.1.2.1 Cutting Forces

The High-Speed Steel (HSS) with a 10mm diameter was used to drill at 0.058 mm/rev feed rate and 118° tip angle (Kouam et al., 2010). The machining run was conducted under dry conditions and the feed rate was kept constant to assess the effects of cutting speeds individually. Average thrust forces decrease with increasing cutting speed for AA7075 whereas AA6061-T6, A356-T0, and A319-T0 exhibit fairly constant thrust force as shown in Figure 2.1 (Kouam et al., 2010). It is believed that the observed decrease in thrust forces is due to softening of AA7075 at high cutting speeds facilitated by temperature rises (Songmene et al., 2011).

However, average thrust forces depend more on feed rates since feed rate determines the width of chips which is the main controlling factor of cutting forces. Thrust forces increase with increasing feed rates at different cutting speeds for all four Al alloys as shown in Figure 2.2 (Songmene et al., 2011). Cutting speeds were also varied to facilitate a constant rate of material removal to eliminate any other factor that can possibly lead to misleading results. The 6061-T6, A356-T0, and A319-T0 alloys are only sensitive to feed rates.

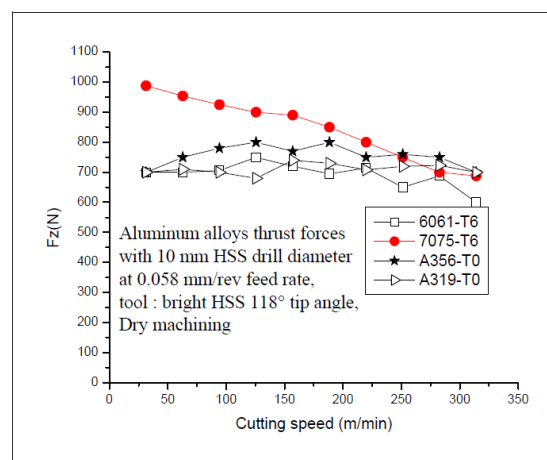


Figure 2.1. Graph of average thrust forces (F_z) at different cutting speeds during drilling of Al alloys 6061-T6, 7075-T6, A356-T0, and A319-T0 (Kouam et al., 2010)

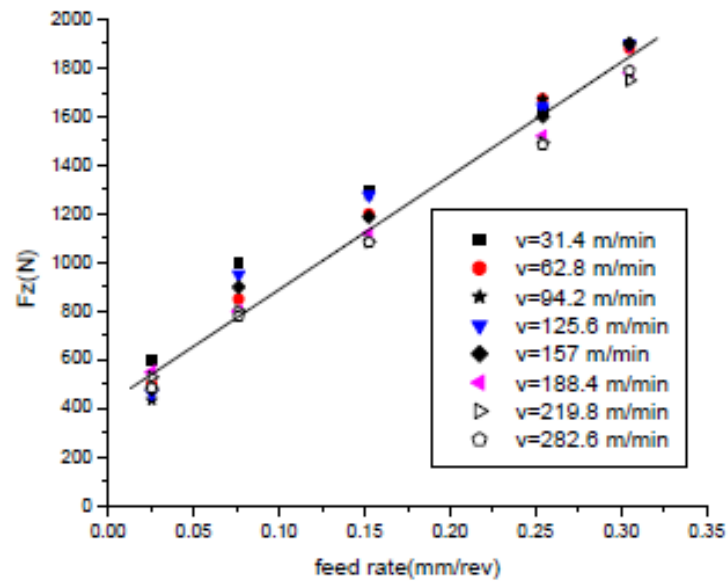


Figure 2.2. Graph of average thrust forces (F_z) at different feed rates and cutting speeds during drilling for AA7075 (Songmene et al., 2011)

2.1.2.2 Tool Life

Machinability is also a function of tool life. Low cutting speeds and feed rates lower than 0.25 mm/rev produce longer continuous chips which can possibly be accompanied by a build-up edge on the cutting edge. The build-up edge protects the cutting edge however when it breaks off, some of the insert materials are removed from the composite resulting in wear and reduced tool life (Songmene et al., 2011). The phenomenon described in this manner is known as adhesion wear which is later discussed in this chapter in section 2.7.2. The machinability performance of 7075-T6 is possible to achieve for selected machining parameters.

2.1.2.3 Surface Roughness

Surface finish is dependent on cutting speeds and feed rates. Long continuous chips may incur damage to a machined surface and the cutting insert (Songmene et al., 2011) since chip breakability is one of the difficulties in machining of Al alloys. However, high cutting speeds and low feed rates produce small and segmented chips for 7075-T6 producing a better surface finish, hence higher cutting speeds facilitate better surface finish (Parhad et al., 2015).

2.2 Carbide-Based Cutting Inserts

Carbides were first developed with the intention to replace the costly diamond wire dies (Upadhyaya et al., 1998). Different carbide alloys that were developed include tungsten carbide (WC), niobium carbide (NbC), titanium carbide (TiC), tantalum carbide (TaC), and others useful carbides. The WC was the earliest discovery while other carbides were developed in attempt to find alternatives for WC due to the

scarcity and lack of supply of W worldwide. Continuous discoveries of alternative carbides are also driven by the scarcity of Co, which is the most common binding metal for WC based cutting inserts and the health challenges associated with Co and WC. Tungsten and Cobalt are elements of economic value and regarded as elements that are in the greatest risk of supply in the whole world ranked at 8.1 in the scale of 0 - 10. The ranks of elements of economic value are shown in Table 2.2 (Survey, 2015).

China is reported to be consuming over 55% of the total worldwide produced W, leaving the rest of the world to share only the remaining 45% (Garside, 2019). South Africa is under a group of countries sharing 5% of the total produced W with the rest of Africa and other continents. Figures 2.3 and 2.4 (Garside, 2019) represents percentage consumption worldwide. The risk of supply of W and Co is the driving force for this study to find alternative elements of economic value. South African industries which suffer the most from lack of supply of W and Co include logistics (transportation businesses), mining, industrial use, and construction since they consume 69% of the total supplied W as shown in Figure 2.5 (Reutte, 2017). This read is focused in the aerospace industry (transportation) which takes part in the 32% of the total W supply. The data is somewhat similar to South Africa’s for the reason that the stated industries are also big in the Republic of South Africa. Figure 2.5 below represents in pie charts the stats prepared based on data gathered in 2017.

Table 2.2. Current Risk of supply of chemical or element groups which are of economic value (Survey, 2015)

British Geological Survey

Risk list 2015—Current supply risk for chemical elements or element groups which are of economic value.

Element or element group	Symbol	Relative supply risk index	Leading producer	Top reserve holder
rare earth elements	REE	9.5	China	China
antimony	Sb	9.0	China	China
bismuth	Bi	8.8	China	China
germanium	Ge	8.6	China	
vanadium	V	8.6	China	China
gallium	Ga	8.6	China	
strontium	Sr	8.3	China	China
tungsten	W	8.1	China	China
molybdenum	Mo	8.1	China	China
cobalt	Co	8.1	DRC	DRC
indium	In	8.1	China	
arsenic	As	7.9	China	
magnesium	Mg	7.6	China	Russia
platinum group elements	PGE	7.6	South Africa	South Africa
lithium	Li	7.6	Australia	Chile

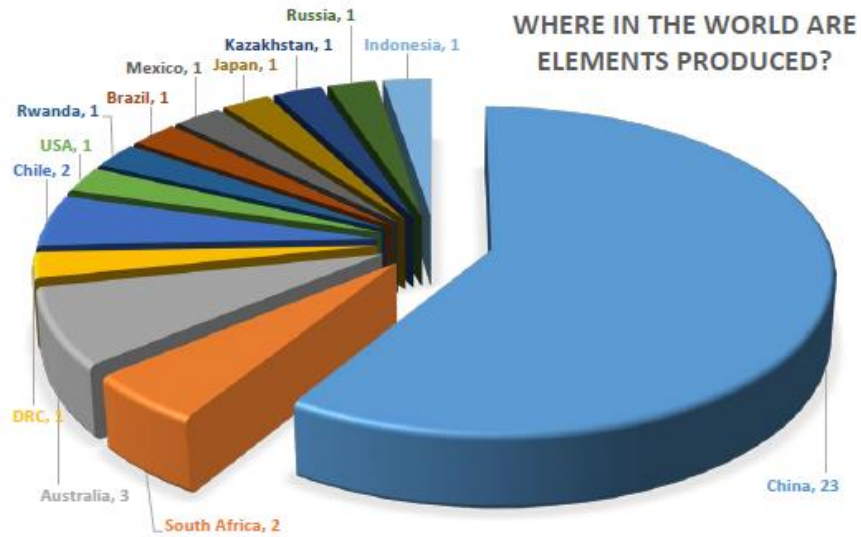


Figure 2.3. Number of times a country is the leading global producer of group of elements of economic value (Survey, 2015)

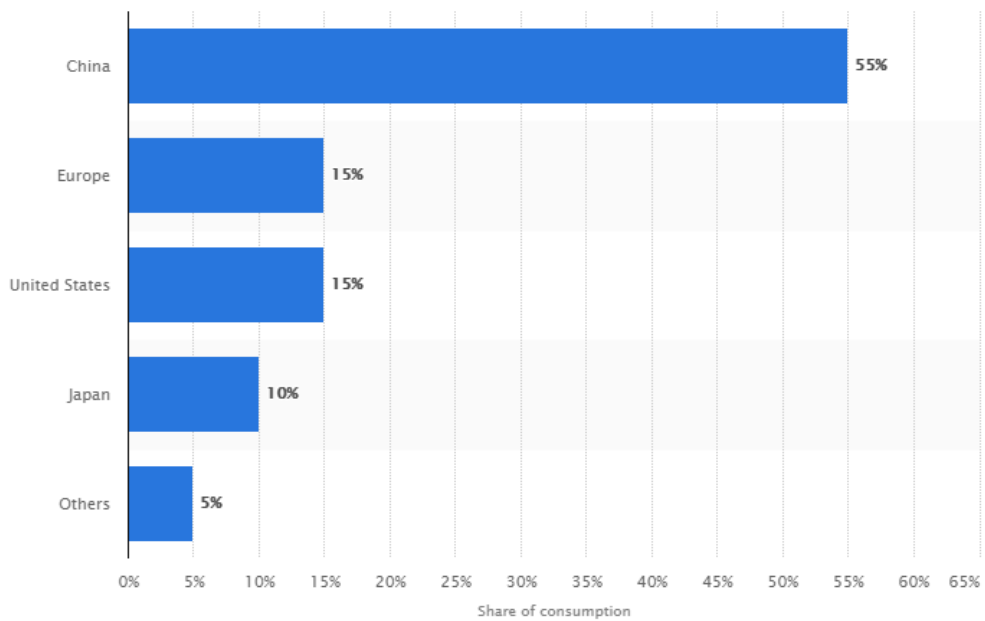


Figure 2.4. Percentage share of consumption of elements of tungsten (W) worldwide (Garside, 2019)

Tungsten: End Use Industries 2017
[International Tungsten Industry Association (ITIA)]

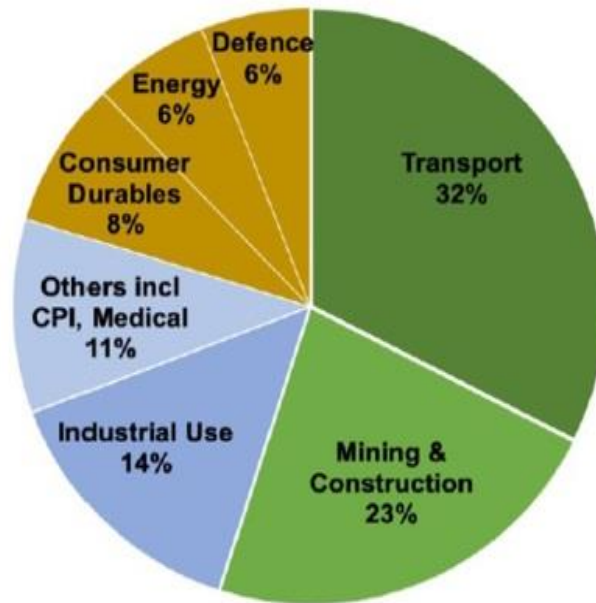


Figure 2.5. Illustrated tungsten percentage use in each industry internationally in 2017 (Reutte, 2017)

Niobium carbide is a potential substitute for tungsten carbide since they have similar mechanical properties. Table 2.3 (Huang et al., 2015) below outlines the similarities and differences between properties of NbC and WC.

Table 2.3. Principal Physical properties of Niobium Carbide compared to Tungsten Carbide

[Property]	NbC	WC
Density (g/cm ³)	7.70	16.63
Melting Point (°C)	3520	2870
Microhardness Hvo.2 (GPa)	17-22	24-28
Toughness K _{IC} (MPa m ^{1/2})	7.0-8.5	6.0-8.0
Thermal Conductivity (W m ⁻¹ K ⁻¹)	14	84
Specific Gravity J g ⁻¹ K ⁻¹)	0.351	0.203
Bulk Modulus (GPa)	300-315	390-410
Elastic Modulus (GPa)	380-480	700-730

2.2.1 Tungsten Carbide

Tungsten carbide is the hard component of WC-Co cutting inserts and they are produced by carburisation of W or WO_3 . Tungsten carbides are composites produced by a process called powder metallurgy that involves mixing a metal of interest with carbon, pressed, and heat treated to produce a composite material (Genga, 2014). The production of WC begins with the mixing of Tungsten (W) and a block of Carbon (C) black and the mixture is heat treated at a temperature between 1400 and 1800 °C (Upadhyaya et al., 1998).

The WC is reported to have a hardness within the range 24-29 GPa and a fracture toughness within the range of 6.0-8.0 $MPa \cdot m^{1/2}$ as shown in Table 2.3 (Huang et al., 2015). The WC has good hardness and that makes it a good material for cutting insert although it has low fracture toughness. The high thermal conductivity of WC is $84 \text{ W} \cdot \text{m}^{-1} \cdot \text{K}^{-1}$ and this allows for lower machining temperatures as opposed to NbC with a thermal conductivity of $14 \text{ W} \cdot \text{m}^{-1} \cdot \text{K}^{-1}$ (Huang et al., 2015). Materials with high thermal conductivity rapidly conduct heat from the region of heat generation (Balaji et al., 1999). The heat energy generated during machining by friction between WC based inserts and the workpiece is quickly transmitted from the workpiece-insert interface.

Tungsten carbide is reported to have a modulus of elasticity within the range 700-730 GPa, approximately twice the elastic modulus of NbC which is within the range 380-480 GPa. Elastic modulus, also referred to as Young's modulus, is the measure of material's resistance to load-deformation or plastic deformation (Heindl & Mong, 1936). The WC composite is less likely to deform in shape (bend or stretch) during machining when subjected to compressive and bending forces as compared to NbC.

Tungsten carbide accounts for the hardness and wear resistance of the WC-Co alloy and the Co binder improves the fracture toughness and ductility (Upadhyaya et al., 1998). Cobalt is commonly a good choice of binder due to WC wettability and good WC solubility in Co binder phase at sintering temperature (Sun et al., 2019). Wettability is the ability of a metal binder (Co) to attach firmly and maintain contact with WC grain surface. The WC-Co combination results in good mechanical strengths and abrasive wear resistance (Sun et al., 2019). Cobalt is reported to qualify as a better binder for WC based inserts due to the below reasons ("Carbide Properties Inc. Cobalt as a Carbide Binder,," 2021):

- High melting point at 1493°C
- Good wettability with WC at a temperature of 1275°C
- Maintains good mechanical strengths at high temperatures

- Cobalt dissolves approximately 10 wt% of WC at 1275°C

In addition to the lack of supply of WC and Co, it is also reported that WC and Co are the potential cause of environmental harm and pose a health risk to employees (Upadhyaya et al., 1998). Exposure to toxic carbide powders is more evident during powder preparation, sintering and machining of the final product into desired shapes of cutting inserts (Upadhyaya et al., 1998). Table 2.4 (Niobelcon, 2007) outlines the hazard classes and possible hazards to human beings.

Carbides that pose none or little health risks include TiC, NbC, TaC, Cr₃C₂, and Mo₂C (Upadhyaya et al., 1998). Cobalt is also reported to be a potential cause of shortness of breath, asthma, and dry coughs, however, Nickel which is the suggested substitute for a metal binder is suspected to be the cause of dermatitis (Upadhyaya et al., 1998).

Table 2.4. Summary of health and safety classifications (Niobelcon, 2007)

Substance	CAS {EINECS}	Hazard Class and Classification Code			
		Mutagenic Category 2	Carcinogenic Category 1A	Reproductive toxicity Category 1B	Carcinogenic Category 2
Co ₃ O ₄	[1308-06-1] {215-157-2}	Yes (H341, suspected to be the cause genetic defects)	Yes (H350, potential cause of cancer when inhaled)	Yes (H360, suspected to cause infertility or damage unborn child)	-
WO ₃	[1314-35-8] {215-231-4}	-	-	-	Yes (H341, suspected to be the cause cancer)
Nb ₂ O ₅	[1313-96-8] {215-213-6}	-	-	-	-

2.2.2 Niobium Carbide

Niobium carbide is produced by a reaction between Niobium Peroxide (Nb_2O_5) and carbon (Upadhyaya et al., 1998). The production process occurs in two consecutive steps, first the carburisation in hydrogen at 1700 °C and then carburisation in a vacuum space at 1600 °C (Upadhyaya, 1998). The produced NbC is the hard component in NbC-Ni sample and Nickel (Ni) is the tough component. Nickel is the most common binder for NbC based cutting inserts.

Niobium carbide has a hardness within a range 17-22 GPa and a fracture toughness within the range 7.0-8.5 $\text{MPa}\cdot\text{m}^{1/2}$ (Huang et al., 2015). Niobium carbide also has good mechanical properties and it is listed amongst the hardest composite materials in Figure 2.6; this makes it a possible substitute for WC although it has lower hardness and wear resistance (Woydt & Mohrbacher, 2014). The NbC has a melting point of 3520°C, a higher melting point than that of WC at 2870°C (Huang, S et al., 2016). Due to the high melting point, NbC based inserts can machine at higher temperatures than those produced from WC. Tungsten carbide-based inserts would be more likely to experience thermal softening at high machining temperatures than niobium carbide-based inserts. The NbC has approximately half the density of WC hence twice the number NbC composites can be produced from the same mass as WC.

Some of the advantages of NbC were reported as below (Woydt & Mohrbacher, 2014):

- Reduced inertia during machining due to lower density than the WC
- Has similar hot hardness to WC at temperatures above 700°C
- Less environmental health risks than WC

2.3 Milling and Mixing Carbide Powders

Mixing of carbide powder and binding metal follows after the production of carbide powders. Carbide powders and binding metals are normally mixed and crushed together with the use of ball mills or attritor mills (Upadhyaya et al., 1998). Attritor mills reduce porosity by reducing binding metal grain sizes. Uniform distribution of the binder metal is ensured by lining the balls with 2.5-3.0 times weight (wt.) ratio of the total binding metal (Upadhyaya et al., 1998). Distribution is furthermore altered by the addition of carbide powder with different grain sizes (Leo Dev Wins & Varadarajan, 2012; Naves et al., 2013). Larger vibratory mills have proved to achieve better crushing results within 48 hours whereas rotating mills take over 7 days to achieve the same level of performance (Ghani et al., 2013).

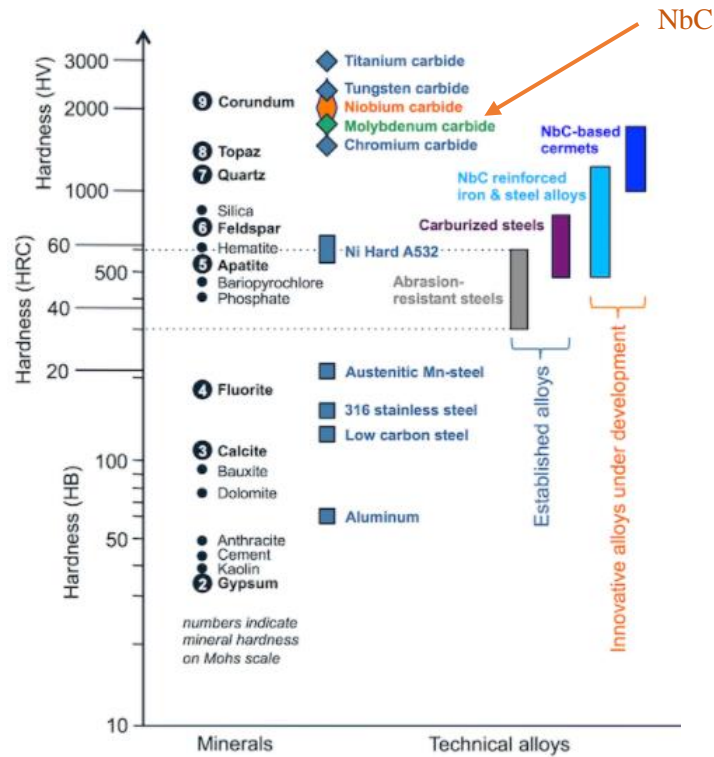


Figure 2.6. Hardness ranks of minerals and technical compounds (Woydt & Mohrbacher, 2014)

The first stage of milling is crushing larger carbide particles and finer particles are achieved by attrition. Based on Upadhyaya's (Upadhyaya et al., 1998) report, the rate at which the mill rotates is directly proportional to the grain size reduction. Below is the formulated relationship where $n_{critical}$ is the spindle speed in RPMs and D is the diameter of powder grains:

$$n_{critical} = \frac{42.3}{D} \quad \text{Equation 2.1}$$

Upadhyaya (Upadhyaya et al., 1998) also reports that it is better to operate at 70-80% of the critical speed. Higher rpm speed achieves better grain crushing but increases temperatures greatly such that lubrication is necessary. Liquids such as hexane, alcohols, acetone etc. are applied for cooling and prevention of any possible oxidation during the process. A well crushed mixture with acceptable grain particle sizes continues to the sintering stage of the manufacturing process.

2.4 Sintering Techniques

Carbide and binder metal are mixed and milled together as described in section 2.3. A well-mixed carbide-binder mixture is heat treated in a furnace and densified into a composite cutting material. The process of heat treatment of carbide mixture at temperatures below the melting point of a carbide is known as Sintering. Sintering improves mechanical properties such as hardness, Transverse Rupture Strength (TRS), fracture toughness, and modulus of elasticity (Genga, 2014; Upadhyaya et al., 1998).

Sintering is dependant on parameters such as time, temperature, powder compact composition, grain sizes, and density of the powder (German et al., 2006). Longer sintering times and high temperature are required to get the desired amount of particle bonding in the powder compact. Although shorter sintering time is more desirable, high sintering temperatures are uneconomical since this would require frequent expenditure on maintenance of the sintering furnace (Cabrera, 1950). The compositions in the powder mixture would consist of selected carbides with desired properties that improve the mechanical properties of the final sintered product. Densification is achievable much quicker when powder compact contains a component that forms a liquid phase (binder metals such as Co and Ni) at the sintering temperature. It is reported that trace amounts of oxygen in the powder compact result in loss of carbon from the carbide (WC and NbC) (Upadhyaya et al., 1998).

Sintering time determines of the extent of grain growth during coarsening and hence effecting the mechanical properties of the product samples. Finer particle grains sinter much quicker and the powder mix shrinks more than a coarser compact with larger grain particles (Upadhyaya et al., 1998). However, the density of the compact also plays a role in the efficiency of the sintering process. Higher density increases contact areas between powder particles and densification is efficient. Higher compact density is a result of finer grain particles and lower porosity (Upadhyaya et al., 1998). The dilemma is finer grains are more likely to finer particles at high density have high carbide-carbide grain contact area and the areas of contact is where necks initiate. The powder compact is heated to sintering temperature where densification and shrinkage occur, necks grow, and new necks form as pores shrink and new grain contact regions form. This phenomenon describes carbide grain growth and coarsening as depicted in Figure 2.7. Necks formulate and grow as a result of diffusion (volume diffusion, surface diffusion, and grain-boundary diffusion), condensed atoms on grain surface, and plastic flow (Bockstiegel, 1956; Cabrera, 1950; Herring, 1950; Schwed, 1951; Ya, 1945). Neck formation and grain growth are reported to be a function of sintering time and ruled by Kuczynski's model as described below:

$$\left(\frac{x}{a}\right)^n \sim t \quad \text{Equation 2.2}$$

x – neck width, a - particle diameter, and t – sintering time

n = 7 for surface diffusion, n = 5 for condensed atoms, and n = 2 for plastic flow (Kuczynski, 1949). Surface diffusion is the main driving force for neck formation, grain growth, and coarsening.

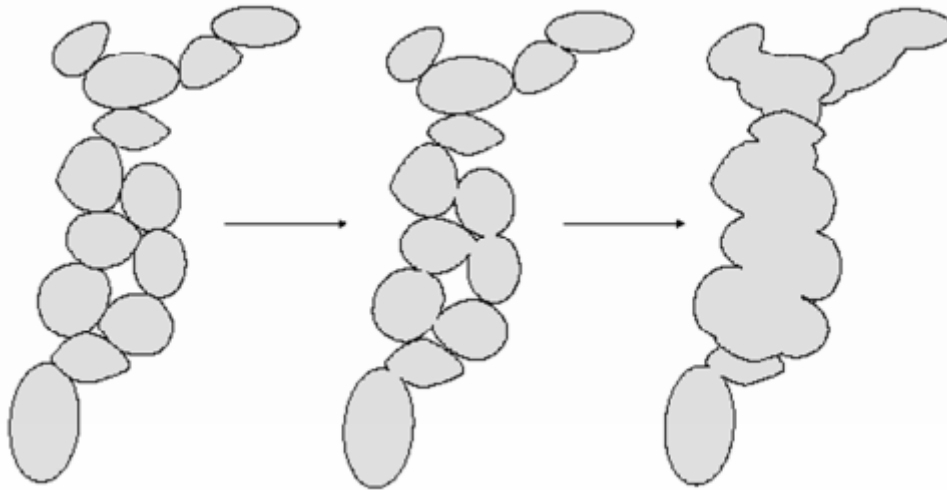


Figure 2.7. Neck formation and resulted grain growth (German et al., 2006)

In Figure 2.8 are graphs of growing neck widths versus sintering dwell time at different sintering temperatures. Neck widths increase with increased dwell time and temperatures. A longer holding time allows for grain growth.

2.4.1 Spark Plasma Sintering

Spark Plasma Sintering (SPS) is a powder densification process that is pressure driven and concurrently applies electric current discharge to activate and accelerate the consolidation process (Han & Nishimura, 2014). The powder mixture is pressed to a certain pressure and low voltage-high density current is passed through the powder. The powder compact is rapidly heated concurrently to a sintering temperature (within the range 1200-1450 °C) suitable for the desired level of compaction. Compaction is achieved at a temperature below the binder melting point. Upadhyaya et al. reports SPS to be applicable at a temperature of 1250 °C, heat rate of 20 °C/min, and 1 hour holding time (Upadhyaya, 1998). However, Garbiec et al. also reported that it was possible to achieve full densification at 1300 °C under 80 MPa pressure, heating rate of 400 °C·min⁻¹, and 5 minutes dwell time (Garbiec & Siwak, 2019). Required dwell time decreases when sintering temperature and heating rate are increased. It is reported that high densification was achievable at as low pressure as 10 MPa by passing high voltage and current through a titanium powder mixture (Saito & Sawaoka, 1973).

The first generation of SPS equipment made use of a 60 µF capacitor that could be charged to 15 kV, the capacitor was developed by Saito et al. (Saito et al., 1974). The powder compact is first put under 58.5 MPa pressure and an electric charge is passed through the powder sample (Mamedov, 2002) to achieve the desired compaction. The recent and last generation of SPS machines was developed in Japan with DC generator of 2-20 kA current (Mamedov, 2002). To date, SPS chambers are manufacture for different samples with a wide range of specifications.

Figure 2.10 (Mamedov, 2002) is an example of the SPS setup, the upper and lower punches squeeze the powder sample to a pressure suitable for the desired level of compaction. The punches and pressed powder are set up inside a sintering furnace. The punches are connected to positive and negative electrodes which are also connected to the DC pulse generator. Examples of the SPS machine and a densified product sample are shown in Figures 2.9 (TotalMateria, 2012) and 2.11 respectively. The SPS makes use of water to cool down the hot compact at a desired cooling rate, and the cooling rate can be specified on the SPS controller.

Some of the benefits of the SPS technique are listed below (Mamedov, 2002; TotalMateria, 2012):

- Powder compact activation by the electric current pulse
- Breakdown of the oxides on the surface of powder particles by the high-density electric current
- Shorter dwell time than the conventional sintering
- Low sintering temperature
- Minimised surface diffusion due to rapid heating (hence minimised neck formations and coarsening)
- Finer carbide grain particles produced
- High densification achievable

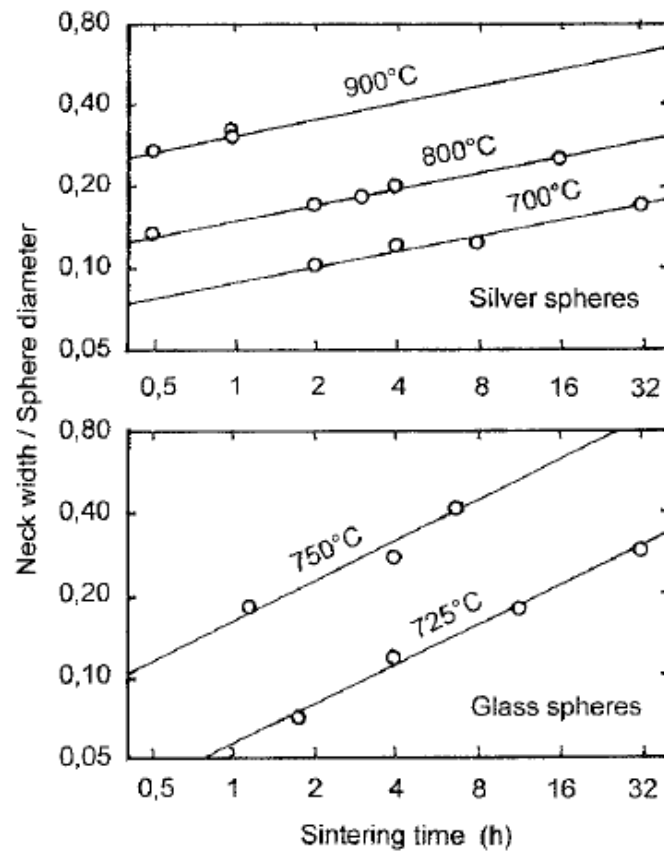


Figure 2.8. Neck growth between spherical particles as a function of sintering dwell time and temperature (German et al., 2006)

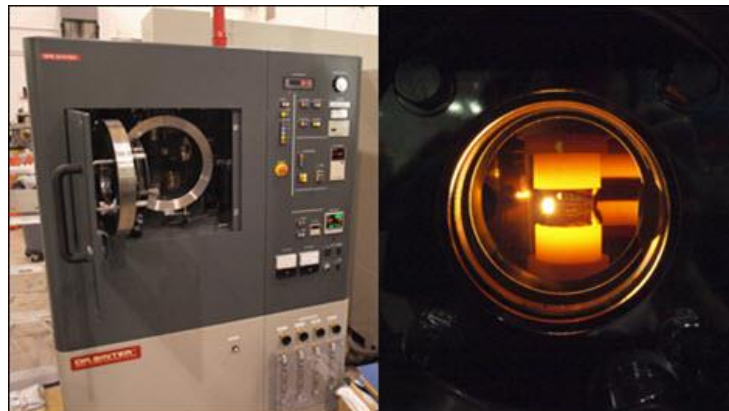


Figure 2.9. Spark Plasma Sintering chamber (TotalMateria, 2012)

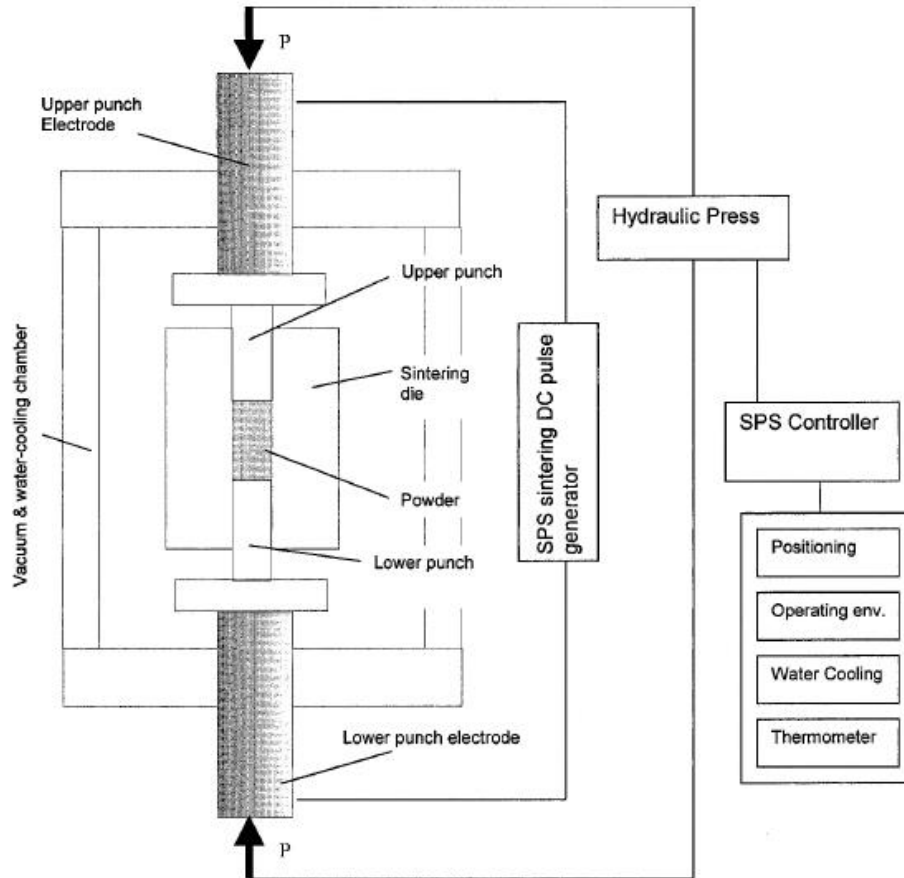


Figure 2.10. Spark Plasma Sintering equipment setup (Mamedov, 2002)



Figure 2.11. Spark plasma sintered samples (TotalMateria, 2012)

2.4.2 Liquid Phase Sintering

Liquid phase sintering (LPS) is a consolidation process that involves components of multiple phases, carbide solid particles coexist with the liquid phase of melted binder metal at high sintering temperatures (Mataix, 2016). The LPS process occurs in three stages which include heating of the powder compact, melting of the binder metal, rearrangement of solid carbide grains and the last stage is final

densification. In the first stage of sintering, the powder mix is heated at a low heating rate and solid densification occurs. The second stage of sintering involves melting the binder as the compact reach high temperatures close to the binder melting point. At this stage, the carbide particles rearrange as the melted binder penetrates and populates the pores between carbide grain particles; the melted binder begins to wet the carbide grain surface. In the third stage of sintering, more binder particles melt increasing the solubility of solids in the liquid phase. The liquid phase increases surface diffusion, neck formation, and grain growth. The four LPS stages are depicted in Figure 2.12 (German et al., 2009).

The formation of the liquid binder phase at high temperatures increases penetration of the binder in-between carbide particles. Solid particles are soluble in the liquid phase as a result of wetting on the solid grain surface. It is preferred to have three conditions under which LPS is conducted, which are the use of low temperatures, high solubility of carbide grains in the binder phase, and wettability of carbide grains by the binder phase (Upadhyaya, 1998). Wettability is governed by the contact angle between the carbide grains and the liquid phase. Low contact angles allow for the liquid phase to spread and attach firmly to the surface of carbide grains (Mataix, 2016). High contact angle represents poor wettability and solubility which can result in swelling and binder phase coming out of the compact sample (German et al., 2009). This is shown in Figure 2.13.

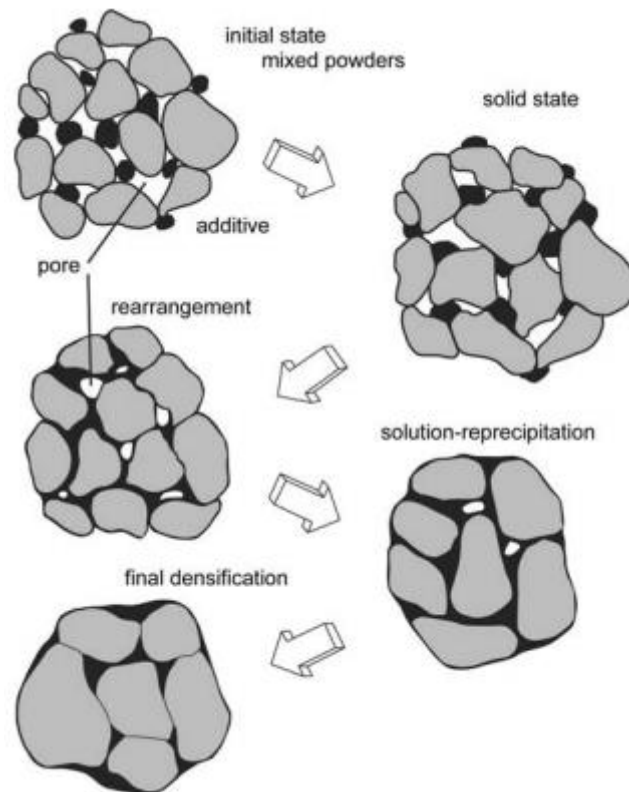


Figure 2.12. The microstructure of changes that occur during the LPS process (German et al., 2009)

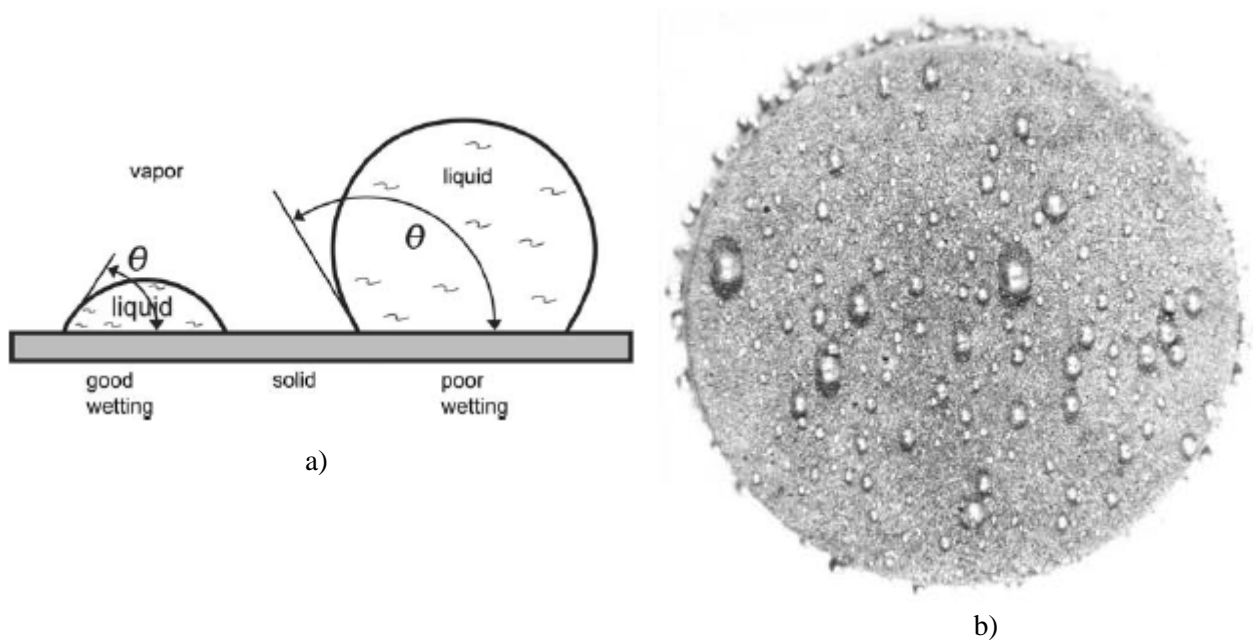


Figure 2.13. a) Contact angles indicating good and poor wetting, and b) compact swelling and binder phase coming out of the sample due to poor wettability during the LPS process (German et al., 2009)

Mataix's report states that the WC-Co composition can be sintered at 1430 °C and 8 minutes holding time, although full densification was also achieved within 30 minutes dwell time at 1600 °C (Mataix, 2016). Dwell time can be reduced by increasing sintering temperature. Some of the parameters that determine the success of LPS are the initial solid particle size and liquid volume fraction. The finer the particle size, the quicker the densification. Figure 2.15 (Mataix, 2016) is an example of LPS application on alumina-glass of different particle sizes. Particles of size 2.1 μm reached full densification well below 10 minutes and 3.6 μm and 5.9 μm sizes reached the same densification at exactly 20 minutes. Figure 2.14 (German et al., 2009; Kwon & Messing, 1990) shows graphically the influence of liquid volume fraction on dwell time. The higher the binder vol.%, the quicker it is to reach full densification. The dilemma is that too much liquid binder phase may lead to a false account of full densification (Mataix, 2016). Samples with 20 vol.% and 10 vol.% liquid phase were reported to have reached full densification at 3 and 30 minutes sintering times respectively and Mataix reported that densification began to decrease past 30 minutes.

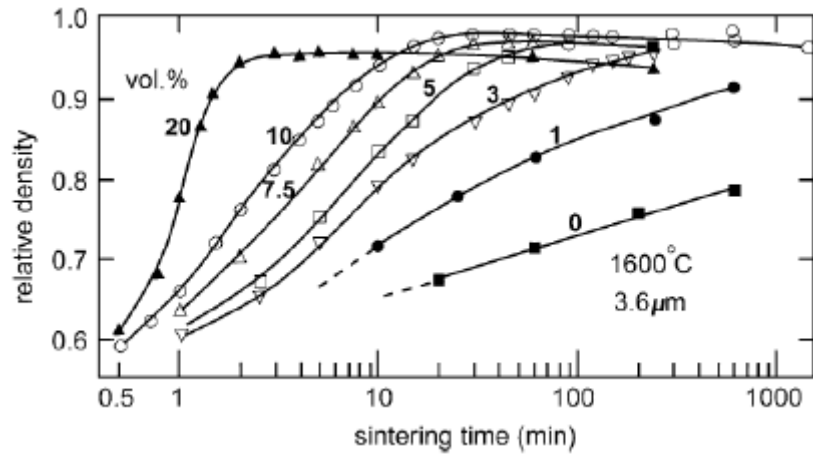


Figure 2.14. Densification at 1600 °C for alumina-glass with different liquid vol.% (German et al., 2009; Kwon & Messing, 1990)

Disadvantages of LPS include:

- Increased surface diffusion due to fluid flow
- Grain growth and grain coarsening during the process
- Requires high temperatures to melt the binder
- Longer sintering time

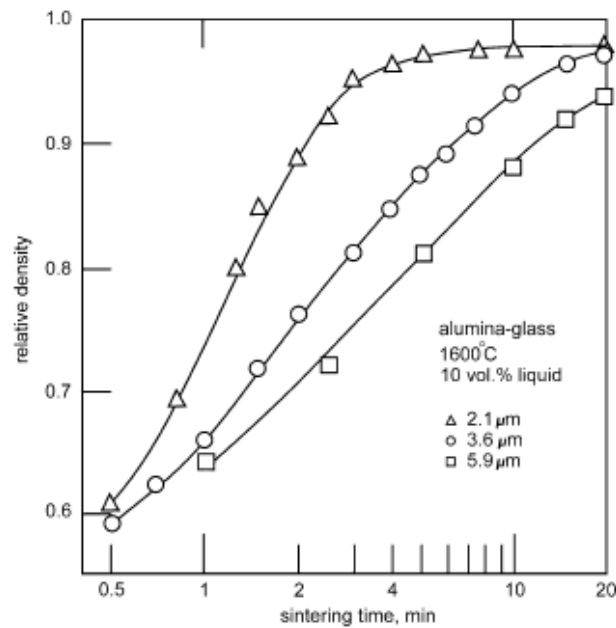


Figure 2.15. LPS of alumina-glass with 10% liquid volume at 1600 °C with different particle sizes (Mataix, 2016)

2.4.3 SPS versus LPS

The main differences between LPS and SPS are as tabulated in table 2.5:

Table 2.5. SPS vs LPS

	SPS	LPS
Heating Rate	High	Low
Temperature	<1300 °C	>1450 °C
Resulted grains size	Fine	Coarse
Dwell time	Short	Long
Densification	High	Relatively Low

2.5 Mechanical Properties

Mechanical properties of cemented carbides include hardness, fracture toughness, and transverse rupture strength. Properties of cemented carbides are affected by parameters of production processes which include sintering techniques, sintering temperature and time, initial carbide grain sizes, carbide milling parameters, etc.

2.5.1 Hardness

Hardness is an important property of hard metals and a requirement for metalworking purposes. Hardness is a material's ability to withstand localized plastic deformation and scratching (Murugan, 2020). Hardness is used as a measure of material strength. The WC and NbC grain sizes are the determinants of the hardness of cemented carbide inserts. The finer the carbide grains the harder the cermet material however, better solubility of carbide in the binder liquid phase also increases hardness (German et al., 2009; Upadhyaya et al., 1998). Exposure to high temperatures decreases hardness (Nguyen, 2018).

2.5.2 Fracture Toughness

Fracture toughness is the material's ability to withstand bending without crack propagation or fracture (Murugan, 2020). Materials with high fracture toughness are sometimes referred to as ductile. Ductile materials have the ability to withstand permanent plastic deformation (Murugan, 2020). Fracture toughness is also dependent on grain sizes and indirectly proportional to hardness. Finer carbide grains produce cermets of lower fracture toughness. The indirect relationship is only with dependency on grain sizes, there is no correlation between hardness and fracture toughness regarding other factors such as carbide solubility in metal binder.

2.6 Carbide Additives

Carbide additives are added to the WC-Co or NbC-Ni systems to improve the mechanical properties of the resulting sintered product. Some of the effective additives include carbides such as Titanium Carbide (TiC), Tantalum Carbide (TaC), Molybdenum Carbide (Mo_2C), and Chromium Carbide (Cr_3C_2). The NbC is also used as an additive to alter WC-Co grain growth (Genga, 2014). The Cr_3C_2 , NbC, TaC, and TiC are reported to be good grain growth inhibitors; the order of effectiveness was reported to be $\text{Cr}_3\text{C}_2 > \text{NbC} > \text{TaC} > \text{TiC}$ (Genga, 2014). Hardness can be increased through either grain growth refinement or through the addition of secondary hardening phases such as TiC. Titanium carbide has a higher hardness (>27 GPa) than the WC and NbC and TiC increases hardness when added to WC-Co and NbC-Ni systems; although, it is reported that TiC has poor solubility in Co and Ni due to poor wetting of TiC (Upadhyaya, 1998). However, the addition of Mo or Mo_2C is reported to improve the wetting of TiC by the Co and Ni binders. The Mo addition to TiC-Ni reduces contact angle from 30° to 0° (German et al., 2009).

2.7 Wear Mechanisms

Material wear is the gradual removal of solid particles from surfaces that are in mechanical contact (Saverio, 2014). Wear is a result of different mechanisms which include abrasion, adhesion, diffusion, chemical, and wear due to plastic deformation (Odelros, 2012). The aspects of wear mechanisms are described below.

2.7.1 Abrasive Wear

During machining, hard grain particles are detached from the composite cutting material as a result of friction between insert-workpiece surfaces. Abrasion can be described as the rubbing and ploughing of hard particles on the soft material. The insert and workpiece are two bodies and the hard particles give rise to the third body. Two materials rubbing against each other result in higher wear than three bodies

(Odelros, 2012). Abrasive wear increases at high temperatures due to the decrease in material hardness at elevated temperatures (Odelros, 2012; Varga, 2017).

2.7.2 Adhesive Wear

Hard particles of the insert weld together on the cutting edge of the insert at elevated temperatures (Luigino et al., 2007). Adhesion is more likely to occur at high temperatures and pressures. High cutting speeds and temperatures may not only cause weld between hard particles, but they also cause chip weld leading to build-up edge (Luigino et al., 2007). The build-up edges protect the cutting edge from wear; however, when they break off during machining some of the insert materials are removed with chips and this phenomenon described is also known as adhesion wear (Ingle, 1993). Adhesive wear is also referred to as attrition wear (Wright & Bagchi, 1981).

2.7.3 Diffusive Wear

Diffusive wear occurs by diffusion of atoms from the cutting material to the machined surface at high machining temperatures (Odelros, 2012). Atoms diffusion from a cutting material results in loss of atoms of hard particles leaving a soft cutting edge that wears out by abrasion and adhesion (Odelros, 2012). Luigino et al. reported that diffusive wear is mainly dependent on the solubility of the cutting material in the workpiece (Luigino et al., 2007) and it is the main cause of crater wear as chips come in contact with the rake face.

2.7.4 Chemical Wear

Chemical wear is a result of chemical reactions that occur at the tool-workpiece interface which leads to the formation of an oxide layer on the insert surface (Childs et al., 2000). Oxides are products of oxidation reaction at the insert surface at high machining temperatures. The oxide layer acts as a protection layer from wear and breaking off leads to chipping if the oxide layer is brittle (Odelros, 2012). In many cases, a good solubility has been realised between Co and Al at high machining temperatures (Yan et al., 2008) which initiated chemical wear.

2.7.5 Wear due to Plastic Deformation

Plastic deformation occurs at the cutting edge and at the surface of the cutting material under high cutting forces and temperatures. Plastic deformation results in changes in tool geometry and loss of materials from the cutting insert (Odelros, 2012).

2.8 Tool Wear

Cutting inserts fail due to two mechanical conditions, premature failure and tool wear. Premature failure entails temperature failure and fracture failure. Temperature failure is due to a rapid increase in

temperature which causes thermal shock or softening of the cutting edge resulting in loss of edge. Fracture failure is often a result of low fracture toughness. Tool wear can be categorised into different types which include crater wear, flank wear, chipping, and notch wear (Odelros, 2012). Insert failure is a result of the combination of the different types of wear.

2.8.1 Crater Wear

Crater wear occurs when chips erode the rake face by diffusion and adhesion (Viktor, 2011). As crater wear grows, the cutting edge is exposed (results in a sharp edge) which reduces the cutting forces and lowers the strength of the cutting edge (Viktor, 2011). Crater wear is a result of diffusion that occurs at the rake face at high temperatures. The loss of atoms at the rake face allows for abrasion and adhesion wear to take place as shown in Figure 2.16 (Viktor, 2011).

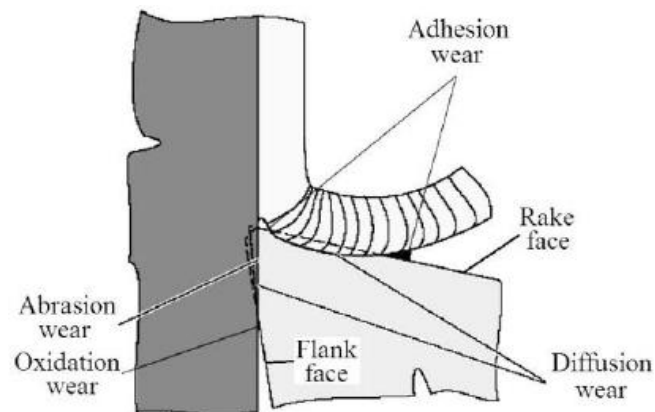


Figure 2.16. Flank and rake faces where flank and crater wear occur (Viktor, 2011)

The adhesion that occurs at the tips of the crater further increase crater wear and may result in chip welding at high cutting temperatures. The condition of inserts is monitored by the depths and lengths measurement of wear. Crater depth (KT) and crater width (KB) are measured using a profilometer as the measure of crater wear (Childs et al., 2000) as shown in Figure 2.17.

2.8.2 Flank Wear

Flank wear occurs on the relief face and wear takes place by diffusion, abrasion, and chemical wear (oxidation reaction) mechanisms at the tool-workpiece interface (Dadić, 2013); however, abrasion and chemical wear are more dominant (Childs et al., 2000). The face at which flank wear occurs is shown in Figure 2.16. Maximum flank wear (VB_{max}) is measured using an optical microscope to assess the condition of a cutting insert as shown in Figure 2.17 (Dadić, 2013).

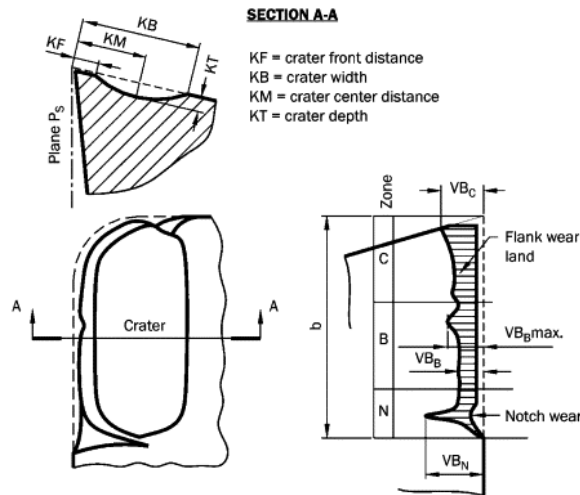


Figure 2.17. Measures of crater and flank wear (Dadic, 2013)

The tool failure criteria for roughing, semifinishing and finishing are determined by the measured value of VB_{max} 600 μ m and 300 μ m respectively (Boothryd & Knight, 2006; Genga et al., 2020).

2.8.3 Chipping

Chipping is the breaking off of materials from the cutting insert which can be a result of the cutting material being subjected to sudden loads at high machining forces and thermal shock due to sudden increases in temperature (Childs et al., 2000).

2.8.4 Notch

A notch is formed at the flank and crater faces resulting in a groove that is shown in Figure 2.17. Odelro reported based on Turkes et al. discussion that notch wear is a result of chemical wear and occurs as initiation of fracture propagation (Turkes et al., 2011). A notch often results in fracture failure. Measurement of VB_N (shown in Figure 2.17) at microscopic level serves as a measure of notch wear.

2.9 CNC Milling Machine

The worldwide major shift from the 2nd to 3rd industrial revolution came with a greater demand for modern engineering products at a later stage. In this age of science and mass production, continuous research further cautioned the importance of surface textures of machined parts. The automotive and aerospace industries grew and machining manufacturing required more time and effort to meet the growing demand and required qualities of products. The invention of Computer Numerical Control (CNC) machines made machining practices easier, faster, and more accurate (Sairavali & Dr. Reddy, 2020). The operator sets up a program on the CNC with the desired machining parameters and runs the program based on the required dimensional specifications and shape. The CNC machine can do drilling, turning, and milling of workpieces.

2.10 Machining Parameters

Machining parameters are the main determinants of machining product quality and safety of operation cutting speed, depth of cut, and feed rate. The responses to these parameters include cutting forces, temperature rises, and surface roughness. A combination of parameters is chosen for each machining run to facilitate a constant material removal rate during roughing semi-finishing, and finishing. High cutting speeds aid chip removal from an insert edge. This helps avoid chip welding improving the quality of the end product.

2.10.1 Cutting Speed

Cutting speed is the tangential linear equivalent of spindle speed (Baskar, 2010). The units for cutting speed and spindle speed are meter per minute (m/min) and raps per minute (RPM) respectively. Equation 2.3 relates cutting speed to spindle speed and conversion between the two:

$$\text{Cutting Speed } (v_c) = \frac{\pi \times D \times N}{1000} \quad \text{Equation 2.3}$$

where v_c (m/min) is the linear cutting speed, D (mm) is the diameter of the cutter and N (rev/min) is the spindle speed. Cutting speed determines the machining criteria, roughing, semi-finish, and finishing. Low cutting speeds are used for roughing and high cutting speeds facilitate finishing. Baskar conducted a research study on optimisation of machining parameters and reported that a decline in surface roughness with increasing speeds hence facilitating finishing at high cutting speeds (Baskar, 2010).

The study of cutting temperatures and forces as responses to cutting speeds can be complex as they are dependent on the type of workpiece material and its properties, the machining criteria, the cutting insert, the lubrication technique in place etc. In literature, it is reported that increased cutting speed results in a decrease in cutting forces and increased temperatures (Mohammad et al., 2017). Figures 2.18 and 2.19 show examples of the relationship between cutting speeds, forces, temperatures, and depth of cut during machining of carbon steel with the use of a 6mm carbide flute as a cutting insert.

Increased temperature reduces the hardness of a cutting insert hence allowing the possibility of abrasion and diffusion phenomena, which gives rise to flank wear. An increase in cutting speeds increases the number of times an insert enters the workpiece hence increasing the number of mechanical shocks per minute.

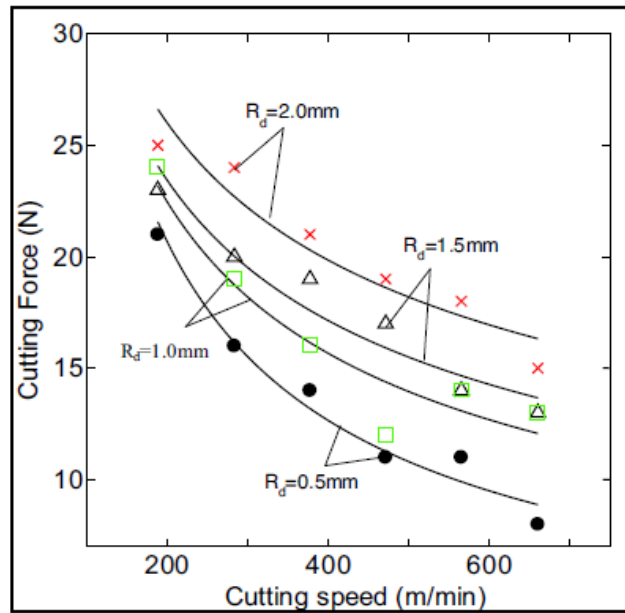


Figure 2.18. Cutting force decrease as the cutting speed increase (Mohammad et al., 2017)

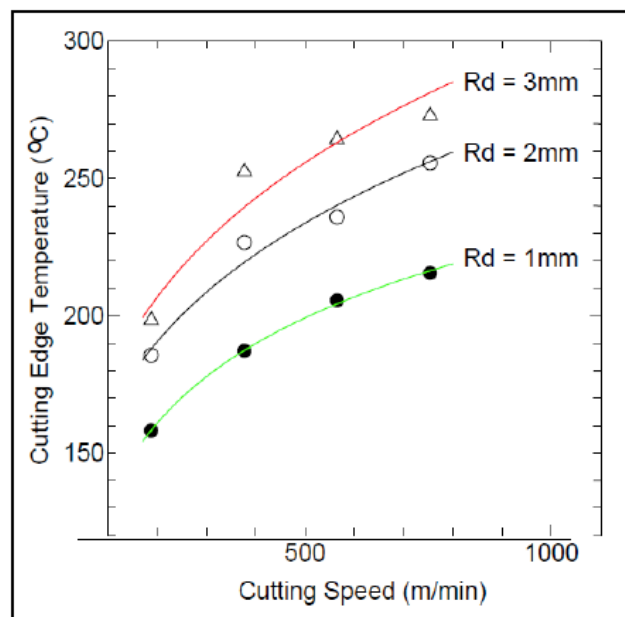


Figure 2.19. Graph of cutting speed against cutting edge temperature at different depths of cut (Mohammad et al., 2017)

This outlines critical cutting speeds to the shelf life of cutting inserts hence increased cutting speeds increased the insert wear rate and lowering tool shelf life (Caldeirani & Diniz, 2002).

2.10.2 Feed Rate

Feed rate is the relative linear velocity at which the cutter is forced along the workpiece during milling (Basil, 2015). The alteration of cutting speeds affects the feed per tooth, this further affects the feed rate which can therefore be calculated using the below relationship:

$$v_f = \frac{f_z \times z \times v_c \times 1000}{\pi \times D} \quad \text{Equation 2.4}$$

where f_z is the feed per tooth, z is the number of teeth, and v_f is the feed rate.

Figure 2.20 shows an increase in cutting forces with increased feed rate per tooth from 0.05 - 0.10 m/min and 0.10 - 0.15 m/min; the cutting speed was kept constant at 150 m/min. Altas et al. (Altas & Caliskan, 2016) conducted two experiments for two different insert compositions for the same set of parameters and the force-feedrate trends are similar.

The effects of feed rate on temperature, forces, and tool life are separate from the effects of cutting speed however, they show the same trends. Increasing feed rate is reported to increase machining forces and temperatures. A similar trend is evident with feed per tooth (Altas & Caliskan, 2016). However, feed rate increases surface roughness of the machined surface hence high feed rates are for roughing machining criteria (Altas & Caliskan, 2016).

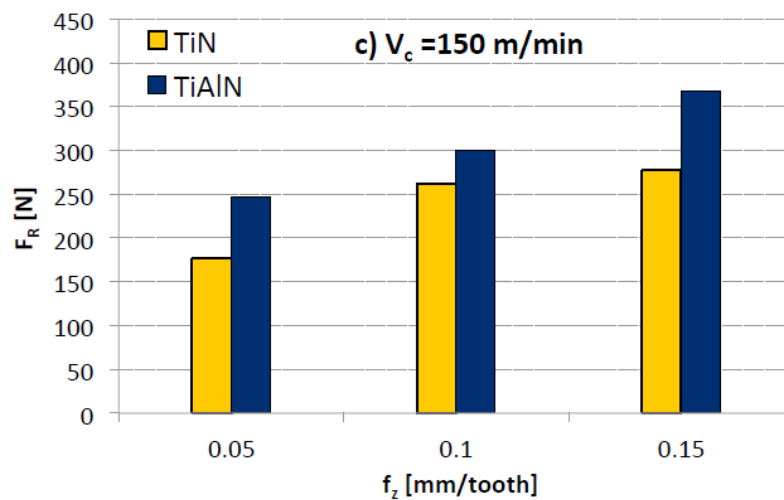


Figure 2.20. The change of the resultant cutting force (FR) as a function of feed rate at different cutting speeds (Altas & Caliskan, 2016)

2.10.3 Depth of Cut

Depth of cut is how deep the cutting insert is forced into the workpiece; depth of cut can be expressed in the axial or radial direction. Figure 2.21 (Muhammad et al., 2017) depicts the differences between axial (a_p) and radial (a_e) depths of cut.

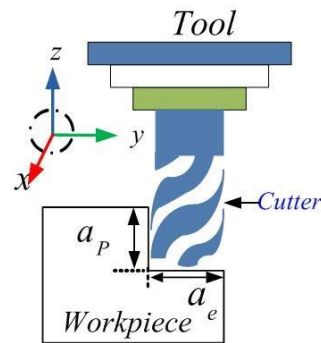


Figure 2.21. Schematic diagram of milling process. Note, a_p is the axial depth of cut and a_e is the radial depth of cut (Muhammad et al., 2017)

An increased radial depth of cut increases cutting temperatures and forces as seen in Figures 2.18 and 2.19. However, the axial depth of cut a_p is more dominant for the current face milling discussion and Muhammad et al. reports a similar trend for axial depth of cut (Muhammad et al., 2017). Increased axial depth of cut increases cutting temperatures and forces, this results in an increase in surface roughness (Muhammad et al., 2017). Figure 2.22 (Baskar, 2010) represents the relationship between the depth of cut and surface roughing. This suggests that shallower depths of cut facilitate a better surface finish.

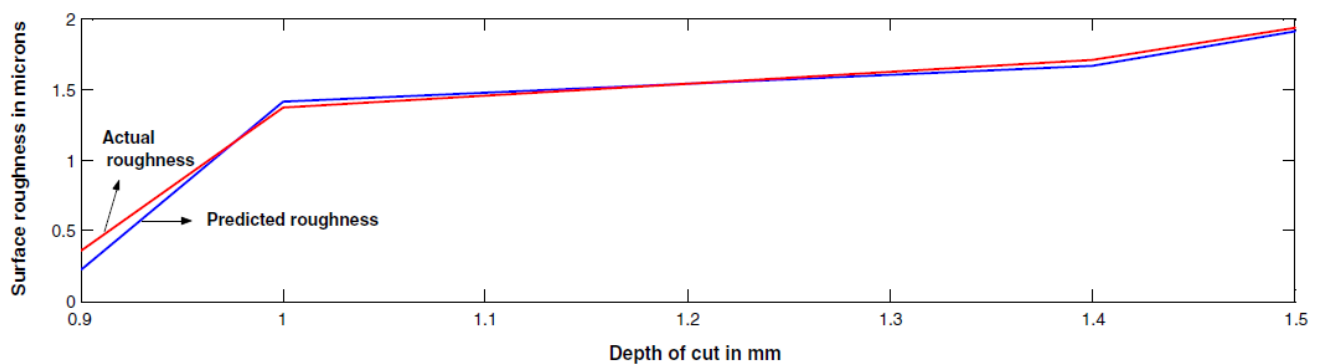


Figure 2.22. Axial depth of cut versus machining time and surface roughness for mild steel (Baskar, 2010)

2.11 Lubrication

Application of lubricants is reported to lower thrust forces, temperature rises, improve insert tool life and improved surface finish (Barczak & Batako, 2012). Lubrication techniques are distinguishable by the chemical composition and methods of application. Conventional lubrication, also referred to as flood lubrication or wet, incur large amounts of fluid and Minimum Quantity Lubrication (MQL) are the commonly applied techniques.

2.11.1 Flood

Flood is the traditional technique that has very common side effects that are economic and health-wise. Lubricants are generally expensive to purchase and to maintain (Koné et al., 2013) taking between 7.5% and 17% of the total costs of a complete machining process (Rozzi et al., 2010). When used in large amounts, they pose harmful effects to the environment and workers' health (Wichmann et al., 2013) and (Jabbar, 2018). Machining operations allow the growth of bacteria and aerosols. Inhaled bacteria and aerosols pose health risks including dermatitis, respiratory disorders, and cancer (Abdalla et al., 2007). Flood cooling utilises large amounts of fluids increasing the chances of health infection. Coolants have also been reported to take 31.8% of energy usage in Toyota metal working processes (Dahmus & Gutowski, 2004). From the environmental point of view, greenhouse gases (CO₂) are released in excess amounts by Toyota hence significantly affecting global warming (Ginting et al., 2015). The cost of CO₂ emission in the USA is \$12 per CO₂ tonne (Bernstein et al., 2007).

Figure 2.23 demonstrates how waste lubricants are harmful to the surrounding ground and the report states that Donhad Company incurred cleanup costs of over \$40,000 (Ginting et al., 2015).



Figure 2.23. Donhad polluted coolant waste bin (Ginting et al., 2015)

2.11.2 MQL

Due to the economic and health challenges of flood cooling, better lubricants, and new methods of application have been developed. Research proposed and reported a few alternatives which include

cryogenic cooling using liquid nitrogen (Ravi & Kumar, 2011), compressed cold air, and MQL (Dhar et al., 2006). Minimum quantity lubrication (Li, 2006) and compressed air (Rahman et al., 2003) are reported better preferred green fluid applications based on the main factors, such as low costs of producing and application. Boswell et al. (Boswell & Voges, 2011) report states that MQL and air can be applied together and in some cases, water emulsions are added in place of air. Compressed chilled air is usually applied at a pressure 5 bar (Irfan et al., 2013). Minimum quantity lubrication applies rates of 50 - 500 ml/hr to the cutting edge-workpiece interface (Jayal & Balaji, 2009). This technique minimises the large use of fluids significantly by 3 - 4 orders in comparison to flood cooling (Boubekri & Shaikh, 2014).

Green MQL fluids are produced from vegetable oils and synthetic esters (Woods, 2005). Vegetable oils are composed of different esters, products of glycerin and fatty acids, and they are with unsaturated bonds (double bond and triple bonds). The unsaturated bonds are reported to be the cause of easy degradation of MQL fluids by bacteria oxidation (Boubekri & Shaikh, 2014). Synthetic Polycol esters on the other hand are products of polyhydric alcohols. Examples of synthetic fluids include Perfluoropolyether (PEFE) (Dosbaeva et al., 2008) and carboxylic acid with polyalcohols. Lubricants are available in four different forms such as straight oil (vegetable neat oil), soluble oil (emulsifiable oil), semisynthetic fluids and synthetic fluids (Coppus, n.d.). Synthetic fluids are most preferred also because they give better lubrication (Itoigawa et al., 2006). Part of the scope of this study investigates different lubrication techniques at different machining conditions and environments.

Chapter 3: Objectives

- To investigate the effect of spark plasma sintering on insert hardness and fracture toughness for better machining performance as compared to the conventional liquid phase sintering, based on tool life, cutting forces, cutting temperature and machined surface roughness.
- To investigate the mechanical properties (hardness, fracture toughness) of NbC based inserts and compare them to WC based inserts.
- To investigate the machining performance and flank wear experienced by NbC based inserts and compare them to WC based inserts.
- To investigate the effects of the use of minimum quantity lubrication (MQL) on insert tool wear and cooling during machining and compare MQL to dry and flood cooling.

Chapter 4: Apparatus

This section outlines and describes the different instruments used for the course of the experiment. The experiment was performed in four main parts which are preparation of workpiece, machining, flank wear measurements, and surface roughness measurements. Cutting force (measurements in the XYZ directions) and temperature readings were taken during machining. Insert flank wear and surface roughness of the machined surface were taken immediately after each machining run.

4.1 Workpiece Preparation

A plate of AA7075 of dimensions 1000 x 990 x 20mm in Figure 4.1 was cut into 30 workpieces of dimensions 200 x 160 x 20mm as shown in Figure 4.2. A band-saw machine in Figure 4.3 was used to cut the AA7075 plate into desired dimensions of workpieces.

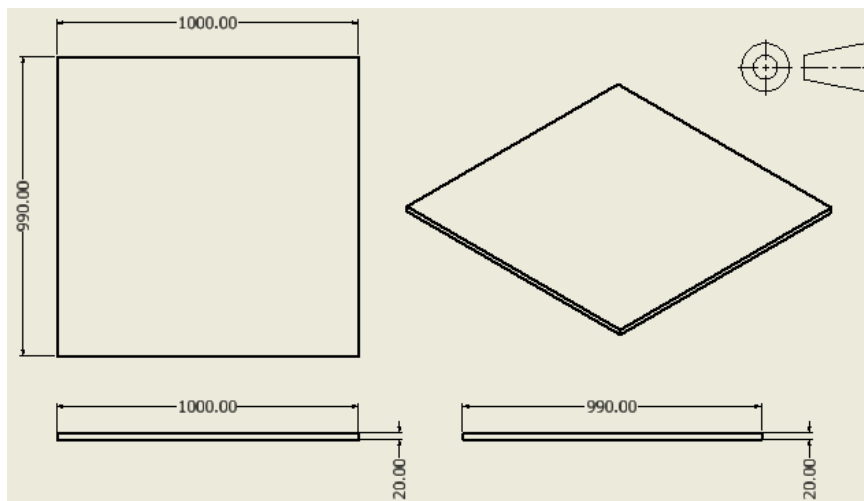


Figure 4.1. Third angle orthogonal projection of the AA7075 plate with dimensions 1000 x 990 x 20mm

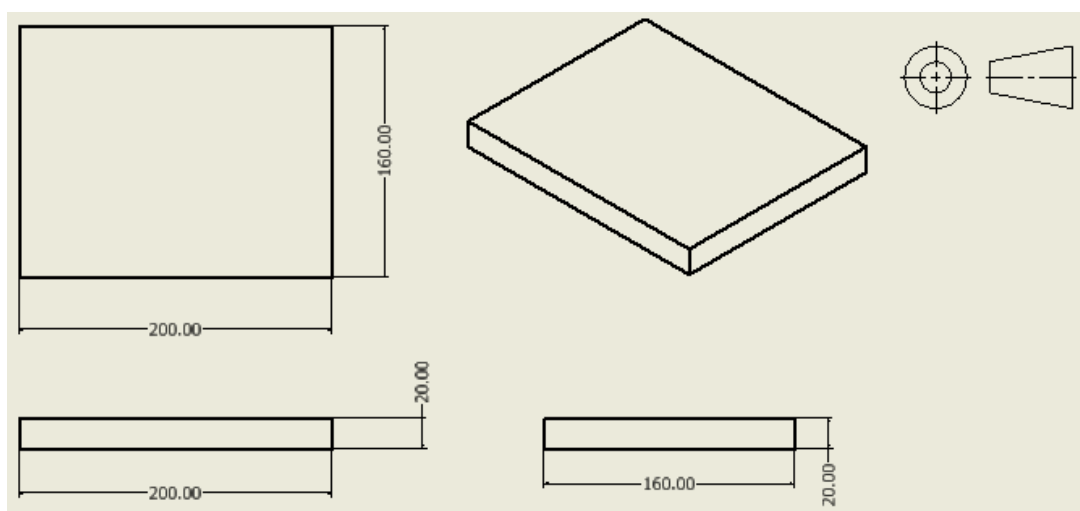


Figure 4.2. Third angle orthogonal projection of the workpiece with dimensions 200 x 160 x 20mm



Figure 4.3. Startrite 30RWH, model 600 band-saw machine

4.2 Cemented Carbides (Cutting inserts)

Six cutting inserts (3 WC and 3 NbC based face mill inserts) of the same shape and different compositions were used for machining. Each insert had 8 cutting edges. Four inserts were manufactured by Liquid Phase Sintering (LPS) and two were manufactured by Spark Plasma Sintering (SPS). Table 4.1 outlines the edges used for each test run, one insert used three edges for each machining criterion (e.g. for roughing each insert used one edge for dry, one edge for flood, and one edge for MQL conditions; the same applied for semi-finishing and finishing).

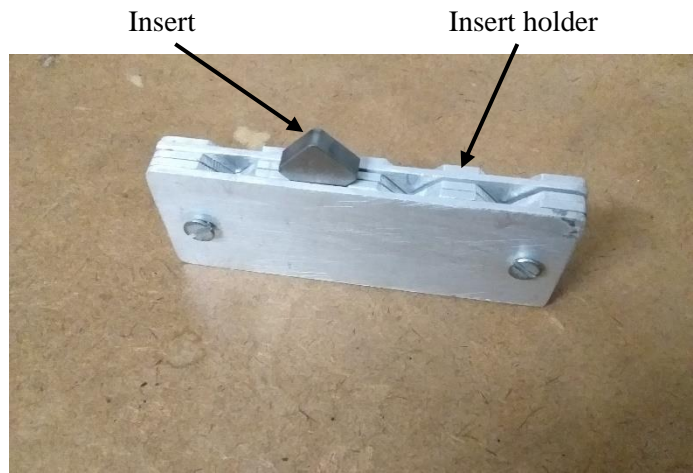
Table 4.1. Cutting inserts and the edges used for each machining criterion

Cemented carbide	Insert	Lubrication	Cutting edge		
			Roughing	Semi-finishing	Finishing
WC based inserts	W1-L	Dry	-	-	-
		Flood	6.1.5	6.1.7	6.1.8
		MQL	6.0.1	6.1.1	6.1.3
	W1-S	Dry	11.1.1	11.1.2	11.1.3
		Flood	11.0.2	11.0.3	11.0.4
		MQL	11.1.5	11.1.6	11.0.1
	M1-L	Dry	7.1.1	7.1.4	7.1.5
		Flood	7.0.3	7.0.5	7.0.8
		MQL	7.1.6	7.1.7	7.0.1
NbC based inserts	R1-L	Dry	2.1.7	2.1.8	2.0.1
		Flood	2.0.6	2.0.7	2.0.8
		MQL	2.0.2	2.0.3	2.0.5
	G1-S	Dry	9.1.3	9.1.6	9.1.7
		Flood	-	-	9.0.7
		MQL	9.1.8	9.0.1	9.0.2
	G1-L	Dry	3.1.1	3.1.3	3.1.4
		Flood	-	-	3.0.7
		MQL	3.1.5	3.1.8	3.0.1

Dimension of each of the 6 inserts was 12.7 x 12.7 x 4.7 mm and round corners of radius 1.6 mm. each cutting edge had the rake angle of 20° and 0.2 mm camfer. Figure 4.5 shows the insert shape and dimensions of inserts.

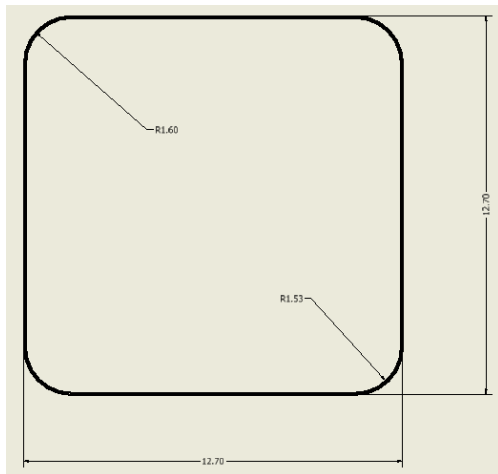


a) Cutting Insert

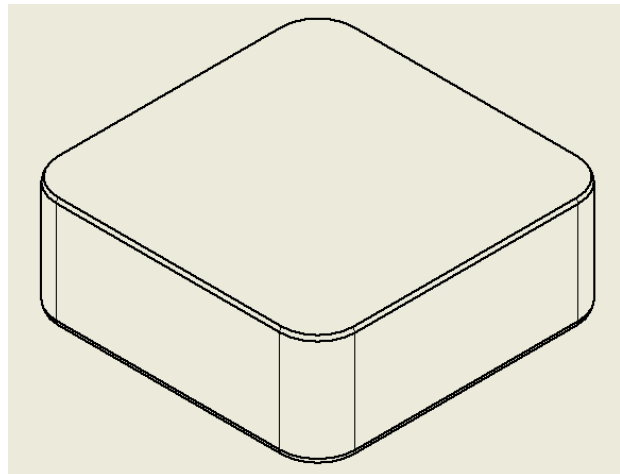


b) Insert holder used during flank wear measurements

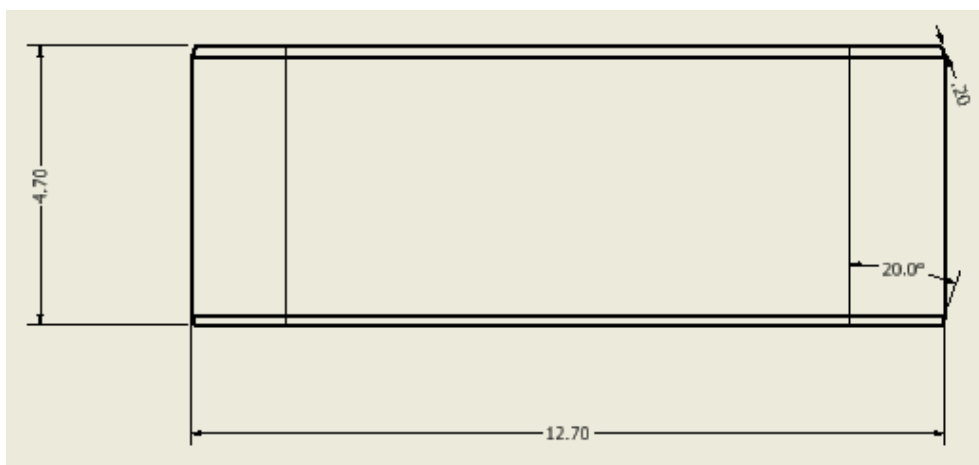
Figure 4.4. a) Cutting insert used during machining and b) insert holder used to hold inserts during wear measurements.



a) Top View



b) Isometric View



c) Front View

Figure 4.5. Inserts drawing with dimensions.

4.3 Insert Holder (Tool)

A cutting tool shown in Figure 4.6 was used to hold and secure inserts during machining. Only one insert was clamped to the holder for each machining run; however, the tool can hold a maximum of 5 inserts at a time.



Figure 4.6. Cutting tool

4.4 GX1000 CNC Machine

The Bridgeport GX1000 CNC model was programmed for each machining run and the machine can be used for drilling, turning, and milling. For the current research experiment, the GX1000 was used for face milling. The cutting speed, spindle speed, feed rate, and depth of cut were varied on the Fanuc series oi-MC control panel of the CNC machine. A test run ensured that the program works as required. The GX1000 and its control panel are shown in Figure 4.7. Figure 4.8 shows experimental setup for machining during dry, flood and MQL.



a) Bridgeport GX1000 CNC Machine



b) The Fanuc series oi-MC Control Panel

Figure 4.7. a) The Bridgeport GX1000 CNC machine and b) the Fanuc series oi-MC control panel

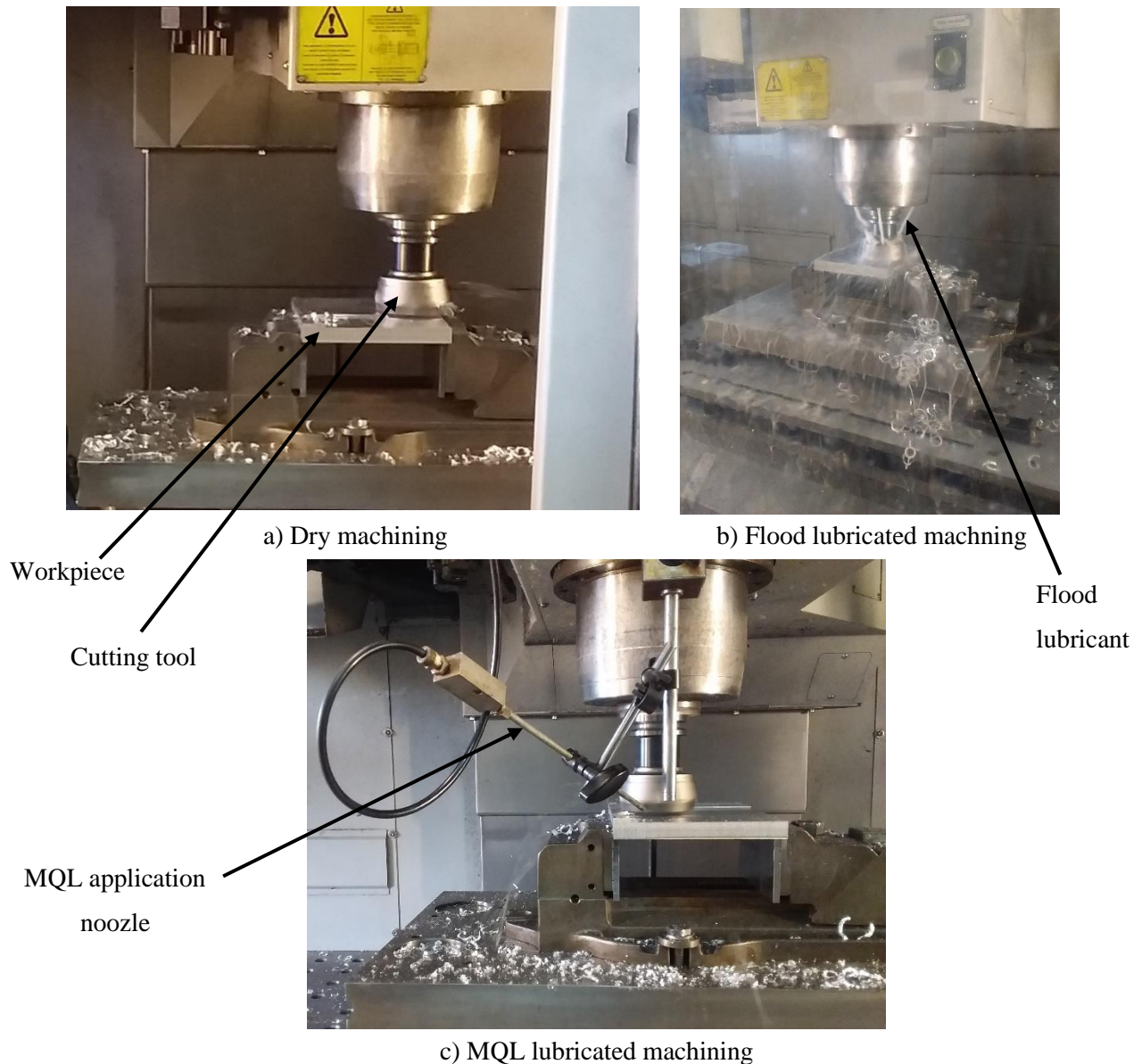


Figure 4.8. a) Dry, b) Flood and c) MQL lubricating conditions during machining trials

4.5 Kistler Dynamometer

The Kistler dynamometer was used to measure cutting forces in the XYZ directions during machining. The Kistler uses a piezoelectric sensor to measure vibrations and moments in all directions; the dynamometer also consists of a DAS (data acquisition system) and charger amplifier. The Kistler dynamometer sampling was set to take 100 readings per second.

The dynamometer was connected to a computer and the force place was mounted on the CNC table. The computer has the dyno User Interface software installed for taking readings, the software was also used to export data into excel spreadsheets. A dongle is inserted in the USB port of computer to connect it to the Kistler dynamometer while taking force readings.



Figure 4.9. Kistler 5697A DAQ System and Multi-Channel Charge Amplifier

4.6 Flir Thermal Imaging Camera

The Flir thermal imaging camera in Figure 4.10 was used to take maximum, minimum, and average temperatures during dry and MQL machining in Figure 4.8a and 4.8c respectively. The thermal imaging camera took 30 readings each second. The camera was connected to a laptop that has a ResearchIR software that takes videos and interprets readings of max, min, and average temperatures. However, the most important is the maximum temperature that is at the tool-workpiece interface.

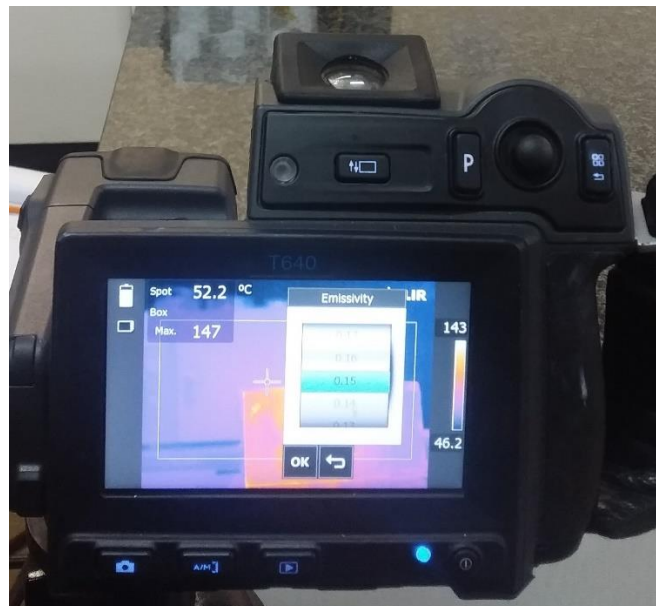


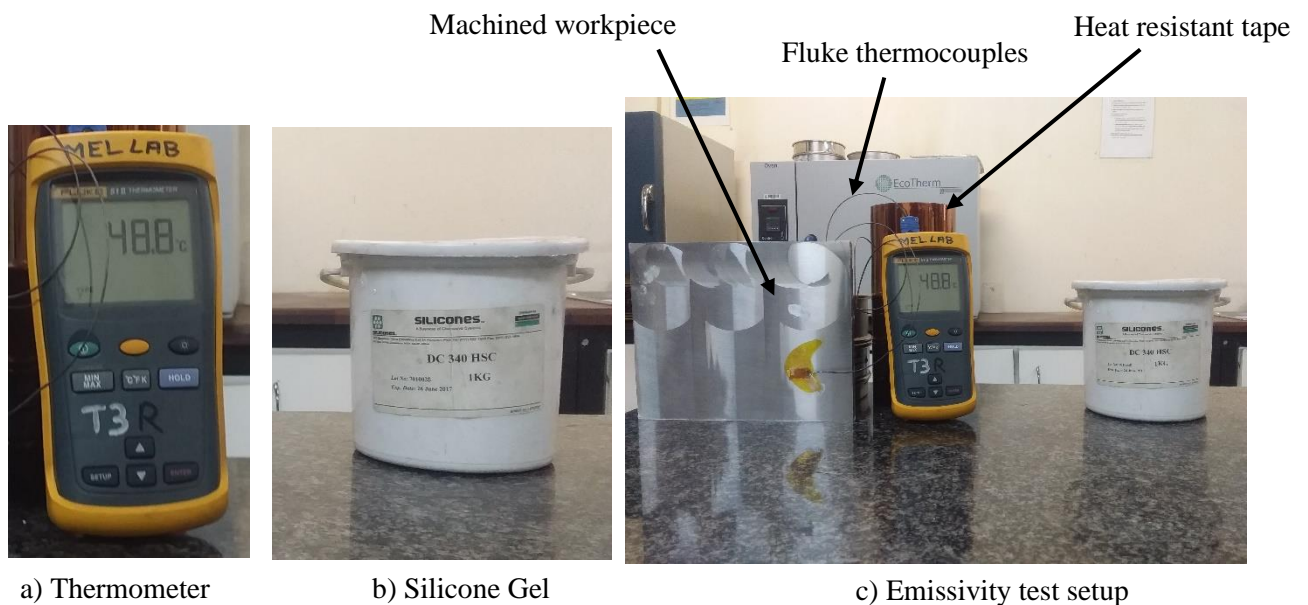
Figure 4.10. Thermal Imaging Camera

4.7 Emissivity Test

The emissivity test was also carried out using the Flir Thermal Imaging camera and this required heating of a machined workpiece to 90°C temperature in the Elite Thermal Systems Furnace for 3 hours dwell time. The furnace is depicted in Figure 4.11. The emissivity test required the use of thermocouples, a thermometer, heat resistant tape, and silicone gel as shown in Figure 4.12.



Figure 4.11. Elite Thermal Systems Furnace



a) Thermometer

b) Silicone Gel

c) Emissivity test setup

Figure 4.12. Thermometer, Silicone Gel, K-Type fluke thermocouples, and Heat resistant tape

Fluke thermocouples were used to read the temperature of the machined surface and the thermometer displayed the temperature readings. Silicone gel was applied on the thermocouples to avoid any error

in readings that may be caused by trapped air between the hot workpiece surface and the thermocouple. The heat resistant tape was used to attach the fluke thermocouples to the hot workpiece surface.

4.8 Flank Wear Measurements

Flank wear was measured using the Nikon SMZ1500 optical microscope in Figure 4.13 connected to a computer desktop in Figure 4.14 that has the Nikon data acquisition software installed. The software displays the image of an insert edge and with measuring tools on the software, flank wear was measured. Each insert had flank measured after every single machining run.



Figure 4.13. Nikon SMZ1500 Optical Microscope

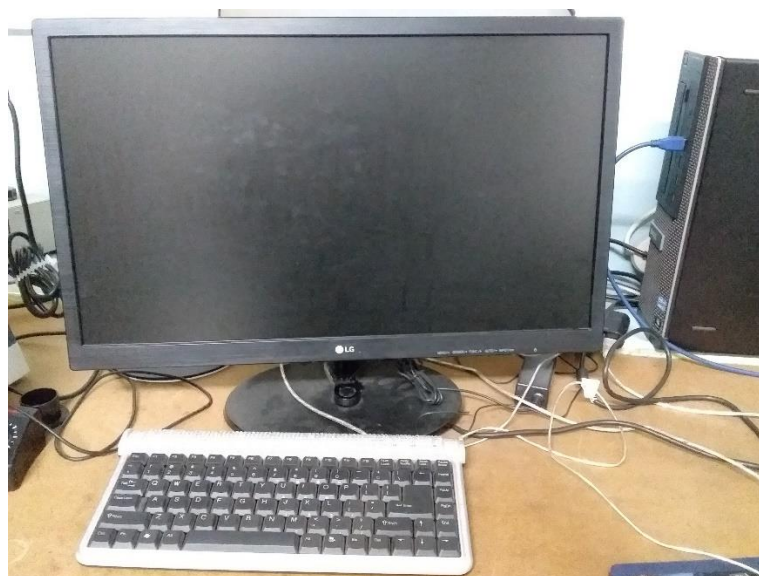


Figure 4.14. Computer desktop connected to the Nikon SMZ1500 optical microscope

4.9 Surface Roughness

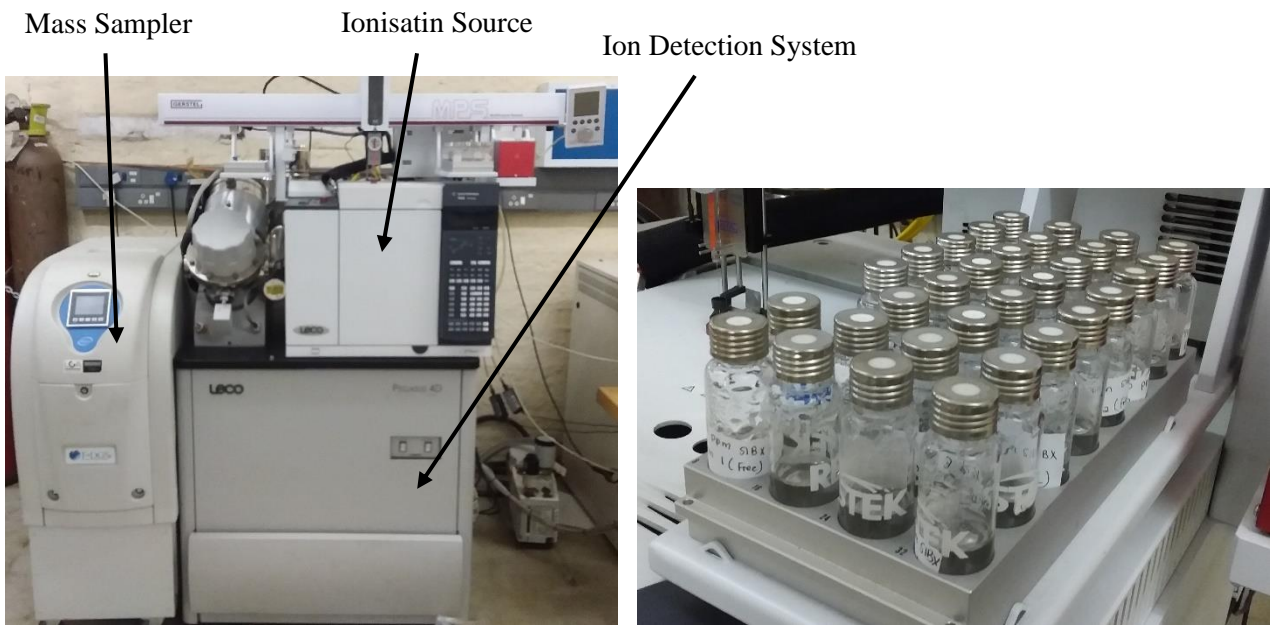
The surface roughness of the machined workpiece surface was measured during finishing criterion of machining using the SRT-6210 roughness tester. The tester has a profilometer that moves in the direction of feed and measures R_a , R_t , R_q , and R_z . The Roughness Average (R_a) is the arithmetic average of the profile heights over the evaluation length of the profilometer. The Maximum Height of the Profile (R_t) distance between the highest and lowest points of the evaluated profile length. Roughness RMS (R_q) is the root mean square of profile heights within the evaluated length. The Average Maximum Height of the Profile (R_z) is the average of successive distances between the highest and lowest points of the chosen samples of evaluation lengths (can be 2 or more sample lengths) Figure 4.12 is a picture of the SRT-6210 roughness tester.



Figure 4.15. SRT-6210 roughness tester

4.10 Lubricant Analysis

The chemical compositions of the flood and MQL lubricants were analysed with the use of the Leco GCxGC-TOF Low resolution mass spectrophotometer shown in Figure 4.13a. The GC-MS equipment has three components assembled together which are ionisation source, mass analyser, and the ion detection system assembled. The ionisation source converts molecules of a sample into gas-phase ions, the mass analyser separates ions according to their mass-to-charge (m/z) ratios, and the m/z ratios are measured together with their abundance. Samples holders are shown in Figure 4.13b. The data was saved and exported on the computer desktop.



a) GC-MS equipment

b) Sample holder

Figure 4.16 a) Leco GCxGC-TOF Low resolution mass spectrophotometer and b) Sample holder

Chapter 5: Experimental Procedures

The experimental procedure of this research study was conducted in three major parts which are face milling (Making use of the CNC machine while taking Force, temperature and surface measurement), insert flank wear measurements and lubricants content analysis (Flood and MQL lubricants analysis). Forces were measured in the XYZ directions using the Kistler force plate, Temperatures were measured using the Thermal Imaging camera focused at the tool-workpiece interface and flank wear measurements were taken using the Nikon Optical Microscope.

5.1 Face Milling Test Conditions

A band-saw machine was used to cut the 1000 x 990 x 20mm AA7075 plate into 30 workpieces of dimension 200 x 160 x 20mm. The CNC machine model GX1000 was used to conduct face milling for three lubricating conditions which are Dry, Flood, and MQL. Within each lubricating condition, three test trials were conducted making a total of 9 tests per cutting insert. The three test trials are Roughing, Semi-finishing, and Finishing, each with a different set of varied parameters. The varied parameters are cutting speed, feed rate, and depth of cut for each test trial. Table 5.1 outlines test conditions for each machining criterion and W1-L, W1-S, M1-L, R1-L, G1-L, and G1-S are short symbols for the 6 cutting inserts used for the course of the experiment.

The research experiment was conducted under three lubricating conditions; dry, flood, and MQL lubrication. In each lubricating condition, there were three machining criteria which are roughing, semi-finishing, and finishing. These were facilitated by cutting speeds 200m/min (roughing), 400m/min (semi-finishing), and 800m/min (finishing). The depth of cut was also varied for each cutting speed to maintain a constant rate of material removal (\dot{V}) for each machining run. The varied cutting speeds, depths of cut, and the calculated rate of material removal over a period of 20 minutes cutting time are tabulated in Table 5.3. Equation 5.1 below was used to calculate the rate of material removal.

$$\dot{V} = a_p \times v_f \times d \quad \text{Equation 5.1}$$

Where \dot{V} is the rate of material removal, a_p is the axial depth of cut, v_f is the feed rate, and d is the cutting width. Each insert edge removed 10666.67 mm³/min of material and a total of 213333.33 mm³ over a cutting period of 20 minutes. The total volume of material removed during the entire experiment was calculated to be 3840000 mm³.

Table 5.1: Milling test conditions, apply dry, flood, and MQL lubricating conditions for rouging, semi-finishing, and finishing. Test no. are machining test counts.

Test no.	Insert	Cutting speed (m/min)	Depth of cut (mm)	Spindle speed (rpm)	Feed rate (mm/min)	Cutting time (min)
Roughing						
1	W1-L [6]	200	2.0	800	80	20
2	W1-S [11]	200	2.0	800	80	20
3	M1-L [7]	200	2.0	800	80	20
4	R1-L [2]	200	2.0	800	80	20
5	G1-L [3]	200	2.0	800	80	20
6	G1-S [9]	200	2.0	800	80	20
Semi-finishing						
7	W1-L [6]	400	1.0	1600	160	20
8	W1-S [11]	400	1.0	1600	160	20
9	M1-L [7]	400	1.0	1600	160	20
10	R1-L [2]	400	1.0	1600	160	20
11	G1-L [3]	400	1.0	1600	160	20
12	G1-S [9]	400	1.0	1600	160	20
Finishing						
13	W1-L [6]	800	0.5	3200	320	20
14	W1-S [11]	800	0.5	3200	320	20
15	M1-L [7]	800	0.5	3200	320	20
16	R1-L [2]	800	0.5	3200	320	20
17	G1-L [3]	800	0.5	3200	320	20
18	G1-S [9]	800	0.5	3200	320	20

Table 5.2: Inserts abbreviations and their compositions

Abbreviation	Composition (wt%)
G1-L	NbC-4Mo ₂ C-4TiC-12Ni
G1-S	NbC-4Mo ₂ C-4TiC-12Ni
R1-L	NbC-4TiC-12Ni
M1-L	WC-0.8Cr ₃ C ₂ -4Mo ₂ C-4TiC-10Co
W1-L	WC-0.8Cr ₃ C ₂ -10Co
W1-S	WC-0.8Cr ₃ C ₂ -10Co

Table 5.3: Calculated constant rate of material removal in volume

PARAMETERS	VALUE			UNITS
Cutting speed	200	400	800	m/min
Depth of Cut	2	1	0.5	mm
Feed rate	80	160	320	mm/min
Cutting width	66.67			mm
Volume removed per minute	10666.67			mm ³ /min
Time of machining	20			min
Volume removed after 20 minutes	213333.33			mm ³
Total Volume removed per insert	213333.33			mm ³
Machining Conditions (Dry, MQL, and Flood)	3			
Volume removed during all 3 conditions	640000			mm ³
Number of inserts	6			
Total Volume removed by all 6 inserts over the entire experiment	3840000			mm ³

5.2 Force Measurement

The Kistler dynamometer was first calibrated to ensure correct measurements are taken during the actual machining.

5.2.1 Kistler Dynamometer Calibration

1. Connect the Kistler charge amplifier to the Data Acquisition System (DAS) via a cable.
2. Connect the dynamometer, the Kistler charge amplifier via a cable and the computer together via cables.
3. Switch on the CNC machine, the Kistler charge amplifier and the computer desktop
4. Insert the Dyno Ware dongle in a free USB port on the computer.
5. Click the 'Meas' button on the Kistler charge amplifier and the green LED light goes on
6. Open the Dyno Ware application on the computer.
7. Click the reset button to refresh the settings.
8. Click on the edit button and edit:
 - The preferred name of the excel spreadsheet of measurement e.g., "Demo" for a calibration trial.
 - Measuring time e.g., 120 seconds for a calibration.
 - Edit the number of reading the dynamometer will take per second e.g., change from 100 to 10 readings per second.
 - Repeat this for every machining run throughout the whole experiment.
9. Click on the 'Doc' button to confirm the name and the measuring time.
10. Click on 'Data Acquisition' and an option to start measuring will pop up.
11. Start the CNC machine.
12. Click start on the Dyna Ware app to start measuring and record the forces.
13. Place one 5kg workpiece on the Kistler force plate and note the changes in force readings.

14. Place another 5kg workpiece and note the changes.
15. Remove the 10kg weight of workpieces at once.
16. The Dyna ware software will stop measuring at 120s or click stop.
17. Save the document of measurements as a CSV excel file.

5.2.2 Precautions

- Ensure the dongle is well inserted to the computer before starting with the measurements.
- The signal cable head connecting to the Kistler charge amplifier is very sensitive and its damage should be avoided at all costs.
- The green LED light should be on before any measurements are taken to avoid errors in measurement.

5.3 CNC Face Milling

5.3.1 Workpiece Machining

1. Clamp the AA7075 workpiece tightly with a vice on the Kistler force plate.
2. Screw in the cutting tool to the top part of the CNC machine.
3. Fit an insert into the insert socket of the cutting tool and screw in the clamp to hold tight the insert.
4. Program the CNC machine with the required parameters for the machining criteria.
5. Test-run the program without cutting to ensure it behaves as required.
6. Run the program to start cutting.
7. Start the Dyna Ware software for taking force measurements in the XYZ directions at the same time when the insert engages with the workpiece to start cutting.
8. The workpiece will be machined according to the loaded program.
9. The software is stopped as soon as the insert edge leaves the workpiece or the software will stop automatically based on the allowable measuring time specified before machining.
10. Replace the insert with another in a specified order stated in Table 5.1.

11. Repeat step 3-10 for each insert for all test conditions described in Table 5.1 for all lubricating conditions.

5.3.2 Precautions

- The insert should be tightly clamped so it does not fly off at high cutting speeds.
- The insert should not however be clamped too tight to avoid the having the insert breaking into halves during machining.
- Do not insert hands into the CNC during machining.
- Ensure each workpiece is machined to a depth of 10mm and not any further, this will avoid any vibrations of the workpiece going deeper in depth which will temper with the force measurements.
- Ensure the right edge is used for cutting as planned for results consistency.
- Wear safety goggles to prevent flying chips from damaging operator's eyes.
- Wear safety boots and trousers.

5.4 Lubrication

Three lubricating conditions are tested for the course of the experiment and each test condition with a different lubricant.

5.4.1 Dry Conditions

1. No coolant required.
2. CNC programs and machining are run as stated in 5.3.

5.4.2 Flood Lubricating Condition

1. Dilute the concentrated flood coolant with water at volume ratio 1:20.
2. Fill the lubricant storage tank in the CNC machine compartment with the flood coolant.
3. Flood lubricant was applied with the use of two centrifugal pumps that delivers the lubricant at a flow rate of 1.39 l/s (5 m³/hr).
4. Open the flood coolant before starting the CNC machine for cutting.

5. During machining, the flood coolant released is filtered and recycled back to the tool-workpiece interface.
6. Repeat step 4 for each insert and machining criteria.
7. Two centrifugal pumps mounted on the CNC runs the flood coolant in pipelines and across filters.

5.4.3 MQL Lubricating Conditions

1. Fill the MQL oil tank with new oil.
2. Set the MQL application rate at 0.03ml/pulse and application time of 0.6 seconds/pulse, the MQL was applied at a flowrate of 0.05 ml/s.
3. Connect an air pipeline supplying compressed air at a pressure of 5MPa from the gas tank.
4. Fit the nozzle to a nozzle holder with an electric magnet.
5. Attach the electric magnet to the top part of the CNC machine focusing the nozzle outlet on the insert cutting edge.
6. Switch on MQL oil supply before starting the CNC machine.

5.4.4 Precautions

- Close the CNC sliding doors to trap flying chips, avoid untidiness during dry and MQL conditions.
- Ensure enough air pressure supply.
- Avoid making skin contact with the concentrated flood coolant, it may cause skin irritation.
- Close the CNC machine to trap the coolant inside the machine, spillage outside the CNC may cause slip, trip, and fall incidents.
- Keep the side trap doors of the CNC machine open to release the steam caused by MQL oil when heated by the temperature rises during machining.
- Keep the lab windows open to take the steam outside.

5.5 Temperature Measurement.

The thermal imaging camera takes a video while recording the maximum and minimum temperatures of the experimental setup during machining. An emissivity test is conducted to calibrate the camera emissivity using a thermometer and thermocouples. The calibration was carried out through the below steps described below.

5.5.1 Flir Thermal Imaging Camera Calibration (Emissivity test)

1. Heat one AA7075 workpiece in an Elite Thermal Systems Furnace to $90^{\circ}C$ temperature.
2. Maintain a constant $90^{\circ}C$ temperature in the furnace for a period of 3 hours.
3. Remove the workpiece after 3 hours and carry out the emissivity test quickly before the workpiece cools down below $50^{\circ}C$.
4. Smear the thermocouple wire with silicon and attach it to the hot surface of the workpiece; use heat resistant tape to cover the thermocouple wire. Silicon ensures no air is trapped since air is a heat insulator which may result in false readings in the thermometer.
5. Place the Thermal Imaging camera less than a meter away from the workpiece and focus it on the workpiece.
6. Read the temperature of the workpiece on the thermometer that is directly linked to the workpiece and record.
7. Adjust the thermal imaging camera to the recorded temperature and record the emissivity.
8. Allow the workpiece to cool down $10^{\circ}C$ from the previously recorded temp.
9. Repeat steps 5-7 one more time and record the second emissivity.
10. The actual emissivity of AA7075 lies between the two recorded emissivity values (0.14 and 0.15).

5.5.2 Measurement

1. Place the Thermal Imaging camera on a tripod stand less than 1 meter away from the tool-workpiece interface just outside the CNC machine.
2. Switch on both the camera and a computer desktop.

3. Focus the camera on the tool-workpiece interface.
4. Connect the camera to the computer via a cable.
5. Open ResearchIR application on the computer.
6. Set the emissivity to be any of the two recorded values in 5.5.1.
7. When the CNC machine is started, click the record button when the insert engages with the workpiece to start cutting.

5.5.3 Precautions

- Take readings as quick as possible during calibration before the workpiece cools down below 50°C (low accuracy in readings below 50°C).
- During calibration, do not focus the camera on the tape. Focus the imaging camera on the workpiece itself.
- Use heat resistant gloves to remove the workpiece from the furnace.
- Do not move the camera while recording.

5.6 Surface Roughness

Surface roughness measurements were taken using the SRT-6210 roughness tester. Surface roughness entails taking readings of R_a , R_q , R_z , and R_t . A surface roughness tester is used to measure all four readings for only the finishing criteria of the experiment. The below procedure was followed:

5.6.1 Roughness Measurements

1. Remove the workpiece from the CNC machine right after machining and place it on a flat bench.
2. Connect the tester profilometer to the tester.
3. Place the tester on the flat machined surface such that the profilometer will move in the direction of the feed.
4. Release and lower the tester plastic support leg to rest on the bench surface.
5. Screw in to hold the support leg still, this will ensure the tester lies flat on the surface each time when taking readings.

6. Switch on the roughness tester.
7. Click the 'CAL' button to refresh and calibrate the tester.
8. Click the 'Start' button to start taking measurements,
9. After the profilometer moved forward and backwards, the screen of the tester will display the Ra value and take the recording.
10. Click the 'RaRz' button to display the Rt, Rq, Rz, and Rt for the safe test and take recordings.
11. Take the four readings at the entry, middle and exit points of cutting insert on the workpiece during machining.
12. Repeat steps 3-11 after machining with each cutter and every machining run.

5.6.2 Precautions

- Ensure that the tester lies flat on the machined surface of the workpiece.
- Ensure that the profilometer moves in the direction of the feed, to avoid inaccurate measurements.
- Allow the workpiece to cool down after dry machining, hot surfaces may damage the profilometer.
- The sensor of the tester is very sensitive and damage to it should be avoided at all costs.
- Do not move the tester when the profilometer if taking measurements.

5.7 Insert Wear Measurement

Insert wear measurements were taken on each insert right after each minute of machining. The apparatus used for measurements is the Nikon SMZ1500 Optical Microscope which is connected to a computer desktop. The computer has a Nikon application software installed. The below procedure is followed on making measurements:

5.7.1 Flank Wear Measurement

1. Switch on the computer and the desktop and the Nikon Optical Microscope.
2. Place an insert on the insert holder.

3. Place the insert holder on the optical microscope.
4. Adjust the lighting on the microscope, shift the stage.
5. Open the Nikon application software.
6. Click the 'Live' button on the software to initialise the camera and the stage will be visible on the software on the computer monitor.
7. Shift the microscope stage back and forth to locate the insert holder and the insert.
8. Specify the magnification value.
9. Adjust the coarse and fine adjustments to focus the microscope and improve the quality of the image.
10. Click on the 'measure' button to access measuring tools.
11. Make use of two red lines to measure the $V_{B \max}$ and V_B .
12. Click the 'Auto Capture' button to take an image of the insert edge.
13. Repeat step 2-11 for each minute of machining for every insert.

5.7.2 Precautions

1. Do not lean on the table while taking measurements, shaking the table makes the microscope lose focus.
2. Ensure the microscope is focused on the right edge.
3. Do not change the magnification for the rest of the research experiment to ensure consistency of measurements.

5.8 Flood and MQL analysis

The flood and MQL were analysed using the Leco GCxGC-TOF Low resolution mass spectrophotometer which suggested the most possible constituents of the sample. The ionisation source, mass analyser, and the ion detection system are the main components of the GC-MS apparatus. The below procedure is followed on making measurements:

5.8.1 Sample Preparation

5.8.1.1 Procedure

1. Measure a 25ml volume of the lubricant using a pipette.
2. Pour the measured 5ml into a conical flask.
3. Add 25ml of the HPLC solvent (Methanol) to make a total of 10ml.
4. Seal the conical flask and pre-heated the sample (at 150°C) while stirring in a heating mantle set up on a magnetic stirrer.
5. Leave the hot sample to cool overnight.

5.8.1.2 Precautions

1. Wear safety goggles and hand gloves.
2. Wear heat resistant gloves during pre-heating of the prepared samples.
3. Contact the operator for direct injections into the GC-MS with other solvents.
4. Do not leave used pipettes/pipette tips, samples, used syringes, and hand gloves on the working station unattended to.

5.8.2 Lubricant analysis

5.8.2.1 Procedure

1. Transfer 10ml sample into a 50ml sample holder.
2. Place the sample on the Gerstel Multi-Purpose Auto Sampler (MPS).
3. 1 uL injected in the injection port (Topaz liner, split single taper gooseneck w/Wool 4mm x 6.5 x 78.5) using a Gerstel MPS.
4. Column type (Rxi-5 Sil MS), length 29.00 m of (30m), with internal diameter 250µm, and film thickness of 0.25 µm with a maximum temperature of 360 °C was used. Helium was used as the carrier gas.

5.8.2.2 Precautions

1. Name each conical flask and sample holder to avoid human error.

Chapter 6: Data Processing

6.1 Cutting Forces

Cutting forces were taken in the XYZ directions using the DynoWare software that recorded 100 measurements per second (high accuracy). The unit for readings taken is Newton (N). Resultant forces were calculated for each of the 100 readings in a second of cutting using equation 6.2.

$$F_R = \sqrt{F_X^2 + F_Y^2 + F_Z^2} \quad \text{Equation 6.2}$$

F_R is the resultant force whereas F_X , F_Y , and F_Z are force reading taken in the XYZ directions. The unit of F_R is N.

Average resultant forces ($F'_{R,ave}$) were calculated for each second of cutting using the mean equation such as equation 6.3.

$$F'_{R,ave} = \frac{\sum F'_{R,i}}{n} \quad \text{Equation 6.3}$$

$F'_{R,i}$ is each of the 100 resultant forces calculated in a second and $\sum F'_{R,i}$ is the sum of resultant forces calculated in a second. Equation 6.4 was used to calculate average resultant forces ($F_{R,ave}$) for each minute of cutting. $F_{R,i}$ is each of the 60 resultant forces calculated in a minute and $\sum F_{R,i}$ is the sum of resultant forces calculated in a minute. The variable n is the number of readings to be computed in the average calculation, n equals 100 when calculating $F'_{R,ave}$, and 60 when calculating $F_{R,ave}$.

$$F_{R,ave} = \frac{\sum F_{R,i}}{n} \quad \text{Equation 6.4}$$

The error in $F_{R,ave}$ was calculated from readings taken in the first 40 seconds of the calibration run, before the workpiece loads were presented. Figure 6.1 shows the graph of $F_{R,ave}$ versus machining time in seconds for the calibration run. The error and fluctuations in $F_{R,ave}$ are due to CNC machine vibrations and circulation of the cutting tool. The error was calculated as the average resultant force using equations 6.2-6.4. The error was calculated to be 13 N.

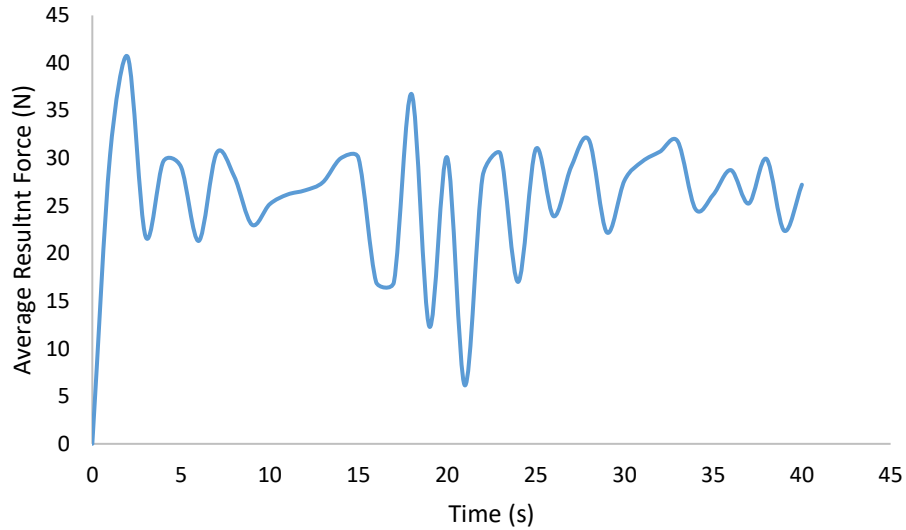


Figure 6.1. Calibration curve showing average resultant force versus time for the first 40 seconds of the calibration run

6.2 Cutting Temperatures

The Flir thermal imaging camera was used to take 30 temperature readings in a second and the thermal imaging camera was calibrated by emissivity tests conducted on the AA7075 machined workpiece surface. Emissivity was found to be between 0.14 and 0.15. The camera took videos during machining while noting the maximum and minimum temperatures of the experimental setup. Data was extracted from videos using the 0.14 and 0.15 emissivity values on the ResearchIR software. The temperature readings were copied and pasted on an excel spreadsheet and the maximum temperature of the 30 readings in a second was selected for analysis. Maximum Average Temperatures (T_a) were calculated in °C using equation 6.5.

$$T_a = \frac{\sum T_{Max, i}}{n} \quad \text{Equation 6.5}$$

$T_{Max,i}$ is each of the 60 maximum temperatures in a minute and $\sum T_{Max,i}$ is the sum of 60 maximum temperature in a minute.

Error in T_a was calculated from the difference between temperature readings extracted at 0.14 and 0.15 emissivity values for the same machining run. Equation 6.6 was used to calculate the described error in T_a . The $T_{a(0.15)}$ and $T_{a(0.14)}$ are the calculated average maximum temperatures at their emissivity value and T_{Error} is the temperature error.

$$T_{Error} = \frac{|T_{a(0.15)} - T_{a(0.14)}|}{2} \quad \text{Equation 6.6}$$

6.3 Flank Wear Rates

Maximum flank wear (VB_{max}) was measured using the Nikon data acquisition software installed on a computer desktop. The VB_{max} was measured in micrometres (μm) for each machining run for a period of 20 minutes. Flank wear rate (FWR) is a measure of how much wear the insert experienced on the relief face per minute. The FWR is calculated from the maximum flank wear rate and insert tool life as shown in equation 6.1.

$$FWR = \frac{VB_{Max}}{t_{Tool\ life}} \quad \text{Equation 6.1}$$

The $t_{Tool\ life}$ is the machining time of insert before reaching failure criteria. The unit for FWR is $\mu\text{m}/\text{min}$. The insert may fail due to flank wear or fracture.

6.4 Surface Roughness

Surface roughness was measured for finishing criteria using the SRT-6210 roughness tester that gives the R_a , R_q , R_z , and R_t readings. However, R_a (unit μm) values were used as a measure of surface roughness. Three readings were taken after each machining run and readings were taken at 1 min, 10 min and 20 min cutting times. Average surface roughness R_a was calculated from all R_a readings taken within the 20 minutes cutting time. Equation 6.7 was used to calculate R_a for each cutting insert.

$$R_a = \frac{\sum R_{a,i}}{n} \quad \text{Equation 6.7}$$

$R_{a,i}$ is each of the surface roughness readings taken during the 20 minutes cutting time, $\sum R_{a,i}$ is the sum of all readings taken for each insert and n is the number of readings taken for each insert within 20 minutes cutting time. The error in R_a for each cutting insert under dry, flood, and MQL conditions was calculated using equation 6.8:

$$R_{a\ error} = \frac{\sigma_{R_a}}{\sqrt{n}} \quad \text{Equation 6.8}$$

$R_{a\ error}$ is the error in R_a , σ_{R_a} is the standard deviation of surface roughness measurements and n is the number of readings taken after each machining run, n always equal to 3 for equation 6.8. The standard deviation of R_a measurements taken was calculated as in the equation 6.9.

$$\sigma_{R_a} = \frac{\sum_1^n (\overline{R_{a,t}} - R_{a,t})^2}{n} \quad \text{Equation 6.9}$$

Chapter 7: Results

The results presented in this chapter were obtained in an attempt to analyse the performance of each of the six cutting inserts during face milling of the aerospace grade Aluminium Alloy 7075 (AA7075) under different parameters and lubricating conditions. Three cutting inserts were produced from Tungsten Carbide (WC) powder material, while three were produced from Niobium Carbide (NbC) powder material. The six inserts were produced by two different sintering techniques, Liquid Phase Sintering (LPS) and Spark Plasma Sintering (SPS), into composite cutting materials.

7.1 Mechanical Properties

The different material used, wt% compositions, and sintering techniques account for the differences in mechanical properties of samples. Table 7.1 presents the hardness (HV_{30}) and fracture toughness (K_{IC}) of each of the six cutting samples:

Table 7.1. Compositions and mechanical properties of cutting samples

Composition	Abbreviation	Sample	HV_{30} (GPa)	K_{IC} (MPa $m^{1/2}$)
WC-0.8Cr ₃ C ₂ -10Co	WC-Cr ₃ C ₂ -Co (LPS)	W1-L	14.50 ± 0.09	11.30 ± 0.17
WC-0.8Cr ₃ C ₂ -10Co	WC-Cr ₃ C ₂ -Co (SPS)	W1-S	14.88 ± 0.21	10.72 ± 0.14
WC-0.8Cr ₃ C ₂ -4Mo ₂ C-4TiC-10Co	WC-Mo ₂ C-TiC-Co (LPS)	M1-L	16.24 ± 0.12	10.97 ± 0.14
NbC-4TiC-12Ni	NbC-TiC-Ni (LPS)	R1-L	11.13 ± 0.13	8.10 ± 0.35
NbC-4Mo ₂ C-4TiC-12Ni	NbC-TiC-Mo ₂ C-Ni (LPS)	G1-L	13.14 ± 0.14	9.52 ± 0.23
NbC-4Mo ₂ C-4TiC-12Ni	NbC-TiC-Mo ₂ C-Ni (SPS)	G1-S	14.80 ± 0.17	8.30 ± 0.18

Figure 7.1 shows the relationship between HV_{30} and K_{IC} . Generally, HV_{30} increased with increased K_{IC} . However, inserts of similar compositions showed an increase in HV_{30} with decreased K_{IC} . The Spark Plasma Sintered (SPS) samples had HV_{30} within the same error margin irrespective of their different K_{IC} whereas the Liquid Phase Sintered (LPS) samples showed a direct relationship between HV_{30} and K_{IC} . Samples produced from WC had higher HV_{30} and K_{IC} than the samples produced by NbC except for the SPS NbC-4Mo₂C-4TiC-12Ni (wt%) sample which had similar HV_{30} to the SPS WC-0.8Cr₃C₂-10Co (wt%) sample. The WC based samples had K_{IC} which were within the same K_{IC} error margin. The LPS samples (NbC-4Mo₂C-4TiC-12Ni and WC-0.8Cr₃C₂-10Co) had higher K_{IC} and slightly lower HV_{30} than their similar SPS produced samples. The NbC based NbC-4TiC-12Ni (wt%) sample had the lowest HV_{30} and K_{IC} whereas the WC LPS WC-0.8Cr₃C₂-4Mo₂C-4TiC-10Co (wt%) had the highest HV_{30} .

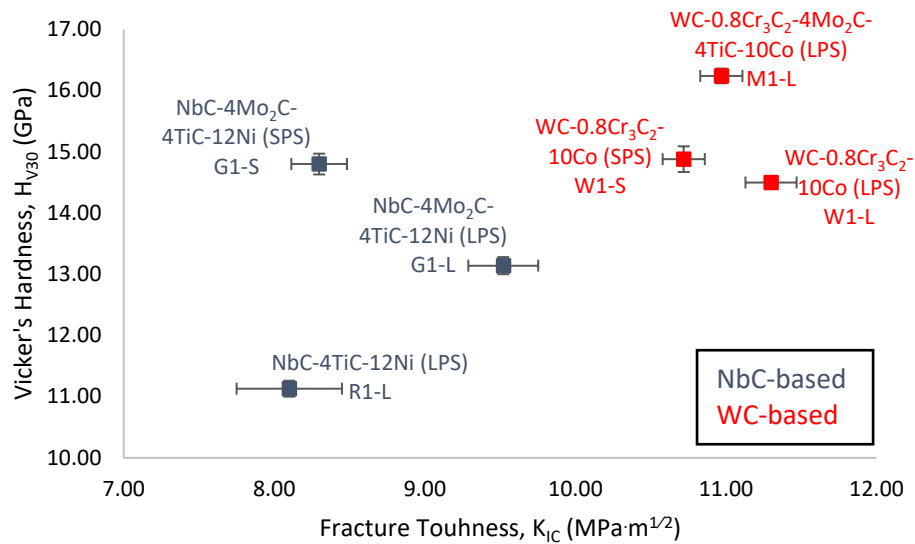


Figure 7.1. Graph of sample hardness (HV_{30}) against fracture toughness (K_{IC})

7.1.1 Hardness (HV_{30})

7.1.1.1 Hardness of WC-Cr₃C₂-Co sample

The WC-0.8Cr₃C₂-10Co (wt%) sample produced by SPS had a HV_{30} of 14.88 ± 0.21 GPa and the LPS WC-0.8Cr₃C₂-10Co (wt%) sample had HV_{30} of 14.50 ± 0.09 GPa (Table 7.1). The SPS technique slightly increased HV_{30} by approximately 0.38 GPa however, considering the error in measurements, the difference in HV_{30} is very insignificant.

7.1.1.2 Hardness of WC-Mo₂C-TiC-Co sample

The LPS WC-0.8Cr₃C₂-4Mo₂C-4TiC-10Co (wt%) sample had HV_{30} of 16.24 ± 0.12 GPa and the LPS WC-0.8Cr₃C₂-10Co (wt%) sample had a HV_{30} of 14.50 ± 0.09 GPa. The LPS WC-0.8Cr₃C₂-4Mo₂C-4TiC-10Co (wt%) sample had 1.74 GPa higher HV_{30} than the LPS WC-0.8Cr₃C₂-10Co (wt%) sample. The 12% increase in HV_{30} could be due to the additions of 4 wt% Mo₂C and 4 wt% TiC. The LPS WC-0.8Cr₃C₂-4Mo₂C-4TiC-10Co (wt%) sample also had 1.36 GPa higher HV_{30} than the SPS WC-0.8Cr₃C₂-10Co (wt%) sample could also be due to the additions of 4 wt% Mo₂C and 4 wt% TiC.

7.1.1.3 Hardness of NbC-TiC-Ni sample

The niobium carbide-based NbC-4TiC-12Ni (wt%) sample had a HV_{30} of 11.13 ± 0.13 GPa and this was the lowest HV_{30} of all produced samples.

7.1.1.4 Hardness of NbC- Mo₂C-TiC-Ni sample

The Liquid phase sintered NbC-4Mo₂C-4TiC-12Ni (wt%) sample had a HV_{30} of 13.14 ± 0.14 GPa and the liquid phase sintered NbC-4TiC-12Ni (wt%) sample had a HV_{30} of 11.13 ± 0.13 GPa. The addition

of Mo₂C to NbC-4TiC-12Ni (wt%) sample increased HV₃₀ by 2.01 GPa, which was an 18% increase. The SPS NbC-4Mo₂C-4TiC-12Ni (wt%) sample had a HV₃₀ of 14.80 ± 0.17 GPa which was 1.66 GPa higher than the LPS NbC-4Mo₂C-4TiC-12Ni (wt%) sample. The SPS technique resulted in a 13% increase in HV₃₀. The SPS NbC-4Mo₂C-4TiC-12Ni (wt%) sample had 3.67 GPa higher HV₃₀ than the LPS NbC-4TiC-12Ni (wt%) sample. The effect of Mo₂C addition and the SPS technique resulted in a 33% increase in HV₃₀ in comparison to the LPS NbC-4TiC-12Ni (wt%) sample. The effect of the addition of Mo₂C to NbC-4TiC-12Ni (wt%) sample was greater than the effect of the SPS technique on HV₃₀.

7.1.2 Fracture Toughness (K_{IC})

7.1.2.1 Fracture Toughness of WC-Cr₃C₂-Co sample

The LPS produced WC-0.8Cr₃C₂-10Co (wt%) sample had a K_{IC} of 11.30 ± 0.17 MPa·m^{1/2} and the SPS WC-0.8Cr₃C₂-10Co (wt%) sample had a K_{IC} of 10.72 ± 0.17 MPa·m^{1/2}. The difference between the K_{IC} of the LPS and SPS produced WC-0.8Cr₃C₂-10Co (wt%) samples was 0.58 MPa·m^{1/2}. This was a very negligible difference hence the SPS had negligible effect on K_{IC}.

7.1.2.2 Fracture Toughness of WC-Mo₂C-TiC-Co sample

The LPS produced WC-0.8Cr₃C₂-4Mo₂C-4TiC-10Co (wt%) sample had a K_{IC} of 10.97 ± 0.14 MPa·m^{1/2}, slightly lower K_{IC} than the LPS WC-0.8Cr₃C₂-10Co (wt%) sample. The addition of Mo₂C and TiC in the LPS WC-0.8Cr₃C₂-4Mo₂C-4TiC-10Co (wt.%) decreased K_{IC} by 0.33 MPa·m^{1/2} compared to the LPS WC-0.8Cr₃C₂-10Co (wt%). However, the 0.33 MPa·m^{1/2} decrease was within the K_{IC} error bars. There was a negligible change in K_{IC} hence the additives had negligible effect on K_{IC}.

7.1.2.3 Fracture Toughness of NbC-TiC-Ni sample

The liquid phase sintered NbC-4TiC-12Ni (wt%) had a K_{IC} of 8.10 ± 0.35 MPa·m^{1/2} which was the lowest K_{IC} of all produced samples.

7.1.2.4 Fracture Toughness of NbC- Mo₂C-TiC-Ni sample

The LPS produced NbC-4Mo₂C-4TiC-12Ni (wt%) sample had a K_{IC} of 9.52 ± 0.23 MPa·m^{1/2} which was 1.42 MPa·m^{1/2} higher K_{IC} than the LPS NbC-4TiC-12Ni (wt%). The 1.42 MPa·m^{1/2} increase in K_{IC} could be due to the addition of Mo₂C to NbC-4TiC-12Ni (wt%) sample. The SPS NbC-4Mo₂C-4TiC-12Ni (wt%) sample had a K_{IC} of 8.30 ± 0.23 MPa·m^{1/2}. The LPS NbC-4Mo₂C-4TiC-12Ni (wt%) sample had HV₃₀ which was 1.22 MPa·m^{1/2} higher than the SPS NbC-4Mo₂C-4TiC-12Ni (wt%) sample and this was due to the LPS technique used for manufacturing.

7.2 Flank Wear Rates

Cutting inserts were manufactured from the samples with the reported mechanical properties in Table 7.2. Flank wear rates were calculated for each cutting insert according to their tool life. Flank Wear Rates (FWR) were used as a measure of insert performance. Machining parameters were manipulated from roughing, semi-finishing to finishing criteria. Flood and MQL were applied under each machining criteria and the decrease in flank wear rates were deemed as a result of better lubrication and cooling effects. The flank wear rates tabulated below showed improvement in tool life under MQL during machining:

Table 7.2. Flank wear rates (FWR) of each insert after face milling

CUTTING SPEED MM/MIN	CUTTING INSERT	FWR ($\mu\text{m}/\text{min}$)		
		DRY	FLOOD	MQL
200	G1-L	13.29	-	10.77
	G1-S	9.63	-	9.86
	M1-L	9.40	9.86	8.71
	R1-L	17.88	19.48	11.69
	W1-L	-	7.33	8.48
	W1-S	8.94	10.08	8.94
400	G1-L	14.67	-	11.46
	G1-S	15.81	-	9.17
	M1-L	13.29	8.94	11.92
	R1-L	13.98	42.02	12.15
	W1-L	-	9.40	8.25
	W1-S	12.15	9.63	7.11
800	G1-L	13.52	30.25	12.61
	G1-S	13.29	32.09	11.92
	M1-L	12.61	8.71	10.08
	R1-L	13.06	166.54	11.92
	W1-L	-	8.71	8.71
	W1-S	10.31	8.71	8.94

Table 7.2 demonstrates the effects of lubrication on flank wear rates during the 18 machining trials. In comparison to dry conditions, flood lubrication decreased flank wear rates in 50% of the test runs whereas MQL decreased flank wear rates in 93% of the machining trials. However, MQL resulted in lower flank wear rates (better tool life) than flood in 65% of machining trials. Generally, it was observed that flank wear rates increased from roughing to semi-finishing and decreased from roughing to finishing.

7.3 Roughing

Each insert machined at a cutting speed of 200 m/min and 2 mm depth of cut for 20 minutes cutting time. Insert failure criteria of $600\mu\text{m}$ VB_{Max} (Boothryd & Knight, 2006) was used for roughing however, premature failure such as mechanical fracture was considered the end of tool life criteria.

7.3.1 Dry

The readings taken includes machining temperatures, forces, and maximum flank wear (VB_{Max}) measurement. Flank wear rates (FWR), average resultant forces ($F_{R, \text{ave}}$), and average temperatures (T_a) were calculated and tabulated in Table 7.3 for dry roughing.

Table 7.3: Comparison of VB_{Max} , FWR, $F_{R, \text{ave}}$, and T_a during dry roughing.

Composition	Inserts	VB_{Max} (μm)	FWR ($\mu\text{m}/\text{min}$)	$F_{R, \text{ave}}$ (N)	T_a (C)
NbC-4Mo ₂ C-4TiC-12Ni	G1-L	265.85	13.30	397.57 ± 13	326.16 ± 16.26
NbC-4Mo ₂ C-4TiC-12Ni	G1-S	192.52	9.63	398.42 ± 13	242.47 ± 5.27
NbC-4TiC-12Ni	R1-L	357.53	17.88	427.97 ± 13	333.05 ± 7.08
WC-0.8Cr ₃ C ₂ -4Mo ₂ C-4TiC-10Co	M1-L	187.93	9.40	386.01 ± 13	314.67 ± 6.72
WC-0.8Cr ₃ C ₂ -10Co	W1-S	178.77	8.94	359.19 ± 13	274.30 ± 5.86

The tungsten carbide-based W1-S insert had better tool life with the lowest VB_{max} and FWR of 178.77 μm and 8.94 $\mu\text{m}/\text{min}$ respectively during dry roughing (Table 7.3). However, W1-S insert also had similar VB_{max} to M1-L and G1-S after 20 minutes of cutting time as seen in Figure 7.3. The NbC based R1-L had poorer performance with the highest VB_{Max} and FWR of 357.53 μm and 17.88 $\mu\text{m}/\text{min}$ respectively (Table 7.3). Figure 7.2c shows chip welding on the R1-L cutting edge. The R1-L insert had a similar life trend to G1-L insert up to 16 minutes, after which VB_{max} sharply increased. Generally, SPS inserts (G1-S and W1-S) had lower V_{Bmax} than LPS inserts (G1-L and R1-L). Tungsten carbide-based inserts had better tool life than niobium carbide-based inserts.

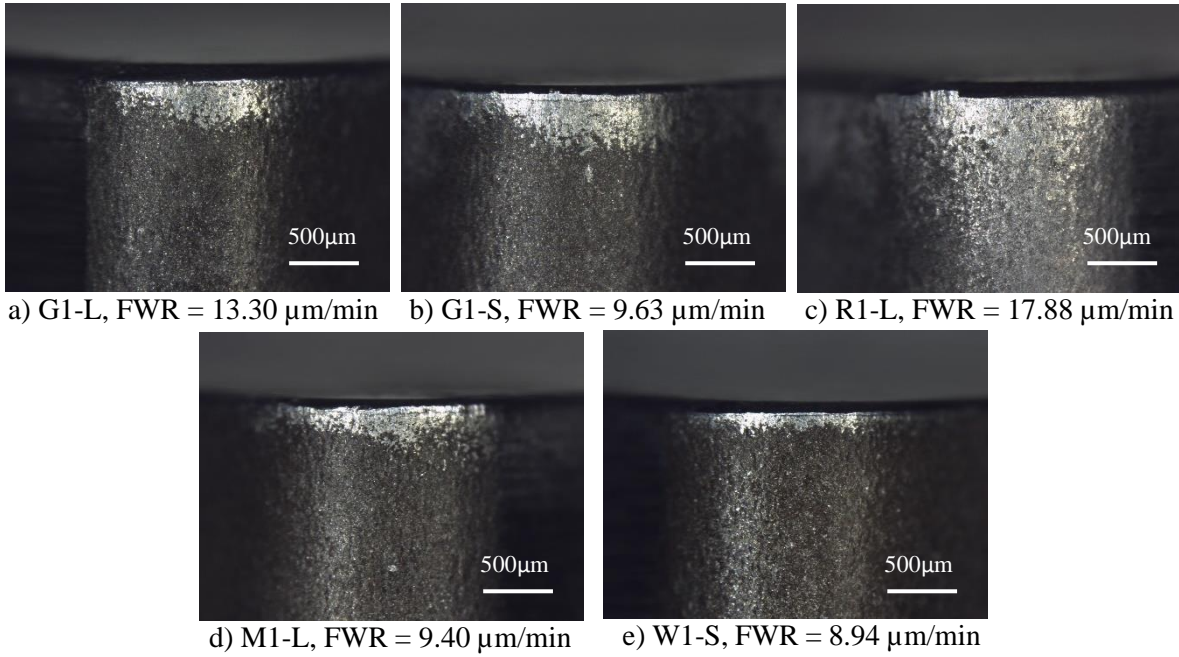


Figure 7.2. Maximum flank wear of a) G1-L, b) G1-S, c) R1-L, d) M1-L and e) W1-S inserts after dry roughing at cutting speed of 200 m/min and 2 mm depth of cut

Figure 7.4 shows the comparison between FWR and insert HV_{30} . Flank wear rate generally decreased with increased insert HV_{30} . Spark plasma sintered inserts (W1-S and G1-S) which had similar HV_{30} , had similar FWR. The LPS insert M1-L on the other hand, which had higher HV_{30} also had similar flank wear rates to the SPS W1-S and G1-S. The NbC based, G1-L, and R1-L, had lower HV_{30} and they have relatively high wear rates.

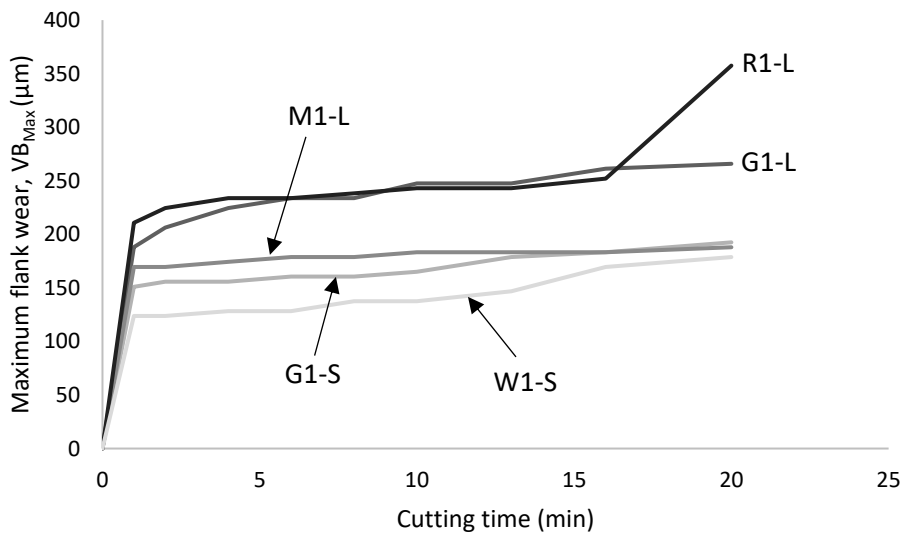


Figure 7.3. Graph of maximum flank wear (VB_{Max}) against cutting time during dry roughing

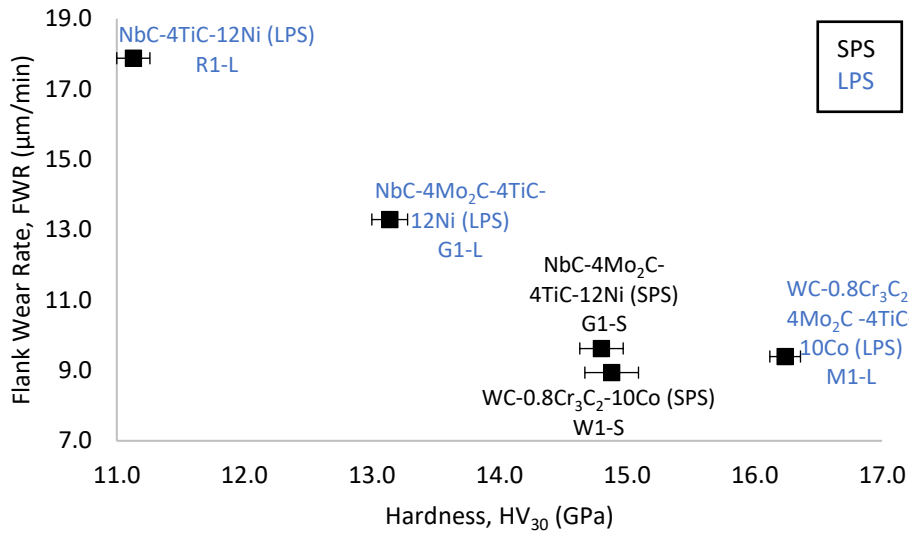


Figure 7.4. Graph of flank wear rate (FWR) against insert hardness (HV₃₀) during dry roughing

Figure 7.5 shows the comparison between FWR and K_{IC} , and FWR decreased with increased K_{IC} . Tungsten carbide-based inserts had higher K_{IC} than the NbC based inserts. Flank wear rate increased with increased K_{IC} amongst the NbC based inserts with similar compositions (G1-S and G1-L).

Figure 7.6 shows the relationship between FWR and $F_{R, ave}$. Average resultant forces increased with increased flank wear rates. The WC based inserts had lower FWR and lower $F_{R, ave}$ than the NbC based inserts. The SPS inserts (both WC and NbC based inserts) had lower FWR and $F_{R, ave}$ compared to LPS sintered inserts.

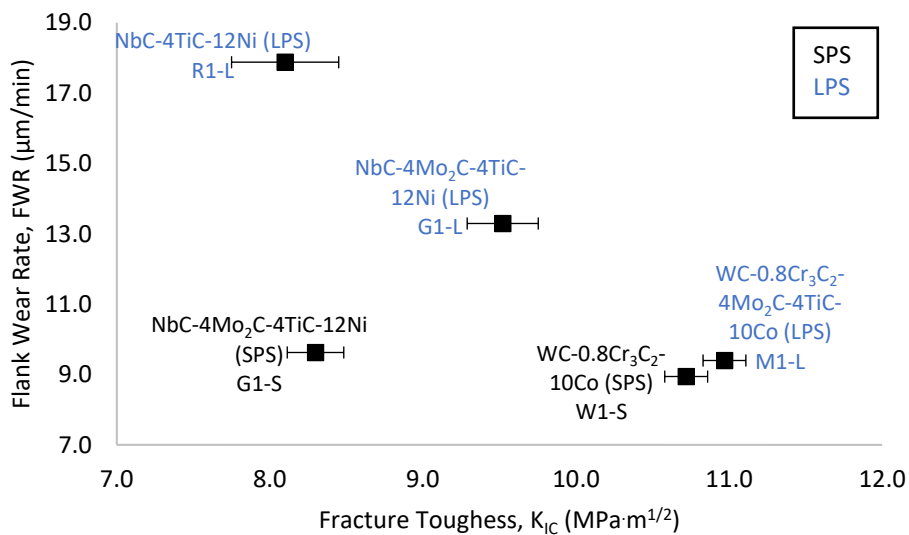


Figure 7.5. Graph of flank wear rate (FWR) against Fracture toughness (K_{IC}) for dry roughing

Figure 7.7 shows the comparison between FWR and T_a . Generally, the T_a increased with increased FWR. Spark plasma sintered inserts had lower FWR and low T_a compared to Liquid Phase sintered inserts. The SPS inserts showed an indirect proportionality between T_a and FWR, T_a decreased with increased in FWR. On the other hand, LPS sintered inserts had high FWR and T_a , and a direct proportionality was observed as increased in T_a with an increase in FWR.

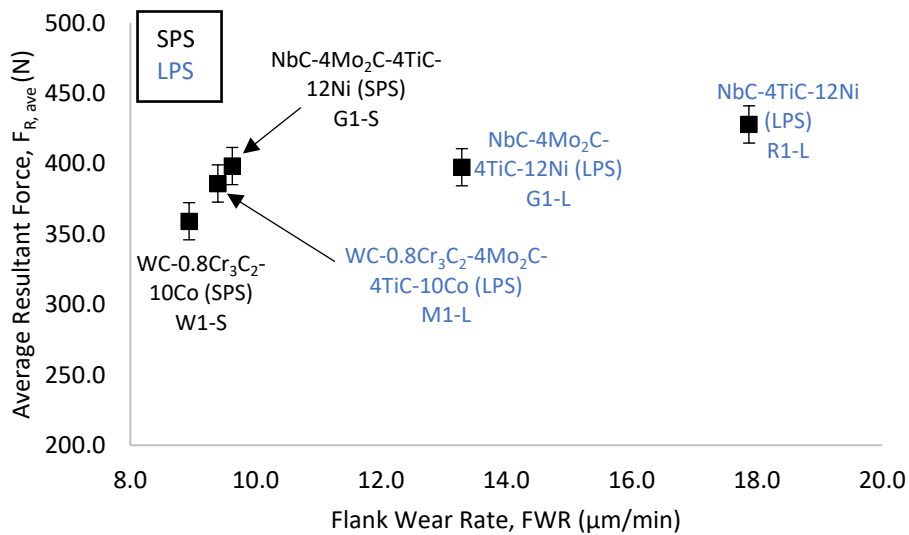


Figure 7.6. Graph of average resultant force ($F_{R,ave}$) against flank wear rate (FWR) during dry roughing

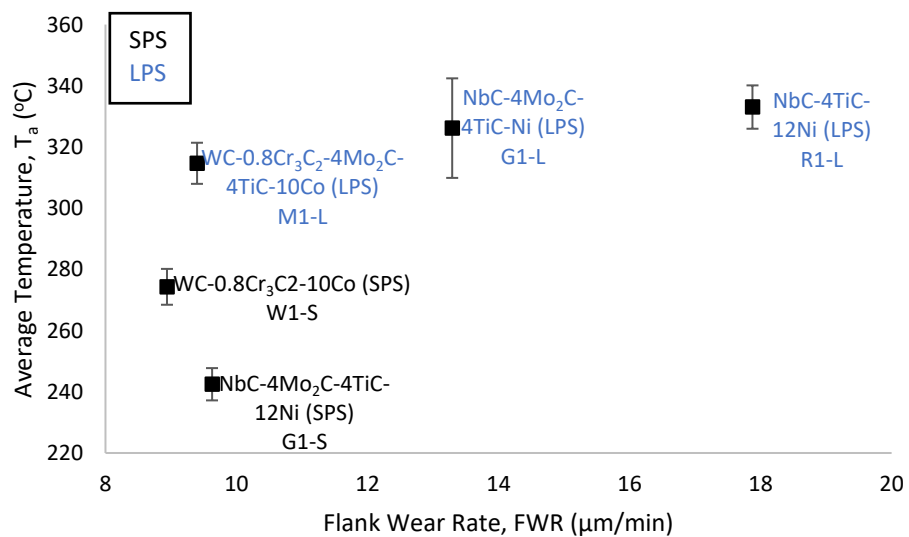


Figure 7.7. Graph of average Temperature (T_a) against flank wear rate (FWR) during dry roughing

Figure 7.8 shows the relationship between $F_{R,ave}$ and insert HV_{30} . There was a negligible change in $F_{R,ave}$ with increased insert hardness. Niobium carbide-based inserts with similar compositions had similar $F_{R,ave}$ with increased HV_{30} . Spark plasma sintered inserts also had similar $F_{R,ave}$ to LPS sintered inserts.

Figure 7.9 shows the comparison between $F_{R,ave}$ and K_{IC} . The $F_{R,ave}$ slightly decreased with increased K_{IC} . Generally, the SPS inserts had similar lower $F_{R,ave}$ and K_{IC} to their corresponding LPS inserts.

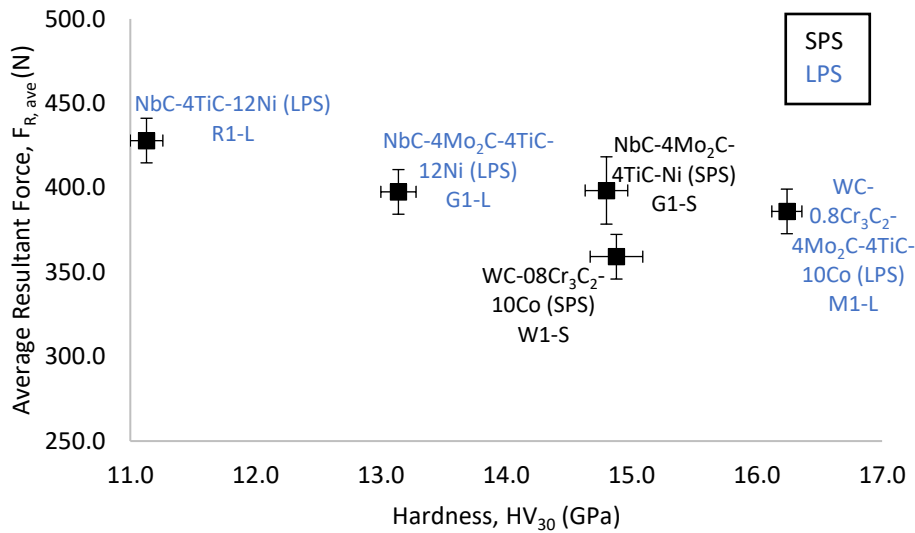


Figure 7.8. Graph of average resultant force ($F_{R,ave}$) against insert hardness for dry roughing

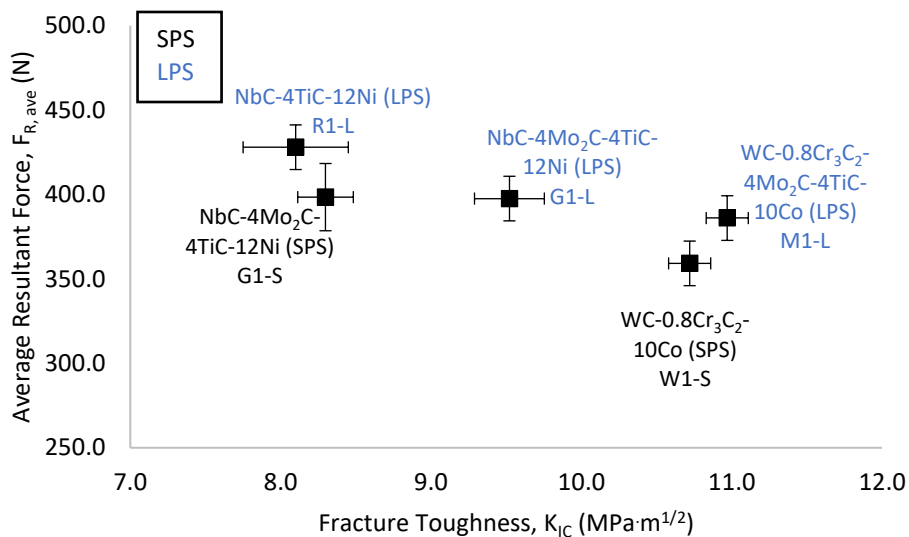


Figure 7.9. Graph of average resultant force ($F_{R,ave}$) against Fracture toughness (K_{IC}) during dry roughing

7.3.2 Flood

The readings taken includes cutting forces and maximum flank wear (VB_{Max}) measurement. It was not possible to measure temperature since the tool-workpiece interface was covered in flood coolant. Temperature rises were assumed to be negligible and similar to that of the coolant since large amounts

of coolant was applied at a flow rate of 1.39 l/s (5 m³/hr). The temperature of the flood coolant was measured to be 25°C. Flank wear rates (FWR) and average resultant forces ($F_{R, ave}$) were calculated and tabulated below in Table 7.4 for flood roughing.

Table 7.4. Comparison of VB_{Max} , FWR, and $F_{R, ave}$ during flood roughing

Composition	Inserts	Vbmx (μm)	FWR ($\mu\text{m}/\text{min}$)	$F_{R, ave}$ (N)
NbC-4TiC-12Ni	R1-L	311.7	19.48	317.39 ± 13
WC-0.8Cr ₃ C ₂ -4Mo ₂ C-4TiC-10Co	M1-L	197.1	9.86	255.94 ± 13
WC-0.8Cr ₃ C ₂ -10Co	W1-L	146.68	7.33	224.58 ± 13
WC-0.8Cr ₃ C ₂ -10Co	W1-S	201.69	10.08	241.79 ± 13

Figure 7.11 compares the insert cutting time to VB_{Max} . Tungsten carbide-based insert W1-L had the best insert tool life with the lowest VB_{Max} and FWR of 146.68 μm and 7.33 $\mu\text{m}/\text{min}$ respectively (Table 7.4). The NbC based insert R1-L had the poorest insert tool life with fracture failure (Figures 7.10 and 7.11) after 16 minutes of machining. Liquid phase sintered insert W1-L had lower VB_{Max} compared to the SPS sintered insert W1-S. Tungsten carbide-based inserts (Figure 7.10b, 7.10c and 7.10d) performed better than the NbC based insert.

Figure 7.12 relates FWR to insert HV_{30} . There was no general correlation between FWR and HV_{30} , although WC based inserts showed a direct relationship. Niobium carbide-based insert (R1-L) on the other hand had the lowest HV_{30} and highest FWR with a shorter insert tool life of 16 minutes and failed by a premature fracture failure.

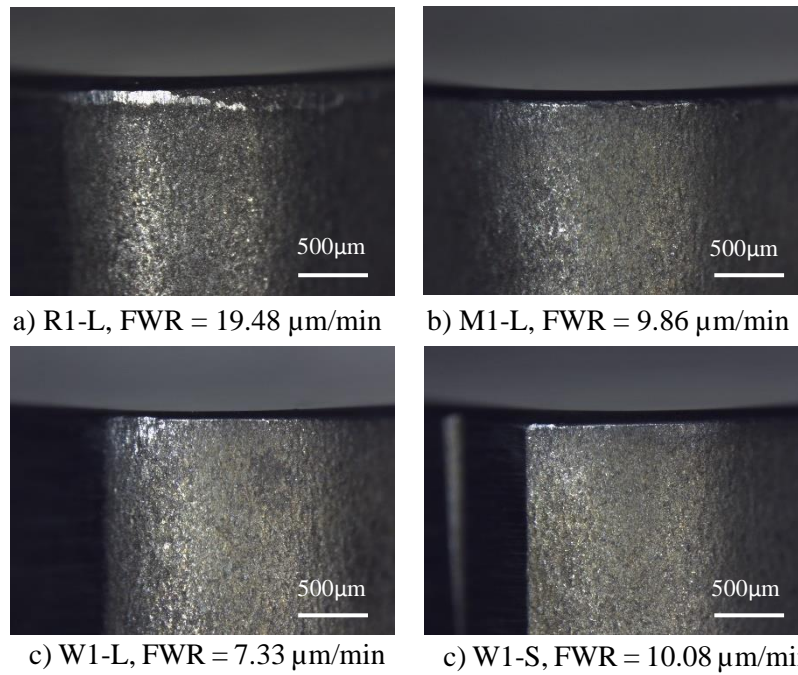


Figure 7.10. Maximum flank wear of a) R1-L, b) M1-S, c) W1-L and d) W1-S inserts after flood roughing at cutting speed of 200 m/min and 2 mm depth of cut

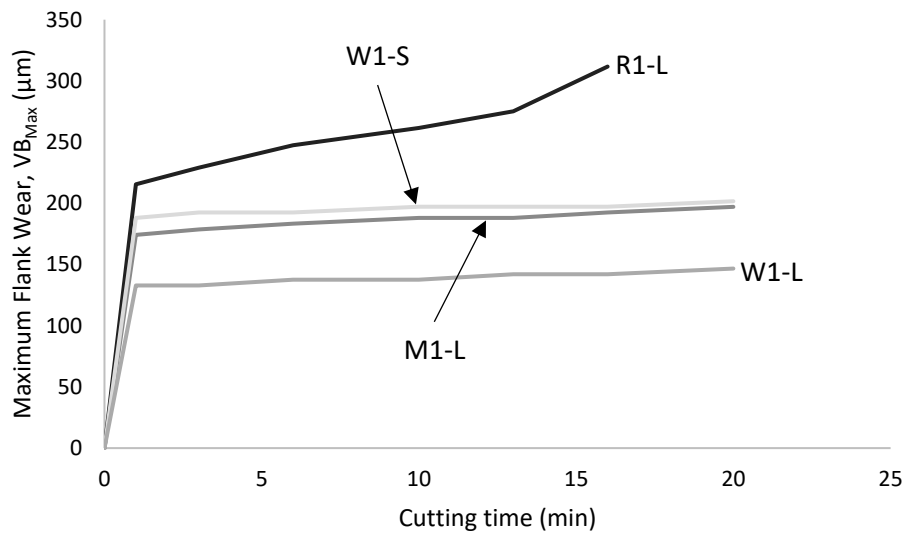


Figure 7.11. Graph of maximum flank wear (VB_{Max}) against cutting time during flood roughing

Figure 7.13 shows the comparison between FWR and K_{IC} . Generally, FWR decreased with increased K_{IC} . Tungsten carbide-based inserts had higher K_{IC} and lower FWR. The NbC based R1-L insert had the lowest insert hardness as seen in Figure 7.12 and lowest K_{IC} in Figure 7.13 and the highest FWR.

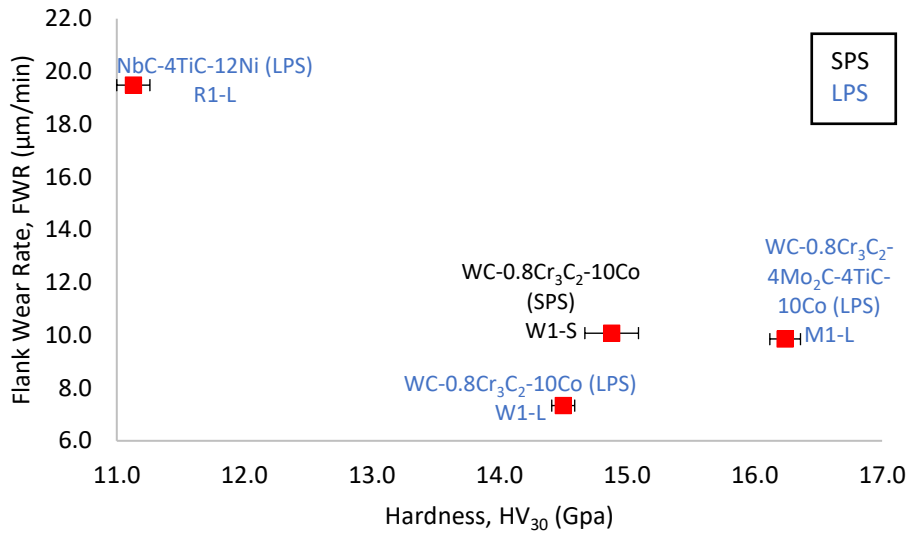


Figure 7.12. Graph of flank wear rate (FWR) against insert hardness (HV₃₀) during flood roughing

Figure 7.14 showed the comparison between $F_{R,ave}$ and FWR. The $F_{R,ave}$ increased with increased FWR. The WC based inserts had lower FWR and $F_{R,ave}$ compared to NbC based inserts. Liquid phase sintered inserts had lower FWR and lower $F_{R,ave}$ compared to SPS sintered inserts.

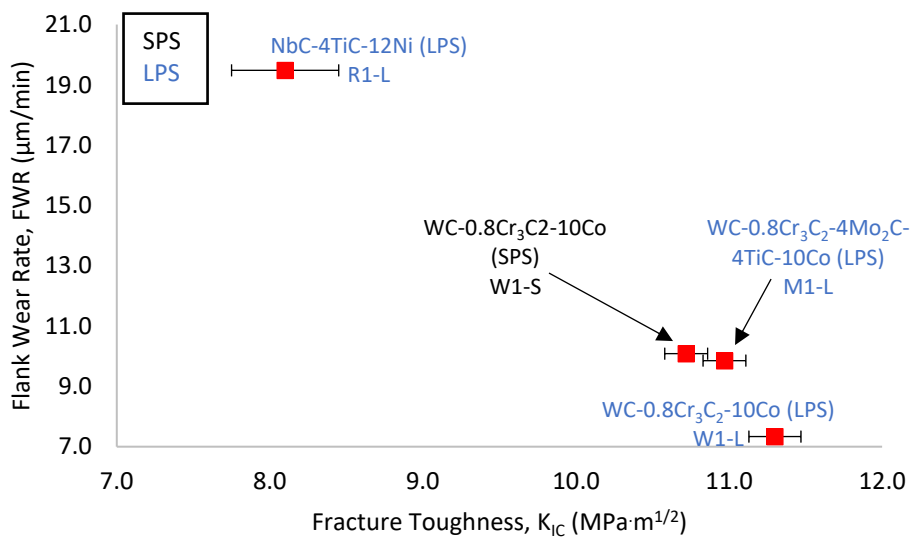


Figure 7.13. Graph of flank wear rate (FWR) against insert fracture toughness (KIC) during flood roughing

Figure 7.15 shows the relationship between $F_{R,ave}$ and insert HV₃₀. Average resultant forces were within the same error margin, there was no general correlation between $F_{R,ave}$ and insert HV₃₀. The WC based inserts showed a direct relationship between $F_{R,ave}$ and insert HV₃₀, $F_{R,ave}$ slightly increased with

increased insert HV_{30} . Niobium carbide-based insert R1-L with the lowest insert hardness experienced the highest $F_{R, ave}$ and WC based inserts with higher HV_{30} experienced relatively low $F_{R, ave}$.

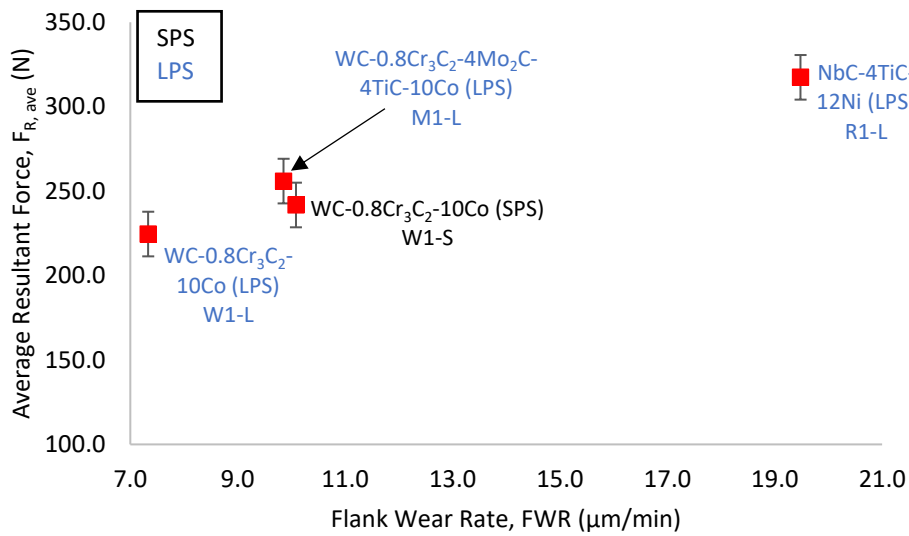


Figure 7.14. Graph of average resultant force ($F_{R, ave}$) against flank wear rate (FWR) during flood roughing

Figure 7.16 shows the relationship between ($F_{R, ave}$) and (K_{IC}). The $F_{R, ave}$ decreased with increased K_{IC} . Niobium carbide-based insert R1-L with the lowest K_{IC} had the highest $F_{R, ave}$.

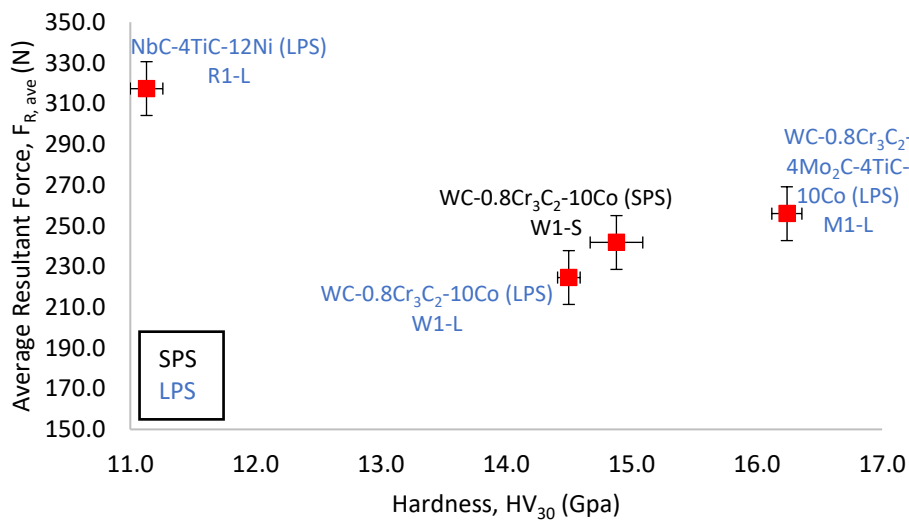


Figure 7.15. Graph of average resultant force ($F_{R, ave}$) against insert hardness (HV_{30}) during flood roughing

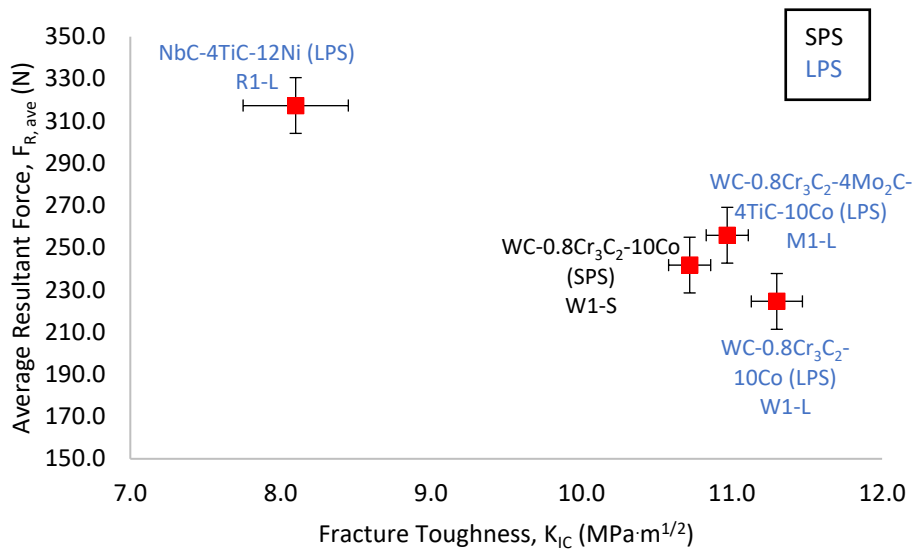


Figure 7.16. Graph of average resultant force ($F_{R,ave}$) against fracture toughness (K_{IC}) during flood roughing

7.3.3 MQL

The MQL was applied at a flow rate of 0.05 ml/s. The readings taken includes maximum flank wear (VB_{Max}), cutting forces and temperature measurement. Flank wear rates (FWR), average resultant forces ($F_{R,ave}$) and average temperatures (T_a) were calculated results and tabulated in Table 7.5 during MQL roughing.

Figure 7.18 shows the comparison between VB_{Max} and cutting time. Tungsten carbide-based W1-L insert had the lowest VB_{max} below 13 minutes. The W1-L insert had VB_{Max} and FWR of 169.60 μm and 8.48 $\mu\text{m}/\text{min}$ respectively (Table 7.5 and Figure 7.17) after 20 minutes cutting, which was similar to those of W1-S and M1-L. Niobium carbide-based insert R1-L had poorer performance having the highest VB_{max} and FWR of 233.77 μm and 11.69 $\mu\text{m}/\text{min}$ respectively. The SPS inserts performance was better than LPS inserts amongst the NbC based inserts (G1-S vs G1-L) and LPS inserts performed better than SPS amongst the WC based inserts (W1-L vs W1-S). Tungsten carbide-based inserts performed better than the Niobium carbide-based inserts.

Table 7.5: Comparison of VB_{Max} , FWR, $F_{R, ave}$, and T_a during MQL roughing

Composition	Inserts	VB_{Max} (μm)	FWR ($\mu\text{m}/\text{min}$)	$F_{R, ave}$ (N)	T_a (C)
NbC-4Mo ₂ C-4TiC-12Ni	G1-L	215.44	10.77	461.99 \pm 13	313.03 \pm 6.69
NbC-4Mo ₂ C-4TiC-12Ni	G1-S	197.10	9.855	451.08 \pm 13	326.37 \pm 6.96
NbC-4TiC-12Ni	R1-L	233.77	11.69	461.62 \pm 13	334.00 \pm 7.09
WC-0.8Cr ₃ C ₂ -4Mo ₂ C-4TiC-10Co	M1-L	174.18	8.709	433.52 \pm 13	285.20 \pm 6.02
WC-0.8Cr ₃ C ₂ -10Co	W1-L	169.60	8.48	523.40 \pm 13	238.12 \pm 5.17
WC-0.8Cr ₃ C ₂ -10Co	W1-S	178.77	8.94	413.71 \pm 13	257.06 \pm 5.55

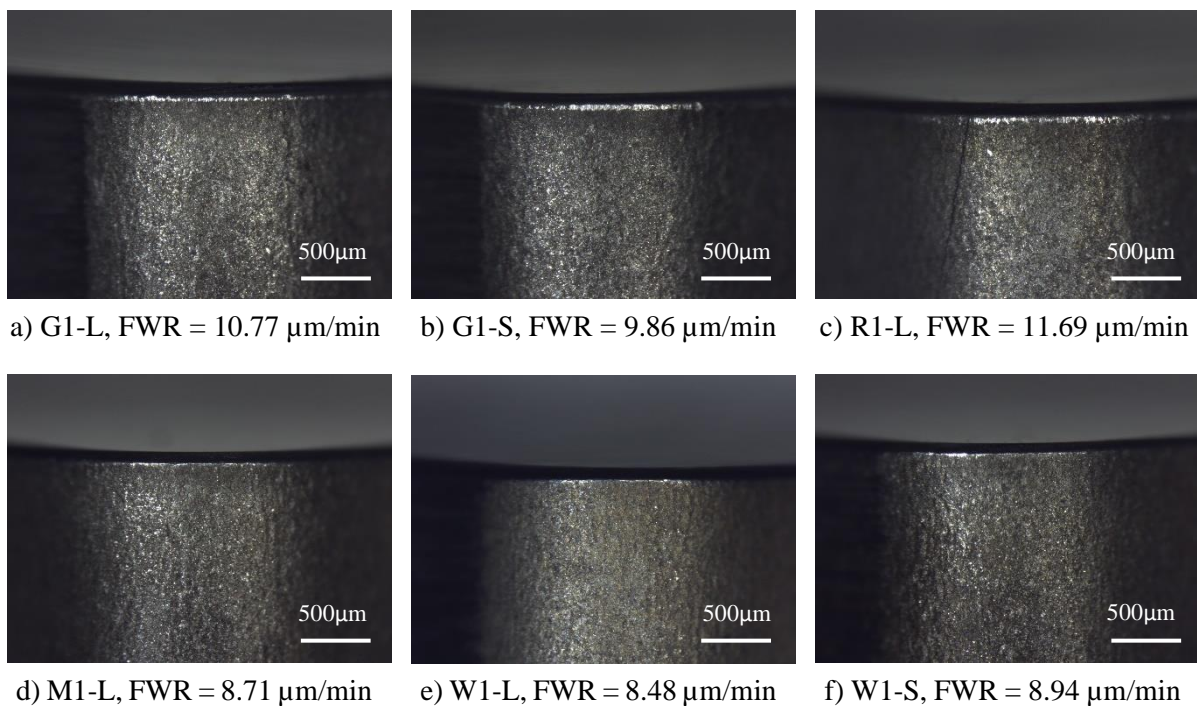


Figure 7.17. Maximum flank wear of a) G1-L, b) G1-S, c) R1-L, d) M1-L, and e) W1-S inserts after MQL roughing at cutting speed of 200 m/min and 2 mm depth of cut

Figure 19 shows the comparison between FWR and insert HV_{30} . Generally, FWR decreased with increased HV_{30} . Spark plasma sintered inserts (G1-S and W1-S) had similar HV_{30} but the NbC based G1-S insert experienced higher FWR than the WC based W1-S insert. Although the SPS G1-S inserts had slightly higher HV_{30} than the LPS W1-L insert, the W1-L insert had lower FWR than the G1-S

insert. The LPS inserts had lower FWR amongst WC based inserts and higher FWR amongst the NbC based inserts.

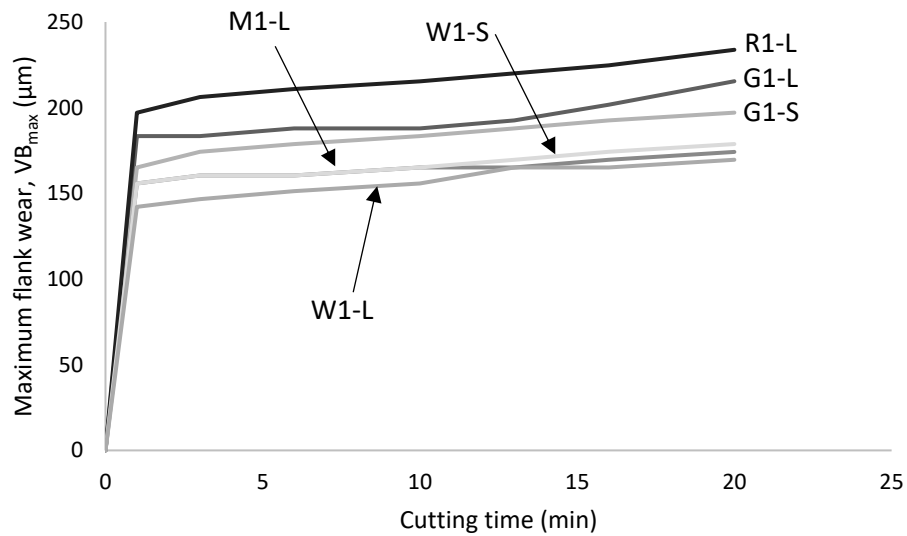


Figure 7.18. Graph of maximum flank wear ($V_{B\max}$) against cutting time (min) during MQL roughing

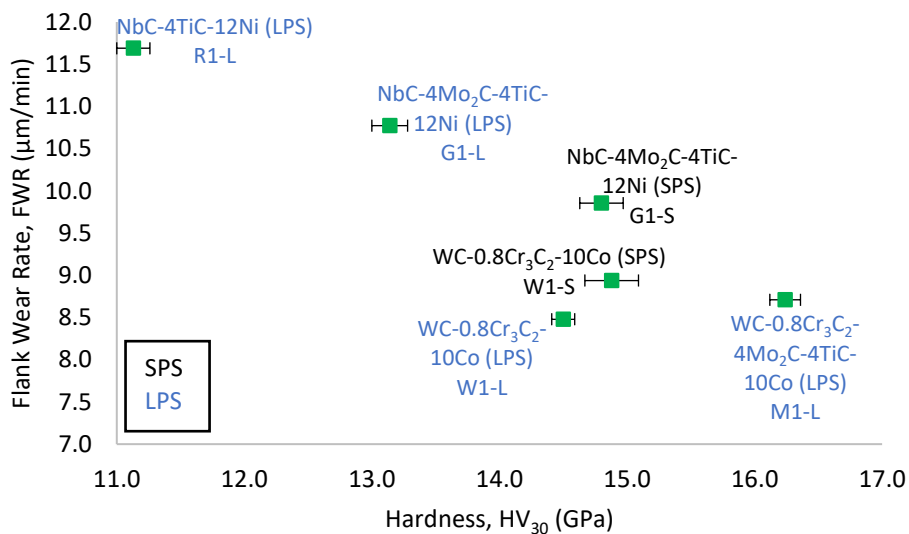


Figure 7.19. Graph of flank wear rate (FWR) against insert hardness (HV_{30}) during MQL roughing

Figure 7.20 shows the comparison between FWR and K_{IC} . The FWR generally decreased with increased K_{IC} . The WC based inserts had the lower FWR and higher K_{IC} than NbC based inserts. Although G1-S insert had similar K_{IC} to R1-L insert, the G1-S had lower FWR than R1-L insert.

Figure 7.21 shows the relationship between FWR and $F_{R,ave}$. The $F_{R,ave}$ increased with increased FWR. The WC based inserts had an indirect relationship between FWR and $F_{R,ave}$, $F_{R,ave}$ decreased with increased FWR. Whereas the NbC based inserts had $F_{R,ave}$ increased with increased FWR. The WC

based inserts had lower FWR than the NbC based inserts. The WC based LPS W1-L insert had lower FWR and higher $F_{R,ave}$ than the WC SPS W1-S insert. The NbC based SPS G1-S insert had lower FWR and lower $F_{R,ave}$ than the NbC LPS G1-L insert. Generally, SPS inserts had lower $F_{R,ave}$ compared to LPS inserts.

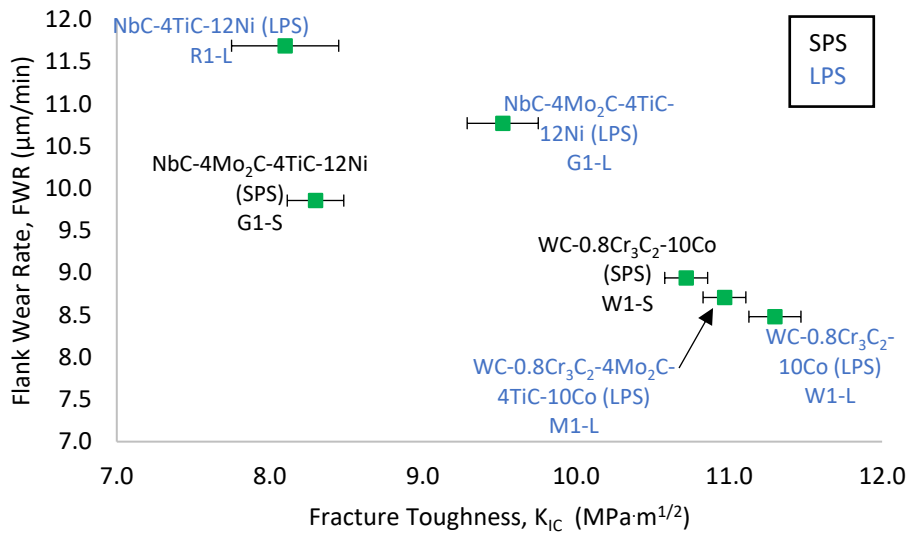


Figure 7.20. Graph of flank wear rate (FWR) against fracture toughness (K_{IC}) during MQL roughing

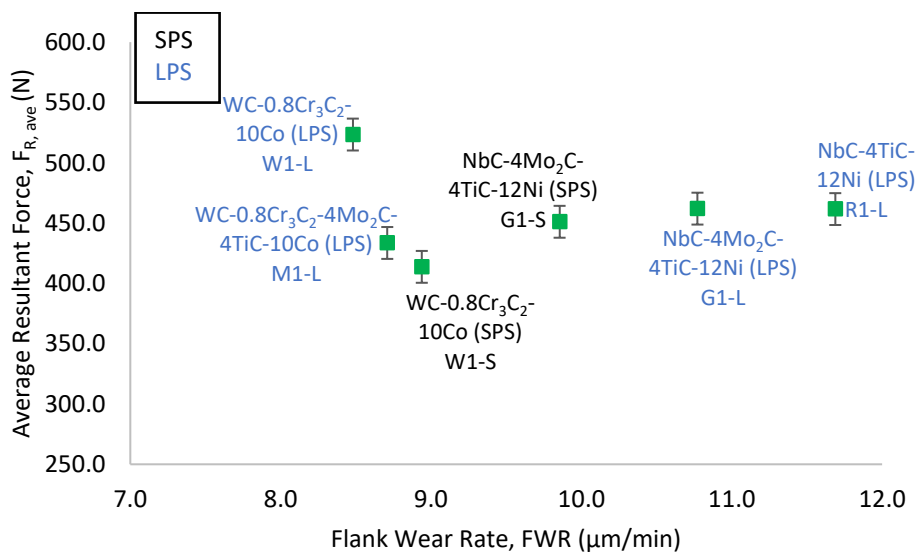


Figure 7.21. Graph of average resultant force ($F_{R,ave}$) against flank wear rate (FWR) during MQL roughing

Figure 7.22 shows the relationship between FWR and T_a and T_a increased with increased FWR. The WC based inserts had lower FWR and lower T_a than the NbC based inserts. The SPS produced inserts (W1-S and G1-S) had higher T_a than their similar LPS inserts (W1-L and G1-L).

Figure 7.23 shows the relationship between the $F_{R, ave}$ and insert HV_{30} . There was no observed general correlation between $F_{R, ave}$ and HV_{30} since they did not show a specific trend. The W1-L insert had the highest $F_{R, ave}$ and the W1-S insert had the lowest $F_{R, ave}$. Spark plasma sintered inserts (W1-S and G1-S) had similar HV_{30} but the G1-S insert had higher $F_{R, ave}$ than the W1-S insert. In comparison to LPS sintered inserts, SPS sintered inserts had lower $F_{R, ave}$ at higher HV_{30} .

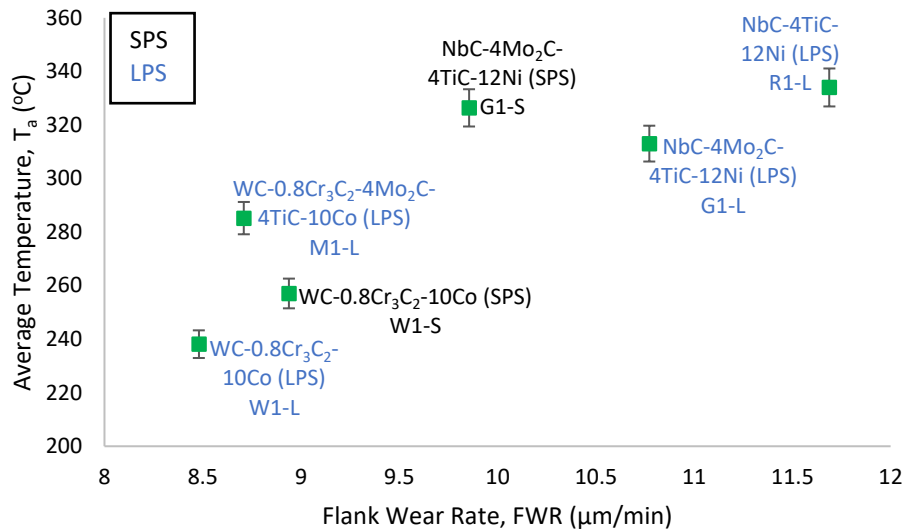


Figure 7.22. Graph of average temperature (T_a) against flank wear rate (FWR) during MQL roughing

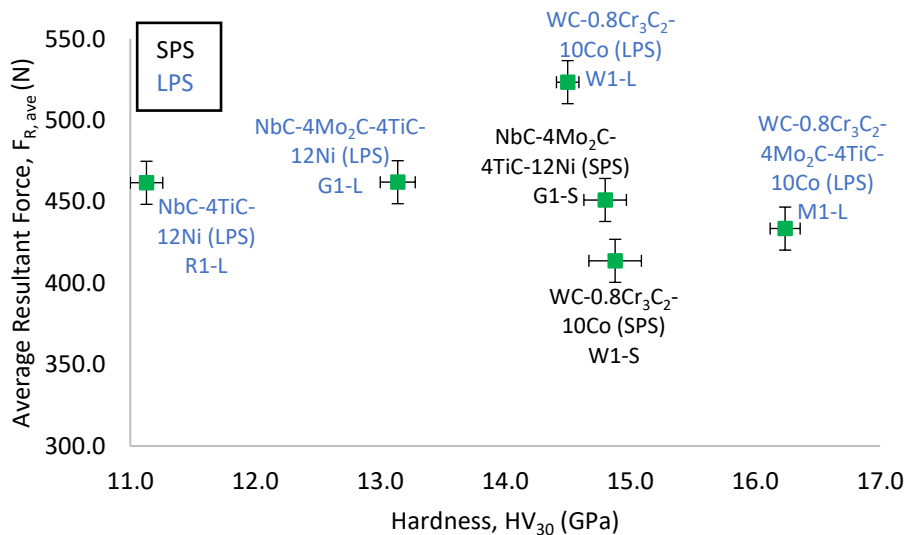


Figure 7.23. Graph of average resultant force ($F_{R, ave}$) against insert hardness (HV_{30}) during MQL roughing

Figure 7.24 shows the comparison between $F_{R, ave}$ and K_{IC} . There is no correlation observed between $F_{R, ave}$ and K_{IC} since most inserts are within the same error margin for $F_{R, ave}$.

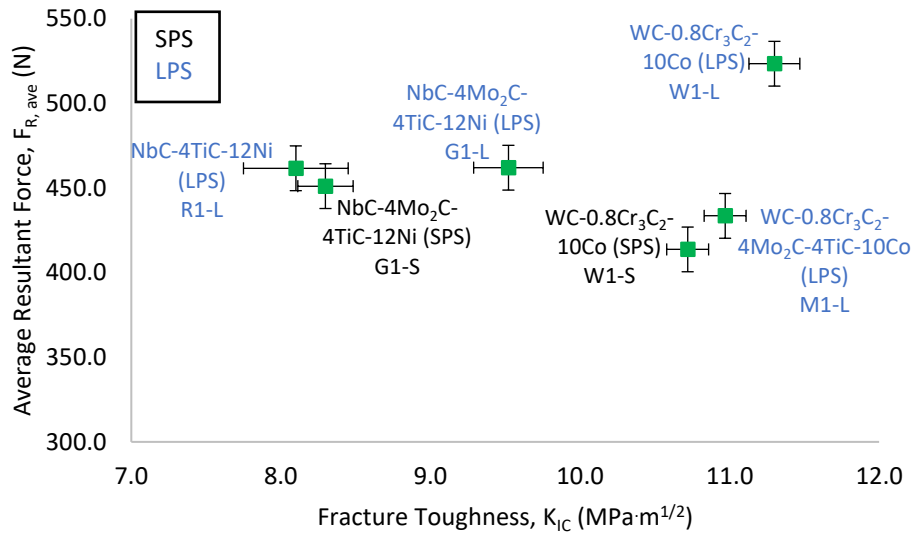


Figure 7.24. Graph of average resultant force ($F_{R,ave}$) against fracture toughness (K_{IC}) during MQL roughing

7.3.4 Dry versus Flood

This subsection reports the comparison between the effects of dry roughing and flood roughing on the FWR and $F_{R,ave}$. Figure 7.25 shows the relationship between $F_{R,ave}$ and FWR rate during roughing. Both dry and flood conditions had an increase in $F_{R,ave}$ with an increase in FWR. Flood lubrication lowered $F_{R,ave}$, however, slightly increased FWR of all cutting inserts.

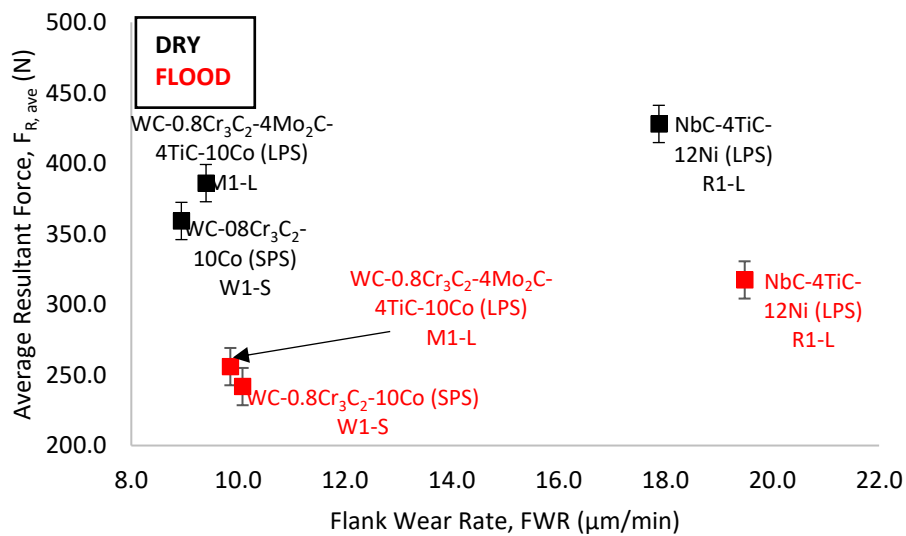


Figure 7.25. Graph of average resultant force ($F_{R, ave}$) against flank wear rate (FWR) during dry and flood roughing

7.3.5 Dry versus MQL

This subsection reports the comparison between the effects of dry roughing and MQL roughing on the FWR, $F_{R, ave}$, and T_a .

Figure 7.26 shows the relationship between the $F_{R, ave}$ and FWR during roughing. Both dry and MQL conditions had a direct proportionality relationship between $F_{R, ave}$ and FWR, $F_{R, ave}$ increased with increased FWR. The FWR of SPS W1-S insert was the same during dry and MQL however, MQL increased the $F_{R, ave}$ of the SPS W1-S insert. Minimum quantity lubrication lowered FWR of LPS inserts (M1-L and R1-L) and slightly increased $F_{R, ave}$.

Figure 7.27 shows the relationship between T_a and FWR. Generally, the MQL lowered both T_a and FWR for the LPS inserts (W1-L and G1-L). The SPS W1-S insert had lower T_a during MQL conditions and FWR was the same as during dry conditions. The SPS produced inserts show an indirect proportionality between FWR and T_a during dry roughing. Conversely, the SPS W1-S insert has a direct proportionality relationship between FWR and T_a during MQL roughing.

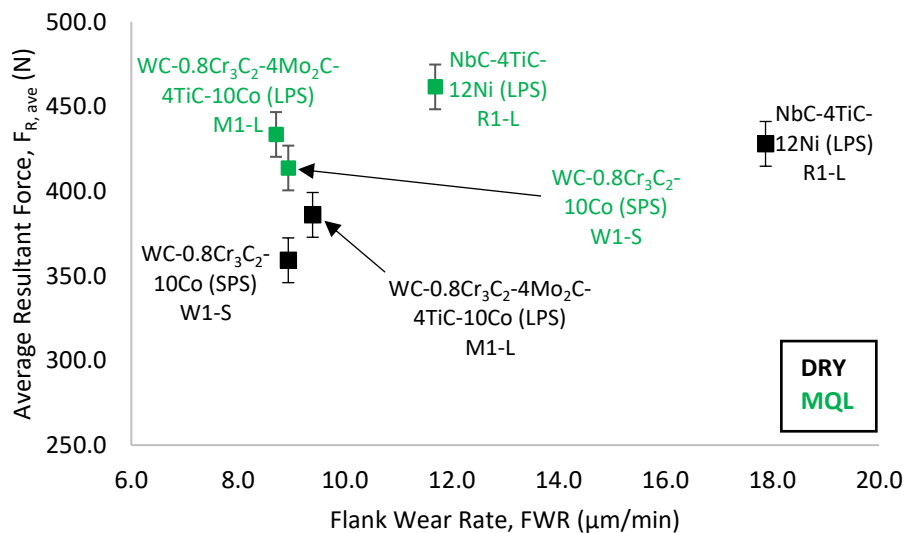


Figure 7.26. Graph of average resultant force ($F_{R, ave}$) against flank wear rate (FWR) during dry and MQL roughing

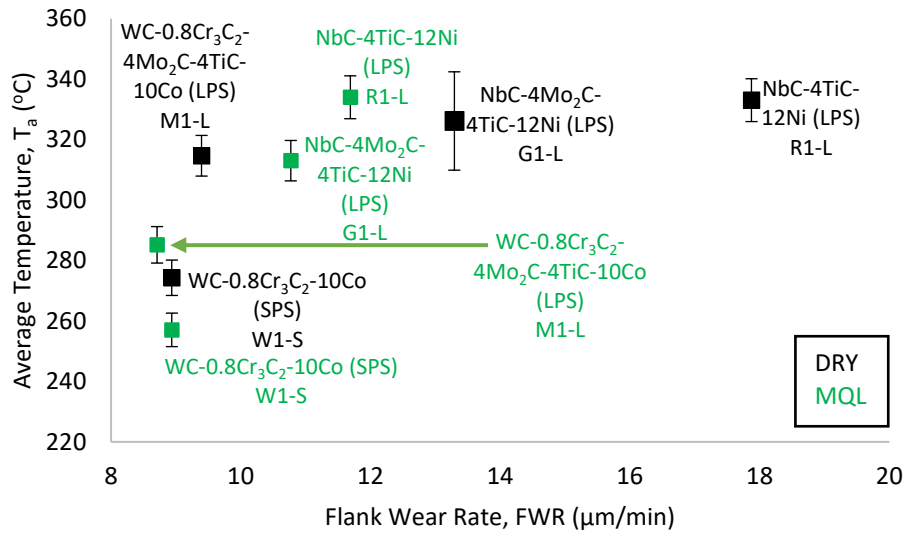


Figure 7.27. Graph of average temperature (T_a) against flank wear rate (FWR) during dry and MQL roughing

7.3.6 Flood versus MQL

This subsection reports the comparison between the effects of flood roughing and MQL roughing on the FWR and $F_{R,ave}$. Figure 7.28 shows the relationship between FWR and $F_{R,ave}$. Minimum Quantity Lubrication lowered FWR although the $F_{R,ave}$ increased in comparison to flood. The use of flood lubrication resulted in a direct relationship between FWR and $F_{R,ave}$ amongst WC based inserts, whereas, MQL show an inverse proportionality relationship.

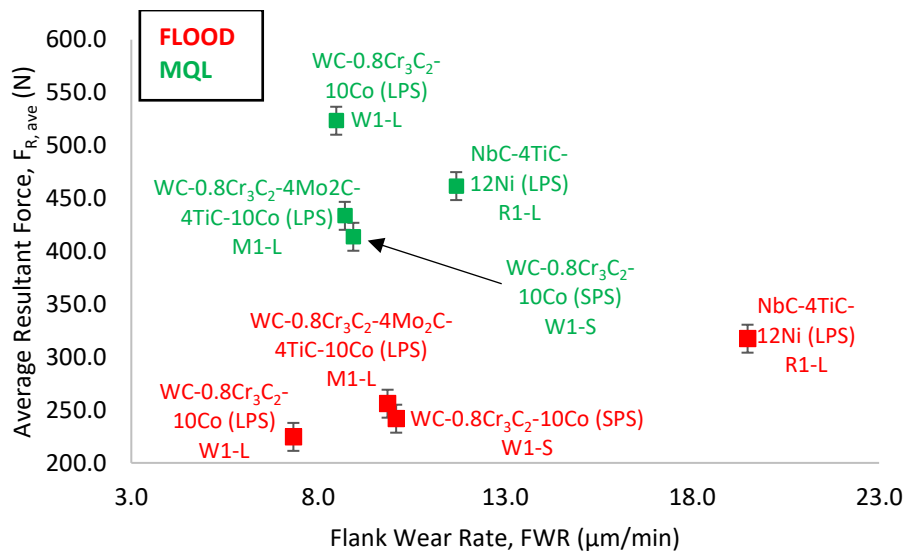


Figure 7.28. Graph of average resultant force ($F_{R,ave}$) against flank wear rate (FWR) during flood and MQL roughing

7.3.7 Overall Analysis of Roughing

The W1-S inserts had the best performance with the lowest VB_{Max} during dry roughing (Figure 7.3) and the W1-L insert had the best performance with the lowest VB_{Max} during flood and MQL roughing (Figures 7.11 and 7.18). The R1-L inserts had the poorest performance with the highest VB_{Max} during dry, flood, and MQL. The WC based inserts had the best performance during all lubricating conditions compared to the NbC based inserts.

Generally, FWR decreased with increased HV_{30} during dry, flood, and MQL roughing (Figures 7.4, 7.12, and 7.19). The G1-S insert had similar HV_{30} to W1-S and W1-L and experienced similar FWR during dry and higher FWR during flood and MQL roughing. The FWR also decreased with increased K_{IC} during dry, flood and MQL (Figures 7.5, 7.13, and 7.20). The R1-L insert had the lowest K_{IC} and the highest FWR.

The $F_{R,ave}$ increased with increased FWR during dry, flood, and MQL roughing (Figures 7.6, 7.14, and 7.21). The WC based inserts had increasing $F_{R,ave}$ with increased FWR during dry and flood, but during MQL roughing, the WC based inserts had an indirect relationship between $F_{R,ave}$ and FWR. The WC based inserts had lower FWR and $F_{R,ave}$ than the NbC based inserts. The SPS produced inserts (W1-S and G1-S) had lower $F_{R,ave}$ than the LPS produced inserts (W1-L, M1-L, G1-L and R1-L) during dry and MQL roughing whereas, during flood, the LPS inserts had lower $F_{R,ave}$ than the SPS inserts.

The T_a increased with increased FWR during dry and MQL roughing (Figures 7.7 and 7.22). The SPS produced inserts had lower FWR and T_a than their similar LPS inserts during dry whereas, the opposite was evident during MQL although the G1-S had lower FWR than the G1-L.

The $F_{R,ave}$ decreased with increased HV_{30} during flood roughing whereas, there was no general correlation between $F_{R,ave}$ and HV_{30} during dry and MQL (Figures 7.8, 7.15, and 7.23). The R1-L insert had the highest $F_{R,ave}$ during dry and flood whereas W1-L had the highest $F_{R,ave}$ during MQL. The W1-S had the lowest $F_{R,ave}$ during dry and MQL roughing. The WC based inserts had similar $F_{R,ave}$ to NbC based inserts during dry and MQL, whereas, during dry flood, the WC based inserts had lower $F_{R,ave}$ and higher HV_{30} than the NbC based inserts. The $F_{R,ave}$ slightly decreased with increased K_{IC} during dry and flood whereas there was no correlation observed during MQL (Figures 7.9, 7.16, and 7.24).

Flood roughing reduced $F_{R,ave}$ and slightly increased FWR (Figure 7.25) whereas the MQL roughing lowered FWR and slightly increased $F_{R,ave}$ of the LPS produced inserts (Figure 7.26). The MQL roughing also lowered T_a of the four selected inserts in Figure 7.27 (W1-S, M1-L, G1-L and R1-L). The MQL roughing had slightly lower FWR and higher $F_{R,ave}$ than the flood roughing.

7.4 Semi-Finishing

Semi-finishing was conducted at a cutting speed of 400m/min and 1mm depth of cut. Each insert machined for 20 minutes of cutting time. Insert failure criteria of 600 μ m $V_{B_{max}}$ was used (Boothryd & Knight, 2006; Genga et al., 2020), however, premature failure due to mechanical fracture also indicated the end of insert life. Flank wear rate was used as a measure of performance for each cutting insert.

7.4.1 Dry

The readings taken include cutting forces, temperatures and maximum flank wear ($V_{B_{max}}$) measurement. Flank wear rates (FWR), average resultant forces ($F_{R, ave}$), and average temperatures (T_a) were calculated, and results tabulated in Table 7.6 for dry semi-finishing.

Table 7.6: Comparison of $V_{B_{max}}$, FWR, $F_{R, ave}$, and T_a during dry semi-finishing.

Composition	Inserts	$V_{B_{max}}$ (μ m)	FWR (μ m/min)	$F_{R, ave}$ (N)	T_a (C)
NbC-4Mo ₂ C-4TiC-12Ni	G1-L	293.36	14.67	262.25 \pm 13	297.16 \pm 6.39
NbC-4Mo ₂ C-4TiC-12Ni	G1-S	316.28	15.81	264.23 \pm 13	313.90 \pm 6.73
NbC-4TiC-12Ni	R1-L	279.61	13.98	270.51 \pm 13	309.60 \pm 6.63
WC-0.8Cr ₃ C ₂ -4Mo ₂ C-4TiC-10Co	M1-L	265.86	13.29	241.49 \pm 13	289.88 \pm 6.24
WC-0.8Cr ₃ C ₂ -10Co	W1-S	242.94	12.15	229.78 \pm 13	280.87 \pm 6.06

Figure 7.30 shows the comparison between $V_{B_{max}}$ and cutting time during dry semi-finishing. The WC based SPS insert W1-S had good tool life with the lowest $V_{B_{max}}$ and FWR of 242.94 μ m and 12.15 μ m/min respectively (Table 7.6, Figure 7.29). The NbC based LPS insert G1-S had the poorest tool life with the highest $V_{B_{max}}$ and FWR of 316.28 μ m and 15.81 μ m/min after 20 minutes of cutting time. The NbC based R1-L performed best amongst the NbC based inserts while the WC based W1-S was the best insert amongst WC based inserts (Figure 7.30). Tungsten carbide-based inserts generally have better tool life than Niobium carbide-based inserts.

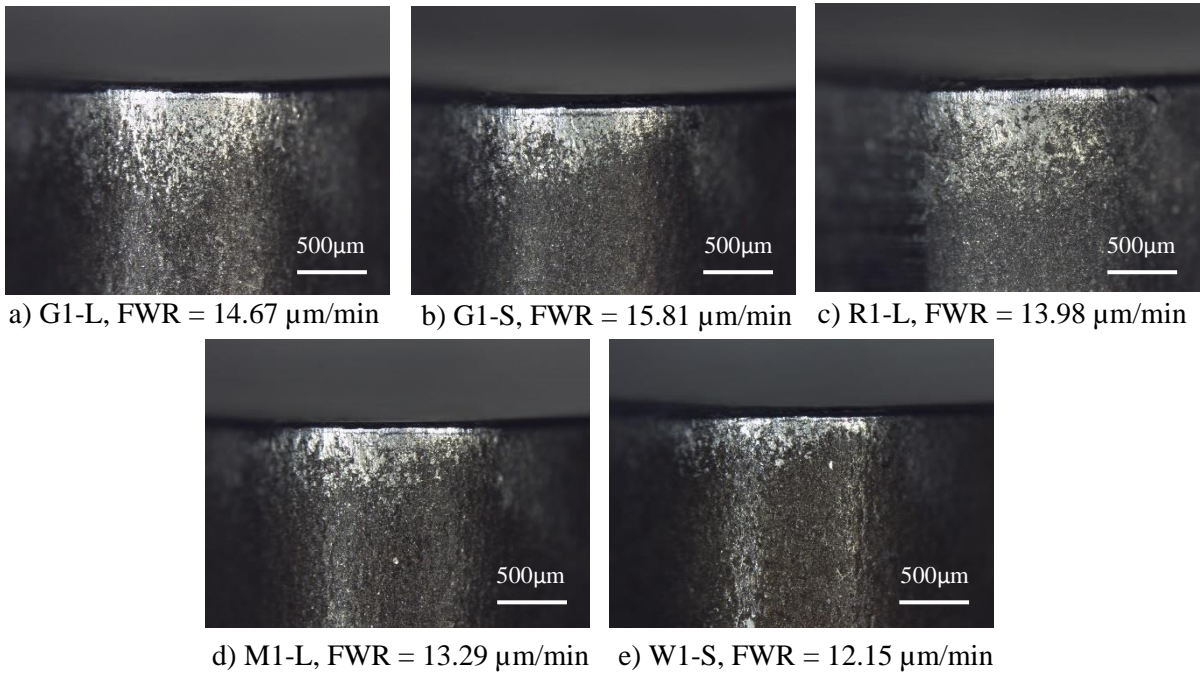


Figure 7.29. Maximum flank wear of a) G1-L, b) G1-S, c) R1-L, d) M1-L, and e) W1-S inserts after dry semi-finishing at cutting speed of 400 m/min and 1 mm depth of cut

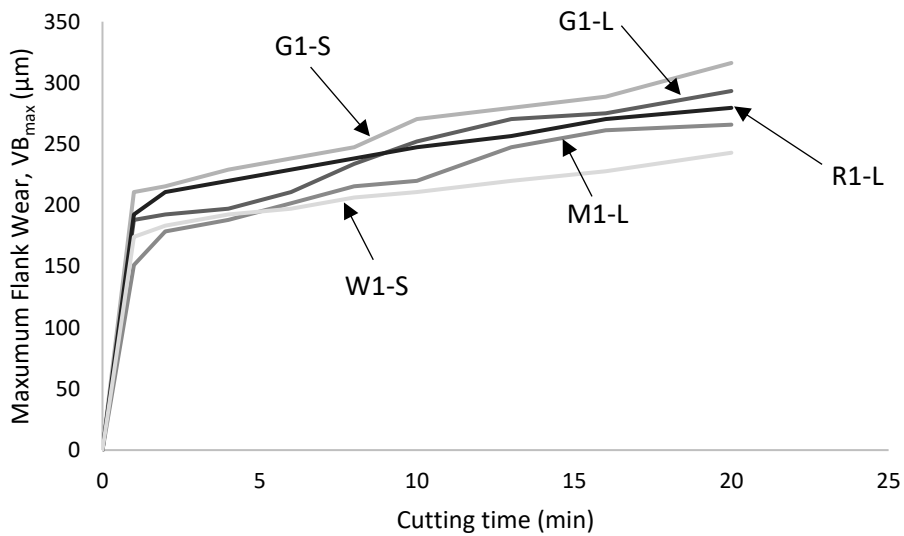


Figure 7.30. Graph of flank wear (VB_{Max}) against cutting time (min) during dry semi-finishing

Figure 32 shows the comparison between FWR and K_{IC} . Generally, FWR decreased with increased K_{IC} . Flank wear rate decreased with increased fracture toughness amongst NbC based inserts. Liquid phase sintered inserts had higher K_{IC} and experienced lower FWR.

Figure 7.33 shows the comparison between $F_{R,ave}$ and FWR. There was a slight increase (negligible) in $F_{R,ave}$ with increased FWR. The WC based inserts had slightly lower $F_{R,ave}$ than the NbC based inserts. Both the NbC and WC based inserts are all within the same $F_{R,ave}$ error margin.

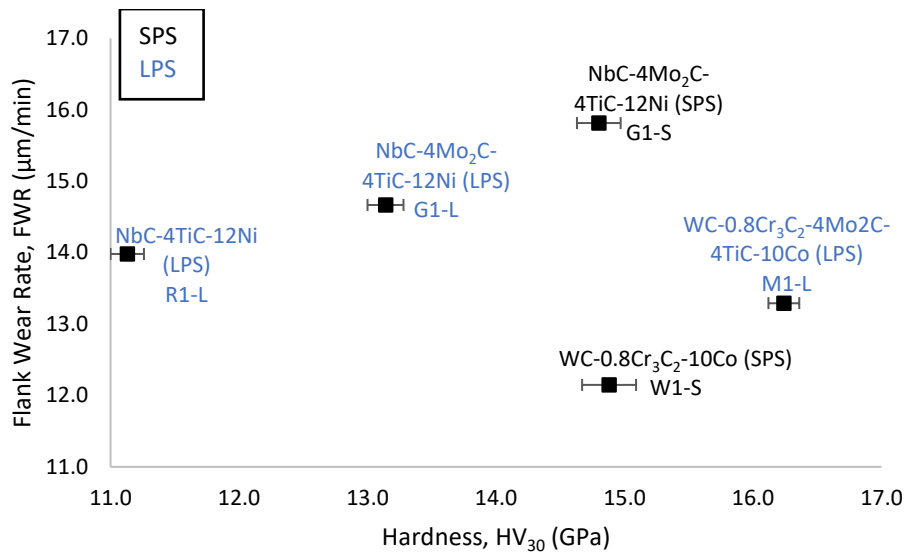


Figure 7.31. Graph of flank wear rate (FWR) against insert hardness (HV₃₀) during dry semi-finishing

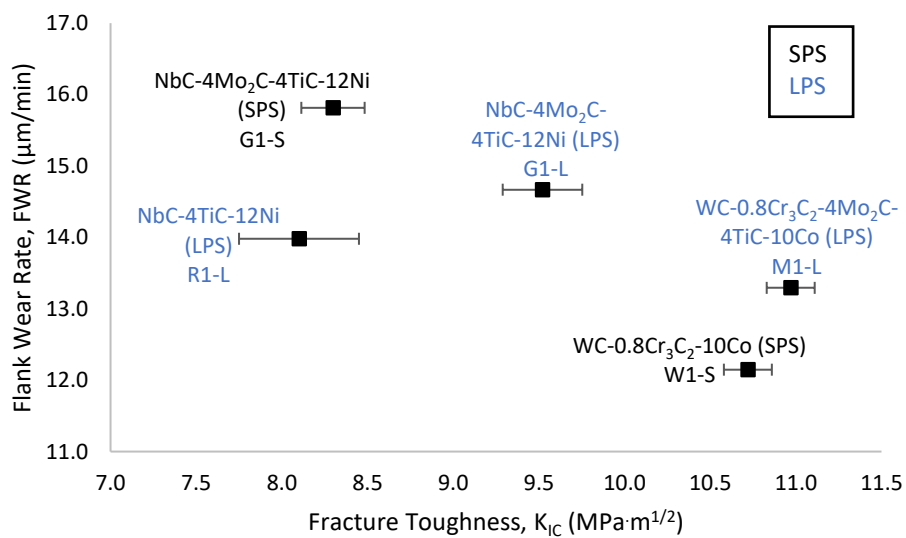


Figure 7.32. Graph of flank wear rate (FWR) against fracture toughness (K_{IC}) during dry semi-finishing

Figure 7.34 shows the comparison between FWR and T_a. The T_a increased with increased FWR. The WC based inserts show lower FWR and T_a compared to NbC based inserts. The WC based inserts (W1-S and W1-L) show a negligible change in T_a with increased FWR. The NbC SPS insert (G1-S) had higher T_a and higher FWR compared to LPS produced insert (G1-L).

Figure 7.35 shows the comparison between F_{R,ave} and HV₃₀. The WC based inserts had high HV₃₀ and slightly lower F_{R,ave} than the NbC based inserts. Both the WC and NbC based inserts had a negligible in F_{R,ave} with increased HV₃₀.

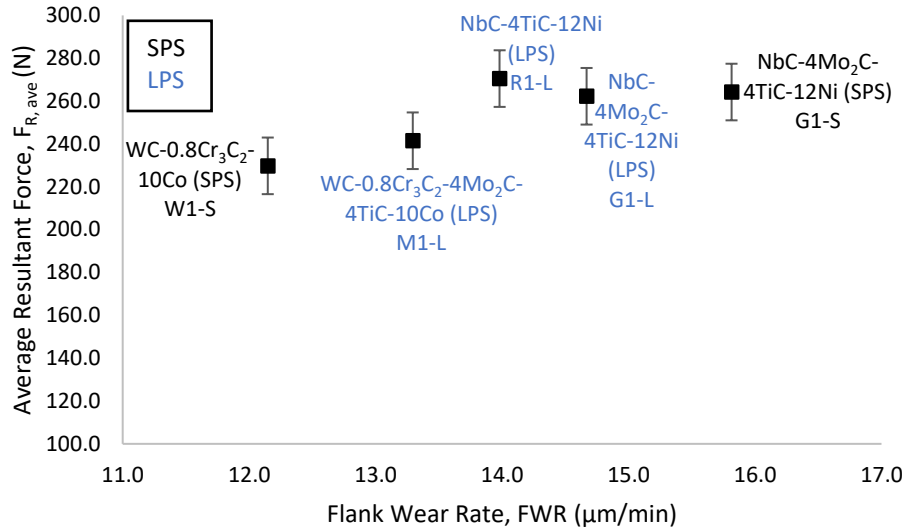


Figure 7.33. Graph of average resultant force ($F_{R,ave}$) against flank wear rate (FWR) during dry semi-finishing

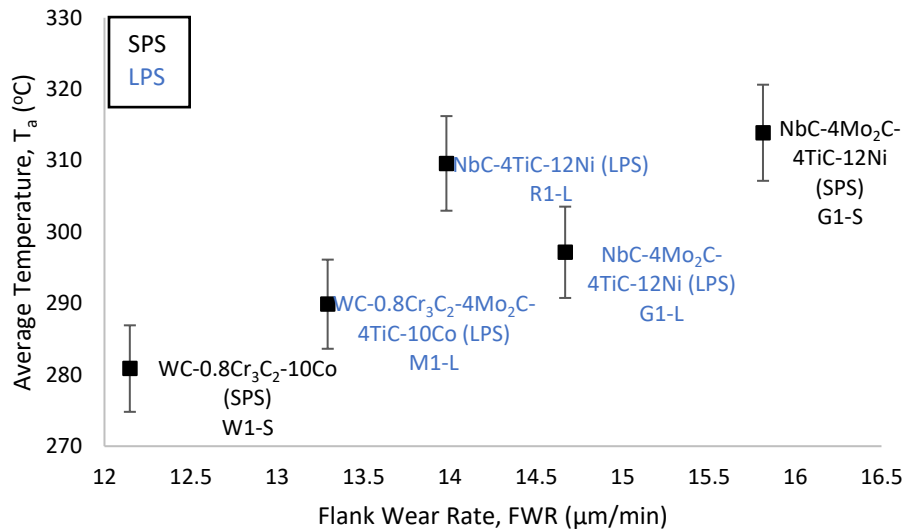


Figure 7.34. Graph of average temperature (T_a) against flank wear rate (FWR) during dry semi-finishing

Figure 7.36 shows the comparison between $F_{R,ave}$ and K_{IC} . The $F_{R,ave}$ slightly decreased with increased K_{IC} . Tungsten carbide-based inserts had higher K_{IC} and lower $F_{R,ave}$ compared to the NbC based inserts.

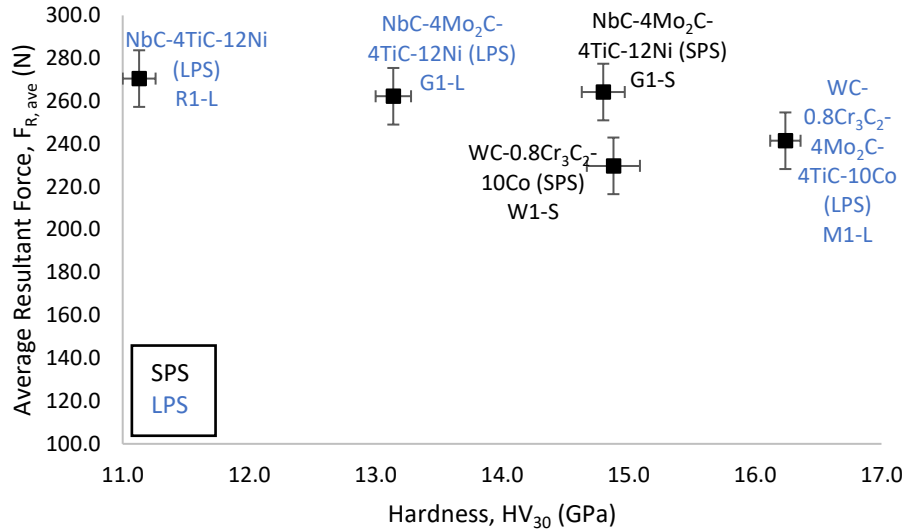


Figure 7.35. Graph of average resultant force ($F_{R,ave}$) against insert hardness (HV_{30}) during dry semi-finishing

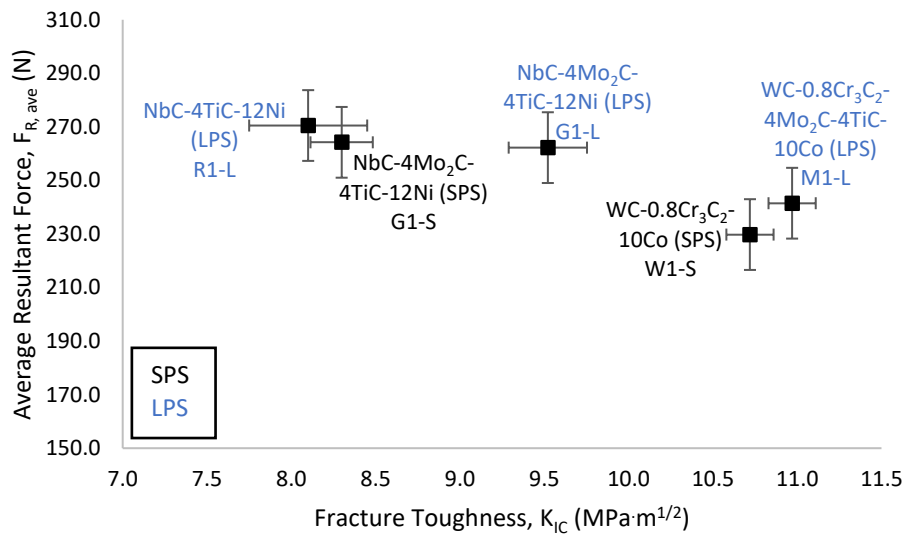


Figure 7.36. Graph of average resultant force ($F_{R,ave}$) against fracture toughness (K_{IC}) during dry semi-finishing

7.4.2 Flood

The readings taken include cutting forces and maximum flank wear (VB_{Max}) measurement. Temperature rises were assumed to be negligible and similar to that of the coolant since large amounts of coolant was applied at a flow rate of 1.39 l/s (5 m³/hr). Flank wear rates (FWR) and average resultant forces ($F_{R,ave}$) were calculated and results are tabulated in Table 7.7 for flood semi-finishing.

Table 7.7: Comparison of VB_{Max} and FWR, $F_{R, ave}$ during flood semi-finishing.

Composition	Inserts	VB_{max} (μm)	FWR ($\mu\text{m}/\text{min}$)	$F_{R, ave}$ (N)
NbC-4TiC-12Ni	R1-L	252.11	42.02	434.09 ± 13
WC-0.8Cr ₃ C ₂ - 4Mo ₂ C-4TiC-10Co	M1-L	178.77	8.94	382.74 ± 13
WC-0.8Cr ₃ C ₂ -10Co	W1-L	187.93	9.40	363.19 ± 13
WC-0.8Cr ₃ C ₂ -10Co	W1-S	192.52	9.63	378.95 ± 13

Figure 7.38 compares the tool life and VB_{max} of cutting inserts for the 20 minutes cutting time. Tungsten carbide-based insert M1-L had the best tool life with the lowest VB_{Max} , and FWR of 178.77 μm and 8.94 $\mu\text{m}/\text{min}$ respectively (Table 7.7, Figure 7.38). The niobium carbide-based insert R1-L had the shortest tool life of 6 mins, highest VB_{Max} of 252.11 μm and fracture failure was considered the end of tool life (Figure 7.37a). Generally, LPS sintered inserts (W1-L and M1-L) had similar performance to SPS sintered inserts (W1-S).

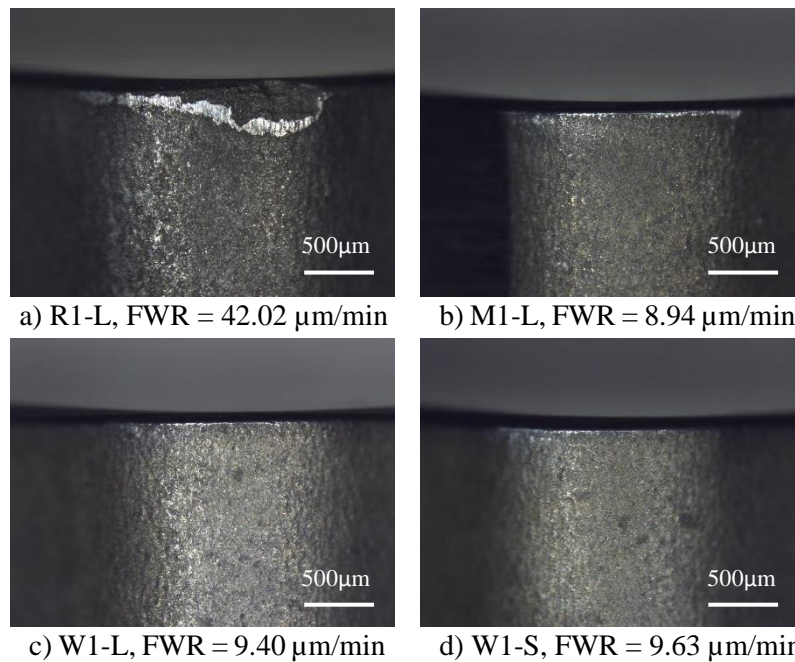


Figure 7.37. Maximum flank wear of a) R1-L, b) M1-L, c) W1-L and d) W1-S inserts after flood semi-finishing at cutting speed of 400 m/min and 1 mm depth of cut

Figure 7.39 shows the comparison between FWR and HV_{30} . Tungsten carbide-based inserts had a higher HV_{30} and lower FWR than the NbC based inserts. The WC based SPS produced insert (W1-S) had higher HV_{30} and similar FWR to the WC based LPS insert (W1-L). Niobium carbide-based insert (R1-L) on the other hand had the lowest HV_{30} and highest FWR with the shortest tool life of 6 minutes.

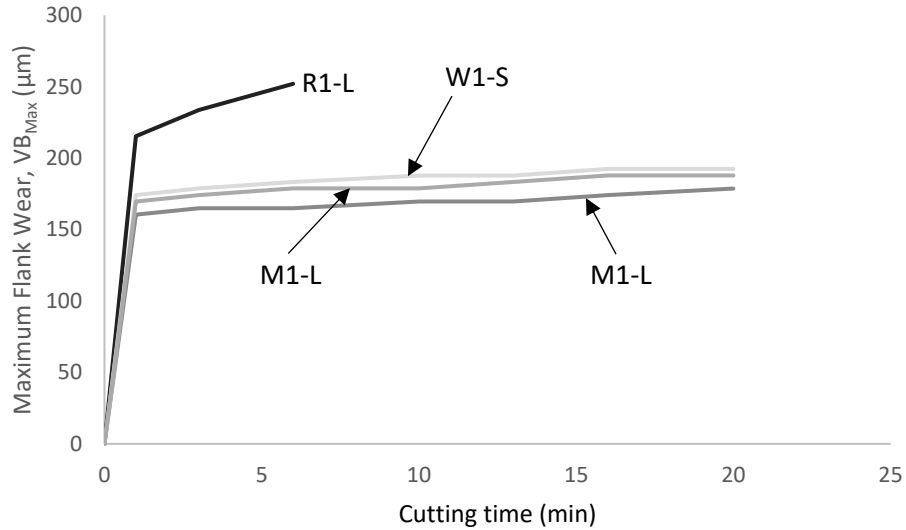


Figure 7.38. Graph of maximum flank wear (VB_{Max}) against cutting time (min) during flood semi-finishing

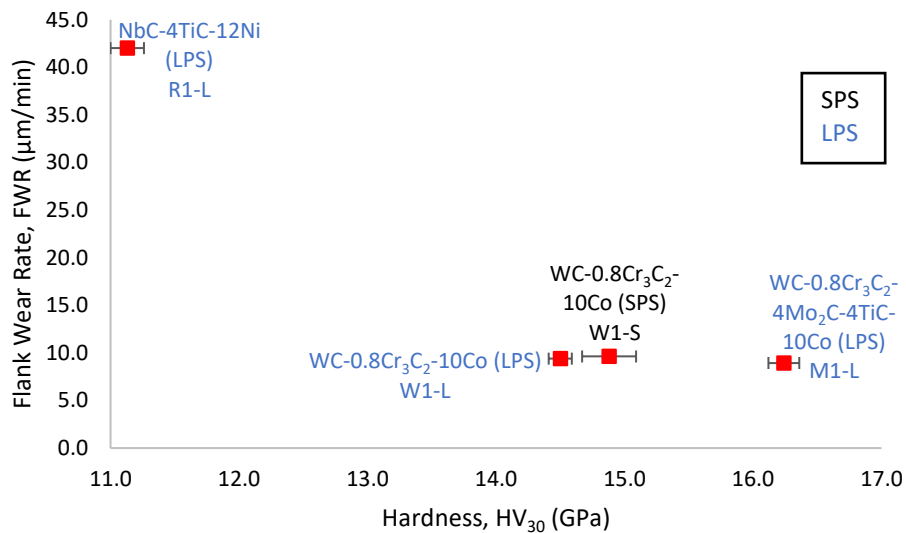


Figure 7.39. Graph of flank wear rate (FWR) against insert hardness (HV_{30}) during flood semi-finishing

Figure 7.40 shows the comparison between FWR and K_{IC} during flood semi-finishing. Tungsten carbide-based inserts had higher K_{IC} and a negligible change in FWR. The NbC based R1-L insert on the other hand had the lowest K_{IC} and highest FWR.

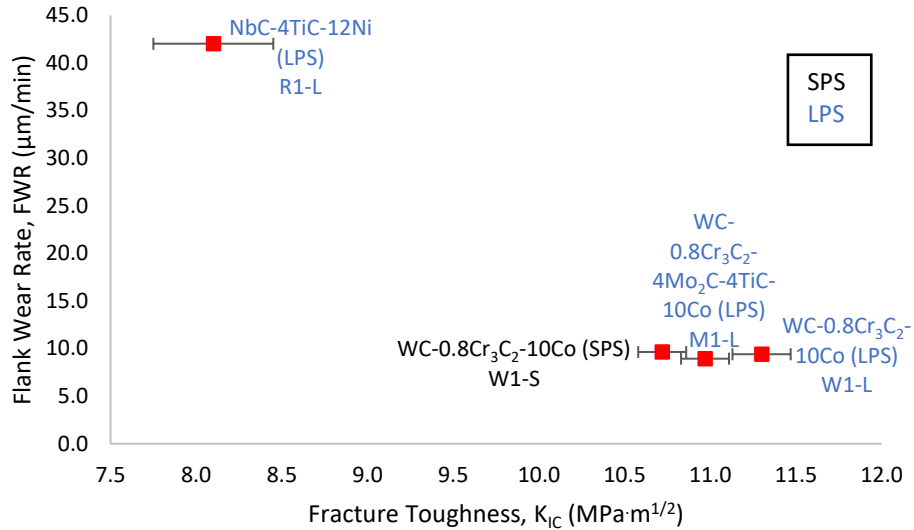


Figure 7.40. Graph of flank wear rate (FWR) against fracture toughness (K_{IC}) during flood semi-finishing

Figure 7.41 shows the comparison between F_{R, ave} and FWR during flood semi-finishing. Tungsten carbide-based inserts had lower FWR and lower F_{R, ave} compared to NbC based insert R1-L. All WC based inserts had F_{R, ave} within the same error margin and FWR were also similar. The WC based inserts had a negligible difference in F_{R, ave} and FWR.

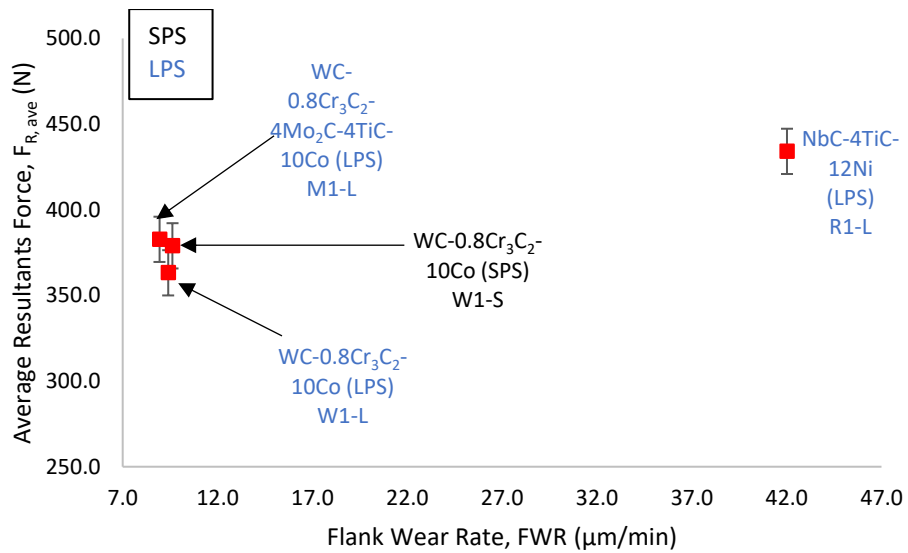


Figure 7.41. Graph of average resultant force (F_{R, ave}) against flank wear rate (FWR) during flood semi-finishing

Figure 7.42 shows the comparison between $F_{R, ave}$ and HV_{30} . Tungsten carbide-based inserts had higher HV_{30} and lower $F_{R, ave}$ compared to NbC based insert R1-L. All WC based inserts had $F_{R, ave}$ within the same error margin. The WC based inserts had a negligible difference in $F_{R, ave}$ with increased HV_{30} .

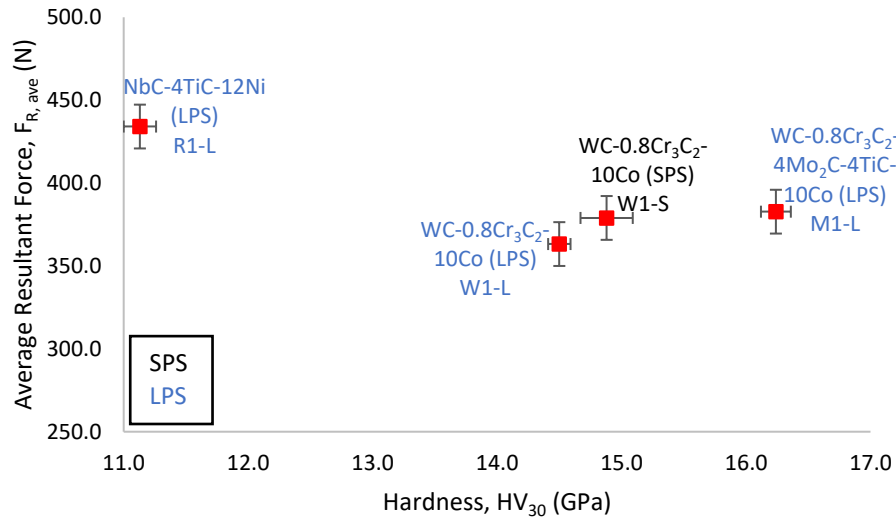


Figure 7.42. Graph of average resultant force ($F_{R, ave}$) against insert hardness (HV_{30}) during flood semi-finishing

Figure 7.43 shows the comparison between $F_{R, ave}$ and K_{IC} during flood semi-finishing. The $F_{R, ave}$ slightly decreased with increased K_{IC} . Tungsten carbide-based inserts had higher K_{IC} and lower $F_{R, ave}$ compared to NbC based insert R1-L. All the WC based inserts had $F_{R, ave}$ within the same error margin. The WC based inserts had a negligible difference in $F_{R, ave}$ with increased K_{IC} .

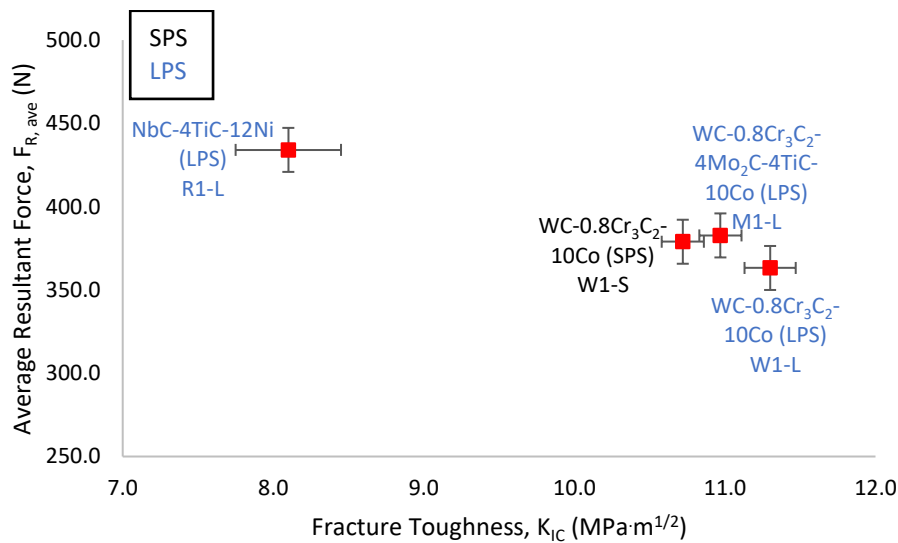


Figure 7.43. Graph of average resultant force ($F_{R, ave}$) against fracture toughness (K_{IC}) during flood semi-finishing

7.4.3 MQL

The MQL was applied at a flow rate of 0.05 ml/s. The readings taken includes cutting forces, temperatures and maximum flank wear (VB_{Max}) measurement. Average resultant forces ($F_{R, ave}$), average temperatures (T_a) and flank wear rates (FWR) were calculated and results were tabulated in Table 7.8 for MQL semi-finishing.

Table 7.8. Comparison of VB_{Max} , FWR, $F_{R, ave}$, and T_a during MQL semi-finishing.

Composition	Inserts	VB_{Max} (μm)	FWR ($\mu\text{m}/\text{min}$)	$F_{R, ave}$ (N)	T_a ($^{\circ}\text{C}$)
NbC-4Mo ₂ C-4TiC-12Ni	G1-L	229.19	11.46	263.55 \pm 13	229.10 \pm 4.99
NbC-4Mo ₂ C-4TiC-12Ni	G1-S	183.35	9.17	260.66 \pm 13	225.26 \pm 4.91
NbC-4TiC-12Ni	R1-L	242.94	12.15	257.28 \pm 13	237.33 \pm 4.55
WC-0.8Cr ₃ C ₂ -4Mo ₂ C-4TiC-10Co	M1-L	238.36	11.92	250.02 \pm 13	233.60 \pm 5.08
WC-0.8Cr ₃ C ₂ -10Co	W1-L	165.02	8.25	233.31 \pm 13	197.92 \pm 4.34
WC-0.8Cr ₃ C ₂ -10Co	W1-S	142.10	7.11	236.03 \pm 13	212.39 \pm 4.64

Figure 7.45 compares the tool life of cutting inserts after 20 minutes of cutting. The W1-S insert had the best tool life with the lowest VB_{Max} and FWR of 142.10 μm and 7.11 $\mu\text{m}/\text{min}$ respectively (Table 7.8, Figure 7.44). The R1-L insert had the highest VB_{Max} of 242.94 μm which was similar to that of M1-L after 20 minutes of cutting time, Figures 7.44c and 44d show similar FWR. Generally, The SPS inserts (W1-S and G1-S) had better tool life than the LPS inserts (R1-L, W1-L and G1-L).

Figure 7.46 shows the comparison between FWR and HV_{30} . The FWR generally decreased with increased insert HV_{30} . The NbC based inserts show an indirect relationship between FWR and HV_{30} . Apart from the M1-L insert, the WC based inserts also show an indirect proportionality relationship between FWR and HV_{30} . Spark plasma sintering technique improved NbC based insert's hardness such that G1-S has similar hardness property to that of W1-S; although G1-S has a slightly high flank wear rate, SPS sintered inserts experience relatively low flank wear rates in comparison to LPS inserts.

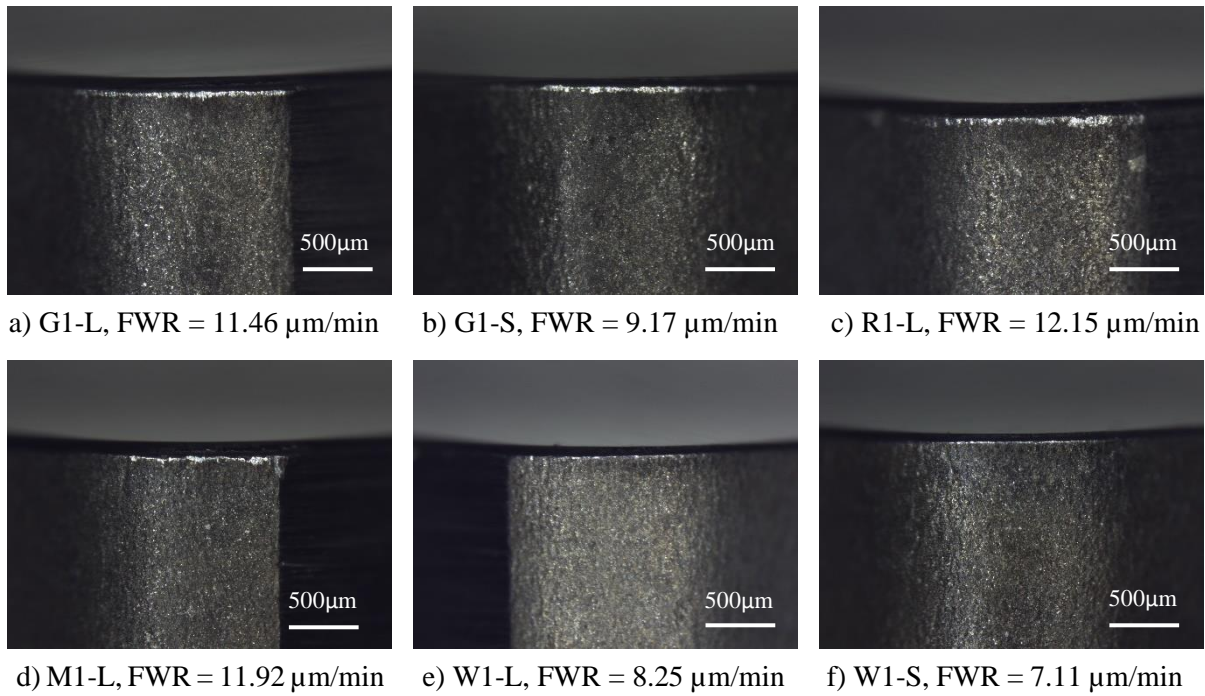


Figure 7.44. Maximum flank wear of a) G1-L, b) G1-S, c) R1-L, d) M1-L, W1-L, and f) W1-S inserts after MQL semi-finishing at cutting speed of 400 m/min and 1 mm depth of cut

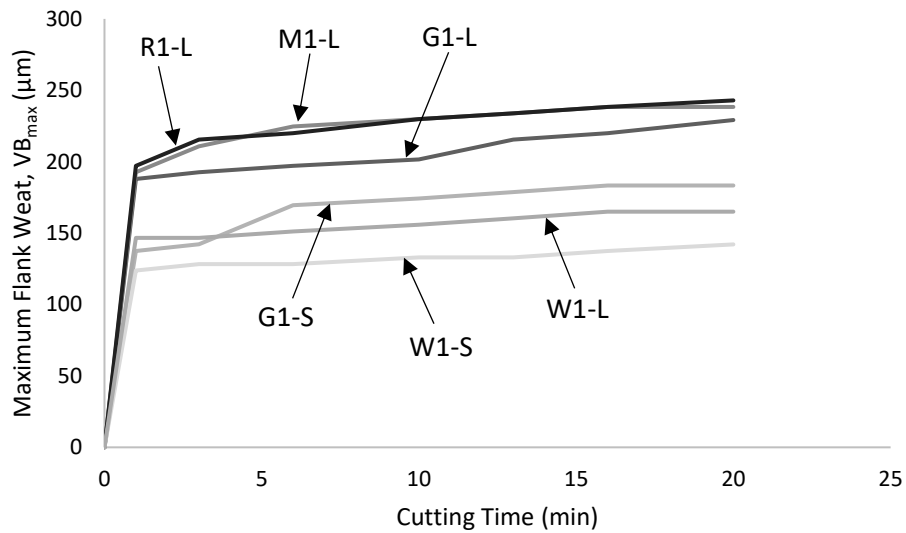


Figure 7.45. Graph of Flank wear (VB_{Max}) against cutting time (min) during MQL semi-finishing

Figure 7.47 shows the relationship between FWR and K_{IC} . There was no general correlation observed between FWR and K_{IC} since the insert plots had no specific trend. It is clear that the change in FWR was a result of another parameter other than K_{IC} .

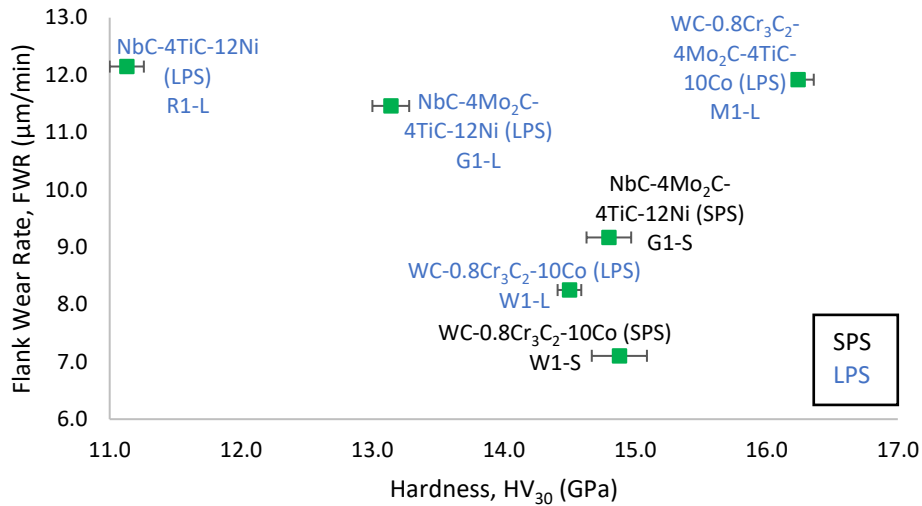


Figure 7.46. Graph of flank wear rate (FWR) against insert hardness (HV₃₀) during MQL semi-finishing

Figure 7.48 shows the relationship between FWR and $F_{R, ave}$. The WC based inserts showed a slight increase in $F_{R, ave}$ with increased FWR. The NbC based inserts showed similar in $F_{R, ave}$ with increased FWR. The negligible changes in $F_{R, ave}$ was within the error margin hence there was no correlation observed between FWR and $F_{R, ave}$.

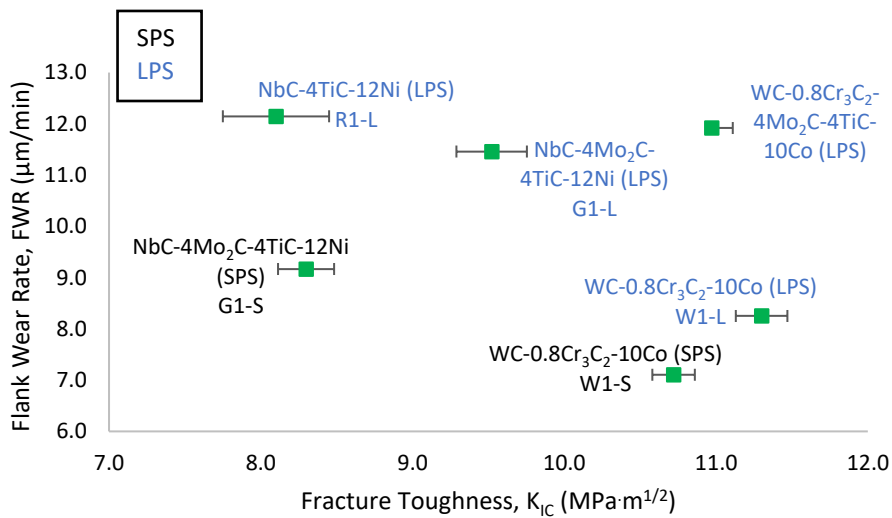


Figure 7.47. Graph of flank wear rate (FWR) against fracture toughness (K_{1C}) during MQL semi-finishing

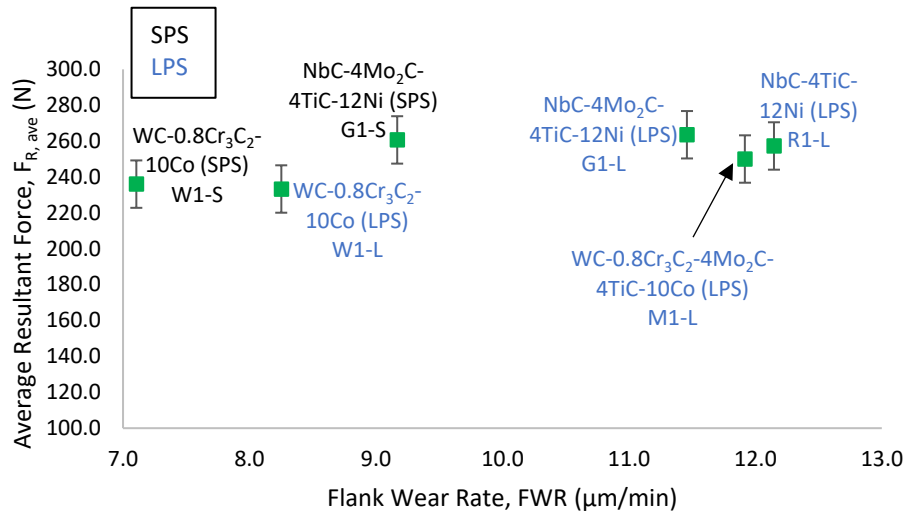


Figure 7.48. Plot of average resultant force ($F_{R,ave}$) against flank wear rate (FWR) during MQL semi-finishing

Figure 7.49 show the comparison between FWR and T_a . Generally, T_a increased with increased FWR. The WC based W1-L and W1-S inserts had the lowest T_a and FWR compared to the NbC based inserts. The WC SPS insert W1-S had lower FWR and higher T_a than the LPS produced W1-L. The NbC based SPS produced G1-S had lower FWR and slightly lower T_a than the LPS produced G1-L. The difference in T_a between G1-L and G1-S was within the error margin. Hence no correlation between FWR and T_a could be established amongst NbC based inserts.

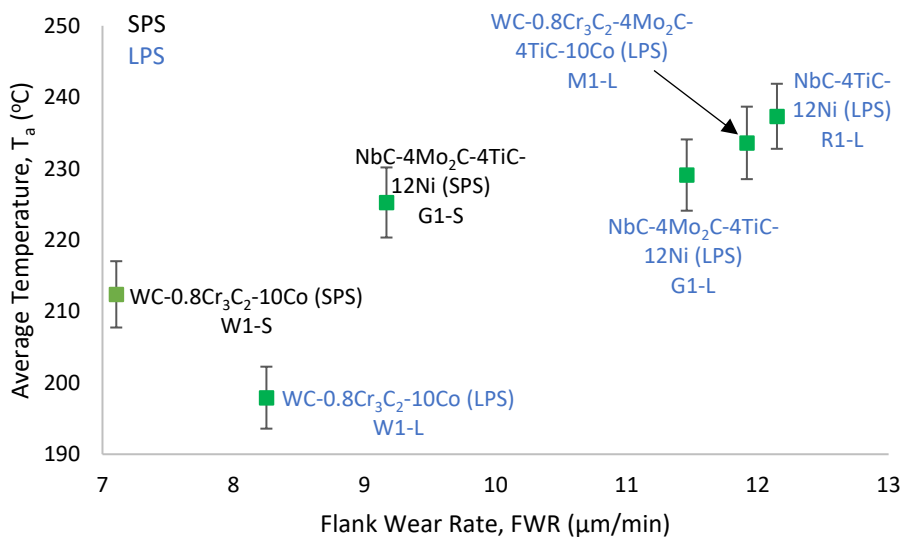


Figure 7.49. Graph of average Temperature (T_a) against flank wear rate (FWR) during MQL semi-finishing

Figure 7.50 shows the relationship between $F_{R,ave}$ and HV_{30} during MQL semi-finishing. Both the WC and NbC based inserts showed a negligible change in $F_{R,ave}$ with increased HV_{30} . The slight differences in $F_{R,ave}$ are within the error margin hence there was no correlation observed between $F_{R,ave}$ and HV_{30} .

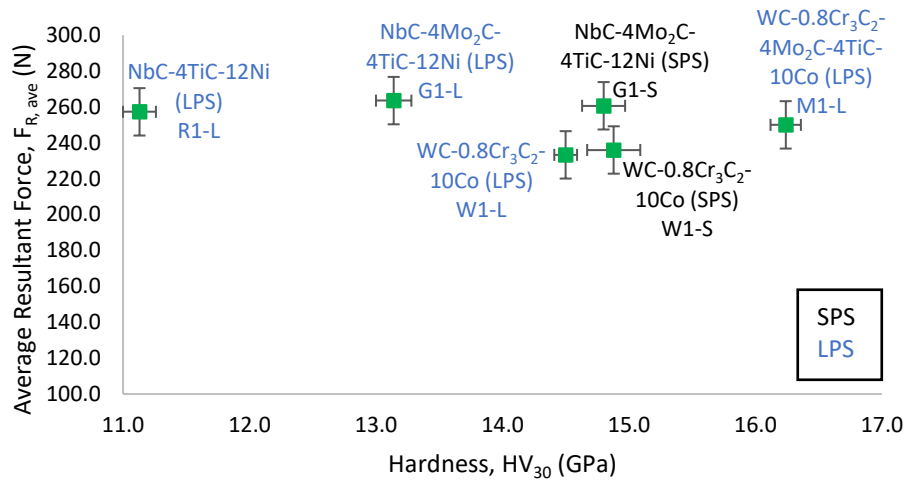


Figure 7.50. Graph of average resultant force ($F_{R,ave}$) against insert hardness (HV_{30}) during MQL semi-finishing

Figure 7.51 shows the relationship between $F_{R,ave}$ and K_{IC} during MQL semi-finishing. Both the WC and NbC based inserts showed a negligible change in $F_{R,ave}$ with increased K_{IC} . The slight changes in $F_{R,ave}$ are within the error margin hence there was no correlation observed between $F_{R,ave}$ and K_{IC} .

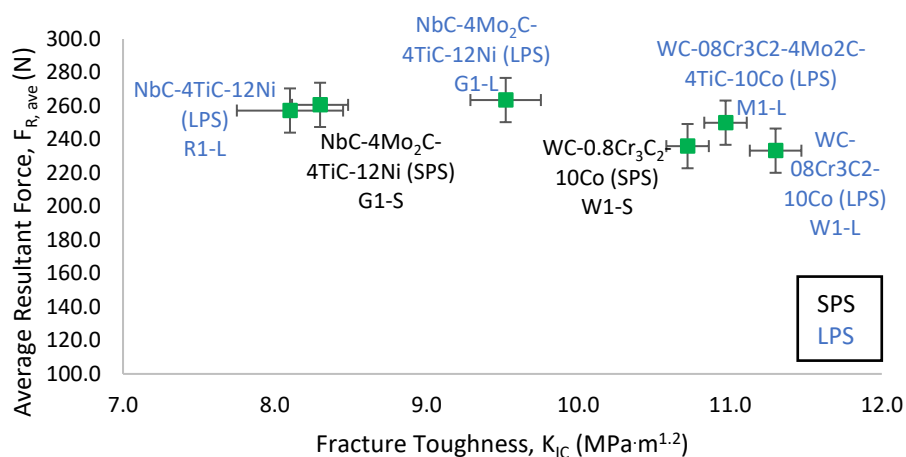


Figure 7.51. Graph of average resultant force ($F_{R,ave}$) against fracture toughness (K_{IC}) during MQL semi-finishing.

7.4.4 Dry versus Flood

This subsection reports the comparison between flood semi-finishing and dry semi-finishing. Three inserts (W1-S, M1-L, and R1-L) were selected as examples to show the correlation between dry and flood. Flank wear rates and average resultant forces are compared for different machining conditions. Figure 7.52 shows the relationship between $F_{R,ave}$ and FWR during semi-finishing. Both dry and flood conditions showed a negligible change in $F_{R,ave}$ with increased FWR. Flood lubrication lowered FWR however increasing $F_{R,ave}$ for WC based inserts, whereas NbC based inserts experienced higher FWR and higher $F_{R,ave}$ with flood lubrication.

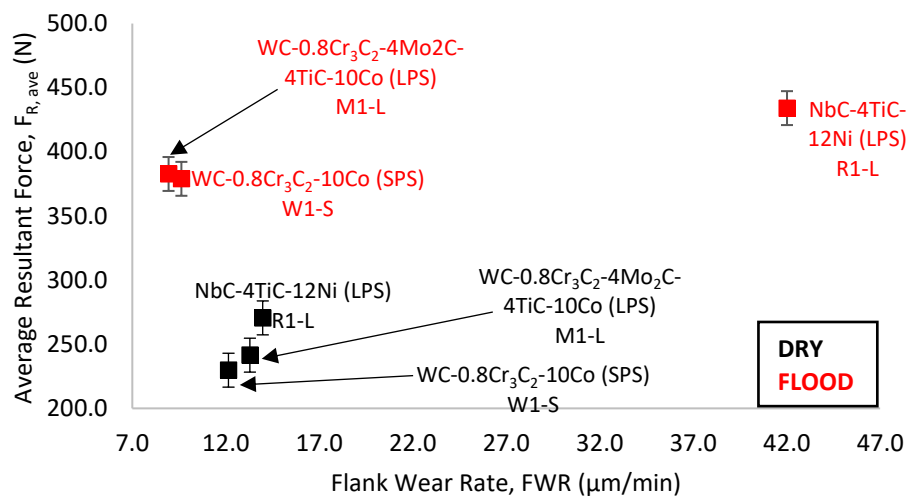


Figure 7.52. Graph of average resultant force ($F_{R,ave}$) against flank wear rate (FWR) during dry and flood semi-finishing

7.4.5 Dry versus MQL

This subsection reports the comparison between MQL semi-finishing and dry semi-finishing. Three inserts (W1-S, G1-S, and G1-L) were selected to show the $F_{R,ave}$ vs FWR correlation and five inserts (W1-S, M1-L, G1-S, G1-L, and R1-L) were selected to show the T_a vs FWR correlation between dry and MQL. Flank wear rates, average resultant forces and average machining temperatures are compared at different machining parameters.

Figure 7.53 show the relationship between $F_{R,ave}$ and FWR during semi-finishing. Both dry and MQL conditions showed a slight increase $F_{R,ave}$ with increased FWR. However, MQL lowered flank wear rate for similar compositions. Inserts had lower FWR during MQL semi-finishing but experienced similar $F_{R,ave}$ during both dry and MQL semi-finishing.

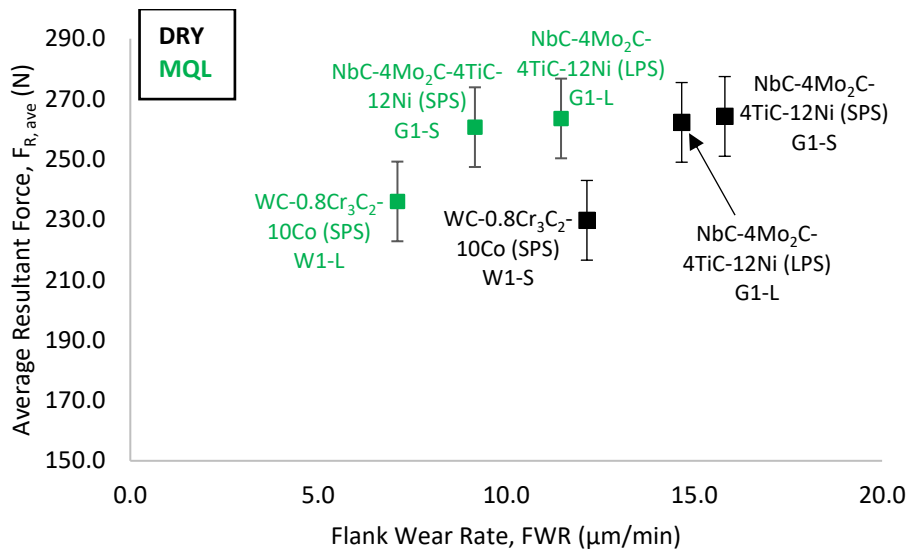


Figure 7.53 Graph of average resultant force ($F_{R,ave}$) against flank wear rate (FWR) during dry and MQL semi-finishing

Figure 7.54 show the relationship between T_a and FWR. Generally, T_a increased with increased FWR, and MQL significantly lowered both FWR and T_a of all LPS and SPS sintered inserts. The use of MQL lowered FWR and T_a of G1-S, from highest FWR and T_a during dry semi-finishing to second lowest during MQL semi-finishing.

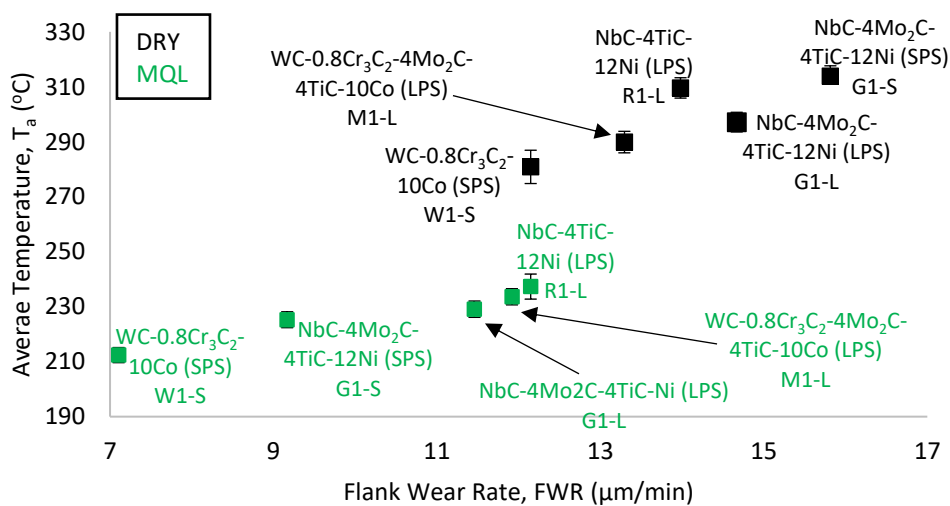


Figure 7.54. Graph of average temperature (T_a) against flank wear rate (FWR) during dry and MQL semi-finishing

7.4.6 Flood versus MQL

This subsection reports the comparison between flood semi-finishing and MQL semi-finishing. Three inserts were selected (W1-S, W1-L, and M1-L) as examples to show the correlation between dry and flood. The FWR and $F_{R,ave}$ are compared at different machining conditions. Figure 7.55 shows the relationship between FWR and $F_{R,ave}$ during semi-finishing. The W1-S and W1-L inserts had lower FWR and $F_{R,ave}$ during MQL semi-finishing whereas, M1-L had lower FWR and higher $F_{R,ave}$ than during MQL compared to flood. The LPS insert W1-L had lower FWR during flood semi-finishing and SPS sintered insert W1-S had lower FWR during MQL (Figure 7.55).

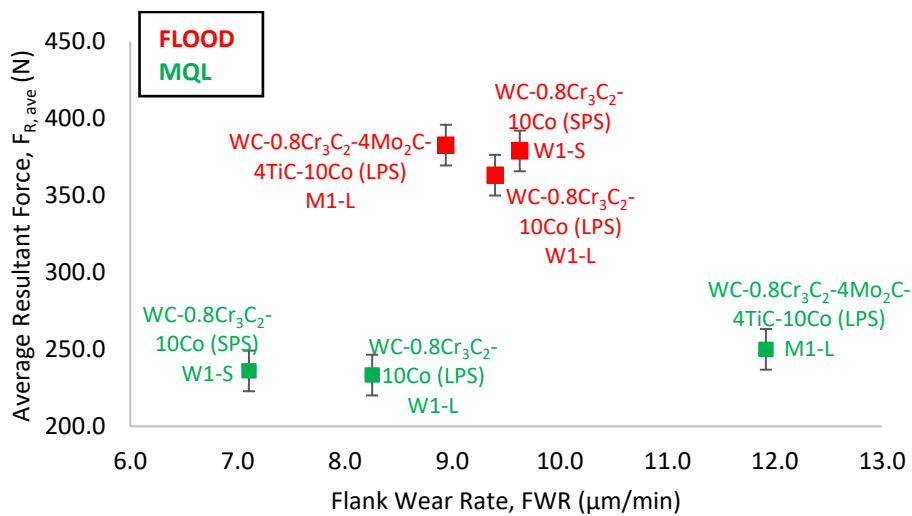


Figure 7.55. Graph of average resultant force ($F_{R,ave}$) against flank wear rate (FWR) during flood and MQL semi-finishing

7.4.7 Overall Analysis of Semi-Finishing

The W1-S inserts had the best performance with the lowest VB_{Max} during dry and MQL semi-finishing (Figures 7.30 and 7.45), and the M1-L insert had the best performance with the lowest VB_{Max} during flood (Figure 7.38). The G1-S inserts had the poorest performance with the highest VB_{Max} during dry whereas the R1-L insert had the poorest performance during flood and MQL semi-finishing. The R1-L insert had a mechanical fracture at 16 minutes of cutting time during flood. The WC based inserts had the best performance during all lubricating conditions compared to the NbC based inserts.

Generally, FWR increased with increased HV_{30} during dry semi-finishing (Figure 7.31) whereas, FWR decreased with increased HV_{30} during MQL semi-finishing (Figure 7.46). The FWR were similar irrespective of the slightly increased HV_{30} during flood semi-finishing although R1-L has the highest FWR (Figure 7.39). The G1-S insert had a similar HV_{30} to W1-S but experienced the highest FWR during dry semi-finishing. The R1-L insert had the lowest HV_{30} and the highest FWR during flood and

MQL. The W1-S insert had the lowest FWR during all lubrication conditions. The FWR decreased with increased K_{IC} during dry (Figure 7.32) and there was no correlation between FWR and K_{IC} during flood and MQL (Figures 7.40 and 7.47). The R1-L insert had the lowest K_{IC} and the highest FWR.

There was a negligible increase in $F_{R, ave}$ with increased FWR during dry, flood, and MQL semi-finishing (Figures 7.33, 7.41, and 7.48). There was no correlation observed between FWR and $F_{R, ave}$ during all lubricating conditions. However, the WC based inserts had slightly lower $F_{R, ave}$ and lower FWR than the NbC based inserts during dry, flood, MQL.

The T_a increased with increased FWR during dry and MQL semi-finishing (Figures 7.34 and 7.49). The WC SPS produced W1-S insert had the lowest T_a and FWR whereas the NbC SPS produced G1-S insert had the highest T_a and FWR during dry semi-finishing. During MQL semi-finishing, the NbC SPS produced G1-S had lower T_a and FWR than the LPS produced G1-L insert, and the WC SPS produced W1-S insert had higher T_a and lower FWR than the WC LPS produced W1-L insert. Generally, the WC based inserts had lower FWR and T_a .

There was negligible change in $F_{R, ave}$ irrespective of the increased HV_{30} during dry, flood, and MQL semi-finishing (Figures 7.35, 7.42, and 7.50). The WC based inserts had slightly lower $F_{R, ave}$ and higher HV_{30} than the NbC based inserts during semi-finishing. The $F_{R, ave}$ slightly decreased with increased K_{IC} during dry and flood whereas there was no correlation observed during MQL (Figures 7.36, 7.43 and 7.51). The WC based inserts had slightly lower $F_{R, ave}$ and higher K_{IC} than the NbC based inserts during semi-finishing.

Flood semi-finishing reduced $F_{R, ave}$ and slightly increased FWR of WC based inserts compared to dry semi-finishing. Flood semi-finishing increased both the $F_{R, ave}$ and FWR of the NbC based R1-L insert compared to dry (Figure 7.52). The MQL lowered FWR and $F_{R, ave}$ were similar to those of dry (Figure 7.53). The MQL also lowered T_a and FWR of the five selected inserts (W1-S, M1-L, G1-L, G1-S, and R1-L) in Figure 7.54. The MQL semi-finishing had lower $F_{R, ave}$ and FWR than flood semi-finishing (Figure 7.55).

7.5 Finishing

Each insert machined for 20 minutes cutting time at 800 m/min cutting speed and 0.5 mm depth of cut. Insert failure criteria of 300 μm VB_{Max} was used for finishing (Boothryd & Knight, 2006; Genga et al., 2020). Premature failure due to mechanical fracture failure was considered the end of tool life. Flank wear rate was used as a measure of performance for each cutting insert.

7.5.1 Dry

The readings taken includes machining forces, temperatures, and maximum flank wear (VB_{Max}) measurement. Flank wear rates (FWR), average resultant forces ($F_{R, ave}$), average temperatures (T_a), and average surface roughness (R_a) were calculated and results tabulated in Table 7.9 for dry finishing.

Table 7.9. Comparison of VB_{Max} , $F_{R, ave}$, T_a , and R_a during dry finishing

Composition	Inserts	VB_{Max} (μm)	FWR ($\mu\text{m}/\text{min}$)	$F_{R, ave}$ (N)	T_a (C)	R_a (μm)
NbC-4Mo ₂ C- 4TiC-12Ni	G1-L	270.44	13.52	374.47 ± 13	162.51 ± 3.57	0.512 ± 0.056
NbC-4Mo ₂ C- 4TiC-12Ni	G1-S	265.86	13.29	380.12 ± 13	179.68 ± 3.75	0.432 ± 0.023
NbC-4TiC- 12Ni	R1-L	261.28	13.06	352.15 ± 13	168.50 ± 3.70	0.610 ± 0.050
WC-0.8Cr ₃ C ₂ - 4Mo ₂ C-4TiC- 10Co	M1-L	252.11	12.61	348.32 ± 13	178.26 ± 3.91	0.511 ± 0.021
WC-0.8Cr ₃ C ₂ - 10Co	W1-S	206.27	10.31	324.46 ± 13	207.71 ± 4.01	0.386 ± 0.034

Figure 7.57 shows the comparison between VB_{Max} and cutting time during dry finishing. The WC based W1-S insert had the best tool life during dry finishing with the lowest VB_{Max} and FWR of 206.27 μm and 10.31 $\mu\text{m}/\text{min}$ respectively (Table 7.9, Figure 7.57), and the G1-L, R1-L and G1-S had the highest VB_{Max} . Spark plasma sintered inserts (G1-S and W1-S) had better tool life compared to LPS sintered inserts (G1-L, R1-L and M1-L). Tungsten Carbide-based inserts had better tool life than Niobium Carbide-based inserts. The G1-S had the best tool life amongst NbC inserts while the W1-L had the best tool life amongst WC based inserts.

Figure 7.58 shows the relationship between FWR and HV_{30} during dry finishing. Inserts with similar composition showed a negligible change FWR with increased HV_{30} . The WC based inserts showed no correlation between FWR and HV_{30} .

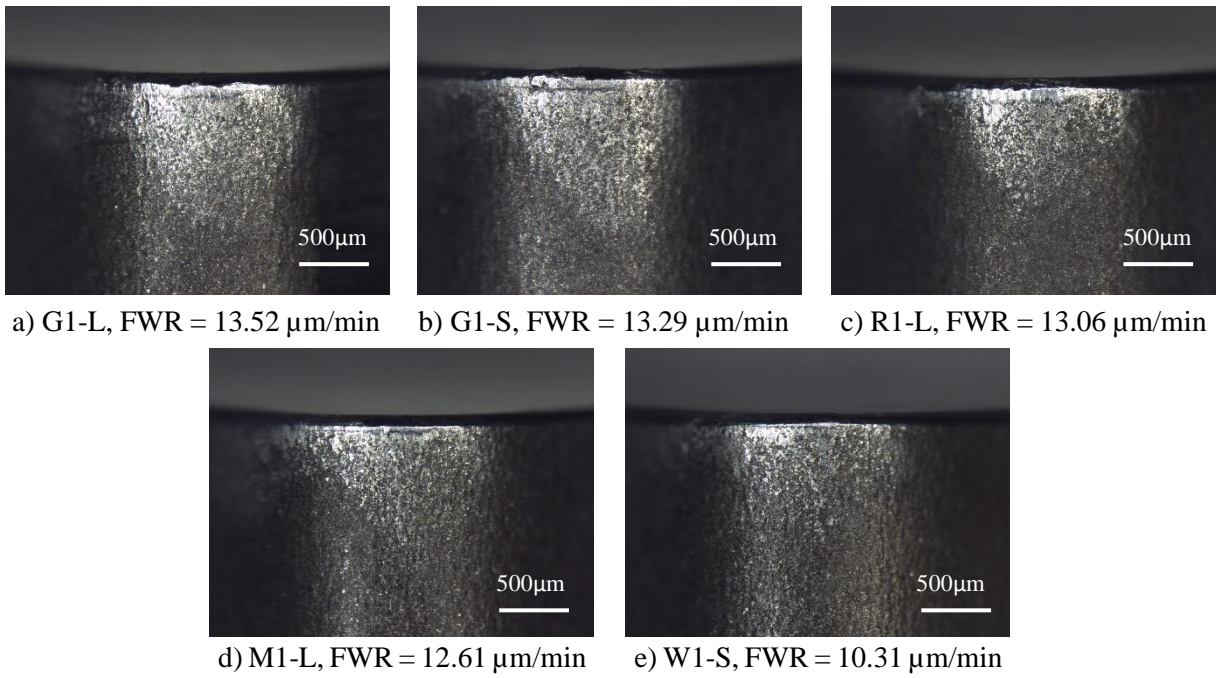


Figure 7.56. Maximum flank wear of a) G1-L, b) G1-S, c) R1-L, d) M1-L, and e) W1-S inserts after dry finishing at cutting speed of 800 m/min and 0.5 mm depth of cut

Figure 7.59 shows the relationship between FWR and K_{IC} . The NbC based inserts showed a negligible change in FWR with increased K_{IC} . There was no correlation drawn amongst NbC based inserts. The WC based inserts showed an increase in FWR with negligible change K_{IC} (within the K_{IC} error margin). Hence the increase in FWR was not due to the change in K_{IC} .

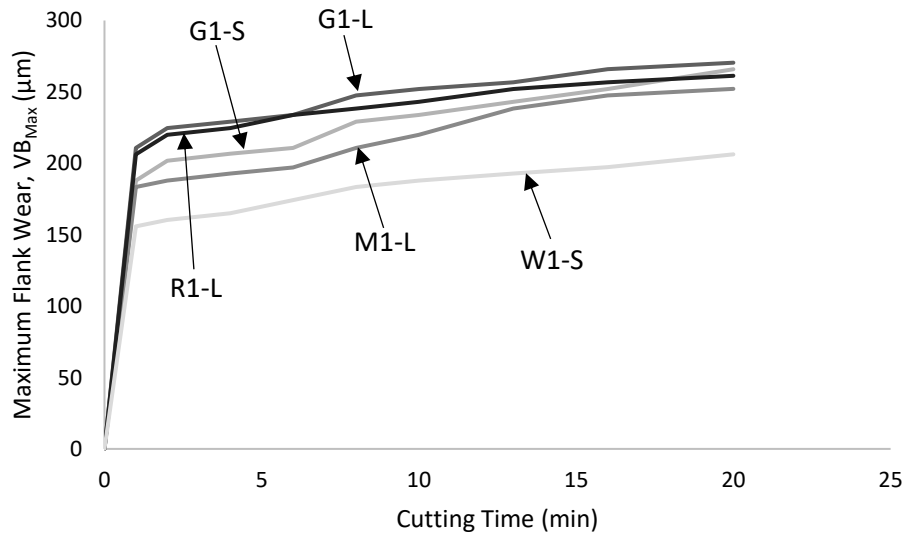


Figure 7.57. Graph of maximum flank wear (VB_{Max}) against cutting time (min) during dry finishing

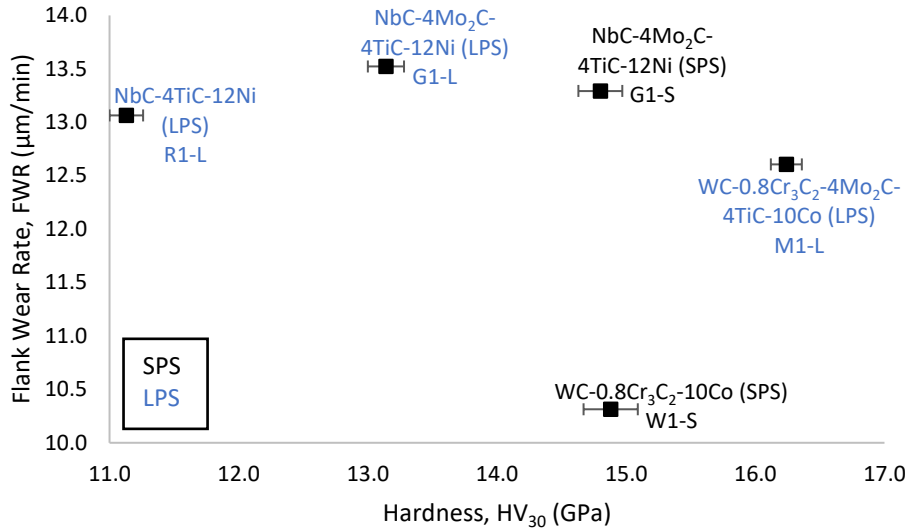


Figure 7.58. Graph of flank wear rate (FWR) against insert hardness (HV_{30}) during dry finishing

Figure 7.60 shows the relationship between $F_{R,ave}$ and FWR. The $F_{R,ave}$ increased with increased FWR. The WC based inserts had lower FWR and lower $F_{R,ave}$ compared to NbC based inserts. The WC SPS insert (W1-S) had slightly lower FWR and lower $F_{R,ave}$ compared to the WC based LPS inserts, whereas the NbC based SPS insert (G1-S) had similar $F_{R,ave}$ and FWR to the NbC based LPS insert (G1-L).

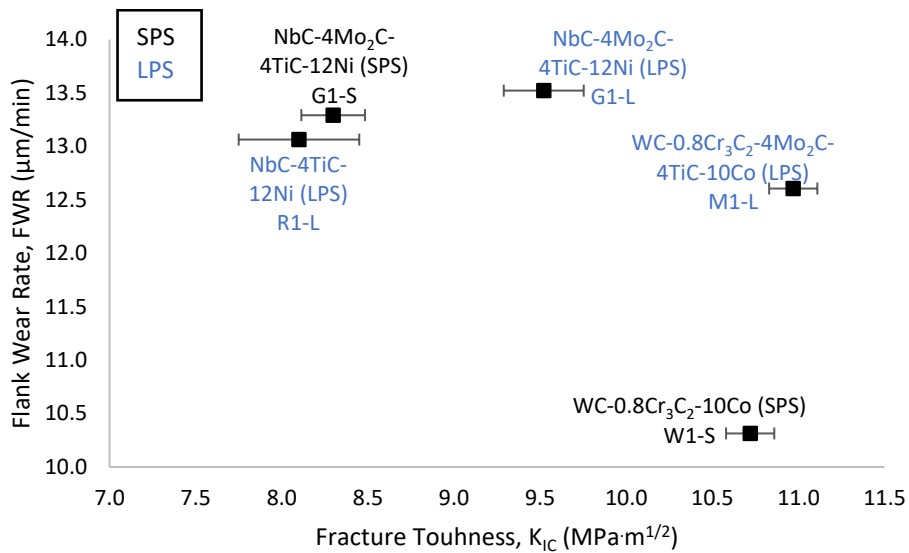


Figure 7.59. Graph of flank wear rate (FWR) against insert fracture toughness (K_{IC}) during Dry finishing

Figure 7.61 shows the comparison between T_a and FWR. Generally, T_a decreased with increased FWR. Tungsten carbide-based inserts had lower FWR and higher T_a than the NbC based inserts. Spark plasma sintered inserts (G1-S) had lower FWR and higher T_a than their similar LPS inserts (G1-L).

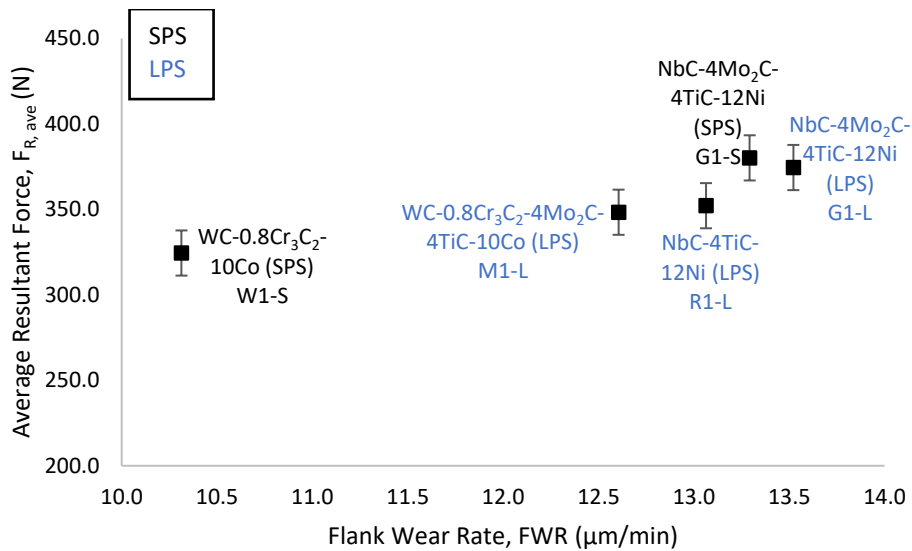


Figure 7.60. Graph of average resultant force ($F_{R,ave}$) against flank wear rate (FWR) during dry finishing

Generally, R_a increased with increased FWR as shown in Figure 7.62. Niobium carbide-based inserts showed an indirect proportionality relationship between R_a and FWR, decrease in R_a with increased FWR. Tungsten carbide-based inserts showed a direct proportionality, R_a increased with increased FWR. The WC based SPS inserts had lower R_a and FWR than the WC based LSP inserts. The NbC based LPS inserts had lower R_a and FWR than the NbC based SPS inserts. Spark plasma sintered inserts had increased R_a with increased FWR and LPS produced inserts had decreased in R_a with increased FWR. The WC based inserts had a better surface finish at lower FWR than the NbC based inserts.

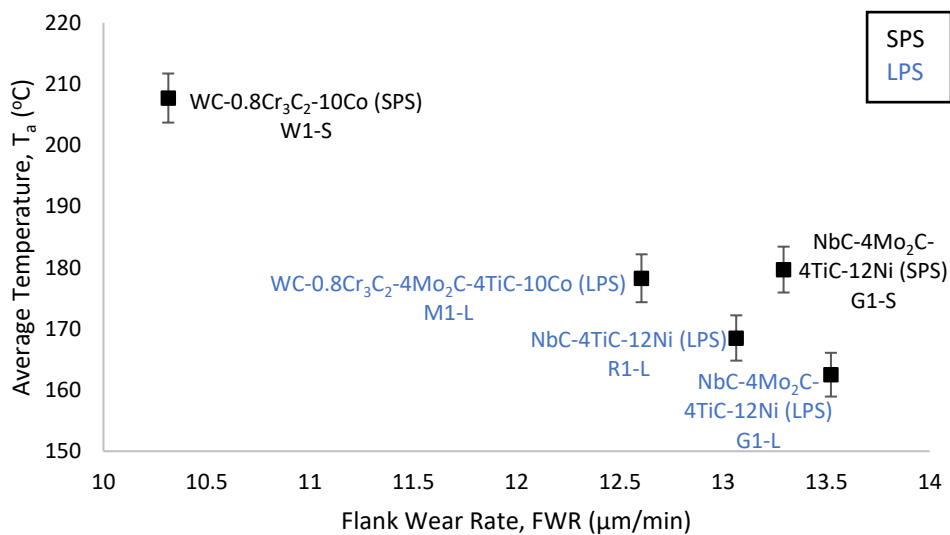


Figure 7.61. Graph of average Temperature (T_a) against flank wear rate (FWR) during dry finishing

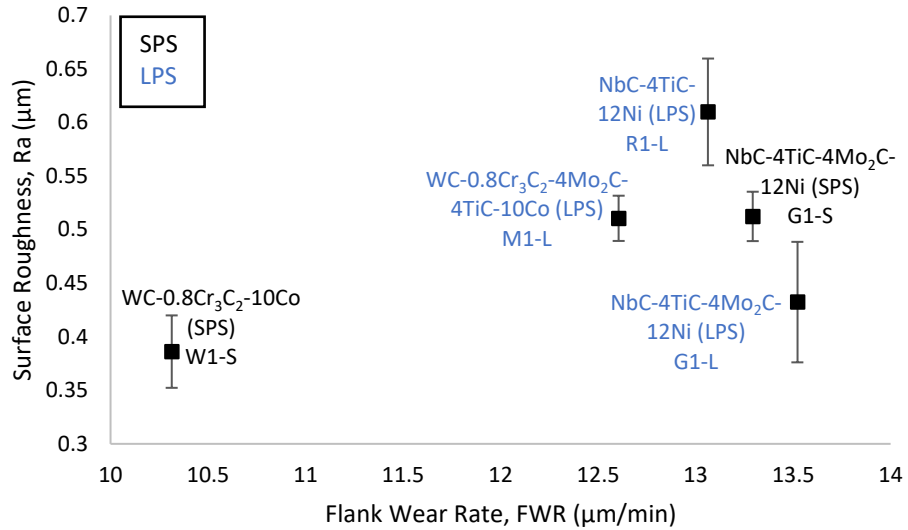


Figure 7.62. Graph of average surface roughness (R_a) against flank wear rate (FWR) during dry finishing

Figure 7.63 shows the relationship between R_a and $F_{R, ave}$. There was no observed general correlation between R_a and $F_{R, ave}$. However, for the WC based inserts, R_a increased with increased $F_{R, ave}$. The LPS sintered inserts showed a decrease in R_a with increased FWR. The W1-S insert had the lowest R_a and $F_{R, ave}$.

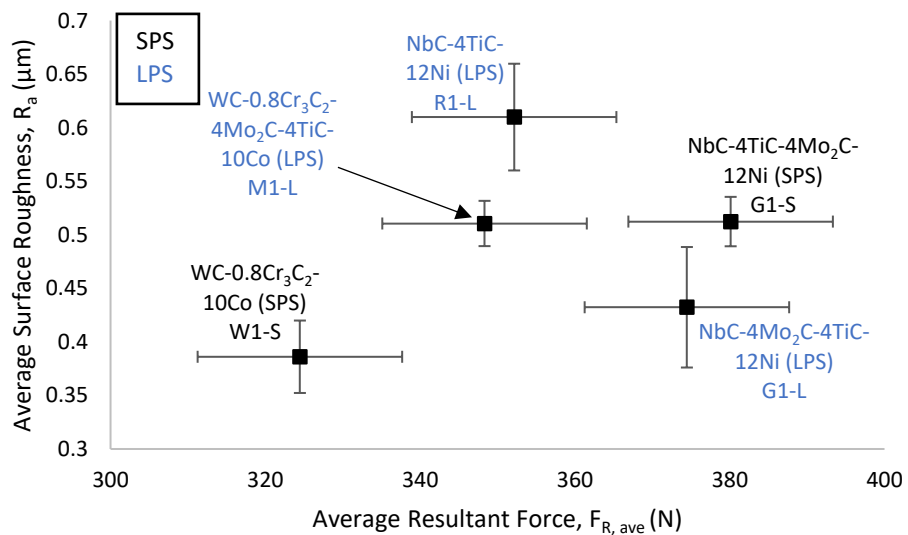


Figure 7.63. Graph of average surface roughness (R_a) against average resultant force ($F_{R, ave}$) during dry finishing

Figure 7.64 shows the comparison between R_a and $F_{R,ave}$. Generally, the R_a decreased with increased T_a . The WC based W1-S insert had the lowest R_a and the highest T_a , and the NbC based R1-L insert had the highest R_a and second lowest T_a . The G1-L had second lowest R_a and the lowest T_a .

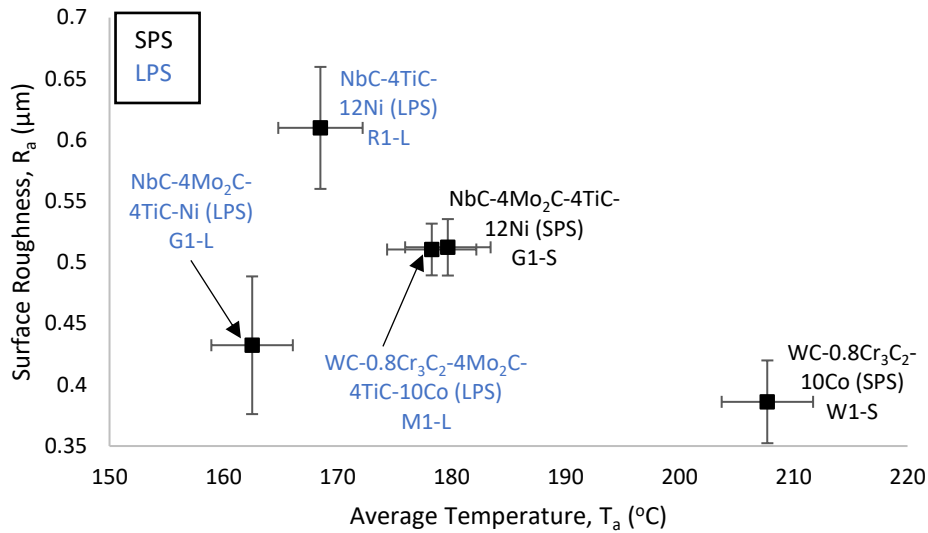


Figure 7.64. Graph of average surface roughness (R_a) against average temperature (T_a) during dry finishing

Figure 7.65 shows the relationship between $F_{R,ave}$ and HV_{30} during dry finishing. Generally, there was a negligible change in $F_{R,ave}$ with increased HV_{30} . The change in $F_{R,ave}$ was within the error margin hence no correlation could be drawn between $F_{R,ave}$ and HV_{30} . However, the W1-S insert had the lowest $F_{R,ave}$.

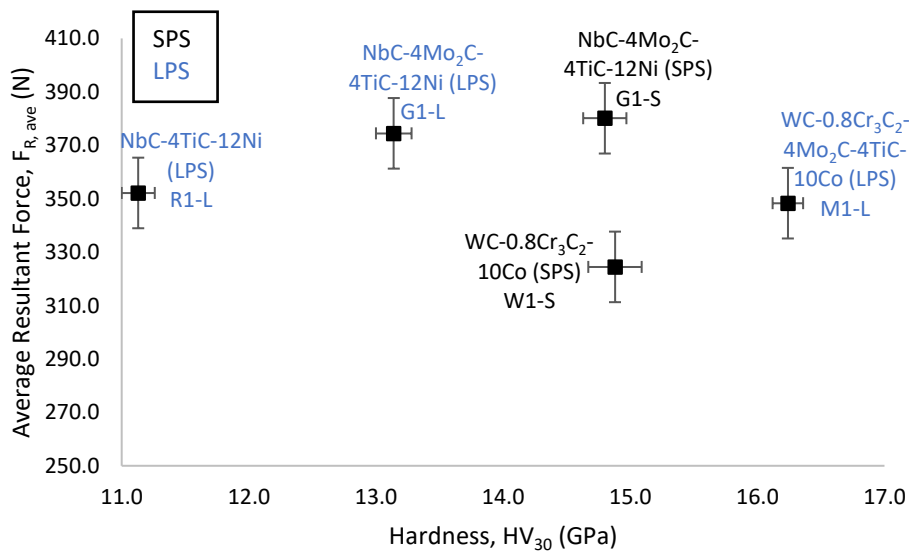


Figure 7.65. Graph of average resultant force ($F_{R,ave}$) against insert hardness (HV_{30}) during dry finishing

Figure 7.66 shows the relationship between $F_{R,ave}$ and K_{IC} during dry finishing. Generally, there was a negligible change in $F_{R,ave}$ with increased K_{IC} . The change in $F_{R,ave}$ was within the error margin hence no correlation could be drawn between $F_{R,ave}$ and K_{IC} .

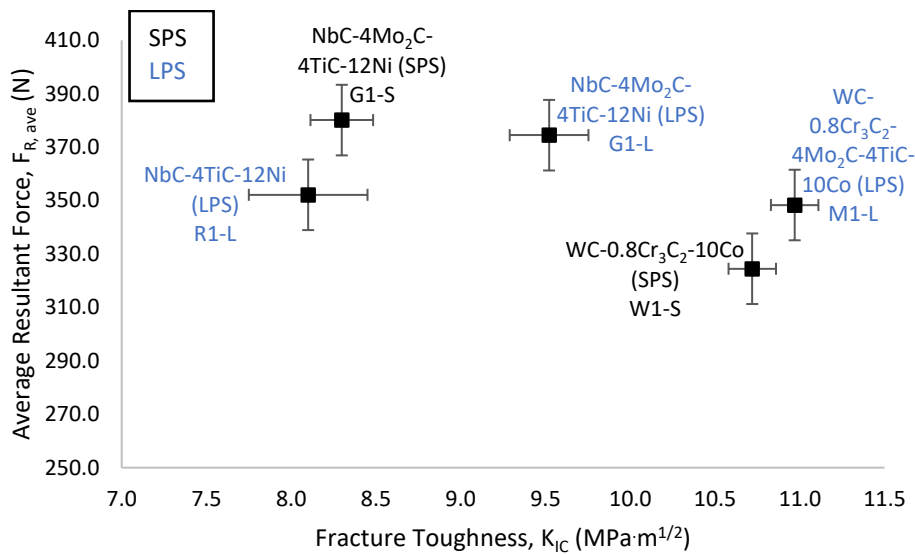


Figure 7.66. Graph of average resultant force ($F_{R,ave}$) against fracture toughness (K_{IC}) during dry finishing

7.5.2 Flood

The readings taken includes machining forces, maximum flank wear (VB_{Max}) and surface roughness measurement. Temperature rises were assumed to be negligible and similar to that of the coolant since large amounts of coolant was applied at a flow rate of 1.39 l/s (5 m³/hr). Flank wear rates (FWR), average resultant forces ($F_{R,ave}$) and average surface roughness (R_a) were calculated and results are tabulated in Table 7.10 for flood finishing.

Figure 7.68 shows the relationship between VB_{Max} and cutting time during flood finishing. Tungsten carbide-based inserts (W1-L, W1-S, and M1-L) had the best tool life with the lowest VB_{Max} and FWR of 174.18 μ m and 8.71 μ m/min respectively (Table 7.10, Figure 7.68). Tungsten carbide-based inserts had better tool life than the NbC based inserts. All NbC based inserts reached the 300 μ m VB_{Max} failure criteria with mechanical fractures before the 20 minutes cutting time (Figures 7.67 and 7.68). The R1-L insert had the highest VB_{Max} and FWR of 499.63 μ m after 3 minutes of cutting due to premature fracture. The G1-L and G1-S failed after 10 minutes of cutting time.

Table 7.10. Comparison of VB_{Max} , $F_{R, ave}$, and R_a during flood finishing

Composition	Inserts	VB_{Max} (μm)	FWR ($\mu\text{m}/\text{min}$)	$F_{R, ave}$ (N)	R_a (μm)
NbC-4Mo ₂ C-4TiC-12Ni	G1-L	302.53	30.25	365.29 ± 13	0.608 ± 0.017
NbC-4Mo ₂ C-4TiC-12Ni	G1-S	320.86	32.09	367.22 ± 13	6.019 ± 0.599
NbC-4TiC-12Ni	R1-L	499.63	166.54	354.07 ± 13	0.503 ± 0.059
WC-0.8Cr ₃ C ₂ -4Mo ₂ C-4TiC-10Co	M1-L	174.18	8.71	384.11 ± 13	0.504 ± 0.028
WC-0.8Cr ₃ C ₂ -10Co	W1-L	174.18	8.71	353.89 ± 13	0.364 ± 0.017
WC-0.8Cr ₃ C ₂ -10Co	W1-S	174.18	8.71	368.70 ± 13	0.466 ± 0.038

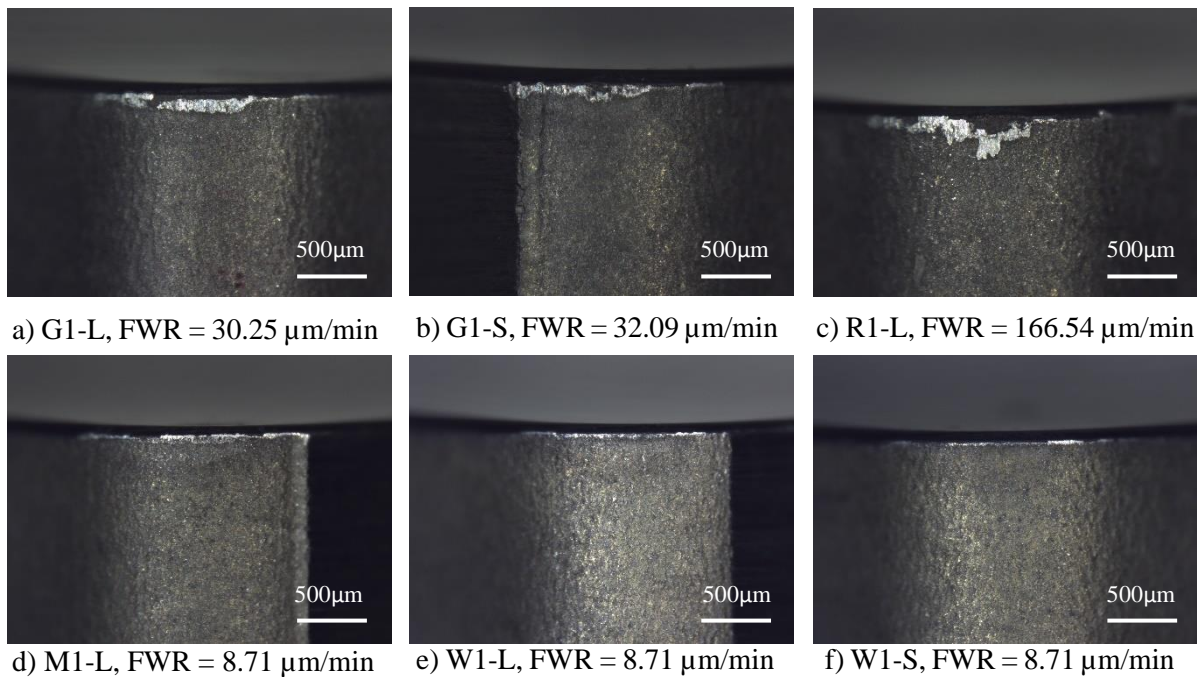


Figure 7.67. Maximum flank wear of a) G1-L, b) G1-S, c) R1-L, d) M1-L, e) W1-L, and f) W1-S inserts after flood finishing at cutting speed of 800 m/min and 0.5 mm depth of cut

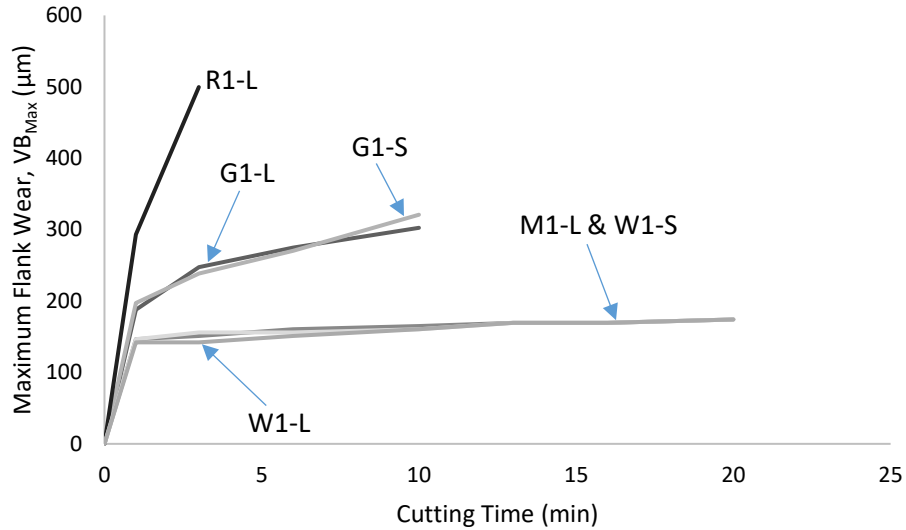


Figure 7.68. Graph of maximum flank wear (VB_{Max}) against time (min) during flood finishing

Figure 7.69 shows the comparison between FWR and HV_{30} during flood finishing. The WC based inserts experienced the same FWR irrespective of their different HV_{30} . A similar trend was observed with the NbC inserts (G1-S and G1-L). The NbC based R1-L insert had the highest FWR and the lowest HV_{30} .

Figure 7.70 shows the comparison between FWR and K_{IC} during flood finishing. The WC based inserts experienced the same FWR irrespective of their different K_{IC} . A similar trend was observed with the NbC inserts (G1-S and G1-L). The NbC based R1-L insert had the highest FWR and the lowest K_{V30} .

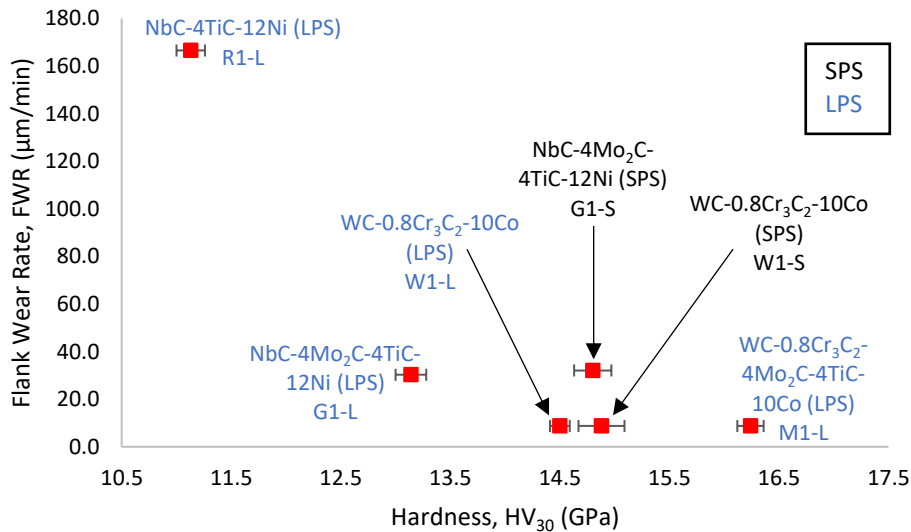


Figure 7.69. Graph of flank wear rate (FWR) against insert hardness (HV_{30}) during flood finishing

Figure 7.71 shows the relationship between $F_{R,ave}$ and FWR during flood finishing. All cutting inserts had similar $F_{R,ave}$ with increased FWR, the $F_{R,ave}$ of all inserts was within the same error margin. The WC based inserts (W1-S, W1-L, and M1-L) had similar FWR and $F_{R,ave}$ within the same error margins. The LPS sintered inserts had lower $F_{R,ave}$ compared to similar SPS produced inserts. The same trend was observed with NbC based inserts.

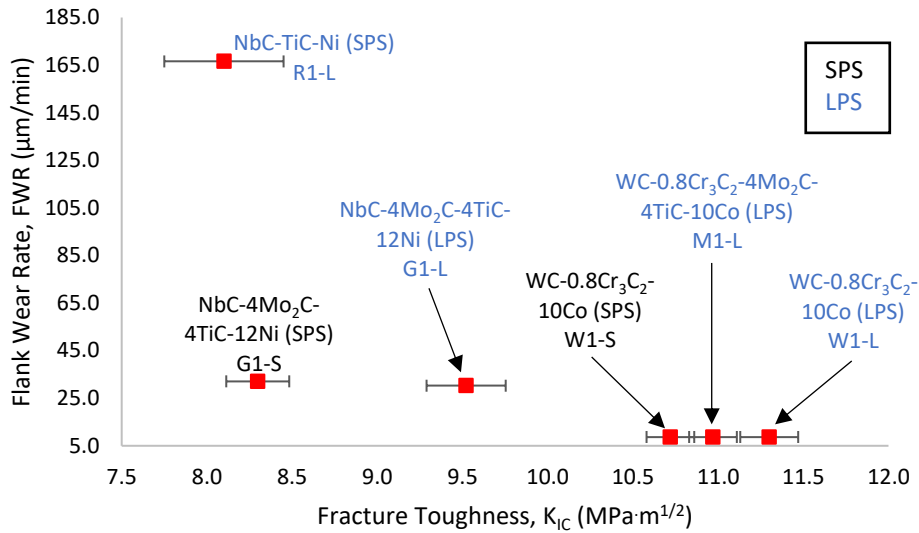


Figure 7.70. Graph of flank wear rate (FWR) against fracture toughness (K_{IC}) during flood finishing

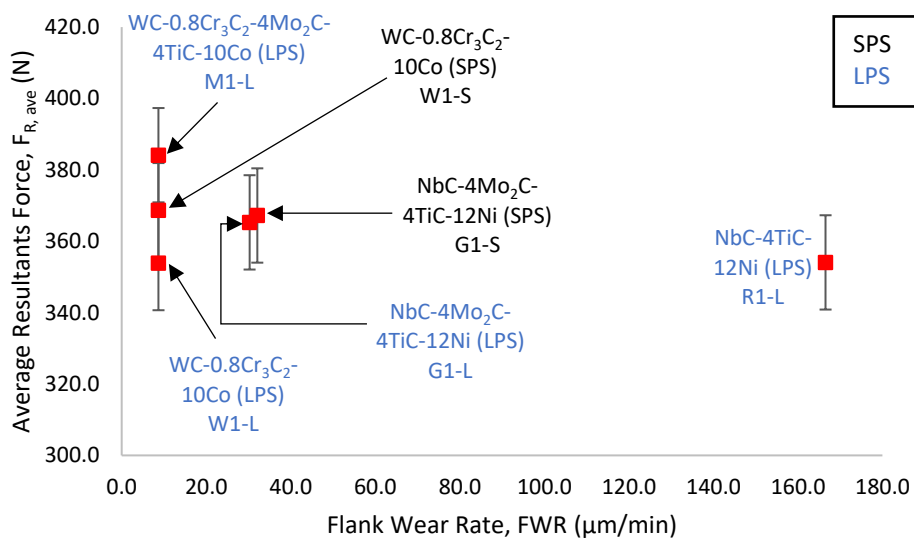


Figure 7.71. Graph of average resultant force ($F_{R,ave}$) against flank wear rate (FWR) during flood finishing

Figure 7.72 shows the relationship between R_a and FWR. Inserts show a negligible change in R_a with increased FWR hence no correlation could be drawn between the R_a and FWR. The NbC based R1-L

insert had the highest FWR during flood finishing and R_a was similar to that of G1-L and the WC based inserts (W1-L, W1-S, and M1-L). The G1-S insert had similar FWR to 1-L but had the highest R_a . The WC based inserts had similar FWR and R_a .

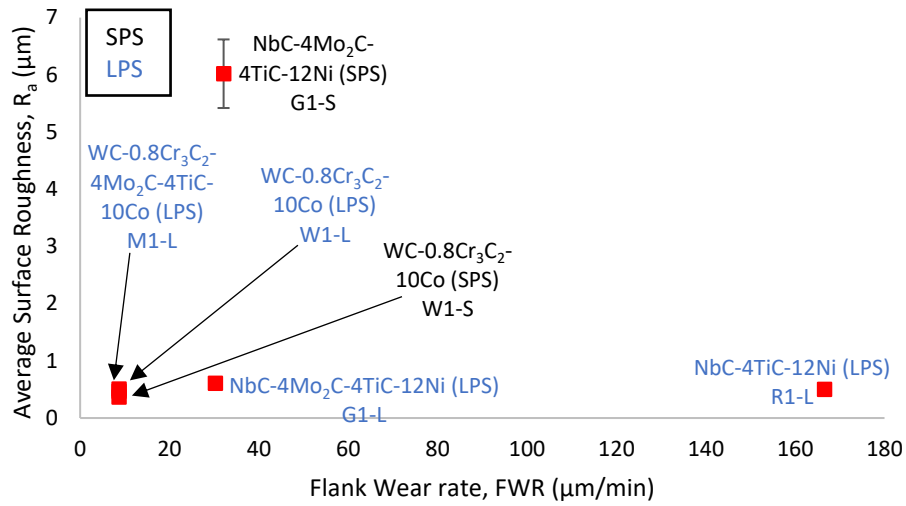


Figure 7.72. Graph of average surface roughness (R_a) against flank wear rate (FWR) during flood finishing

Figure 7.73 shows the comparison between R_a and $F_{R,ave}$. Inserts showed negligible change in R_a with slight increase in $F_{R,ave}$ which was within the same $F_{R,ave}$ error margin. However, the NbC based G1-S insert had the highest R_a at similar $F_{R,ave}$ to all other inserts. Hence there was no observed correlation between R_a and $F_{R,ave}$.

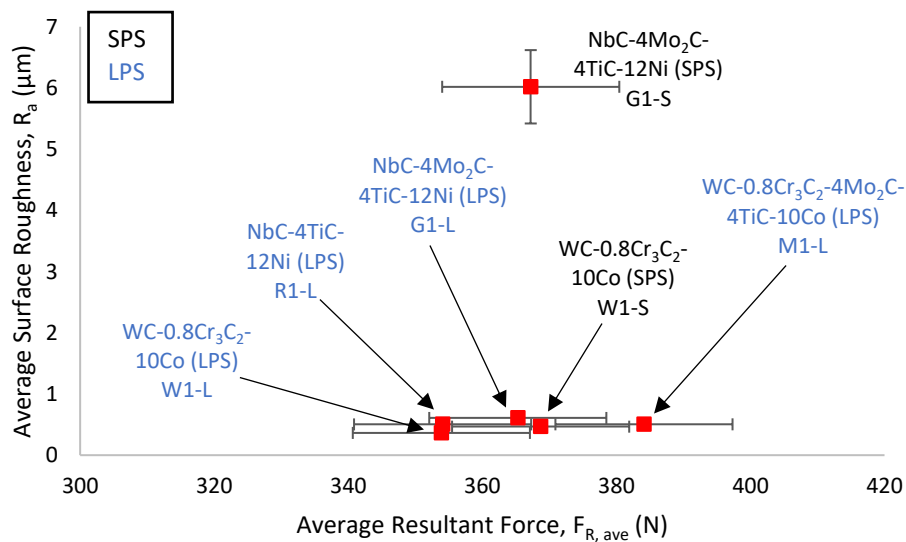


Figure 7.73. Graph of average surface roughness (R_a) against average resultant force ($F_{R,ave}$) during flood finishing

Figure 7.74 shows the relationship between $F_{R, ave}$ and HV_{30} . There was a negligible change in $F_{R, ave}$ with increased HV_{30} . All inserts had similar $F_{R, ave}$ irrespective of the increased HV_{30} . There was no observed correlation between $F_{R, ave}$ and HV_{30} .

Figure 7.75 shows the relationship between $F_{R, ave}$ and K_{IC} . There was a negligible change in $F_{R, ave}$ with increased K_{IC} . All inserts had similar $F_{R, ave}$ irrespective of the increased K_{IC} . There was no observed correlation between $F_{R, ave}$ and K_{IC} .

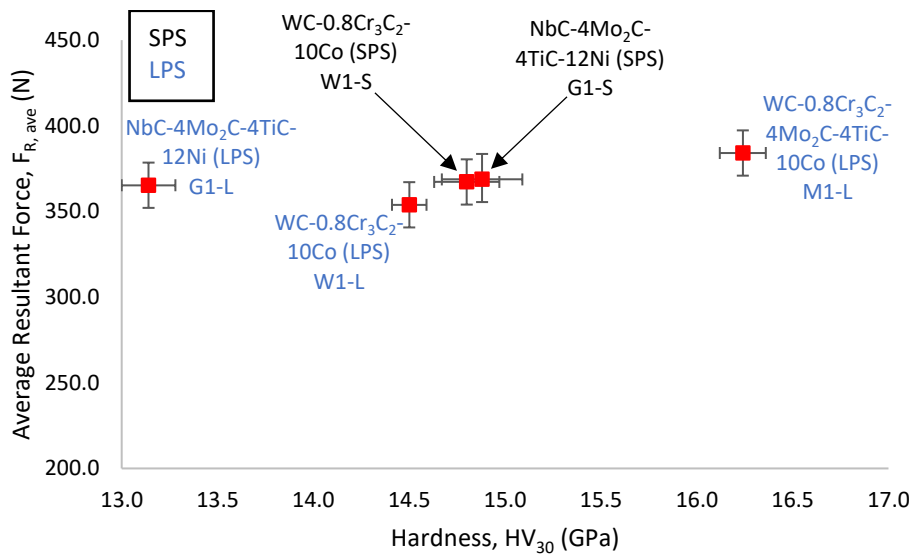


Figure 7.74. Graph of average resultant force ($F_{R, ave}$) against insert hardness (HV_{30}) during flood finishing

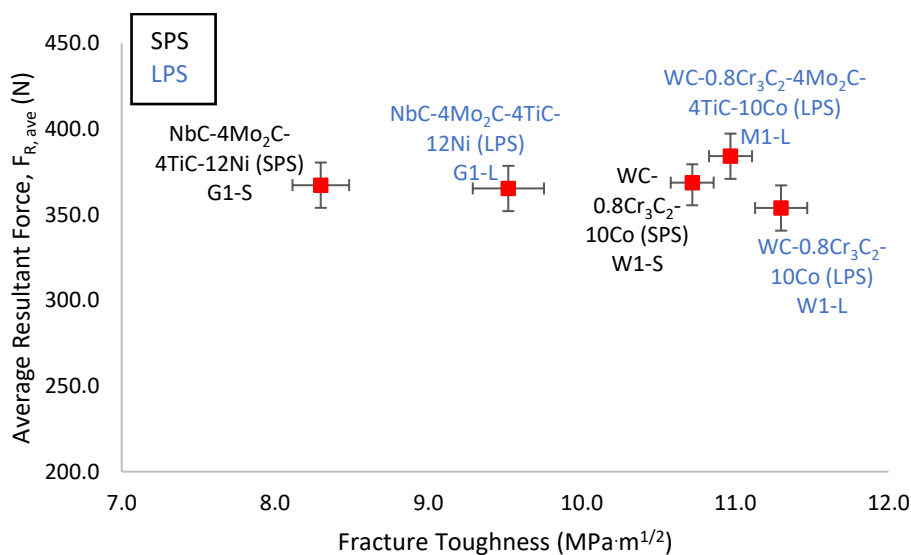


Figure 7.75. Graph of average resultant force ($F_{R, ave}$) against fracture toughness (K_{IC}) during flood finishing

7.5.3 MQL

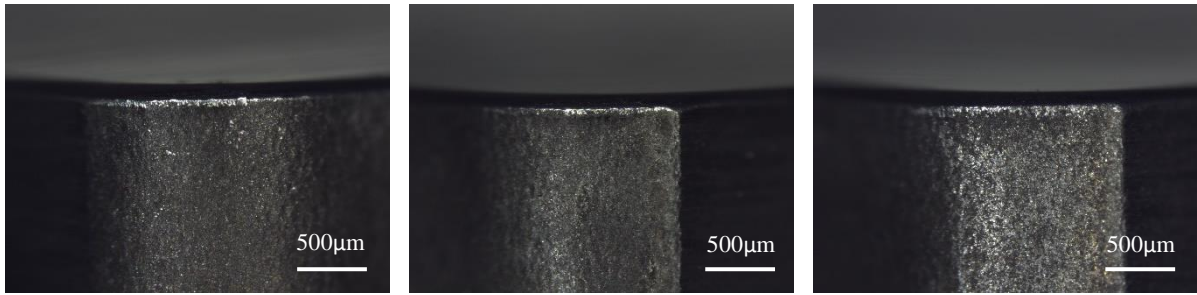
The MQL was applied at flow rate of 0.05 ml/s. The readings taken includes machining forces, temperatures, surface roughness R_a , and maximum flank wear (VB_{Max}) measurement. Average resultant forces ($F_{R, ave}$), average temperature (T_a), average surface roughness (R_a), and flank wear rates (FWR) were calculated and results were tabulated in Table 7.11 for MQL finishing.

Table 7.11. Comparison of VB_{Max} , FWR, $F_{R, ave}$, T_a , and R_a during flood finishing

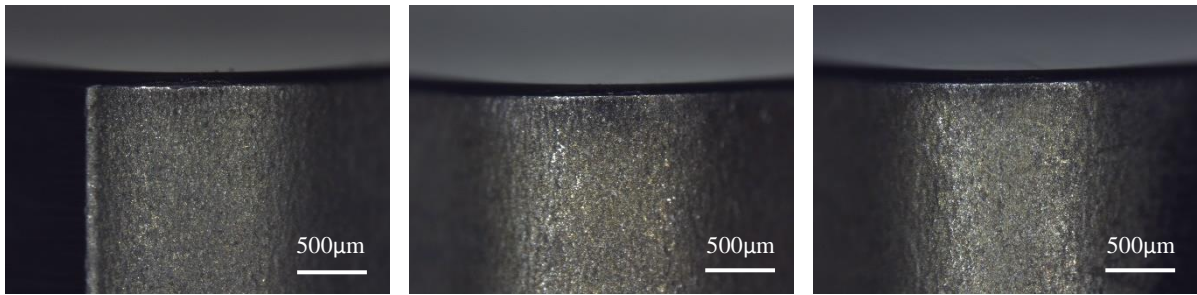
Composition	Inserts	VB_{Max} (μm)	FWR ($\mu\text{m}/\text{min}$)	$F_{R, ave}$ (N)	T_a (C)	R_a (μm)
NbC-4Mo ₂ C-4TiC-12Ni	G1-L	252.11	12.61	296.26 ± 13	134.51 ± 2.98	0.819 ± 0.093
NbC-4Mo ₂ C-4TiC-12Ni	G1-S	238.36	11.92	304.78 ± 13	130.63 ± 2.89	0.565 ± 0.059
NbC-4TiC-12Ni	R1-L	238.36	11.92	293.14 ± 13	127.73 ± 2.83	0.926 ± 0.074
WC-0.8Cr ₃ C ₂ -4Mo ₂ C-4TiC-10Co	M1-L	201.69	10.08	282.10 ± 13	133.23 ± 2.95	3.029 ± 0.023
WC-0.8Cr ₃ C ₂ -10Co	W1-L	174.18	8.71	258.58 ± 13	114.82 ± 2.54	0.754 ± 0.012
WC-0.8Cr ₃ C ₂ -10Co	W1-S	178.77	8.94	274.60 ± 13	127.93 ± 2.76	0.476 ± 0.038

Figure 7.77 shows the comparison between VB_{Max} and cutting time during MQL finishing. The W1-L and W1-S inserts had the best performance with the lowest VB_{Max} of 174.18 $\mu\text{m}/\text{min}$ and 178.77 $\mu\text{m}/\text{min}$ (Table 7.11). The NbC based inserts (G1-L, G1-S, and R1-L) had similar VB_{Max} of 12.6, 11.92, and 11.92 $\mu\text{m}/\text{min}$ respectively. The NbC based inserts had higher VB_{Max} and FWR than the WC based inserts (Figures 7.76 and 7.77).

Figure 7.78 shows the relationship between FWR and HV_{30} . There was no general correlation between FWR and HV_{30} since the insert plots had no specific trend. The NbC based inserts had a negligible change in FWR irrespective of the increased HV_{30} . The WC based inserts also had a negligible difference in FWR with increased HV_{30} , although M1-L had higher FWR and HV_{30} than the W1-L and W1-S.



a) G1-L, FWR = 12.61 $\mu\text{m}/\text{min}$ b) G1-S, FWR = 11.92 $\mu\text{m}/\text{min}$ c) R1-L, FWR = 11.92 $\mu\text{m}/\text{min}$



d) M1-L, FWR = 10.08 $\mu\text{m}/\text{min}$ e) W1-L, FWR = 8.71 $\mu\text{m}/\text{min}$ f) W1-S, FWR = 8.94 $\mu\text{m}/\text{min}$

Figure 7.76. Maximum flank wear of a) G1-L, b) G1-S, c) R1-L, d) M1-L, e) W1-L, and f) W1-S inserts after MQL finishing at cutting speed of 800 m/min and 0.5 mm depth of cut

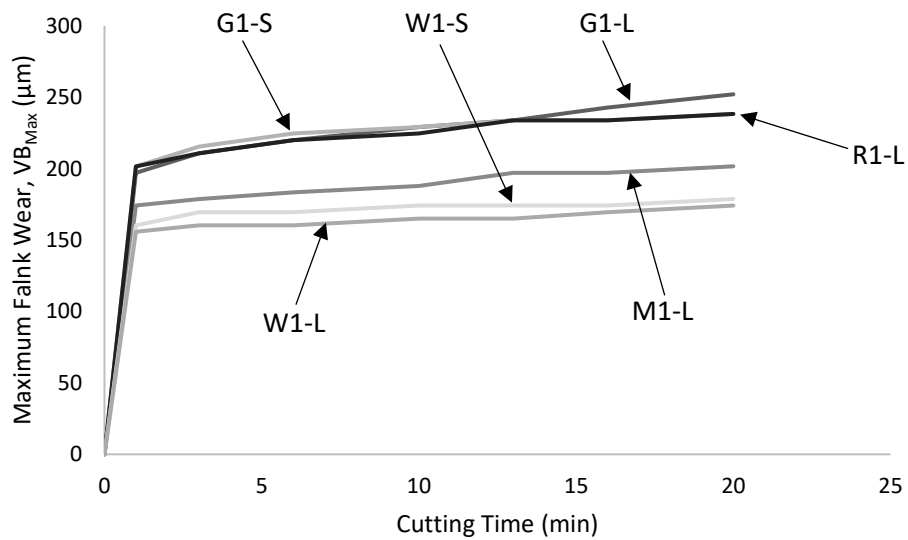


Figure 7.77. Graph of maximum flank wear (VB_{Max}) against cutting time during MQL finishing

Figure 7.79 shows the comparison between FWR and K_{IC} . Generally, the FWR decreased with increased K_{IC} . The tungsten carbide-based inserts had lower FWR and higher K_{IC} than the niobium carbide-based inserts. Both the NbC and WC based inserts had a negligible change in FWR with increased K_{IC} , although the M1-L insert had slightly higher FWR than the W1-L and W1-S inserts.

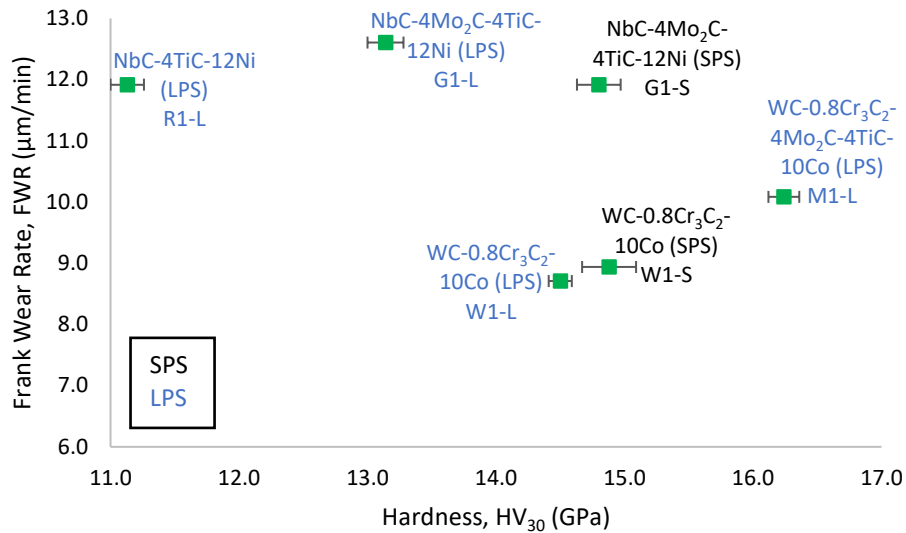


Figure 7.78. Graph of flank wear rate (FWR) against insert hardness (HV₃₀) during MQL finishing

Figure 7.80 shows the relationship between $F_{R,ave}$ and FWR. Generally, the $F_{R,ave}$ slightly increased with increased FWR. The WC based inserts had slightly lower $F_{R,ave}$ and FWR than the NbC based inserts. Although, the increase in $F_{R,ave}$ was within the same error margin.

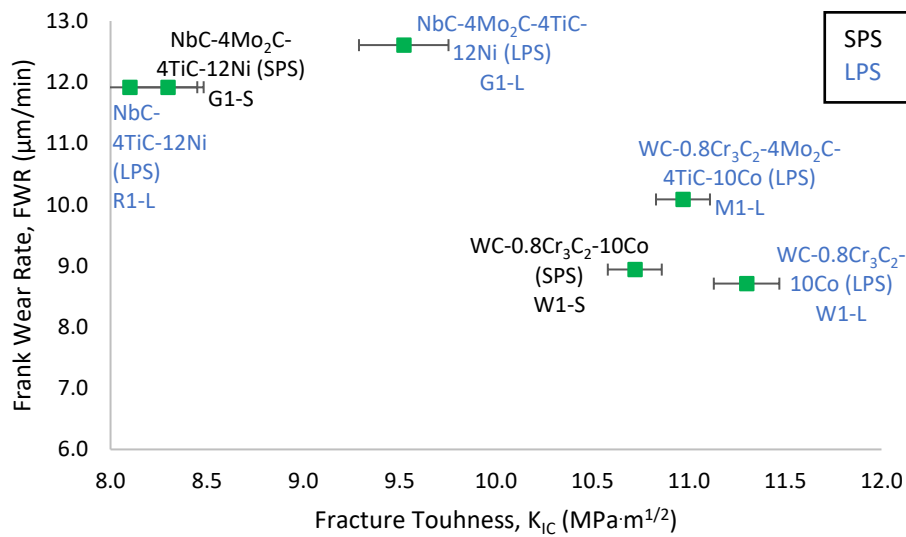


Figure 7.79. Graph of flank wear rate (FWR) against fracture toughness (K_{IC}) during MQL finishing

Figure 7.81 shows the relationship between T_a and FWR during MQL finishing. Generally, T_a increased with increased FWR. The W1-L insert had the lowest T_a and FWR whereas the R1-L insert had the highest T_a and FWR. The W1-L insert had lower T_a and slightly lower FWR than the SPS produced W1-S whereas the G1-L insert had similar T_a and FWR to the SPS produced G1-S.

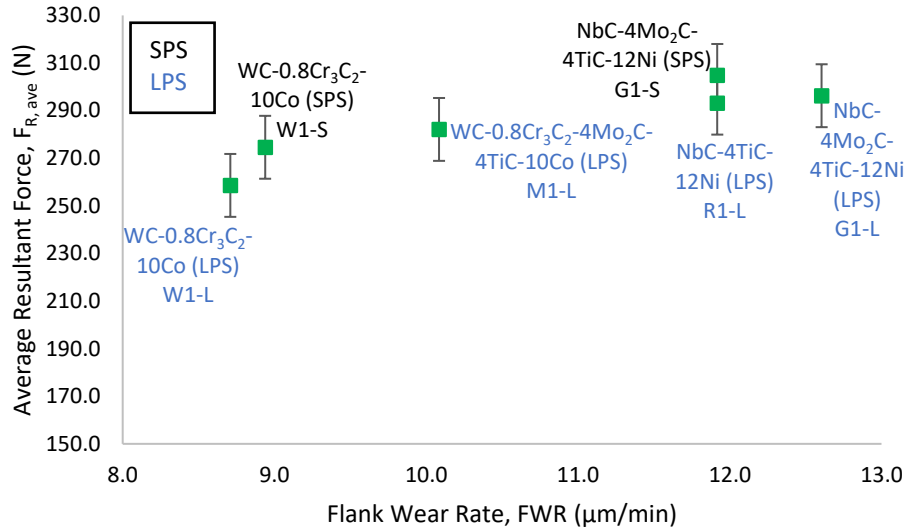


Figure 7.80. Graph of average resultant force ($F_{R, ave}$) against flank wear rate (FWR) during MQL finishing

Figure 7.82 shows the comparison between R_a and FWR. Generally, the FWR had a negligible effect on R_a , there was a negligible change in R_a with increased FWR. Spark plasma sintered inserts (W1-S and G1-S) had a better surface finish (lower R_a) compared to the LPS produced inserts. The W1-L insert gave a better surface finish at lower FWR than all other cutting inserts during MQL finishing.

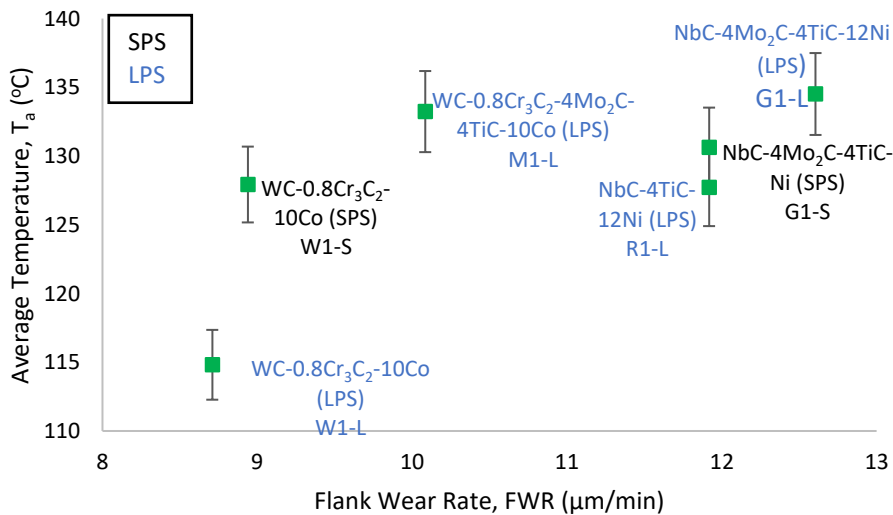


Figure 7.81. Graph of average temperature (T_a) against flank wear rate (FWR) during MQL finishing

Figure 7.83 shows the relationship between $F_{R, ave}$ and R_a . There was a negligible change in the $F_{R, ave}$ and R_a , all inserts had a slight change in R_a and similar $F_{R, ave}$ within the same error margin. There was no observed correlation between $F_{R, ave}$ and R_a . The SPS produced inserts (W1-S and G1-S) had lower R_a compared to the LPS produced inserts.

Figure 7.84 shows the relationship between T_a and R_a . There was no observable correlation between T_a and R_a . Inserts had similar T_a which was within the same error margin. There was no observed correlation between $F_{R,ave}$ and R_a . The W1-L insert had the lowest T_a and similar R_a to G1-L and R1-L, whereas the M1-L insert had the highest R_a . The SPS produced inserts (W1-S and G1-S) had lower R_a compared to the LPS produced inserts.

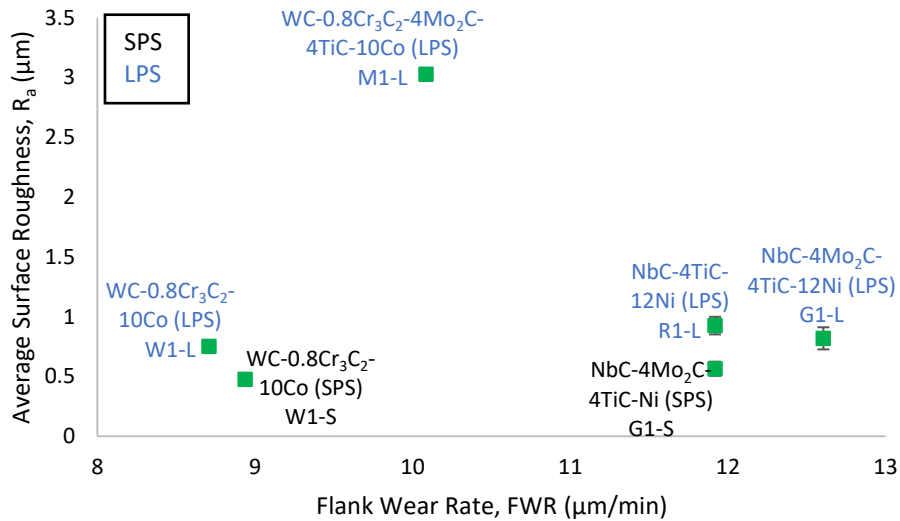


Figure 7.82. Graph of average surface roughness (R_a) against flank wear rate (FWR) during MQL finishing

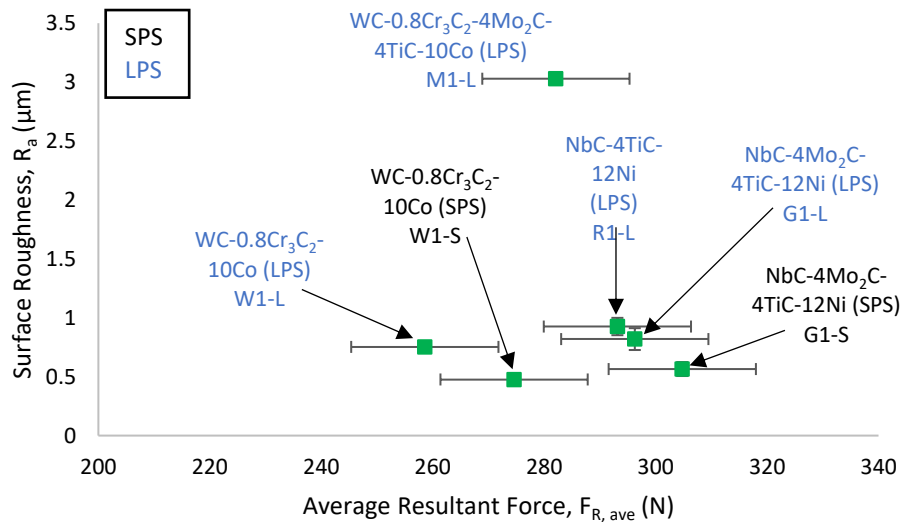


Figure 7.83. Graph of average surface roughness (R_a) against average resultant force ($F_{R,ave}$) for MQL finishing

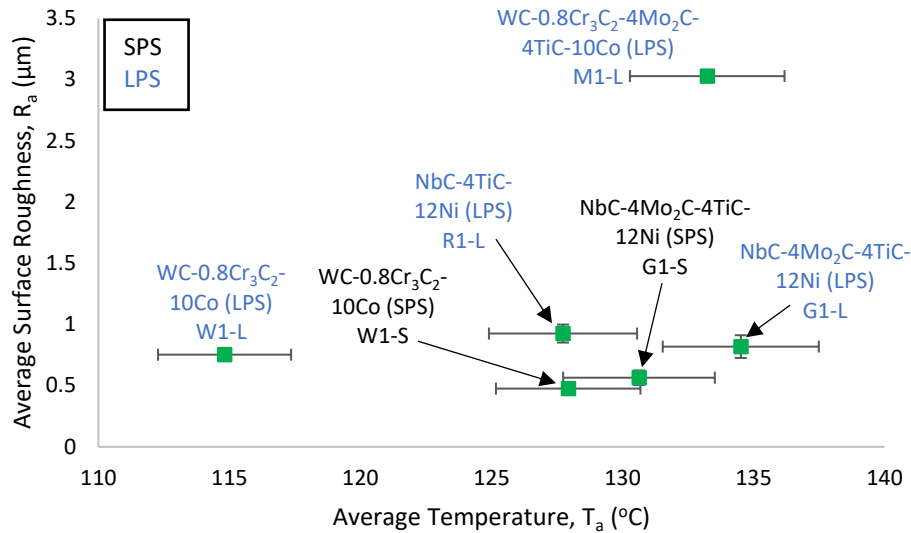


Figure 7.84. Graph of average surface roughness (R_a) against average temperature (T_a) during MQL finishing

Figure 7.85 shows the relationship between $F_{R, ave}$ and HV_{30} . There was a negligible change in $F_{R, ave}$ with increased HV_{30} . The NbC based inserts had $F_{R, ave}$ within the same error margin and the same was observed with WC based inserts. There was no clear trend observed in Figure 7.85, $F_{R, ave}$ were within the same error margin. However, the WC based inserts had lower $F_{R, ave}$ than the NbC based inserts.

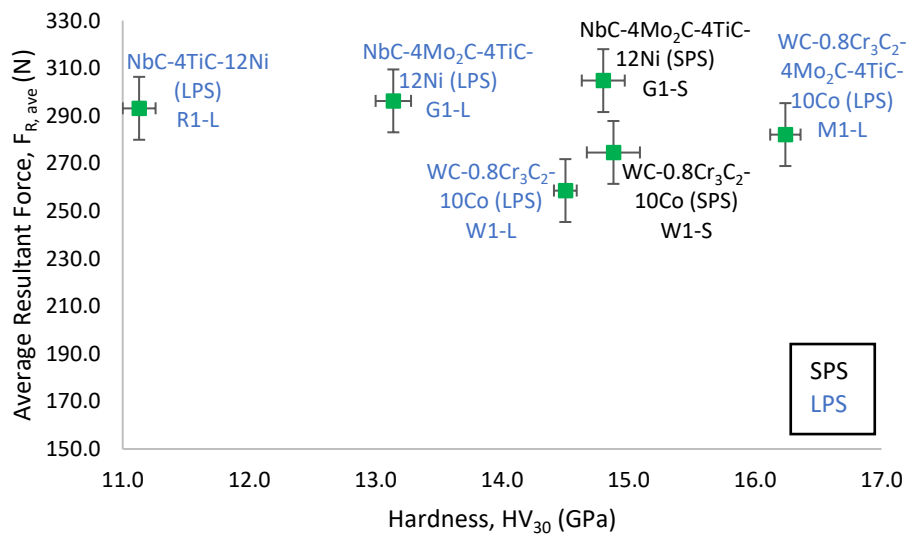


Figure 7.85. Graph of average resultant force ($F_{R, ave}$) against insert hardness (HV_{30}) during MQL finishing

Figure 7.86 shows the relationship between $F_{R, ave}$ and K_{IC} . Generally, the $F_{R, ave}$ slightly decreased with increased K_{IC} however, the decrease was within the $F_{R, ave}$ error margins hence no correlation was drawn

between $F_{R, ave}$ and K_{IC} . Tungsten carbide-based inserts generally had lower $F_{R, ave}$ and higher K_{IC} compared to NbC based inserts.

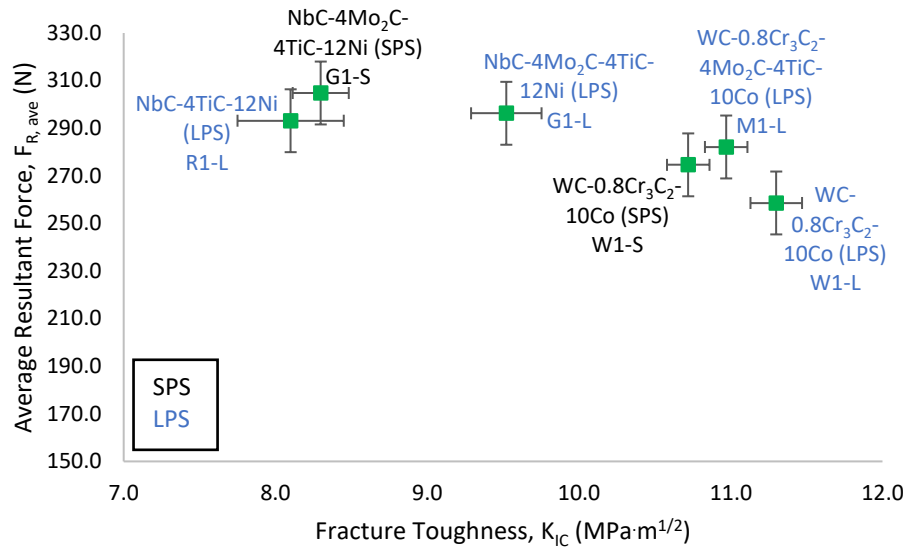


Figure 7.86. Graph of average resultant force ($F_{R, ave}$) against fracture toughness (K_{IC}) during MQL finishing

7.5.4 Dry versus Flood

This subsection analyses the effect of flood lubrication on AA7075 machining during finishing. Four inserts (W1-S, M1-L, G1-S, and G1-L) were selected as examples to show the correlation between dry and flood. Flank wear rates (FWR), average resultant forces ($F_{R, ave}$) and average surface roughness (R_a) were compared for different machining conditions. Figure 7.87 shows the relationship between $F_{R, ave}$ and FWR during finishing. Flood lubrication lowered FWR and increased $F_{R, ave}$ for WC based inserts, while NbC based inserts experienced higher flank wear rates at similar average resultant forces with flood lubrication.

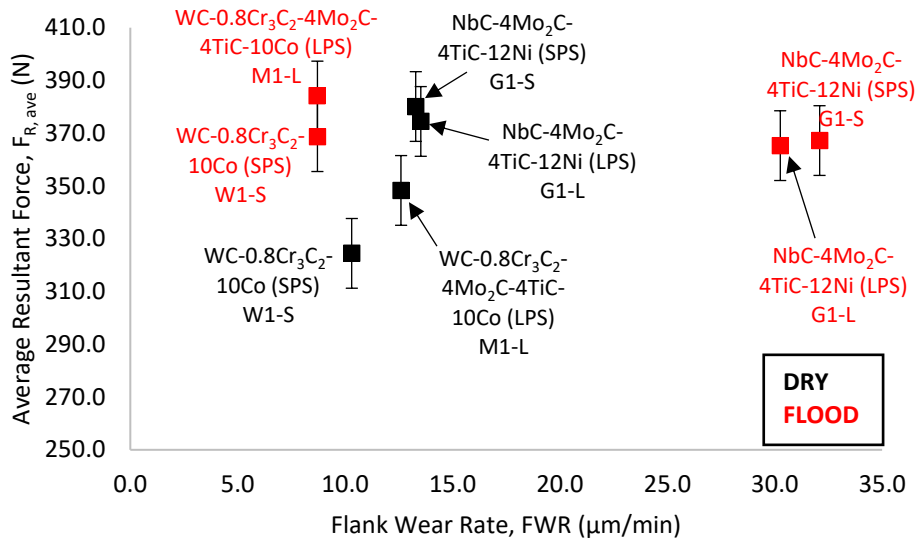


Figure 7.87. Graph of average resultant force ($F_{R,ave}$) against flank wear rate (FWR) during dry and flood finishing

Figure 7.88 shows the relationship between R_a and FWR during finishing. There was no general correlation between R_a and FWR during both dry and flood finishing. Flood finishing decreased FWR and increased R_a of WC based inserts whereas the NbC based insert R1-L had both R_a and FWR increased.

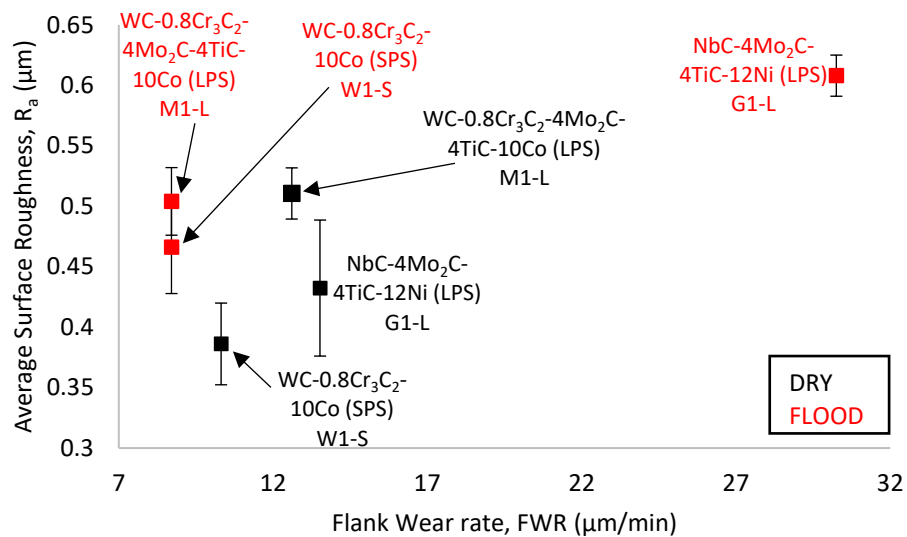


Figure 7.88. Graph of average surface roughness (R_a) against flank wear rate (FWR) during dry and flood finishing

7.5.5 Dry versus MQL

This subsection reports the comparison between MQL finishing and dry finishing. Three inserts (W1-S, G1-S, and G1-L) were selected for FWR vs $F_{R, ave}$, five inserts (W1-S, M1-L, G1-L, G1-S, and R1-L) selected for FWR vs T_a and three inserts (W1-S, G1-S, and R1-L) selected for FWR vs R_a as examples to show the correlation between dry and MQL. Flank wear rates (FWR), average resultant forces ($F_{R, ave}$), average temperature (T_a), and average surface roughness (R_a) were compared for different machining conditions.

Figure 7.89 shows the relationship between $F_{R, ave}$ and FWR during finishing. Both dry and MQL finishing showed an increase in $F_{R, ave}$ with increased FWR, however, MQL significantly lowered both flank wear rates and average resultant forces for all cutting inserts. Figure 7.90 shows the relationship between T_a and FWR during finishing. During dry finishing, inserts had a decreasing T_a with increased FWR whereas there was no correlation between T_a and FWR during MQL finishing. Flank wear rates and average temperatures of all LPS and SPS produced inserts were significantly lowered by MQL finishing.

Figure 7.91 shows the relationship between R_a and FWR during finishing. Minimum Quantity Lubrication generally lowered FWR and increased R_a .

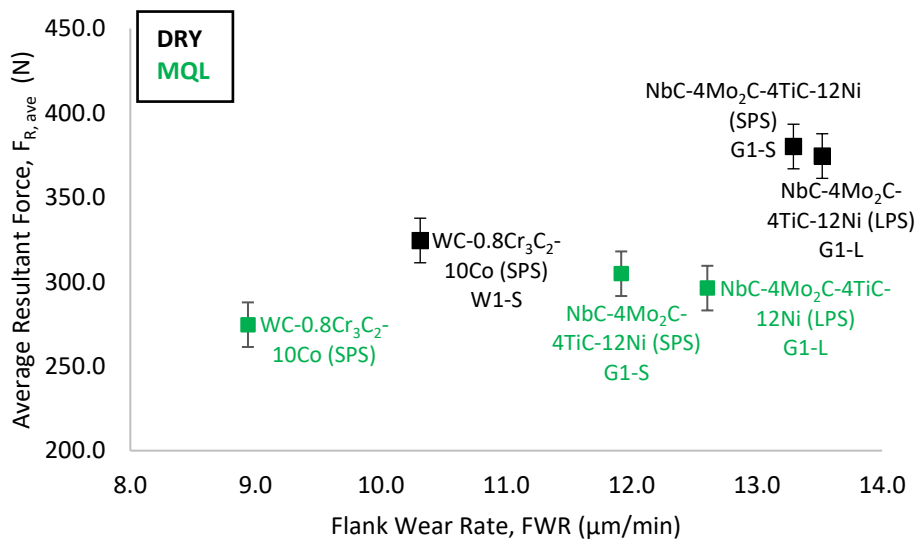


Figure 7.89. Graph of average resultant force ($F_{R, ave}$) against flank wear rate (FWR) during dry and MQL finishing

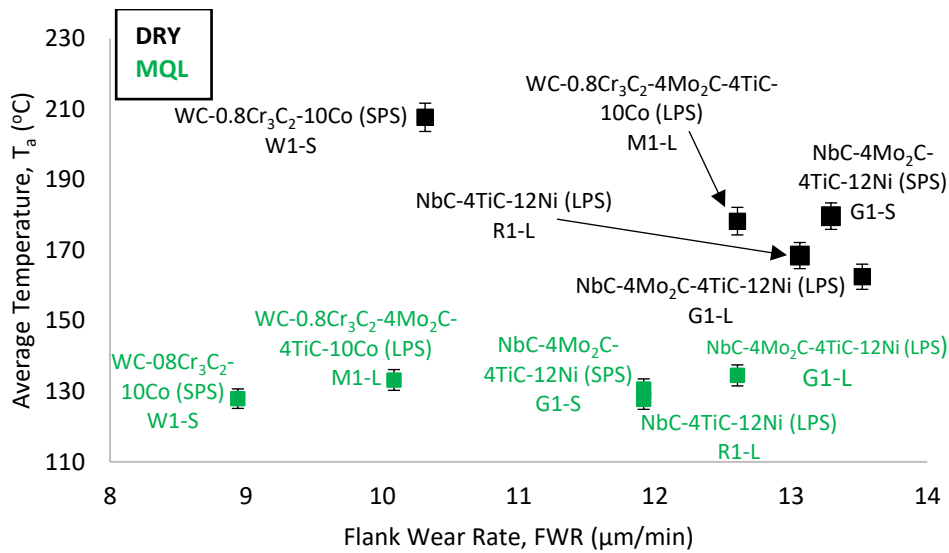


Figure 7.90. Graph of average temperature (T_a) against flank wear rate (FWR) during dry and MQL finishing

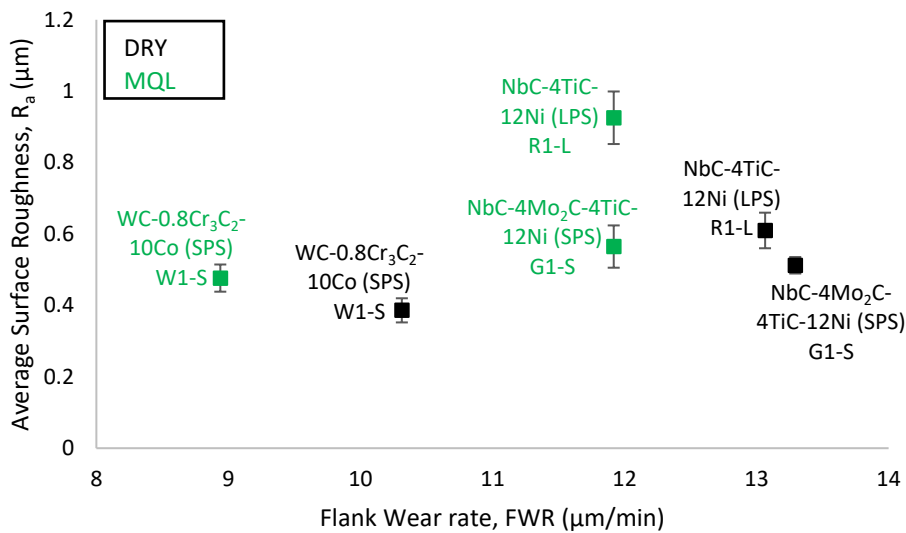


Figure 7.91. Graph of average surface roughness (R_a) against flank wear rate (FWR) during dry and MQL finishing

7.5.6 Flood versus MQL

This subsection reports the comparison between MQL finishing and MQL finishing. Five inserts (W1-L, W1-S, M1-L, G1-L, and G1-S) were selected as examples to show the FWR vs $F_{R,ave}$ and FWR vs R_a correlations between MQL and flood finishing. Flank wear rates (FWR), average resultant forces ($F_{R,ave}$), and average surface roughness (R_a) were compared for different machining conditions.

Figure 7.92 shows the relationship between FWR and $F_{R,ave}$ during finishing. Minimum Quantity Lubrication showed a slight increase in $F_{R,ave}$ with increased FWR whereas there was no correlation observed between the $F_{R,ave}$ and FWR during flood finishing. However, MQL slightly lowered $F_{R,ave}$ for all cutting inserts. The NbC based inserts experienced lower flank wear rates during MQL finishing compared to flood finishing whereas WC based inserts experienced similar flank wear rates to flood and slightly lower $F_{R,ave}$ during MQL lubrication. Figure 7.93 shows the relationship between FWR and R_a during finishing. Flood finishing had lower R_a than the MQL finishing. Although the W1-S had similar FWR and R_a during flood and MQL finishing. Minimum quantity lubrication significantly lowered FWR and increased R_a of NbC based insert G1-L.

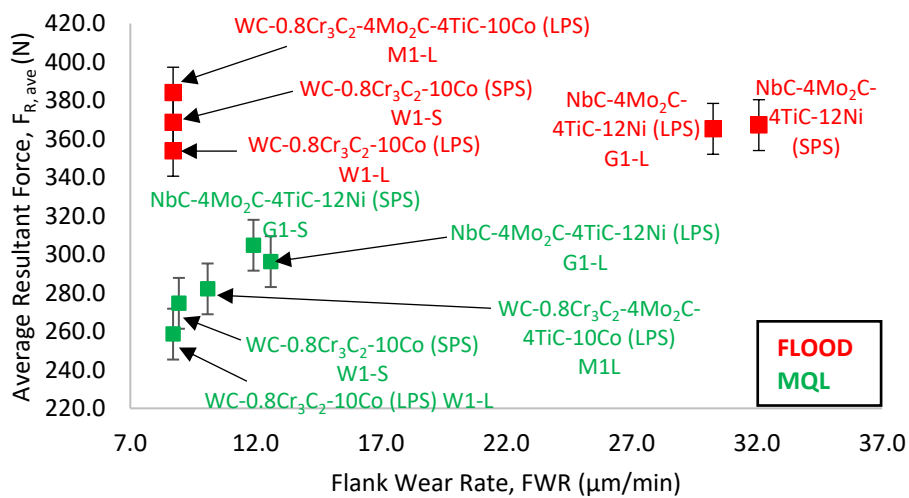


Figure 7.92. Graph of average resultant force ($F_{R,ave}$) against flank wear rate (FWR) during flood and MQL finishing

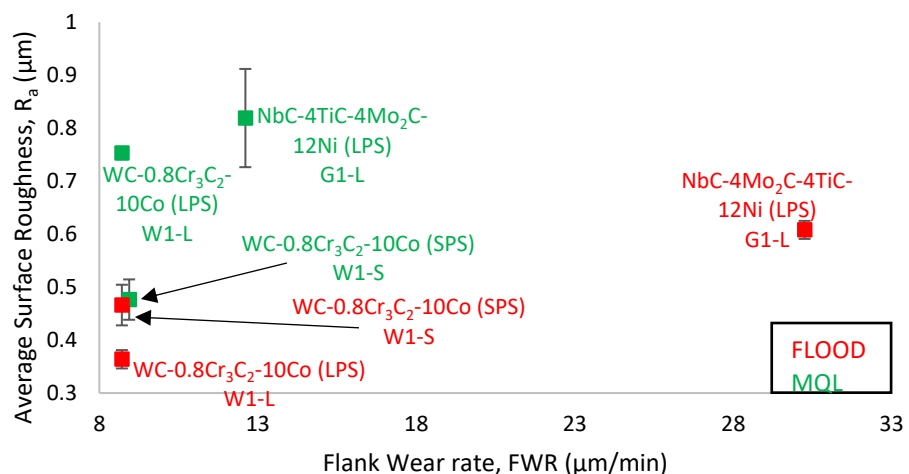


Figure 7.93. Graph of average surface roughness (R_a) against flank wear rate (FWR) during flood and MQL finishing

7.5.7 Overall Analysis of finishing

The W1-S inserts had the best performance with the lowest VB_{Max} during dry finishing (Figure 7.57). The WC based W1-L, W1-S, and M1-L inserts had similar and best performance with the lowest VB_{Max} during flood finishing (Figure 7.68) and the W1-L and W1-S inserts had the best performance during MQL finishing (Figure 7.77). The NbC based G1-L, G1-S, and R1-L inserts had the poorest performance with the highest VB_{Max} during dry, flood, and MQL finishing. The G1-L, G1-S, and R1-L inserts had mechanical fractures before 20 minutes cutting time during flood finishing. The WC based inserts had the best performance during all lubricating conditions compared to the NbC based inserts.

Generally, there was no correlation observed between FWR and HV_{30} during dry finishing although, the WC based inserts showed an increase in FWR with increased HV_{30} (Figure 7.58). There was no correlation between FWR and HV_{30} during flood and MQL finishing (Figures 7.69 and 7.78). There was a negligible change in FWR with increased HV_{30} , and the WC based inserts had higher HV_{30} and lower FWR. There was no correlation observed between FWR and K_{IC} during dry and flood finishing (Figures 7.59 and 7.70), and during MQL finishing, the FWR decreased with increased K_{IC} (Figure 7.79). The WC based inserts had higher K_{IC} and lower FWR than the NbC based inserts.

The $F_{R, ave}$ increased with increased FWR during dry finishing (Figure 7.60) and there was a negligible change in $F_{R, ave}$ with increased FWR during flood and MQL finishing (Figures 7.71 and 7.80). The WC based inserts had lower FWR and lower $F_{R, ave}$ compared to NbC based inserts. During dry finishing, the WC SPS insert (W1-S) had lower FWR and lower $F_{R, ave}$ compared to the WC based LPS inserts, whereas the NbC based SPS insert (G1-S) has similar $F_{R, ave}$ and FWR to the NbC based LPS insert (G1-L).

The T_a decreased with increased FWR during dry finishing (Figure 7.61) and T_a increased with increased FWR during MQL finishing (Figure 7.81). The SPS inserts (G1-S) had lower FWR and higher T_a than their similar LPS produced inserts (G1-L) during dry finishing. The WC SPS produced W1-S insert had lower T_a and slightly lower FWR than the SPS produced W1-S whereas the G1-L insert had similar T_a and FWR to the SPS produced G1-S. Generally, the WC based inserts had lower FWR and higher T_a than the NbC based inserts.

Generally, R_a increased with increased FWR during dry finishing (Figure 7.62) and there was negligible change in R_a with increased FWR during flood and MQL finishing (Figures 7.72 and 7.82). The NbC based inserts showed an indirect proportionality relationship between R_a and FWR during dry finishing, and the opposite was observed for WC based inserts. The NbC based R1-L had the highest R_a during dry, the G1-S insert had the highest R_a during flood, and the M1-L insert had the highest R_a during MQL finishing. During dry finishing, R_a increased with increased T_a (Figure 7.64), and there was no

correlation between R_a and $F_{R, ave}$ (Figure 7.63). During flood, there was no correlation between R_a and T_a or $F_{R, ave}$ (Figures 7.73 and 7.74). During MQL, there was no correlation between R_a and T_a or $F_{R, ave}$ (Figure 7.83 and 7.84).

There was negligible change in $F_{R, ave}$ irrespective of the increased HV_{30} during dry, flood, and MQL finishing (Figure 7.65, 7.74, and 7.85). The WC based inserts had slightly lower $F_{R, ave}$ and higher HV_{30} than the NbC based inserts during finishing. There was no correlation observed between $F_{R, ave}$ and K_{IC} during dry, flood, and MQL (Figures 7.66, 7.753, and 7.86). The WC based inserts had slightly lower $F_{R, ave}$ and higher K_{IC} than the NbC based inserts during finishing.

Flood finishing increased $F_{R, ave}$ and slightly reduced FWR of WC based inserts, and flood finishing reduced the $F_{R, ave}$ and significantly increased FWR of the NbC based inserts (Figure 7.87). Flood finishing increased surface roughness of all NbC based inserts compared to dry finishing (Figure 7.88). The MQL finishing lowered both $F_{R, ave}$ and FWR (Figure 7.89) and MQL finishing also significantly lowered T_a compared to dry finishing (Figure 7.90). However, MQL finishing slightly increased R_a irrespective of the lowered FWR (Figure 7.91). The WC based inserts had lower $F_{R, ave}$ similar FWR, and NbC based inserts had lower $F_{R, ave}$ and FWR during MQL finishing compared to flood finishing (Figure 7.92). However, MQL finishing had a higher R_a than the flood finishing (Figure 7.93).

7.6 Lubricant Analysis

Mass Spectrometry (MS) was used to conduct an analysis of flood and MQL chemical contents. The MS apparatus produces ions from the sample which are separated and quantified according to their different mass/charge ratios (Galen & Feiters, 2016). The resulted mass spectrum indicated the most possible chemical compounds common to the contents of the lubricants. Similarity counts are used to making a judgement as to which compounds are more likely to be present in the lubricants. Compounds with a similarity count greater or equal to 750 are more likely to be present in the sample. However, the suggested compounds are compared to the literature for proper judgement.

7.6.1 Flood Lubricants

Petroleum mineral oils are the main constituents of flood chemical lubricants and these mineral oils are often known as paraffin oils. The Castrol oils under Hysol classification was used as a base for the lubricant. The oils were mixed with water at a volume ratio 1:20. The Hysol EP lubricant is composed of C14-C17 chemicals chains including chlorinated paraffin and 2-butyloctan-1-ol which were noted as environmentally hazardous on the lubricant brand. The analysis using Mass Spectroscopy confirmed the presence of the 2-butyloctan-1-ol chemicals. The chemical mixture is also composed of 1-5 wt.% of triethanolamine which was confirmed by the Mass spectrum.

7.6.2 Minimum Quantity Lubricant

The analysis suggested the presence of palm oil in the MQL lubricant. The MS apparatus generated fatty acid ions which include capric acid, caprylic acid, oleic acid, linoleic acid, and linolenic acid. The fatty acids are the building blocks for palm oil which had similarity counts >750. The MS spectrum also suggested the presence of palmitic esters which were evidently present in the sample however, their similarity counts were <750 hence MQL lubricant used for the course of this research does not contain palmitic esters. The MQL lubricant was found to be purely composed of straight oils which improved the wettability and lubricity however in the absence of water MQL lubricants have a poor cooling effect in comparison to water-based flood lubricants. The application of MQL lubricant in Extreme Pressure (EP) also improved penetrability into the tool-workpiece interface and improved removal of microchips on the insert edge and workpiece surface (Marinescu et al., 2004). The removal of microchips lubricity reduces machining forces and mechanical wear resulting in improved tool life and better machined surface integrity.

Better extreme pressure effect is achieved by low lubricant viscosity as a result of the addition of EP additives (Tai et al., 2011) which are mostly organic compounds. Extreme pressure additives include compounds with phosphorus, sulfur or chlorine. The analysis of MQL lubricants indicates the presence of 2-undecanethiol-2-methyl, Disulfide, di-tert-dodecyl and sulfurous acid which have similarity counts 800, 777, and 854 respectively. However, the most probable additive present in the lubricant is sulfurous acid with the highest similarity count.

Chapter 8: Discussion

8.1 Mechanical Properties of WC and NbC based inserts

The produced samples were tested for their HV_{30} and K_{IC} . It was observed that the sintering techniques used for samples densification and carbide additives had effects on mechanical properties of the samples. The WC-Co system was found to be harder than the NbC-Ni system and this was because the WC has a high hardness within the range 24-28 GPa whereas NbC hardness is within 17-22 GPa (Huang et al., 2015). The WC-Co system had a higher K_{IC} than the NbC-Ni system due to good wettability and solubility of WC in Co binder resulting in a better homogeneous distribution of the Co binder. The HV_{30} and K_{IC} were reported and plotted in Figure 7.1.

8.1.1 Hardness

Spark Plasma Sintered (SPS) and Liquid Phase Sintered (LPS) WC-0.8Cr₃C₂-10Co (wt.%) samples had similar HV_{30} which were within the same HV_{30} error margin. The LPS and SPS techniques had similar effects on densification of the WC-0.8Cr₃C₂-10Co (wt.%) samples. However, the addition of 4 wt.% TiC and 4 wt.% Mo₂C to the LPS WC-0.8Cr₃C₂-10Co (wt.%) sample increased HV_{30} by 12% in the LPS WC-0.8Cr₃C₂-4Mo₂C-4TiC-10Co (wt.%) sample. Titanium carbide (TiC) was reported to be 5GPa harder than WC (Genga, 2014) hence the addition of TiC improved the HV_{30} in the WC-0.8Cr₃C₂-4Mo₂C-4TiC-10Co (wt.%) sample. The TiC was also reported to reduce grain growth during sintering however, poor solubility of TiC in Co binder due to poor wettability was also reported (Upadhyaya et al., 1998). Molybdenum Carbide (Mo₂C) improved the wettability and solubility of TiC in Co (German et al., 2009), facilitating the effect of grain growth inhibition by TiC hence the improved HV_{30} of the LPS WC-0.8Cr₃C₂-4Mo₂C-4TiC-10Co (wt.%) sample. The addition of Mo₂C is also reported to reduce WC grain growth, improving hardness (Genga, 2014).

The LPS NbC-4TiC-12Ni (wt%) sample had the lowest HV_{30} and the addition of 4 wt.% Mo₂C improved the HV_{30} in the LPS NbC-4Mo₂C-4TiC-12Ni (wt%) sample. The addition of Mo₂C improves the wettability and solubility of carbide in the binder phase, however, it is reported that Mo₂C also improves the distribution of the binder phase (Nickel) (Genga, 2014). Hence the LPS NbC-4Mo₂C-4TiC-12Ni (wt%) sample had a higher HV_{30} than the LPS NbC-4TiC-12Ni (wt%) sample. Furthermore, the SPS technique also improved HV_{30} in the SPS NbC-4TiC-12Ni (wt%) sample as a result of reduced grain growth. The low sintering temperatures and short holding time used during SPS reduced particle grain growth (German et al., 2009) hence improving HV_{30} of the SPS NbC-4Mo₂C-4TiC-12Ni (wt%) sample. This phenomenon can be explained further by the Hall-Petch relationship which state that strength in composite materials can be as high as the theoretical strength by reducing grain sizes (Dunstan et al., 2015).

8.1.2 Fracture Toughness

The SPS and LPS WC-0.8Cr₃C₂-10Co (wt.%) samples had a negligible difference of 0.58 MPa·m^{1/2} in K_{IC} hence the SPS and LPS had similar effects on K_{IC} of the WC-0.8Cr₃C₂-10Co (wt.%) sample. The addition of 4 wt.% TiC and 4 wt.% Mo₂C to the WC-0.8Cr₃C₂-10Co (wt.%) sample decreased the K_{IC} by 0.33 MPa·m^{1/2}. The negligible change was within the K_{IC} error margin, hence the sintering techniques and carbide additives had similar effects on K_{IC}. The unchanged K_{IC} is due to the good solubility of WC in Co and good distribution of the Co binder (Upadhyaya, 1998) such that the TiC and Mo₂C additives, sintering temperature, and holding time made no difference in K_{IC}.

The LPS produced NbC-4TiC-12Ni (wt%) sample had the lowest K_{IC} and the additions of 4 wt.% Mo₂C improved K_{IC} in the LPS NbC-4Mo₂C-4TiC-12Ni (wt%) sample. The Mo₂C improved wettability and solubility of TiC and NbC in the Ni binder phase, the addition of Mo₂C promoted and improved the homogeneous distribution of the Ni binder hence improving the K_{IC}. The SPS NbC-4Mo₂C-4TiC-12Ni (wt%) sample had lower K_{IC} than the LPS NbC-4Mo₂C-4TiC-12Ni (wt%) due to the inverse proportionality between grain growth dependant HV₃₀ and K_{IC}. The grain growth dependent HV₃₀ is reported to be inversely proportional to K_{IC} (Genga, 2014). The reduced grain growth during SPS improved HV₃₀ and lowered K_{IC} in SPS NbC-4Mo₂C-4TiC-12Ni (wt%) sample as a result of low sintering temperature and shorter dwell time (German et al., 2009). The SPS NbC-4Mo₂C-4TiC-12Ni (wt%) sample had high HV₃₀ hence the lower K_{IC} compared to the LPS NbC-4Mo₂C-4TiC-12Ni (wt%) sample.

8.2 Flank Wear Rate

The low flank wear rates in the MQL trials were due to better lubrication, which reduced friction and lowered cutting forces at the tool-workpiece interface (Boubekri & Shaikh, 2014; Genga et al., 2016). Generally, it was observed that flank wear rates (FWR) increased from roughing to semi-finishing due to increase in cutting forces as a result of increased collision impact per second (increased cutting speed) (Genga, 2014). The FWR were lowered from semi-finishing to finishing criteria because of the lowered cutting forces due to the workpiece softening effect as a result of increased cutting temperatures.

8.3 Roughing

Roughing was conducted under dry, flood, and MQL conditions. For each machining trial, flank wear rates (FWR), average resultant forces (F_{R, ave}), and average temperature (T_a) were calculated as responses to machining parameters and graphs were plotted from the results in Figures 7.2 – 7.28.

8.3.1 Tool Wear

Graphs of maximum flank wear (VB_{Max}) against cutting time were shown in Figures 7.3 (Dry), 7.11 (Flood), and 7.15 (MQL). All cutting inserts achieved the 20 minutes cutting time. The cutting inserts had $VB_{Max} < 300\mu m$ during dry and flood roughing apart from the R1-L insert that had $VB_{Max} > 300\mu m$. The R1-L insert had a tool life of 16 minutes during flood roughing due to poor lubrication by the water diluted flood lubricant (Kim & Kim, 2015). Under MQL roughing, all cutting inserts had $VB_{Max} < 250\mu m$. Flood roughing generally had higher VB_{Max} than dry and MQL roughing due to poor lubricating effect of water in the flood lubricant. The NbC based G1-S had similar tool life to the WC based inserts due to the similar high hardness.

The W1-S insert had the best performance with the lowest VB_{Max} after 20 mins cutting time during dry roughing (Figure 7.3). However, the NbC based G1-S insert had similar performance to the WC based W1-S due to similar HV_{30} and comparable K_{IC} (Figures 7.4 and 7.5). The W1-L insert had the best performance with the lowest VB_{Max} after 20 mins cutting time during flood and MQL roughing (Figure 7.11(flood), and 7.18(MQL)). The W1-S and W1-L inserts performed better than the NbC based inserts due to their better combination of higher HV_{30} and K_{IC} (Sedla et al., 2019). The R1-L insert had the poorest performance with the highest VB_{Max} during roughing during dry, flood, and MQL roughing to low HV_{30} . Insert resistance to wear is dependent on insert hardness. Inserts with low hardness have low wear resistance (Genga, 2014) and R1-L inserts had low HV_{30} hence lowering tool life. The high wear was due to high machining temperatures and forces that initiated chip weld giving rise to adhesive wear during dry roughing and the high cutting forces during MQL and flood roughing resulted in abrasive wear. The R1-L had a mechanical fracture failure during flood roughing as a result of high cutting forces shown in Figure 7.14 and low K_{IC} . Generally, NbC based inserts had higher VB_{Max} than WC based inserts under all lubricating conditions, which was a result of NbC based inserts having poorer combinations of HV_{30} and K_{IC} than the WC based inserts.

8.3.2 Average Resultant Force

During roughing, the average resultant forces ($F_{R, ave}$) generally increased with increased flank wear rate (FWR) under dry, flood, and MQL conditions (Figures 7.6, 7.14, and 7.21), although WC based inserts had an indirect relationship under MQL conditions as shown in Figure 7.21. The decrease in $F_{R, ave}$ with increased FWR was due to increased average temperatures (T_a) as shown in Figure 7.22 since increased temperatures facilitate workpiece surface softening, lowering cutting forces (Wstawska & Slimak, 2016). Tungsten carbide-based inserts show lower $F_{R, ave}$ than NbC based inserts under all machining conditions due to a better combination of high HV_{30} and K_{IC} in WC-Co inserts (Sedla et al., 2019). The high HV_{30} and K_{IC} resulted in lower FWR and less worn edge, lowering $F_{R, ave}$ (Genga, 2014).

Spark plasma sintered inserts (W1-S and G1-S inserts) had lower $F_{R, ave}$ compared to LPS inserts during dry and MQL roughing in Figures 7.6 and 7.21 respectively. This was because the SPS sintered inserts had lower FWR attributed to high HV_{30} (Mezlini, 2002). The low FWR implied slow wearing of the insert lowering friction forces in the tool-workpiece interface (Hutchings et al., 2006). Under MQL conditions in Figure 7.21, SPS inserts showed a direct relationship between $F_{R, ave}$ and FWR due to increased friction with increased FWR as a result of blunting cutting edge (Genga et al., 2016). However, LPS inserts showed an indirect relationship between $F_{R, ave}$ and FWR due to the increased T_a , decreasing $F_{R, ave}$ (Xu et al., 2018) from the induced workpiece surface softening. The higher blunting in the SPS inserts compared to LPS was attributed to the lower K_{IC} .

The $F_{R, ave}$ decreased with increased HV_{30} during flood roughing (Figure 7.15) due to lowered FWR as a result of increased HV_{30} (Figure 7.12) resulting in a less blunt cutting edge and lowered $F_{R, ave}$. There was no general correlation between $F_{R, ave}$ and HV_{30} during dry and MQL (Figures 7.8 and 7.23). The R1-L insert had the highest $F_{R, ave}$ during dry and flood due to high FWR as a result of low HV_{30} (Figures 7.4 and 7.12). There was no correlation observed between HV_{30} and K_{IC} (Figures 7.9, 7.16, and 7.24).

High cutting forces during roughing was partly caused by the depth of cut and high shearing area from low cutting speed (Wstawska & Slimak, 2016). However, the main cause of high machining forces was the temperature rises that induced chip welding on cutting edges. Figures 7.25 and 7.28 show that flood lubrication significantly lowered $F_{R, ave}$ due to a lubricant layer formed at the tool-workpiece interface (Kaynak et al., 2021). High machining forces cause high temperature rises which then induce thermal softening of the workpiece surface resulting in lower $F_{R, ave}$ (Ahmed et al., 2013). The $F_{R, ave}$ were lower and FWR were higher during flood roughing than during dry roughing due to sliding wear that occurs between two smooth surfaces under load, where insert edge damage does not occur by grooving resulting in low $F_{R, ave}$ (Gahr, 1987). The MQL conditions gave higher $F_{R, ave}$ compared to dry and flood conditions in Figure 7.24 due to cooling of the workpiece which reduced thermally softening hence requiring high cutting forces (Wstawska & Slimak, 2016).

8.3.3 Average Temperature

Generally during roughing, the T_a increased with increased FWR under both dry and MQL roughing as seen in Figures 7.7 and 7.22. The T_a increased with increased FWR due to increased friction which was a result of the blunt edge (Genga et al., 2016).

Spark plasma sintered inserts had increased T_a with increased FWR during MQL roughing whereas, under dry conditions T_a and FWR showed an inverse relationship. The inverse relationship was because the G1-S insert had higher FWR and lower T_a than the W1-S insert. The higher FWR was due to G1-S insert having low K_{IC} (Sedla et al., 2019).

Tungsten carbide-based inserts experienced lower FWR and lower T_a than the NbC based inserts. The lower FWR was due to the WC based inserts having a better combination of high HV_{30} and K_{IC} increasing inserts' wear resistance. The WC inserts had lower T_a due to lower FWR lowering friction during cutting and lowering the T_a (Gahr, 1987). The MQL condition generally lowered cutting T_a due to the cooling effect as the lubricant evaporated on application (Wang & Clarens, 2013).

8.4 Semi-Finishing

Semi-finishing was conducted under dry, flood, and MQL conditions. For each machining condition, flank wear rates (FWR), average resultant forces ($F_{R, ave}$), and average temperature (T_a) were calculated as responses to machining parameters and graphs were plotted from the results (Figures 7.29 – 7.55).

8.4.1 Tool Wear

During semi-finishing, graphs of maximum flank wear (VB_{Max}) against cutting time were plotted as shown in Figures 7.30, 7.38, and 7.45. All cutting inserts achieved 20 minutes cutting time apart from the NbC based R1-L insert which achieved 6 minutes tool life under flood conditions. The inserts had $VB_{Max} < 320\mu m$ under dry conditions and $VB_{Max} < 200\mu m$ under flood conditions, although the R1-L insert had $VB_{Max} 252.11\mu m$ at 6 minutes cutting time due to mechanical fracture failure. The fracture failure experienced by R1-L was due to poor insert HV_{30} and K_{IC} as shown in Figures 7.39 and 7.40. Under MQL conditions, all cutting inserts had $VB_{Max} < 250\mu m$. Flood semi-finishing generally had higher VB_{max} than dry and MQL semi-finishing due to the poor lubrication as a result of the water dilution (Cantley, 2008). The NbC based G1-S insert had a similar life trend to WC based inserts due to the similar high HV_{30} .

The SPS produced W1-S insert had the best overall life trend with the lowest VB_{Max} during dry and MQL semi-finishing due to higher HV_{30} than the LPS inserts. However, the LPS produced W1-L and M1-L inserts had better tool life during flood semi-finishing. The LPS inserts performed better during flood semi-finishing and this was attributed to their higher K_{IC} . Niobium carbide-based inserts generally had higher VB_{Max} compared to WC based inserts under all machining conditions; because of NbC based inserts having poor combination of HV_{30} and K_{IC} , although the G1-S insert had similar tool life to the W1-L insert under MQL conditions (Figure 7.45).

8.4.2 Average Resultant Force

Generally, $F_{R, ave}$ slightly increased with increased FWR during semi-finishing under all machining conditions (Figures 7.33, 7.41, and 7.48) due to increased friction as a result of a quickly deformed edge at high FWR (Genga et al., 2016). However, the change in $F_{R, ave}$ was within the same error margin hence no correlation between $F_{R, ave}$ and FWR could be drawn during semi-finishing. There was also no

observable correlation between $F_{R,ave}$ and HV_{30} or K_{IC} during semi-finishing. Tungsten carbide-based inserts had slightly lower $F_{R,ave}$ compared to NbC based inserts under all machining conditions. The WC based inserts had relatively lower FWR and a better combination of HV_{30} and K_{IC} (Genga, 2014; Sedla et al., 2019).

Figures 7.52, 7.53, and 7.55 show the effects of flood and MQL lubrication on $F_{R,ave}$ during for semi-finishing. Flood semi-finishing had the highest $F_{R,ave}$ and this was due to the dilution of the chemical lubricant with water at a ratio of 1:20 that reduced the lubricity effects (Cantley, 2008). The oils in flood chemical lubricants are good lubricants, however, water is not a good lubricant, but instead a good cooling agent. Having water in large quantity reduces the lubricant viscosity. The water-diluted lubricant forms a layer on the surface of the workpiece that is 1/100 - 1/1000 times the thickness of the conventional oils hence the increased cutting forces (Kim & Kim, 2015). The MQL on the other hand was applied in low quantities and since it consists of pure oils, the lubricating effect was not affected. Hence Figure 7.53 showed that MQL significantly lowered FWR due to a better lubricating effect at the tool-workpiece interface (Kim & Kim, 2015). The comparison between flood and MQL (Figure 7.55) showed that MQL semi-finishing had lower FWR and $F_{R,ave}$ due to better lubrication, although the WC based M1-L insert FWR increased under MQL. The MQL lubricant was applied in mists form via a nozzle and compressed air at high speed, the high kinetic energy enabled greater penetrative capability into the tool-workpiece interface (Rabiei et al., 2015).

8.4.3 Average Temperature.

During semi-finishing, T_a generally increased with increased FWR under both dry and MQL conditions (Figures 7.34 and 7.49). The increased T_a with increased FWR was due to increased friction as the cutting edge worn out quickly (Genga et al., 2016). However, WC based inserts showed an indirect relationship between T_a and FWR in relation to W1-L and W1-S of similar composition during MQL semi-finishing. The FWR decreased with increased insert HV_{30} as shown in Figure 7.46, the decrease in FWR resulted in reduced frictional force (Hutchings et al., 2006) hence temperature rises were minimised.

The SPS and LPS inserts both had increased T_a with increased FWR under both dry and MQL conditions (Figure 7.34 and 7.49). The WC based W1-S insert had the lowest FWR and T_a under dry conditions, whereas the NbC based G1-S insert had the highest T_a . The high T_a of the G1-S insert was due to high FWR as a result of low K_{IC} (Wayne, 2016). Spark plasma sintered inserts had lower FWR than the LPS inserts under MQL conditions due to higher HV_{30} and wear resistance. The SPS inserts also had lower T_a than LPS inserts, this was due to lower flank wear (less blunting) minimizing friction and temperature rises during machining (Gahr, 1987).

Tungsten carbide-based inserts experienced lower FWR and T_a compared to the NbC based inserts, the low T_a of WC based inserts was due to the low FWR that slightly reduced frictional force (Figure 7.33) resulting in low temperature rises. Figure 7.54 shows the effect of MQL on FWR and T_a . Minimum quantity lubrication significantly lowered both FWR and T_a due to the lubricant layer formed on the workpiece surface and the cooling effect as a result of lubricant evaporation on application (Wang & Clarens, 2013). The W1-S insert was the best performer with lowest FWR, $F_{R, ave}$, and T_a during semi-finishing because of a better combination of HV_{30} and K_{IC} (Sedla et al., 2019).

8.5 Finishing

Finishing was conducted under dry, flood, and MQL conditions. For each machining condition, flank wear rates (FWR), average resultant forces ($F_{R, ave}$), average temperature (T_a), and average surface roughness (R_a) were calculated as responses to machining parameters. Graphs were plotted from results under the results section (Figures 7.53 – 7.93).

8.5.1 Tool Wear

During finishing, graphs of maximum flank wear (VB_{Max}) against cutting time were plotted as shown in Figures 7.57, 7.68, and 7.77. All WC cutting inserts reached 20 minutes of cutting time under flood conditions with the exception of the NbC based G1-L, G1-S, and R1-L inserts with tool life of 10 minutes, 10 minutes, and 3 minutes respectively. The short tool life is attributed to poor combination of HV_{30} and K_{IC} . All cutting inserts had $VB_{Max} < 270\mu m$ under dry conditions. During flood finishing, the WC based inserts had $VB_{Max} < 175\mu m$ and the NbC based inserts had $VB_{Max} > 300\mu m$. All NbC based inserts failed before 20 minutes during flood finishing due to low fracture toughness (Wayne, 2016); the observed failures and high FWR were partly due to the poor lubricating effect that comes with a water-diluted flood lubricant (Kim & Kim, 2015). The R1-L insert had fractured prematurely with VB_{Max} of approximately $500\mu m$ after 3 minutes cutting time and this was due to R1-L having the lowest K_{IC} . The MQL lubrication significantly reduced flank wear compared to dry and flood finishing, all cutting inserts had $VB_{Max} < 250\mu m$.

Spark plasma sintered W1-S insert had the best tool life with the lowest VB_{Max} during dry finishing, whereas the LPS W1-L insert had better tool life under flood and MQL conditions. The W1-S insert was best during dry finishing due to better combination of HV_{30} and K_{IC} (Sedla et al., 2019). During flood and MQL conditions, the W1-L insert had better tool life because of its slightly higher K_{IC} than the W1-S insert resulting in better impact resistance (Genga, 2014). Niobium carbide-based inserts had the highest VB_{Max} during dry and MQL conditions, whereas under flood conditions, R1-L insert had the highest VB_{Max} followed by G1-L and G1-S. Niobium carbide-based inserts generally had higher VB_{Max} than the WC based inserts under all machining conditions due to a poor combination of HV_{30} and K_{IC} (Wayne, 2016). Although G1-S insert had similar HV_{30} to W1-L and W1-S inserts, the low fracture

toughness property made the G1-S insert more susceptible to mechanical wear and crack propagation (Genga, 2014).

8.5.2 Average Resultant Force

The $F_{R,ave}$ slightly increased with increased FWR during dry and MQL finishing (Figures 7.60 and 7.80) due to increased frictional forces as a result of quickly wearing of the cutting edge (Hutchings et al., 2006). The NbC based G1-L insert had higher FWR and lower $F_{R,ave}$ than the G1-S insert during dry and MQL finishing. This was due to the G1-L insert having higher T_a that resulted in workpiece softening and reduced $F_{R,ave}$ (Wstawska & Slimak, 2016). Tungsten carbide-based inserts had lower $F_{R,ave}$ compared to NbC based inserts under all machining conditions due to lower FWR as a result of better combinations of K_{IC} and HV_{30} (Sedla et al., 2019).

Under dry and MQL conditions (Figures 7.60 and 7.80), both LPS and SPS produced inserts showed increased $F_{R,ave}$ with increased FWR due to the increase in frictional force as the cutting edge worn quickly. However, under flood conditions, both LPS and SPS produced inserts had $F_{R,ave}$ within the same error margin irrespective of the increased FWR. Under flood and MQL conditions, LPS inserts had lower $F_{R,ave}$ than SPS inserts, although G1-S has higher $F_{R,ave}$ than G1-L under MQL lubrication due to G1-S having high HV_{30} . The LPS inserts had lower $F_{R,ave}$ under flood and MQL conditions due to higher K_{IC} and high impact resistance (Genga, 2014).

There was a negligible change in $F_{R,ave}$ with increased HV_{30} or K_{IC} during dry, flood, and MQL finishing (Figure 7.65, 7.74, and 7.85). This was the same during roughing and semi-finishing. This indicated that there was no co-dependency between mechanical properties and the cutting forces during AA7075 face-milling.

Figures 7.87, 7.89, and 7.92 showed the effects of flood and MQL on $F_{R,ave}$ during finishing. Under all lubrication, average resultant forces increase with increasing flank wear rates. Flood conditions slightly reduced FWR and increased $F_{R,ave}$ for WC based inserts (Figure 7.87); the increased $F_{R,ave}$ was due to the hardened workpiece surface as a result of the cooling effect (Wstawska & Slimak, 2016). The MQL on the other hand is applied in mists at low quantity but still significantly lowered both FWR and $F_{R,ave}$ due to a good lubricating layer formed between the tool-workpiece interface (Kim & Kim, 2015). The comparison between flood and MQL (Figure 7.92) indicated that the MQL finishing had lower FWR and $F_{R,ave}$ and it was also due to better penetrability into the tool-workpiece interface as a result of the application at high velocity (Marinescu et al., 2004; Tai et al., 2011).

8.5.3 Average Temperature.

During finishing, T_a generally decreased with increased FWR under dry conditions (Figure 7.61) whereas T_a increased with increased FWR under MQL conditions (Figure 7.81). The decrease in T_a under dry conditions was in the order $W1-S > G1-S > M1-L > R1-L > G1-L$ and increased $F_{R, ave}$ was also in a similar order. This was an abnormal behavior between $F_{R, ave}$ and T_a (indirect relationship), T_a had a decreasing trend in Figure 7.61 whereas $F_{R, ave}$ had an increasing trend in Figure 7.60. The decrease in T_a under was due to the decreased HV_{30} in a similar order with similar FWR (Figure 7.58), decreasing HV_{30} decreased wear resistance and sliding wear hence the decreasing temperature in the tool-workpiece interface (Hutchings et al., 2006). The T_a increased with increased FWR during MQL finishing due to increased frictional forces as a result of blunt cutting edge (Genga et al., 2016; Hutchings et al., 2006). The WC based inserts had higher T_a during dry finishing than during MQL finishing. The high T_a during dry finishing was attributed to the absence of cooling lubricant at a high cutting speed (800m/min).

The SPS and LPS produced inserts both had increased T_a with increased FWR during MQL finishing. The SPS produced W1-S and G1-S inserts had lower FWR and higher T_a compared to their similar LPS produced inserts during dry finishing; this was due to high hardness and high wear resistance. The LPS produced W1-L and G1-L inserts had lower FWR and lower T_a compared to their similar SPS produced inserts during MQL finishing; this was due to high K_{IC} which lowered FWR, insert surface roughness and frictional force hence the low T_a (Hutchings et al., 2006).

Figure 7.91 showed the effect of MQL lubrication on FWR and T_a . Minimum quantity lubrication significantly lowered both FWR and T_a due to the lubricant layer formed on the workpiece surface and the cooling effect of lubricant evaporation during machining.

8.5.4 Average Surface Roughness

Graphs of FWR versus R_a during finishing were shown in Figures 7.62, 7.72, and 7.82 under dry, flood, and MQL machining conditions respectively. Generally, R_a increased with increased FWR during dry finishing (Figure 7.62). Flank wear is initiated by wearing out of tough sections of the insert cutting edge exposing hard particles. Detached hard particles result in abrasive wear between the insert and the workpiece resulting in increased FWR, $F_{R, ave}$, and poor surface finish (Palanikumar et al., 2008) which can be described as waviness and irregularities on the machined surface (Bhushan, 2001). There was no correlation observed between R_a and FWR during flood and MQL finishing (Figures 7.72 and 7.82), there was a negligible change in R_a with increased FWR due to similar $F_{R, ave}$ that were within the same error margin. The negligible change in R_a was also due to the cooling that reduced workpiece softening resulting in similar $F_{R, ave}$ and R_a .

Niobium carbide-based inserts showed decreasing R_a with increased FWR during dry roughing (Figure 7.62). The decreased R_a was mainly due to the decreased K_{IC} in the order R1-L<G1-S<G1-L which resulted in the decrease in $F_{R, ave}$ in the order R1-L<G1-S<G1-L, although, the SPS G1-S insert had slightly higher $F_{R, ave}$ than G1-L inserts (Figure 7.65) as a result of G1-S having relatively higher HV_{30} . The R1-L insert gave the highest R_a which was attributed to R1-L insert having the lowest K_{IC} .

Tungsten carbide-based inserts had lower R_a and lower FWR compared to NbC based inserts during finishing. Although WC based inserts had higher HV_{30} , their high K_{IC} was the main reason for the good surface finish. Tungsten carbide-based inserts also had lower $F_{R, ave}$ and lower T_a (Figures 7.63, 7.64, 7.73, 7.83, and 7.84) which were critical for acceptable surface integrity (Lekam, 2016). However, the WC based M1-L insert had the highest R_a under MQL conditions due to higher cutting T_a whereas, under flood conditions, G1-S had the highest R_a due to the mechanical fracture at the tip of the cutting edge (Figure 7.67b).

Spark plasma sintered inserts (G1-S and W1-S) had better surface finish than LPS produced inserts under dry and MQL conditions, and this was due to high T_a (Figures 7.57 and 7.75). The high temperature led to workpiece surface softening, lowering machining forces and flank wear rates hence resulting in lower surface roughness (Baskar, 2010).

Flood lubrication increased both R_a and FWR for NbC based inserts compared to dry (Figure 7.88) due to the increased $F_{R, ave}$ (Figure 7.87) from poor lubrication that comes with the water-diluted lubricant (Cantley, 2008). However, flood lubrication increased R_a and reduced FWR for WC based inserts with the exception of M1-L that had decreased R_a and FWR. The use of MQL reduced FWR and increased R_a for both WC and NbC based inserts. Both flood and MQL increased R_a due to the lowered machining T_a (Figure 7.90) preventing workpiece surface softening and although machining $F_{R, ave}$ and FWR were reduced (Wstawska & Slimak, 2016).

Chapter 9: Conclusion and recommendations

9.1 Conclusion

According to the study and comparisons done in this research, tungsten carbide-based inserts generally performed better than niobium carbide-based inserts. Two sintering techniques, spark plasma sintering and liquid phase sintering, were used to produce samples from which cutting inserts were manufactured. The SPS produced samples with higher HV_{30} than LPS samples. The SPS NbC composition NbC-4TiC-4Mo₂C-12Ni (wt.%) had high HV_{30} similar to WC samples. The LPS produced samples with slightly higher K_{IC} and slightly lower HV_{30} than the SPS produced samples.

The SPS inserts performed better under dry conditions due to their high HV_{30} which resulted in better resistance to wear, and increased tool life. The SPS NbC based NbC-4TiC-4Mo₂C-12Ni (wt.%) insert performed best amongst the NbC based inserts, having similar tool life to WC based inserts under dry machining conditions. The LPS inserts performed better under flood and MQL due to high K_{IC} . Flood conditions lowered the cutting forces and increased FWR during roughing however, during semi-finishing, and finishing, flood lubrication increased cutting forces and FWR. This was due to poor lubrication of the water-diluted flood chemical oils.

Minimum quantity lubrication lowered machining forces, temperatures and FWR compared to dry machining during roughing, semi-finishing, and finishing. The machining criteria were established by altering cutting speeds, roughing at 200m/min and 2mm depth of cut, semi-finishing at 400m/min and 1mm depth of cut, and finishing at 800m/min and 0.5mm depth of cut. Although MQL resulted in slightly higher surface roughness than during dry and flood machining, the measured surface roughness was between 0-0.9 μ m.

9.2 Recommendations

- The optimisation of MQL application and flow rates should be further investigated as this might result in better surface integrity.
- Further investigation should be conducted to increase the K_{IC} of the NbC-4Mo₂C-4TiC-12Ni sample produced by SPS as it had similar HV_{30} to WC-Co samples making it a possible alternative for WC-Co inserts.
- The carbide additives (Mo₂C and TiC) should be optimised for NbC based inserts to improve HV_{30} and K_{IC} for better machining performance
- Flood machining is not suitable for machining of AA7075 with the use of NbC based inserts due to high cutting forces and FWR as a result of mechanical wear which resulted in mechanical fractures and shortened tool life.
- Further investigation should be carried out in optimisation of flood lubricant dilution ratios for better lubrication and minimise chemical wear initiated by water.

References

- Abdalla, H. S., Baines, W., McIntyre, G., & Slade, C. (2007). Development of novel sustainable neat-oil metalworking fluids for stainless steel and titanium alloy machining - Part 1 - Formulation development. *Journal of Advanced Manufacturing Technology*, 34, 21–33.
- Aerospace. (2016). History of Aluminium in the Aerospace Industry. *Aluminium, Metal Supermarkets*.
- Ahmed, A. D., Hassan, M. A., Shukor, M. H. A., & Pa, N. M. (2013). *Investigate the Lubrication Effects on Cutting Force and Power Consumption in Up and Down End Milling*.
- Ali, H. M., Iqbal, A., & Li, L. (2013). A comparative study on the use of drilling and milling processes in hole making of GFRP composite. *Sadhana*, 38(4), 743–760.
- Altas, E., & Caliskan, H. (2016). THE EFFECT OF CUTTING CONDITIONS ON CUTTING FORCES IN MILLING OF TI6AL4V ALLOY. *Article*.
- Balaji, A. K., Sreeram, G., Jawahir, I. S., & Lenz, E. (1999). The Effects of Cutting Tool Thermal Conductivity on Tool-Chip Contact Length and Cyclic Chip Formation in Machining with Grooved Tools. *CIRP Annals*, 48(1), 33–38.
- Barczak, L. M., & Batako, A. D. (2012). Application of minimum quantity lubrication in grinding. *Materials and Manufacturing Processes*, 27(4), 406–411. <https://doi.org/10.1080/10426914.2011.577866>
- Basil, A. (2015). A Study of the Effect of (Cutting Speed, Feed Rate and depth of cut) on Surface Roughness in the Milling Machining EFFECT OF CURRENT AND ELECTRODE MATERIAL ON MATERIAL REMOVAL RATE (MRR) AND SURFACE ROUGHNESS (RA) IN EDM PROCESS View project Studying The. *Eng. &Tech.Journal*, Vol.33(8), 1785–1797. <https://www.researchgate.net/publication/314229791>
- Baskar, N. (2010). *Particle swarm optimization technique for determining optimal machining parameters of different workpiece materials in turning operations*.
- Bernstein, L., Bosch, P., Canziani, O., Chen, Z., Christ, R., & Davidson, O. (2007). Climate change 2007: synthesis report. An assessment of the Intergovernmental Panel on Climate Change. *Retrieved March, 20, 2011*.
- Bhushan, B. (2001). *2.1 The Nature of Surfaces*.
- Bockstiegel, G. (1956). On the Rate of Sintering. *J. Metals*, 8, 580–585.
- Boothryd, G., & Knight, W. A. (2006). *Fundamentals of Machining and Machine Tools*, 3rd ed., Taylor & Francis Group, Florida, USA, 2006. *Taylor & Francis Group, Florida, USA, 3*.

- Boswell, B., & Voges, E. (2011). The Effect of Combined Cold Air and Minimum Liquid Cooling on End Milling. *Mechanical, Industrial, and Manufacturing Engineering--Proceedings of 2011 International Conference on Mechanical, Industrial, and Manufacturing Engineering*.
- Boubekri, N., & Shaikh, V. (2014). Minimum Quantity Lubrication (MQL) in Machining: Benefits and Drawbacks. *Journal of Industrial and Intelligent Information*, 3(3), 205–209. <https://doi.org/10.12720/jiii.3.3.205-209>
- Cabrera, N. (1950). Sintering of Metal Particles. *J. Metals*, 188 Trans, 667.
- Caldeirani, J. F., & Diniz, A. E. (2002). Influence of Cutting Conditions on Tool Life, Tool Wear and Surface Finish in the Face Milling Process. *J. Braz. Soc. Mech. Sci*, 24(1).
- Cantley, R. E. (2008). The effect of Water in Lubricating Oil on Bearing Fatigue Life. *ASLE Transactions*, 20(3), 244–248.
- Carbide Properties inc. Cobalt as a Carbide binder. (2021). *Carbide Processors*.
- Carter, S. (2013). High Speed Machining – High Speed Cutting. *Trade Magazine, Manufacturing Engineering and Tooling Production*.
- Childs, T., Maekawa, K., Obikawa, T., & Yamane, Y. (2000). Metal Machining – Theory and Applications. *Arnold*. isbn: 0-340-69159-X.
- Coppus. (n.d.). Unique, portable dust collection systems also employee coolers for hot areas, unique products. *Millbury, MA*, 508, 756–8391.
- Da Silva, B. R., Machado, R. A., Ezugwu, O. E., Bonney, F. J., & Sales, W. (2013). Tool life and wear mechanisms in high speed machining of Ti–6Al–4V alloy with PCD tools under various coolant pressures. *Journal of Materials Processing Technology*, 213(8), 1459–1464.
- Dadic, Z. (2013). Tribological principles and measures to reduce cutting tools wear. *International Conference “Mechanical Technologies and Structural Materials”Split*.
- Dadić, Z. (2013). Tribological principles and measures to reduce cutting tools wear. *International Conference “Mechanical Technologies and Structural Materials”Split, September*.
- Dahmus, J. B., & Gutowski, T. G. (2004). An environmental analysis of machining. *In ASME 2004 International Mechanical Engineering Congress and Exposition*, 643–652.
- Dewes, S. R., Chua, S. K., Newton, G. P., & Aspinwall, K. D. (1999). *Temperature Measurement when High Speed Machining Hardened Mould/die Steel*. 92–93, 293–301.
- Dhar, N., Islam, M., Islam, S., & Mithu, M. (2006). The influence of minimum quantity of lubrication (MQL) on cutting temperature, chip and dimensional accuracy in turning AISI-1040 steel. *Journal*

of Materials Processing Technology, 171, 93–99.

- Dosbaeva, J., Fox-Rabinovich, J., Dasch, & Veldhuis, S. (2008). Enhancement of wet- and MQL-based machining of automotive alloys using cutting tools with DLC/polymer surface treatments. *Journal of Materials Engineering and Performance*, 17(3), 346–351.
- Dunstan, D. J., Bushby, A. J., & Li, Y. (2015). The Hall-Petch effect as a manifestation of the general grain size effect. *Proceedings of The Royal Society A Mathematical Physical and Engineering Sciences*.
- Gahr, K. H. Z. (1987). Tribology Series. *Sliding Wear*, 10, 351–495.
- Galen, P. M., & Feiters, M. C. (2016). *Mass Spectrometry part of the Instrumental Analysis in (Bio) Molecular Chemistry*. October, 1–65.
- Garbiec, D., & Siwak, P. (2019). Microstructure and properties of WC-Co and WC-FeNi cemented carbides produced by FAST / SPS. *National Workshop on Spark Plasma Sintering, October*, 8–11. <https://www.researchgate.net/publication/337102724>
- Garside, M. (2019). Distribution of tungsten consumption worldwide between 2012 and 2016, by country. *Global Tungsten Consumption Share by Country 2012-2016*. <https://www.statista.com/statistics/1009699/tungsten-consumption-distribution-worldwide-by-country/>
- Genga, R. M. (2014). *MICROSTRUCTURE AND PROPERTIES OF SELECTED WC-CEMENTED CARBIDES MANUFACTURED BY SPS METHOD*. September.
- Genga, R. M., Cornish, L. A., Woydt, M., Polese, C., & JanVanVuuren, A. (2016). NbC: A MACHINING ALTERNATIVE FOR DRY AND MQL FACE-MILLING OF GREY CAST IRON (GCI). *Wold PM2016 Congress. Engineering, Mechanical, Industrial & Aeronautical, South Africa, Bs 1452*, 1–6.
- Genga, R. M., Rokebrand, P., Cornish, L. A., Zeman, P., Brajer, J., Woydt, M., van Vuuren, A. J., & Polese, C. (2020). Roughing, semi-finishing and finishing of laser surface modified nickel bonded NbC and WC inserts for grey cast iron (GCI) face-milling. *International Journal of Refractory Metals and Hard Materials*, 86(October 2019). <https://doi.org/10.1016/j.ijrmhm.2019.105128>
- German, R. M., Ma, J., Wang, X., & Olevsky, E. (2006). Processing model for tungsten powders and extension to nanoscale size range. *Powder Metallurgy*, 49(1), 19–27. <https://doi.org/10.1179/174329006X94690>
- German, R. M., Suri, P., & Park, S. J. (2009). Review: Liquid phase sintering. *Journal of Materials Science*, 44(1), 1–39. <https://doi.org/10.1007/s10853-008-3008-0>

- Ghani, J. A., Haron, C. H. C., Hamdan, H. S., Md Said, A. Y., & Tomadi, S. T. (2013). Failure mode analysis of carbide cutting tools used for machining titanium alloy. *Ceramics International*, 39(1), 4449–4456.
- Ginting, Y. R., Boswell, B., Biswas, W., & Islam, M. N. (2015). Investigation into alternative cooling methods for achieving environmentally friendly machining process. *Procedia CIRP*, 29(December), 645–650. <https://doi.org/10.1016/j.procir.2015.02.184>
- Grosz, P., & Geralt, T. (1971). German Combat Planes: A Comprehensive Survey and History of the Development of German Military Aircraft from 1915 to 1945. *New York: Doubleday*.
- Han, Y. H., & Nishimura, T. (2014). Guest editorial : Spark plasma sintering. *Advances in Applied Ceramics*, 113(2), 65–66. <https://doi.org/10.1179/1743675314Z.000000000184>
- Harradine, P., & Quinlivan, J. T. (1989). Composites and the Commercial Jet – A Boeing Viewpoint. *AIAA-89-2126, Aircraft Design and Operations Conference*.
- Heindl, R. A., & Mong, L. E. (1936). YOUNG ' S MODULUS OF ELASTICITY , STRENGTH , AND EXTENSIBILITY OF REFRACTORIES IN TENSION. *Part of Journal of Research of the National Bureau of Standards*, 17.
- Henry, R. C., & McGraw, H. (1991). Industrial and Engineering Materials. *Science and Technology of Wood: Structure, Properties, Utilization*.
- Herring, C. (1950). Effects of Change of Scale on Sintering Phenomena. *J. Appl. Phys*, 21(4), 301–303.
- Huang, S. G., Vleugels, J., Mohrbacher, H., & Woydt, M. (2016). *Densification and tribological profile of niobium oxide WEAR*. 352–353, 65–71.
- Huang, S. G., Vleugels, J., Vanmeensel, K., Mohrbacher, H., & Woydt, M. (2015). Microstructure and Mechanical Properties of NbC Matrix Cermets Using Ni Containing Metal Binder Proc. *Euro PM2015 – Hard Materials, Reims, France*.
- Hutchings, I., Gee, M., & Santner, E. (2006). Friction and Wear. *Springer Handbook of Materials Measurement Methods*.
- Imran, M., & Khan, A. R. A. (2019). Characterization of Al-7075 metal matrix composites: A review. *Journal of Materials Research and Technology*, 8(3), 3347–3356. <https://doi.org/10.1016/j.jmrt.2017.10.012>
- Ingle, S. S. (1993). The micromechanisms of cemented carbide cutting tool wear. *Doctoral Thesis, McMaster University Hamilton, Ontario*.
- Irfan, U., Kubilay, A., & Fevzi, B. (2013). An experimental investigation of the effect of coating

- material on tool wear in micro milling of Inconel 718 super alloy. *Wear*, 300(1/2), 8–19.
- Itoigawa, F., Childs, T. H. C., Nakamura, T., & Belluco, W. (2006). Effects and mechanisms in minimal quantity lubrication machining of an aluminum alloy. *Wear*, 260, 339–344.
- Jabbar, M. A. (2018). Metalworking Fluid Exposure and Consequences on Skin Health in a Metal Machining Factory: Review Article. *International Journal for Empirical Education and Research*, April, 27–35. <https://doi.org/10.35935/edr/24.3527>
- Jantunem, E. (2002). A summary of methods applied to tool condition monitoring in drilling. *International Journal of Machine Tools and Manufacture*, 997–1010.
- Jayal, A. D., & Balaji, A. K. (2009). Effects of cutting fluid application on tool wear in machining: Interactions with tool-coatings and tool surface features. *Wear*, 267(9/10), 1723–1730.
- Jilani. (2014). *Difference Between Aluminum and Titanium*. *Differencebetween.net*.
- Kaynak, Y., Gharibi, A., Umit, Y., & Aslantas, K. (2021). *A comparison of flood cooling , minimum quantity lubrication and high pressure coolant on machining and surface integrity of titanium Ti-5553 alloy A comparison of fl ood cooling , minimum quantity lubrication and high pressure coolant on machining and su. August 2018*. <https://doi.org/10.1016/j.jmapro.2018.06.003>
- Kim, H., & Kim, D. (2015). Water Lubrication of Stainless Steel using Reduced Graphene Oxide Coating. *Nature Publishing Group, C*, 1–13. <https://doi.org/10.1038/srep17034>
- Koné, F., Czarnota, C., Haddag, B., & Nouari, M. (2013). Modeling of velocity-dependent chip flow angle and experimental analysis when machining 304L austenitic stainless steel with groove coated-carbide tools. *Journal of Materials Processing Technology*, 213(7), 1166–1178.
- Kouam, J., Masounave, J., & Songmene, V. (2010). Pre-holes Effect on Cutting Forces and Particle Emission During Dry Drilling. *49th Annual Conference of Metallurgists of CIM. Vancouver, BC, Canada*, 253–263.
- Kuczynski, C. G. (1949). Self-diffusion in Sintering of Metallic Particles. *J. Metals*, 1(2), 169–178.
- Kwon, O. H., & Messing, G. L. (1990). *J Am Ceram Soc.* 73, 275. <https://doi.org/10.1111/j.1151-2916.1990.tb06506.x>
- Lawal, S. A., Choudhury, A. I., & Nukman, Y. (2013). Developments in the formulation and application of vegetable oil-based metalworking fluids in turning process. *International Journal of Advanced Manufacturing Technology*, 67(1765–1776).
- Lekam, O. N. (2016). Optimizing the surface integrity of machined Ti-6Al-4V using advanced carbide inserts and minimum quantity lubrication. *University of Witwatersrand, School of Mechanical*,

- Leo Dev Wins, K., & Varadarajan, K. A. (2012). Simulation of surface milling of hardened AISI4340 steel with minimal fluid application using artificial neural network. *Advances in Production Engineering & Management*, 7(1), 51–60.
- Li, K. M. (2006). *Predictive modeling of near dry machining: mechanical performance and environmental impact.*
- Luigino, F., Fabrizio, M., Settineri, L., & Umbrello, D. (2007). Wear modelling in mild steel orthogonal cutting when using uncoated carbide tools. *Wear*, 262, 545–554.
- MaClure, T. F., Adams, R., Gugger, M. D., & Gressel, M. (2007). *Comparison of Flood vs. Microlubrication on Machining Performance.* available: http://www.unist.com/pdfs/articles/AR_flood_v_micro.pdf
- Mamedov, V. (2002). *Spark plasma sintering as advanced PM sintering method.* 45(4), 322–327. <https://doi.org/10.1179/003258902225007041>
- Marinescu, I. D., Rowe, W. B., Dimitrov, B., & Inasaki, I. (2004). *Tribology of Abrasive Machining Processes. Chapter 14: Processes Fluids for Abrasive Machining.* 531–585.
- Mataix, D. B. (2016). Non-conventional sintering techniques. *Universitat Politècnica de València Instituto de Tecnología de Materiales Spain*, 1–34.
- Metal-Supermarkets. (2015). 7 Things to consider when choosing an aluminium grade, Aluminium tips and hints. *Aerospace Industry.*
- Mezlini, S. (2002). *Relationship between Hardness and Abrasive Wear for some Aluminium Alloys. March 2016.* <https://doi.org/10.4028/www.scientific.net/MSF.396-402.1517>
- Mohammad, A. K., Abdullah, Y., Shazali, S. T. S., Islam, M. S., & Mohd Said, M. A. (2017). Study Of Cutting Edge Temperature And Cutting Force Of End Mill Tool In High Speed Machining. *University of Malaysia Sarawak (UNIMAS), Malaysia.*
- Mohammed, I., & Anwar Khan, R. A. (2019). Characterization of Al-7075 metal matrix composites. *A Review*, 3347–3356.
- Mohan, K., Suresh, J. A., Ramu, P., & Rengaswamy, J. (2016). Microstructure and Mechanical Behavior of Al 7075-T6 Subjected to Shallow Cryogenic Treatment. *Journal of Materials Engineering and Performance.*
- Muhammad, B. B., Wan, M., Feng, J., & Zhang, W. (2017). Dynamic Damping of Machining Vibrations. *A Review.*

- Murugan, S. S. (2020). Mechanical Properties of Materials: Definition, Testing and Application. *International Journal of Modern Studies in Mechanical Engineering (IJMSME)*, 6(2), 28–38. <https://doi.org/http://doi.org/10.20431/2454-9711.0602003>
- Naves, G. V. T., Da Silva, B. M., & Da Silva, J. F. (2013). Evaluation of the effect of application of cutting fluid at high pressure on tool wear during turning operation of AISI 316 austenitic stainless steel. *Wear*, 302, 1201–1208.
- Nelson, R. J., & Millner, D. R. (1972). *Powd. Met*, 15(30), 347.
- Nesterenko, G. I., Kulemin, A. V., S, K. A., & Basco, V. N. (2019). Comparison of the characteristics of modern aluminum alloys. *Article in Zavodskaya Laboratroya. Diagnostika Materialov*, 85(7), 50–55.
- Nguyen, O. (2018). Mechanical Properties of Metal Definition. *Tulsa Welding Shool*. <https://www.tws.edu/blog/welding/what-are-the-mechanical-properties-of-metals/>
- Niobelcon. (2007). Summary of health & safety classifications and labeling within REACH (extract). *Niobium Carbide*. https://www.niobelcon.com/NiobelCon/niobium/niobium_carbide/
- Norgren, S., Garcia, J., Blomqvist, A., & Yin, L. (2015). Trends in the p/m hard metal industry. *Int. J. Refract. Met. Hard Mater*, 48(31).
- Odelros, S. (2012). *Tool Wear in Titanium Machining.Pdf*. 31(1), 75–80.
- Palanikumar, K., Muthukrishnan, N., & Hariprasad, K. S. (2008). Surface roughness parameters optimization in machining A356/SiC/20p metal matrix composites by PCD tool using response surface methodology and desirability function. *Machining Science and Technology*, 12(4), 529–545. <https://doi.org/10.1080/10910340802518850>
- Parhad, P., Likhite, A., Bhatt, J., & Peshwe, D. (2015). The Effect of Cutting Speed and Depth of Cut on Surface Roughness During Machining of Austempered Ductile Iron. *Transactions of the Indian Institute of Metals*, 68, 99–108.
- Popa, A., Dessen, G., Baili, M., & Dutilh, V. (2012). Investigation of tool failure modes and machining disturbances using monitoring signals. *Advanced Materials Research*, 423(December), 128–142. <https://doi.org/10.4028/www.scientific.net/AMR.423.128>
- Prakash, L., & Vinod, K. S. (2014). fundamentals and general applications of hardmetals. *Comprehensive Hard Materials*, 29.
- Rabiei, F., Rahimi, A. R., Hadad, M., & Ashrafiyou, M. (2015). Performance improvement of minimum quantity lubrication (MQL) technique in surface grinding by modelling and optimization. *Journal of Cleaner Production*, 86.

- Rahman, M., Kumar, A. S., & Ling, M. (2003). Effect of chilled air on machining performance in end milling. *The International Journal of Advanced Manufacturing Technology*, 21, 787–795.
- Ravi, S., & Kumar, P. (2011). Experimental investigations on cryogenic cooling by liquid nitrogen in the end milling of hardened steel. *Cryogenics*, 51, 509–515.
- Reutte. (2017). Tungsten in 2017. *International Tungsten Industry Association: End Use Consumption*.
- Rozzi, J. Z., Sanders, J. K., & Chen, W. (2010). The experimental and theoretical evaluation of an indirect cooling system for machining. *J. Heat Transfer*, 133(3), 1–10.
- Sairavali, M. S., & Dr. Reddy, M. A. (2020). *Optimization of machining parameters for face milling operations in vertical CNC milling machine using Taguchi method*.
- Saito, S., Ishiyama, T., & Sawaoka, A. (1974). *Bull. Tokyo, Inst. Technol.*, 120, 137.
- Saito, S., & Sawaoka, A. (1973). *Powder Metall.* 5, 70.
- Saverio, A. (2014). Tribological interactions of modern biomaterials used in total hip arthroplasty (THA). *Perspectives in Total Hip Arthroplasty*, Woodhead Publishing, 99–116. <https://www.sciencedirect.com/science/article/pii/B9781782420316500076>
- Schwed, P. (1951). Surface Diffusion in Sintering of Spheres on Planes. *J. Metals*, 3, 245.
- Sedla, M., Bati, B., & Podgornik, B. (2019). *Influence of the substrate hardness and fracture toughness on the dynamic wear properties of coated tool steels INFLUENCE OF THE SUBSTRATE HARDNESS AND FRACTURE TOUGHNESS ON THE DYNAMIC WEAR PROPERTIES OF COATED TOOL STEELS VPLIV TRDOTE IN LOMNE @ ILAVOST. October 2020.* <https://doi.org/10.17222/mit.2018.242>
- Singh, B. A., & Singh, G. (2017). *Study of Mechanical Properties Of Al 7075 Alloy after Heat Treatment*. 35(1539020), 1–35. <https://doi.org/10.13140/RG.2.2.14392.44801>
- Siniawski, M., & Bowman, C. (2009). Metal working fluids: finding green in the manufacturing process. *Industrial Lubrication and Tribology*, 61(2), 60–66.
- Snowball, R. F., & Millner, D. R. (1968). *Powd. Met*, 11(21), 23.
- Songmene, V., Khettabi, R., Zaghbani, I., Kouam, J., & Djebar, A. (2011). Machining and Machinability of Aluminum Alloys. *Aluminium Alloys, Theory and Applications*, February. <https://doi.org/10.5772/14888>
- Souto, M. V. M., De Araujo, C. P. B., Lima, M. J. S., Borges, F. M. M., Gomes, U. U., & De Souza, C. P. (2018). Synthesis and characterization of niobium carbide with copper addition obtained via gas solid reaction. *Materials Research*, 21(3). <https://doi.org/10.1590/1980-5373-MR-2016-1108>

- Straffelini, G. (2015). Lubrication and lubricants. *Springer Tracts in Mechanical Engineering*, 11, 61–84. https://doi.org/10.1007/978-3-319-05894-8_3
- Sun, J., Zhao, J., Gong, F., Ni, X., & Li, Z. (2019). Development and Application of WC-Based Alloys Bonded with Alternative Binder Phase Development and Application of WC-Based Alloys Bonded with Alternative. *Critical Reviews in Solid State and Materials Sciences*, 44(3), 211–238. <https://doi.org/10.1080/10408436.2018.1483320>
- Survey. (2015). An update to the supply risk index for elements or element groups that are of economic value. *Survey, British Geological*.
- Tai, B. L., Dasch, J. M., & Shih, A. J. (2011). Evaluation and comparison of lubricant properties in minimum quantity lubrication machining. *Machining Science and Technology*, 15(4), 376–391. <https://doi.org/10.1080/10910344.2011.620910>
- Tash, M., Samuel, F. H., Mucciardi, F., Doty, H. W., & Valtierra, S. (2006). Effect of metallurgical parameters on the machinability of heat-treated 356 and 319 aluminum alloys. *Materials Science and Engineering*, 434, 207–217.
- TotalMateria. (2012). *Spark Plasma Sintering*. <https://www.totalmateria.com/page.aspx?ID=CheckArticle&site=ktn&NM=292>
- Totten, G. E., & MacKenzie, D. S. (2003). Handbook of Aluminum, Vol. 1: Physical Metallurgy and Process. *Marcel Dekker Inc., New York*, 114–168.
- Turkes, E., Orak, S., Neselie, S., & Yaldiz, S. (2011). Linear analysis of chatter vibration and stability for orthogonal cutting in turning. *International Journal of Refractory Metals and Hard Materials*, 29, 163–169.
- Turner, P., & St. Nowarra, J. H. (1971). An Aircraft Album. *New York*. <https://doi.org/ISBN 0-668-02506-9>
- Upadhyaya, G. S. (1998). CEMENTED TUNGSTEN CARBIDES. Production, Properties and Testing. In *Indian Institute of Technology, Kanpur, India* (Vol. 5, Issue 30 V). <http://www.sciencedirect.com/science/article/pii/B9780815514176500101%5Cnhttp://www.sciencedirect.com/science/article/pii/B9780815514176500198%5Cnhttp://www.sciencedirect.com/science/article/pii/B9780815514176500186%5Cnhttp://www.sciencedirect.com/science>
- Upadhyaya, G. S., Tobergte, D. R., & Curtis, S. (1998). CEMENTED TUNGSTEN CARBIDES. Production, Properties and Testing. In *Indian Institute of Technology* (Vol. 5, Issue 30 V). <http://www.sciencedirect.com/science/article/pii/B9780815514176500101%5Cnhttp://www.sciencedirect.com/science/article/pii/B9780815514176500198%5Cnhttp://www.sciencedirect.com/s>

- Varga, M. (2017). High temperature abrasive wear of metallic materials. *AC2T Research GMBH*, 376–377, 443–451.
- Viktor, P. A. (2011). Turning, Tool wear types and common tool wear evaluation characteristics. *Modern Machining Technology*. <https://doi.org/Standard ISO 3685:1993>
- Wang, S., & Clarens, A. F. (2013). Analytical model of metalworking fluid penetration into the flank contact zone in orthogonal cutting. *Journal of Manufacturing Processes*, 15(1), 41–50.
- Warren, A. S. (2004). Developments and challenges for aluminum - A boeing perspective. *Materials Forum*, 28, 24–31.
- Wayne, S. F. (2016). *Cutting Tool Materials: Mechanical Properties - Wear Resistance Relationships*. January. <https://doi.org/10.1080/05698198608981695>
- Wichmann, H., Stache, H., Schmidt, C., Winter, M., Bock, R., Herrmann, C., & Bahadir, M. (2013). Ecological and economic evaluation of a novel glycerol based biocide-free metalworking fluid. *Journal of Cleaner Production*, 43, 12–19.
- Woods, S. (2005). Going green. *Cutting Tool Engineering*, 57(2).
- Woydt, M., & Mohrbacher, H. (2014). The tribological and mechanical properties of niobiumcarbides (NbC) bonded with cobalt or Fe₃Al. *Wear*321, 321, 1–7.
- Wright, P. K., & Bagchi, A. (1981). Wear mechanisms that dominate Tool-life in Machining. *Journal of Applied Metalworking*, 1, 15–23.
- Wstawska, I., & Slimak, K. (2016). The influence of cooling techniques on cutting forces and surface roughness during cryogenic machining of titanium alloys. *Arch. Mech. Tech*, 36, 12–16.
- Xu, C., Dou, J., Chai, Y., Li, H., Shi, Z., & Xu, J. (2018). *The relationships between cutting parameters, tool wear, cutting force and vibration*. 10(1), 1–14.
- Ya, I. F. (1945). Viscous Flow of Crystalline Bodies under Action of Surface Tension. *J. Phys (U.S.S.R.)*, 9, 385.
- Yan, X. T., Jiang, C., & Eynard, B. (2008). Advanced Design and Manufacture to Gain a Competitive Edge. *New Manufacturing Techniques and Their Role in Improving Enterprise Performance*, Springer-Verlag, London, UK.
- Yoshio, B. (2015). Extra super duralumin and successive aluminum alloys for aircraft. Journal of Japan Institute of Light Metals. *Sumitomo Light Metal Ind. Ltd., Japan*, 39(5), 378.

Zadshakoyan, M., & Pourmostaghimi, V. (2015). Cutting Tool Crater Wear Measurement in Turning Using Chip Geometry and Genetic Programming. *International Journal of Applied Metaheuristic Computing*, 6(1), 47–60. <https://doi.org/10.4018/ijamc.2015010104>